PEOPLE'S DEMOCRATIC REPUBLIC OF ALGERIA

MINISTRY OF HIGHER EDUCATION AND SCIENTIFIC RESEARCH

UNIVERSITY OF ECHAHID HAMMA LAKHDAR – EL OUED

FACULTY OF EXACT SCIENCES

DEPARTMENT OF CHEMISTRY

رقم الترتيب: .....

رقم التسلسل: .....

MASTER'S THESIS

Submitted in partial fulfillment of the Requirements for Professional Master's degree

Field: Chemistry

Specialization: Analytical Chemistry

THESIS TITLE

Intelligent Design of a Novel Nanocomposite for Eco-Circular Applications: Wastewater Remediation, Bioactivity, and Irrigation Using RSM Mapping and AI-Driven Optimization

Defended on: June 14, 2026

Presented by:

Abdesslam Soltani

Mouna Slimani

Before the Examination Committee:

Name	Rank	Role	Affiliation
Ammar Zobeidi	Professor	Chairperson	University of Echahid Hamma Lakdar – El Oued
Ahmed Mehellou	Professor	Examiner	University of Echahid Hamma Lakdar – El Oued
Larbi Haddad	Professor	Supervisor	University of Echahid Hamma Lakdar – El Oued

Academic Year: 2025/2026


بسم الله الرحمن الرحيم

Thesis Acknowledgements

First and foremost, we would like to express our deepest gratitude to our supervisor, **Prof. Larbi Haddad**, for his invaluable guidance, unwavering support, and immense patience throughout this research. His profound expertise, insightful critiques, and continuous encouragement were instrumental in shaping this work and inspiring our academic growth. We are truly honored to have conducted our research under his exceptional supervision.

We are also sincerely grateful to **Prof. Ammar Zobeidi** for honoring us by serving as the Chairman of the examination committee, and to **Prof. Ahmed Mehellou** for serving as the Examiner and providing valuable insights and constructive feedback to improve this work.

Our sincere thanks go to the entire faculty and administrative staff of the Department of Chemistry for providing a supportive and stimulating academic environment.

We would like to extend our special appreciation to **Dr. Raouia Lebbihi** for her vital assistance and expertise in the gelatin synthesis and germination tests, and to **PhD student Zahra Itim** for her dedicated collaboration and support during the synthesis of the composite material.

Our heartfelt gratitude goes to **Dr. Yacine Labbi** for his outstanding contribution to the computational analysis and artificial intelligence-based optimization component of this work. His mastery of AI algorithms and their scientific applications, delivered with remarkable efficiency and expertise, significantly elevated the quality and depth of this research.

We express our sincere gratitude to **Prof. Nadji Tarchoun** (Higher Agronomic Institute of Chott-Mariem, Sousse) for his invaluable contribution to the statistical analysis of the germination studies.

We are highly indebted to the Research Laboratory of Applied Chemistry and the Environment (ACE) at the Faculty of Exact Sciences for generously hosting us and providing the hospitality and resources necessary to carry out a significant portion of the experimental work. In particular, we wish to thank the laboratory engineer, **Mr. Ali Tliba**, for his technical assistance and guidance.

Furthermore, we are grateful to the Department of Physics for granting us access and support to perform the X-ray diffraction (XRD) analyses, which were vital for our material characterization.

We also thank the pedagogical laboratories of the Faculty of Technology and the Faculty of Natural and Life Sciences for granting us access to the lyophilizator required for gelatin synthesis. Our appreciation is also extended to the pedagogical laboratories of the Department of Chemistry (Faculty of Exact Sciences), with a special note of gratitude to the engineers – **Mrs. Kenza**, **Mrs. Hafidha**, and **Mrs. Karima** – for their kind assistance and technical support.

In Memoriam

On a profound note, we wish to dedicate a special tribute to the memory of the late **Prof. Djamal Atia**, our esteemed former Head of the Department of Chemistry. Though this academic year began under his leadership and guidance, his untimely passing left a profound void. We honor his enduring scientific legacy, his dedicated service, and the human impact he left on our department; he remains deeply missed and respectfully remembered in our hearts and work.

Finally, we would like to thank everyone who contributed to this work, whether directly or indirectly, through their help, encouragement, and support.

الإهداء

أهدي نتائج هذا الجهد وعصارة هذا العمل

إلى التي أهدتني نور الحياة وتعهدت برعاية خطواتي ورسمت معي أحلام حياتي والدتي الحبيبة أطال الله في عمرها وأدامها لي نبعا صافيا أمحو به كدر الأيام.

إلى من زرع في قلبي حب العلم ووضع بين جنباتي القوة والعزيمة والدي الغالي الذي طالما شجعني وساعدني لإتمام دراستي حفظه الله لنا جميعا.

إلى إخوتي الأعزاء حفظهم الله.

إلى أساتذتي الكرام.

إلى كل الأهل والأصدقاء وزملائي الدراسة.

عبد السلام

الإهداء

الحمد لله الذي يسر لي البدايات وبلغنا النهايات

من قال أنا لها نالها

إلى الذي نرين اسمي بأجمل الألقاب، من دعمني بلا حدود وأعطاني بلا مقابل . . . .

من علمني أن الدنيا كفاح وسلاحه العلم والمعرفة

دعمي الأول في مسيرتي وسندي ومسندي وملاذي

بعد الله .

إلى فخري واعتزازي

. . .أبي الغالي . . .

إلى من جعل الله الجنة تحت أقدامها واحتضنني قلبها قبل يدها وسهلت لي الشدائد بدعائها

إلى القلب الحنون وسر قوتي ونجاحي

. . .أمي الحبيبة . . .

إلى ضلعي الثابت وأمان أيامي

إلى من شددت عضدي بهم فكانوا لي ينابيعًا ارتوي منها ، إلى خيرة أيامي وصفوتها إلى قرة عيناي

. . .إخوتي وأخواتي . . .

إلى من كان عونًا وسندًا في هذا الطريق . . .

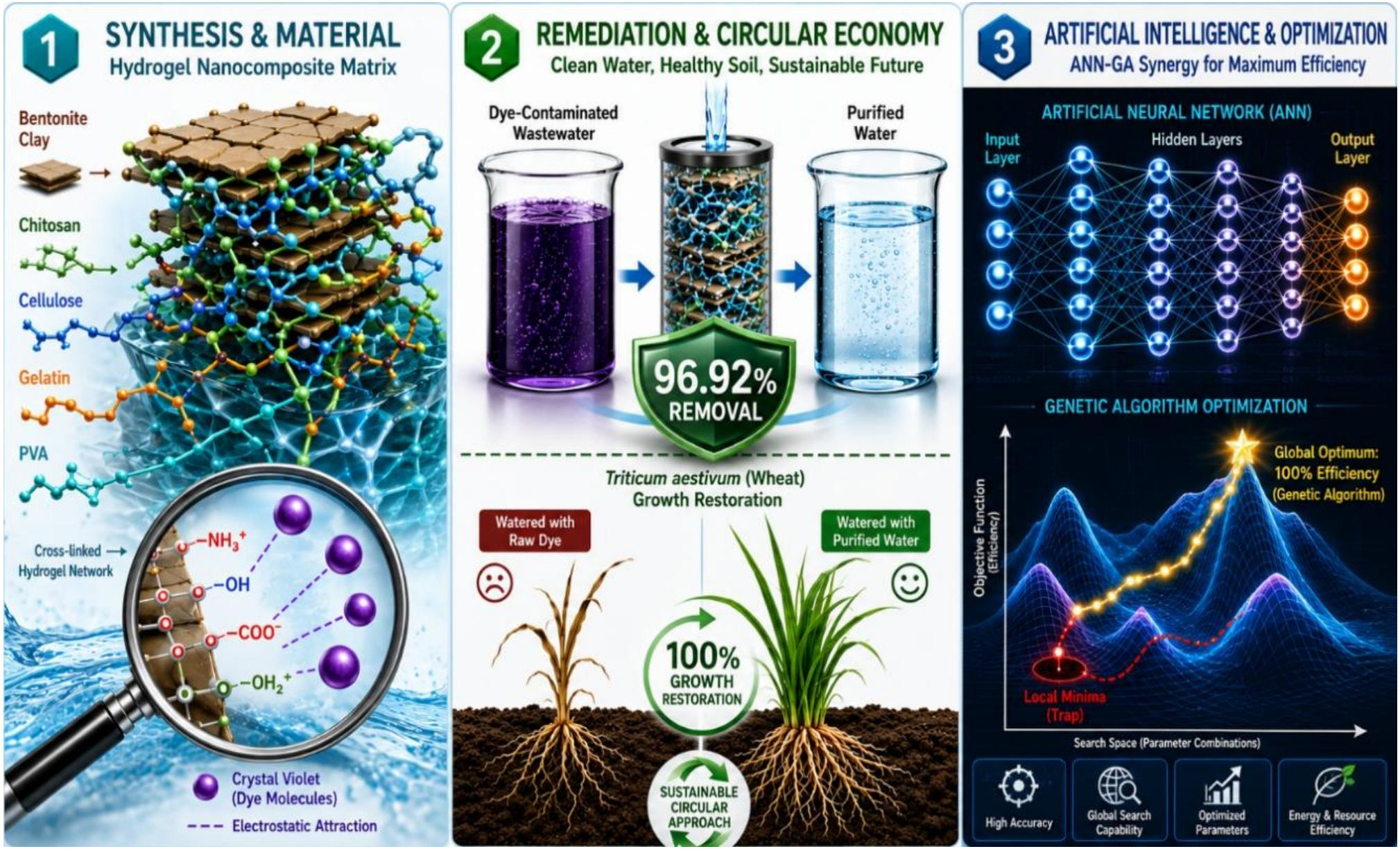
أُهديكم هذا الإنجاز وثمرة نجاحي الذي لطالما تمنيته

ها أنا اليوم أُكملت وأتممتُ أول ثمراته بفضله سبحانه وتعالى

فالحمد لله على ما وهبني

مُنى

Graphical Abstract



Abstract

The discharge of toxic industrial dyes like Crystal Violet severely threatens aquatic ecosystems. Because traditional treatment methods are expensive and energy-intensive, developing low-cost, multi-functional bio-sorbents offers a sustainable and sustainable path toward a circular environmental economy. To address this challenge, this study introduces a sustainable, multi-disciplinary solution: a novel, intelligent hybrid quinary nanocomposite matrix (BCCG/PVA) synthesized via a thermal cross-linked route. Characterization via FTIR-ATR and XRD confirmed dense active functional group integration and successful biopolymer chain intercalation within the silicate layers of the clay. Systematic batch adsorption experiments were carried out using BBD to map the combined effects of adsorbent mass, contact time, and solution pH. The material achieved an outstanding maximum empirical Crystal Violet removal efficiency of 96.92%, with equilibrium data fitting the Langmuir non-linear models. To ensure the treated effluent's safety for agricultural re-use, in vivo wheat seed (Triticum durum) germination assays were conducted; dye polluted wastewater caused severe stunted growth ($P < 0.0001$), whereas irrigation with the BCCG/PVA-remediated water completely reversed toxic stress. Additionally, advanced computational intelligence modeling was applied to optimize process automation. A comparative machine learning study revealed that a three-layer Artificial Neural Network (ANN) mapped multi-variable adsorption dynamics with superior precision ($R^2 = 0.9984$), compared to empirical Response Surface Methodology (RSM). To capture the true global operational optimum, evolutionary metaheuristic search tracks were evaluated; a Genetic Algorithm (GA) successfully bypassed local minima traps to achieve a 100% theoretical removal efficiency at a minimized adsorbent mass threshold ($m = 0.0487$ g, $t = 19.07$ min, $pH = 9.20$). Finally, in vitro therapeutic screenings proved that the smart composite exhibits powerful, dose-dependent antimicrobial zones of inhibition against Escherichia coli and Staphylococcus aureus, alongside excellent antifungal capabilities.

In conclusion, this work demonstrates that the smart cross-linked BCCG/PVA nanocomposite serves as an exceptionally efficient, safe, and robust platform that seamlessly bridges the gaps between high-performance environmental remediation, circular agricultural irrigation, biomedical material design, and advanced AI-driven process automation.

***Keywords**:* Water Treatment; Quinary hybrid bio-composites; Crystal Violet adsorption; Seed germination bioactivity; Artificial Neural Networks; Genetic Algorithm optimization.

الملخص

يُشكل تصريف الأصباغ الصناعية السامة، مثل البنفسجي البلوري، تهديدًا خطيرًا للنظم البيئية المائية. ونظرًا لارتفاع تكلفة طرق المعالجة التقليدية واستهلاكها الكبير للطاقة، فإن تطوير مواد مازة حيوية متعددة الوظائف ومنخفضة التكلفة يُعدّ مسارًا مستدامًا نحو اقتصاد بيئي دائري. ولمعالجة هذا التحدي، تُقدم هذه الدراسة حلًا مستدامًا متعدد التخصصات: مصفوفة نانوية هجينة خماسية جديدة وذكية BCCG/PVA تم تصنيعها عبر مسار الربط الحراري. وقد أكدت خصائصها، التي تم تحليلها باستخدام تقنيتي FTIR-ATR وXRD، تكاملًا كثيفًا للمجموعات الوظيفية النشطة وتداخلًا ناجحًا لسلاسل البوليمر الحيوي داخل طبقات السيليكات في الطين. أُجريت تجارب امتزاز منهجية على دفعات باستخدام تصميم بوكس-بنكن BBD لرسم خرائط التأثيرات المشتركة لكتلة المادة المازة، وقت التلامس، ودرجة حموضة المحلول. وقد حققت المادة كفاءة إزالة تجريبية قصوى متميزة للبنفسجي البلوري بلغت 96.92%، مع توافق بيانات التوازن مع معادلة نموذج لانغمير غير الخطية. لضمان سلامة المياه المعالجة لإعادة استخدامها في الزراعة، أُجريت اختبارات إنبات بذور القمح Triticum durum في الحقل؛ حيث تسببت المياه الملوثة بالأصباغ في توقف نمو حاد ($P < 0.0001$)، بينما أدى الري بالمياه المعالجة بمركب BCCG/PVA إلى عكس الإجهاد السام تمامًا. بالإضافة إلى ذلك، طُبقت نماذج ذكاء حسابي متقدمة لتحسين آلية العملية. وكشفت دراسة مقارنة للتعلم الآلي أن شبكة عصبية اصطناعية ثلاثية الطبقات ANN رسمت ديناميكيات الامتزاز متعددة المتغيرات بدقة فائقة $R^2 = 0.9984$، مقارنةً بمنهجية سطح الاستجابة التجريبية RSM. وللوصول إلى الوضع الأمثل التشغيلي العام الحقيقي، جرى تقييم مسارات البحث التطوري الميتاهوريستية. نجحت خوارزمية جينية في تجاوز مصائد الحد الأدنى المحلي لتحقيق كفاءة إزالة نظرية بنسبة 100% عند عتبة كتلة مُصغِّرة للمادة المازة $m = 0.0487$ غرام، $t =$ 19.07 دقيقة، $pH = 9.20$. وأثبتت التجارب العلاجية المخبرية أن المركب الذكي يُظهر مناطق تثبيط قوية مضادة للميكروبات تعتمد على الجرعة ضد بكتيريا الإشريكية القولونية والمكورات العنقودية الذهبية، إلى جانب قدرات ممتازة مضادة للفطريات.

في الختام، يُبين هذا العمل أن المركب النانوي الذكي المتشابك BCCG/PVA يُشكل منصة فعالة وآمنة وقوية للغاية، تُسد الفجوات بسلاسة بين المعالجة البيئية عالية الأداء، والري الزراعي الدائري، وتصميم المواد الطبية الحيوية، وأتمتة العمليات المتقدمة المدعومة بالذكاء الاصطناعي.

الكلمات المفتاحية: معالجة المياه؛ مركبات حيوية هجينة خماسية؛ امتزاز البنفسجي البلوري؛ النشاط الحيوي لإنبات البذور؛ الشبكات العصبية الاصطناعية. تحسين الخوارزمية الجينية.

Résumé

Le rejet de colorants industriels toxiques tels que le violet de cristal menace gravement les écosystèmes aquatiques. Les méthodes de traitement traditionnelles étant coûteuses et gourmandes en énergie, le développement de biosorbants multifonctionnels et peu coûteux offre une voie durable vers une économie circulaire. Pour relever ce défi, cette étude propose une solution durable et multidisciplinaire : une nouvelle matrice nanocomposite hybride quinaire intelligente (BCCG/PVA) synthétisée par une voie de réticulation thermique. La caractérisation par FTIR-ATR et XRD a confirmé une intégration dense de groupes fonctionnels actifs et une intercalation réussie de chaînes de biopolymères au sein des couches de silicate de l'argile. Des expériences d'adsorption par lots systématiques ont été menées à l'aide d'un BBD afin de cartographier les effets combinés de la masse d'adsorbant, du temps de contact et du pH de la solution. Le matériau a atteint une efficacité empirique maximale exceptionnelle d'élimination du violet de cristal de 96,92 %, les données d'équilibre s'ajustant aux modèles non linéaires de Langmuir. Afin de garantir la sécurité de l'effluent traité pour une réutilisation agricole, des essais de germination in vivo sur des graines de blé (Triticum durum) ont été menés ; les eaux usées contenant le colorant ont provoqué un retard de croissance sévère ($P < 0,0001$), tandis que l'irrigation avec l'eau traitée par le BCCG/PVA a complètement inversé le stress toxique. De plus, une modélisation avancée par intelligence computationnelle a été appliquée pour optimiser l'automatisation du processus. Une étude comparative d'apprentissage automatique a révélé qu'un réseau neuronal artificiel (RNA) à trois couches cartographiait la dynamique d'adsorption multivariable avec une précision supérieure ($R^2 = 0,9984$), par rapport à la méthodologie empirique de surface de réponse (RSM). Afin de déterminer le véritable optimum opérationnel global, des trajectoires de recherche métaheuristique évolutive ont été évaluées ; un algorithme génétique (AG) a réussi à contourner les pièges des minima locaux pour atteindre une efficacité d'élimination théorique de 100 % à un seuil de masse d'adsorbant minimisé ($m = 0,0487$ g, $t = 19,07$ min, $pH = 9,20$). Enfin, des criblages thérapeutiques in vitro ont démontré que le composite intelligent présente de puissantes zones d'inhibition antimicrobienne, dépendantes de la dose, contre Escherichia coli et Staphylococcus aureus, ainsi que d'excellentes capacités antifongiques.

En conclusion, ces travaux démontrent que le nanocomposite BCCG/PVA réticulé intelligent constitue une plateforme exceptionnellement efficace, sûre et robuste qui comble de manière transparente les lacunes entre la remédiation environnementale haute performance, l'irrigation agricole circulaire, la conception de matériaux biomédicaux et l'automatisation avancée des processus pilotée par l'IA.

Mots-clés : Treatment d'eau; Biocomposites hybrides quinaires ; Adsorption du cristal violet ; Bioactivité de germination des graines ; Réseaux neuronaux artificiels ; Optimisation par algorithmes génétiques.

List of Tables

Table	Title	Page
I.1	Approach Comparison: Top - down Vs Bottom – up	**11**
I.2	The most extensively recognized and employed green chemistry metrics	**13**
I.3	Method Comparison: Chemical Vs Green Synthesis	**14**
II.1	Physical Vs Chemical adsorption	**36**
III.1	List of chemical reagents, their CAS numbers, and Providers	**54**
III.2	Laboratory equipment and instruments	**55**
III.3	List of laboratory glassware and apparatus	**55**
III.4	Physicochemical properties of Crystal Violet & Methyl Orange dyes	**62**
III.5	Coded and actual variables and their levels in Box-Behnken Design	**64**
IV.1	Major Characteristic peaks and properties of BCCG/PVA components	**80**
IV.2	Average crystallite size calculations using various datapoints	**81**
IV.3	Comparison between the calculated CI and that of similar composites in the literature	**82**
IV.4	Analysis of Variance (ANOVA), Fit Statistics & Model Comparison Statistics	**87**
IV.5	Experimental and Predicted Values for Reaction Yield (R%)	**99**
IV.6	PFO & PSO model adsorption kinetic parameters at different concentrations	**102**
IV.7	Diffusion models constants for the adsorption of BCCG/PVA at different initial concentrations	**103**
IV.8	Adsorption isotherm models of Crystal Violet onto BCCG/PVA	**106**
IV.9	Thermodynamic parameters for CV adsorption at different temperatures	**109**
IV.10	ANOVA analysis of germination percentage, root length, shoot length, and SL/RL in germinated wheat seedlings under different irrigation treatments (Control, CV-treated, and CV-polluted)	**117**

IV.11	Experimental and model-predicted Crystal Violet removal efficiency (R%) for the 17 BBD runs, with corresponding absolute percentage errors for ANN, RSM, and ELM models	**118**
IV.12	Summary of predictive performance metrics (MAE, RMSE, MAPE, and R^2) for ANN, RSM, and ELM models evaluated on the BBD experimental dataset	**126**
IV.13	Statistical Performance and Computational Benchmarking of Metaheuristic Optimizers	**129**
IV.14	Run-by-Run Experimental Versus Predicted Dye Removal Efficiencies (R%) Using Metaheuristic Optimizers	**132**
IV.15	Critical Assessment of Consolidation Parameters, Complexity Metrics, and Localized Process Optimization Boundaries	**136**
IV.16	Effect of UV radiation on CV removal efficiency over time	**138**
IV.17	Results of antibacterial tests	**142**

List of Figures

Figure	Title	Page
I.1	Classification of Nanomaterial based on origin, composition and structure/dimensions	**8**
I.2	Principal of a modern UV – Vis spectrophotometer	**16**
I.3	A Typical ATR Accessory	**17**
I.4	Diagram of a common XRD instrumental layout	**19**
I.5	Modern SEM instrumentation diagram	**20**
II.1	Methods of water treatment via nano/composite materials	**33**
III.1	General Experimental Procedure Diagram	**56**
III.2	Crystal Violet (a) & Methyl Orange (b) dye UV-Vis spectrums	**62**
IV.1	Extracted Gelatin FTIR spectrum	**73**
IV.2	FTIR spectrums of the synthesized composite and its components: (A) BCCG/PVA Vs Chitosan; (B) BCCG/PVA Vs Cellulose & Bentonite; (C) BCCG/PVA Vs PVA & Gelatin	**75**
IV.3	FTIR spectral comparison between the soluble and granulated (bead) forms of the BCCG/PVA compound	**76**
IV.4	Effect of solution pH on the FT-IR spectra of the synthesized composite	**76**
IV.5	FTIR spectra of Crystal Violet as well as the hybrid composite before and after adsorption	**77**
IV.6	XRD diffractogram of BCCG/PVA before & After CV adsorption	**78**
IV.7	Scanning electron microscopy (SEM) images of the extracted camel bone gelatin powder: (a) at 300 μm scale, and (b) at 10 μm scale	**83**
IV.8	UV-Vis absorption spectrum of the extracted Gelatin	**84**
IV.9	ΔpH Vs Initial pH Graph for pHpzc Determination	**85**
IV.10	Preliminary adsorption efficiency screening of Methyl Orange and Crystal Violet dyes on the BCCG/PVA hybrid composite	**86**
IV.11	Predicted vs. Actual values	**90**

IV.12	One-Factor Plot	**92**
IV.13	The mutual interaction between BCCG/PVA dose and contact time	**94**
IV.14	The mutual interaction between adsorbent dose and pH	**95**
IV.15	The mutual interaction between contact time and pH	**95**
IV.16	The optimal values	**96**
IV.17	Influence of initial dye concentration and contact time on adsorption capacity	**101**
IV.18	Weber-Morris intra-particle diffusion plots	**103**
IV.19	Effect of concentration on equilibrium adsorption capacity	**105**
IV.20	Non-linear fit for adsorption Isotherms	**106**
IV.21	Van 't Hoff plot for Crystal Violet (CV) adsorption	**109**
IV.22	CV adsorption mechanism on BCCG/PVA	**112**
IV.23	Germination and seedling development of Triticum durum at day 2 and day 10 under Control, CV-Treated, and CV-Polluted conditions	**113**
IV.24	Effects of CV on germination percentage (%) of 10-day-old wheat seedlings under various irrigation treatments	**114**
IV.25	Effects of CV on root length of 10-day-old wheat seedlings under various irrigation treatments	**115**
IV.26	Effects of CV on shoot length of 10-day-old wheat seedlings under various irrigation treatments	**116**
IV.27	Effects of CV on SL/RL of 10-day-old wheat seedlings under various irrigation treatments	**117**
IV.28	Overlay of actual and model-predicted CV removal efficiency (R%) across the 17 BBD experimental runs for ANN, RSM, and ELM models	**119**
IV.29	Parity plots of predicted versus experimental removal efficiency (R%) for ANN, RSM, and ELM models	**121**
IV.30	Run-wise absolute percentage prediction error.	**122**

IV.31	Comparative bar chart of predictive error metrics (MAE, RMSE, and MAPE) for ANN, RSM, and ELM models applied to Crystal Violet adsorption data	**123**
IV.32	Coefficient of determination (R^2) for ANN, RSM, and ELM models	**124**
IV.33	Mean squared error (MSE) convergence curve of the ANN model during training over 10,000 epochs	**125**
IV.34	Correlation Parity Plots Mapping Experimental vs. Predicted Dye Removal Efficiency (R%)	**130**
IV.35	Comprehensive Visual Breakdown of Multi-Criteria Statistical Error Profiles Across All Implemented Frameworks	**131**
IV.36	Detached Multi-Panel Modeling Trajectories and Curve-Fitting Alignments Across Successive Design Points	**134**
IV.37	Consolidated Multi-Model Line Graph Mapping Experimental Versus Predicted Process Trajectories	**135**
IV.38	Photodegradation kinetics under intense UV radiation	**138**
V.39	Schematic representation of the agar well diffusion assay used to evaluate the antifungal activity of BCCG/PVA against Candida albicans and Aspergillus niger	**140**
IV.40	Antifungal activity of the BCCG/PVA against Candida albicans and Aspergillus niger	**141**
IV.41	Antibacterial activity of BCCG/PVA against Escherichia coli and Staphylococcus aureus	**142**
IV.42	*Schematic workflow of the 96-well microplate hemolysis assay used to evaluate the hemocompatibility of the nanocomposite BCCG/PVA.*	**144**
IV.43	*Hemolytic activity of the nanocomposite BCCG/PVA (coded NH) at different concentrations against human erythrocytes.*	**145**
IV.44	*Hemolytic activity of BCCG/PVA (Coded NH) at different concentrations. Bars represent mean hemolysis percentage, and error bars indicate standard deviation (n = 3).*	**145**

List of Appendices

Appendix	*Title*	*Page*
	Appendix A	
A.1	Benchtop centrifuge device (DLAB DM0412P)	*161*
A.2	Fourier-Transform Infrared Spectroscopy (FTIR) spectrometer equipped with Diamond ATR.	*161*
A.3	UV-Visible spectrophotometer (DLAB SP-V1100)	*162*
A.4	Laboratory freeze-dryer / Lyophilizer (Christ Alpha 1-4 LDplus).	*162*
A.5	Digital pH and temperature meter (Adwa AD1030)	*163*
A.6	Laboratory drying oven (ELES Heat)	*163*
A.7	High-capacity centrifuge instrument (Sigma 3-16L)	*164*
A.8	Double-beam UV-Vis spectrophotometer (Shimadzu UV-1900i).	*164*
A.9	Digital heating mantle with magnetic stirring.	*165*
A.10	Ultrasonic water bath (Powersonic).	*165*
A.11	Thermostatic shaking water bath (Memmert).	*166*
A.12	X-ray Diffractometer.	*166*
A.13	Phenom ESEM.	*167*
	Appendix B	
B.1	Experimental variations in dye removal efficiency under different optimized parameters via RSM.	*168*
B.2	Prepared gelatin solution gel.	*168*
B.3	Transparency and physical inspection of the structured biopolymer matrix.	*169*
B.4	Extracted camel bone ossein pieces obtained after the thermal extraction process of gelatin.	*169*
B.5	Formation of the hybrid bio-composite beads in alkaline coagulation bath.	*170*

B.6	Purified and dried gelatin powder extracted from camel bones.	*170*
B.7	Synthesized final hybrid bio-composite BCCG/PVA powder after drying and crushing.	*171*
B.8	Scanning electron microscopy (SEM) images of the BCCG/PVA powder: (a) Before Adsorption at 300 μm scale, and (b) After Adsorption at 5 μm scale.	*171*
B.9	BCCG/PVA – CV solutions in the UV chamber.	*172*

Appendix C

Plagiat Similarity Report	*173*

List of Abbreviations

Symbol	English Terminology	Arabic Terminology
ANN	Artificial Neural Networks	الشبكات العصبية الاصطناعية
ANOVA	Analysis of Variance	تحليل التباين
BBD	Box–Behnken Design	تصميم بوكس بنكن
BCCG/PVA	Bentonite – Chitosan – Cellulose – Gelatin – PVA	بنتونيت – شيتوزان – سليلوز – جيلاتين - PVA
C.V%	Coefficient of Variation	معامل الاختلاف
CV	Crystal Violet dye	صبغة البنفسجي البلوري
CFU	Colony Forming Unit	وحدة تكوين المستعمرة
COD	Chemical Oxygen Demand	الطلب الكيميائي للأكسجين
DO	Dissolved Oxygen	الأكسجين المذاب
EC	Electrical Conductivity	الناقلية الكهربائية
ELM	Extreme Learning Machines	آلات التعلم الفائق
FT-IR	Fourier Transform Infrared Spectroscopy	مطيافية الأشعة تحت الحمراء بتحويل فورييه
GA	Genetic Algorithms	الخوارزميات الجينية
GP	Germination Percentage	نسبة الإنبات
GWO	Grey Wolf Optimizer	خوارزمية محسن الذئب الرمادي
IUPAC	International Union of Pure and Applied Chemistry	الاتحاد الدولي للكيمياء البحتة والتطبيقية
MAE	Mean Absolute Error	متوسط الخطأ المطلق
MAPE	Mean Absolute Percentage Error	متوسط الخطأ المطلق النسبي
MHA	Mueller–Hinton Agar	آغار مولر هينتون
MO	Methyl Orange	صبغة المثيل البرتقالي
MSE	Mean Square Error	متوسط مربع الخطأ
NPs	Nanoparticles	جسيمات نانوية

PFO	Pseudo First Order	نموذج شبه الدرجة الأولى
pH_{pzc}	pH at the Point of Zero Charge	الرقم الهيدروجيني عند نقطة تعادل السطح
PSO	Particle Swarm Optimization	خوارزمية أمثلة سرب الجسيمات
PSO	Pseudo Second Order	نموذج شبه الدرجة الثانية
RL	Root Length	طول الجذر
RMSE	Root Mean Square Error	جذر متوسط مربع الخطأ
RSM	Response Surface Methodology	منهجية الاستجابة السطحية
SDA	Sabouraud Dextrose Agar	آغار سابورو دكستروز
SE mean	Standard Error of the Mean	الخطأ المعياري للمتوسط
SEM	Scanning Electron Microscopy	المجهر الإلكتروني الماسح
SL	Shoot Length	طول البرعم
Std. dev	Standard Deviation	الانحراف المعياري
TDS	Total Dissolved Solids	المواد الصلبة الذائبة الكلية
UV-Vis	Ultraviolet–Visible Spectroscopy	مطيافية الأشعة فوق البنفسجية والمرئية
VDW	Van der Waals Forces	قوى فاندر فالس
XRD	X-Ray Diffraction	حيود الأشعة السينية

Table of Contents

Acknowledgment		i
Dedications		ii
Abstracts		iii
List of Tables		iv
List of Figures		v
List of Appendices		vi
List of Abbreviations		vii
Table of Contents		viii
GENERAL INTRODUCTION		
General Introduction		1
General Introduction References		4
THEORETICAL PART		
Chapter I: Fundamentals of Nanomaterials Chemistry		
I.1	Introduction	7
I.2	Classification of Nanomaterials	7
I.2.1	Classification based on Composition	8
I.2.2	Classification based on Dimensions	9

I.2.3	Classification based on Origin	9
I.3	Techniques of Nanomaterial Synthesis	10
I.3.1	Comparative Study: Bottom–Up vs Top–Down	10
I.3.1.1	The Top-Down Approach	10
I.3.1.2	The Bottom-Up Approach	11
I.3.1.3	Comparison between the two approaches	11
I.3.2	Comparative Study: Chemical Synthesis vs Green Synthesis	12
I.3.2.1	Chemical Synthesis (Chemical Vapor Deposition & Sol-Gel)	12
I.3.2.2	Green Synthesis	12
I.4	Nanomaterial Characterization Techniques	14
I.4.1	Ultraviolet–Visible Spectroscopy (UV-Vis)	15
I.4.2	Fourier Transform Infrared spectroscopy (FT-IR)	16
I.4.3	X-ray Diffraction (XRD)	18
I.4.4	Scanning Electron Microscopy (SEM)	19
I.4.5	Surface Charge Analysis & pHpzc	21
Chapter One References		23
Chapter II: Adsorption Insights on Water Treatment		

II.1	Introduction to Water Pollution	29
II.1.1	Definitions and Concepts	29
II.1.1.1	Surface Water	29
II.1.1.2	Groundwater	29
II.1.1.3	Clean Water	29
II.1.1.4	Water Pollution	29
II.1.1.5	Turbidity	29
II.1.1.6	pH Level	29
II.1.1.7	Water Hardness	29
II.1.1.8	Total dissolved solids (TDS)	29
II.1.1.9	Electrical Conductivity (EC)	29
II.1.1.10	Dissolved Oxygen (DO)	29
II.1.1.11	Chemical oxygen demand (COD)	30
II.1.1.12	Alkalinity	30
II.1.1.13	Heavy Metals	30
II.1.1.14	Salinity	30
II.1.2	Sources of Water Pollution	30

II.1.3	Types and Classification of Pollutants	30
II.1.3.1	Organic Pollutants	30
II.1.3.2	Inorganic Pollutants	31
II.2	Fundamental Properties of Nanomaterials Related to Water Treatment	31
II.2.1	Reactivity and Surface Area	31
II.2.2	Chemical and Thermal Stability	31
II.2.3	Biological and Microbiological Properties	32
II.2.4	Catalysis Properties	32
II.2.5	Magnetic Properties	32
II.2.6	Functionalization	32
II.3	Water Treatment Methods Using Nanomaterials	33
II.3.1	Catalysis	33
II.3.2	Disinfection	34
II.3.3	Filtration	34
II.3.4	Adsorption	34
II.4	Adsorption in Water Treatment	34
II.4.1	Defining and distinguishing Adsorption	35

II.4.2	Types of adsorbents	35
II.4.3	Physical Vs Chemical Adsorption	36
II.4.4	Intermolecular forces behind physical adsorption	37
II.4.4.1	Dispersion forces	37
II.4.4.2	forces of interaction and repulsion	38
II.4.4.3	Dipole – dipole interactions	38
II.4.5	Bonding in chemical adsorption	38
II.4.6	Factors influencing adsorption	39
II.4.6.1	The characteristics of the adsorbent’s surface	39
II.4.6.2	Nature of Adsorbate	39
II.4.6.3	Contact Time	39
II.4.6.4	Temperature	39
II.4.6.5	Adsorbate concentration (Dose)	39
II.4.6.6	The pH	40
II.4.7.1	Adsorption Isotherms	40
II.4.7.2	The Langmuir Isotherm	40
II.4.7.3	The Freundlich Isotherm	41

II.4.7.4	The Sips Isotherm	41
II.4.7.5	The Toth Isotherm	42
II.4.8	Adsorption Kinetics	42
II.4.8.1	Pseudo-First-Order Model (PFO)	42
II.4.8.2	Pseudo-Second-Order Model (PSO)	43
II.4.8.3	Intraparticle Diffusion Model (Weber-Morris)	43
II.4.9	Adsorption Thermodynamics	44
II.5	Introduction to Intelligent Computational Modeling in Water Treatment	44
II.5.1	The Role of Digital Transformation and Machine Learning	44
II.5.2	Classical Statistical Regression vs. Heuristic Machine Learning	45
II.5.3	Artificial Neural Networks (ANN): Multilayer Perceptron and Backpropagation Architecture	46
II.5.4	Extreme Learning Machines (ELM): Randomized Single-Layer Feedforward Networks (SLFNs)	46
II.6	Applications & Uses of Treated Water in Irrigation	47
	Chapter Two References	48
EXPERIMENTAL PART		
Chapter III: Materials & Methods		
III.1	Materials, Reagents & Apparatus	54

III.2	Experimental Procedures & Methods	56
III.2.1	Gelatin Extraction (from Camel Bone)	57
III.2.1.1	Collecting Bone Samples	57
III.2.1.2	Sample preparation	57
III.2.1.3	Bone demineralization	57
III.2.1.4	Alkaline Treatment & Neutralization	57
III.2.1.5	Thermal Treatment	57
III.2.2	Bio-composite Preparation	58
III.2.2.1	Synthesis and Exfoliation of the Pillared Mineral Precursor	58
III.2.2.2	Preparation of the Polymer Matrix	58
III.2.2.3	Hybrid Composite Integration	58
III.2.2.4	Formation, Stabilization, and Rinsing of Composite Beads	59
III.2.3	Characterization of Synthesized Composite	59
III.2.3.1	Synthesis Yield	59
III.2.3.2	pHpzc Determination	60
III.2.3.3	Fourier-Transform infrared spectroscopy (FTIR)	60
III.2.3.4	UV-Visible Spectroscopy (UV-Vis)	60

III.2.3.5	X-Ray Diffraction	61
III.3	Adsorption Applications in Dye Removal	61
III.3.1.1	Model dyes options	61
III.3.1.2	Crystal Violet and Methyl Orange UV-Vis Spectrums	62
III.3.1.3	Crystal Violet and Methyl Orange Calibration Curves	63
III.4	Batch adsorption studies	63
III.5	Adsorption Efficiency Optimization Conditions via Response Surface Methodology (RSM)	64
III.5.1	Dye Removal Efficiency Evaluation	64
III.5.2	Defining the utilized Box-Behnken design	64
III.6	Influence of Contact Time and Adsorption Kinetics	65
III.7	Impact of Thermodynamic Parameters and Temperature	65
III.8	Seed Germination Bioassay & impacts on water phytotoxicity	65
III.9	Environmental Sensing and Photosensitivity Experiments	66
III.10	Biological Activity Assessment	66
Chapter Three References		68
Chapter IV: Results & Discussions		
IV.1	Characterization of Gelatin & BCCG/PVA	72

IV.1.1	Yield Determination	72
IV.1.2	Gelatin Extraction	72
IV.1.3	Composite Synthesis Yield	72
IV.1.4	Fourier Transform Infrared (FTIR) Spectroscopic Analysis	73
IV.1.4.1	Gelatin FTIR spectrums	73
IV.1.4.2	FTIR spectrum analysis for the synthesized composite & its components	74
IV.1.4.3	FTIR Analysis of the effect of gelation and bead formation	75
IV.1.4.4	FTIR analysis of composite stability at different pH levels	76
IV.1.4.5	FTIR analysis of the composite before and after adsorption	77
IV.1.5	XRD Analysis	78
IV.1.6	Scanning Electron Microscopy Morphological Analysis	83
IV.1.7	Gelatin UV–Vis spectrum	84
IV.1.8	Surface Charge Study & pHpzc Determination	85
IV.1.9	Preliminary Evaluation of MO and CV removal efficiencies	86
IV.2	Mathematical Modelling Using Response Surface Methodology (RSM)	87
IV.2.1	Analysis of Variance (ANOVA) for the Quadratic Model	87
IV.2.1.1	Mathematical and statistical significance	88

IV.2.1.2	Algebraic form	88
IV.2.1.3	The Physical Sense	88
IV.2.2	Fit Statistics	89
IV.2.2.1	Statistical and Mathematical Significance	89
IV.2.2.2	The Physical Sense	90
IV.2.3	The Final Equation in Terms of Coded Factors	90
IV.2.3.1	The algebraic form of the equation	90
IV.2.3.2	Statistical and Mathematical Significance	91
IV.2.4	Final Equation in Terms of Actual Factors	91
IV.2.4.1	Statistical and Mathematical Significance	91
IV.2.4.2	The Physical Sense	92
IV.2.5	One-Factor Plots	92
IV.2.5.1	Statistical and Mathematical Significance (Adsorbent Dose, Contact Time, pH Effects)	93
IV.2.5.2	The Physical Sense (Adsorbent Dose, Contact Time, pH Effects)	93
IV.2.6	Interaction Analysis	94
IV.2.6.1	Statistical and Mathematical Significance (Interactions between process parameters)	94
IV.2.6.2	The Physical Sense (Interactions between process parameters)	95

IV.2.7	The Desirability Function & Confirmation Experiment	96
IV.2.7.1	Statistical and mathematical significance	97
IV.2.7.2	Physical Sense	97
IV.2.8	Experimental Vs Predicted (RSM) removal efficiency values	99
IV.2.8.1	Predictive Accuracy of the RSM design	99
IV.2.8.2	Consistency with Statistical Fit	99
IV.2.8.3	Analysis of the response surface methodology model	100
IV.3	Contact Time Effect & Adsorption Kinetics	100
IV.3.1	Analysis of the Pseudo-First-Order (PFO) & Pseudo-Second-Order (PSO) model kinetics	101
IV.3.2	Analysis of Weber-Morris Intra-particle Diffusion Model Kinetics & Rate-Controlling Steps Studies	103
IV.4	Adsorption Isotherm Studies	105
IV.4.1	Suitability of the Langmuir model	107
IV.4.2	Suitability of the Freundlich model	107
IV.4.3	Suitability of the Sips model	108
IV.4.4	Suitability of the Toth model	108
IV.5	Adsorption Thermodynamics Analysis	109
IV.6	Adsorption Mechanism	110

IV.7	Treated Water & Irrigation: Seed Germination Study	113
IV.7.1	Effect of CV on Seed Germination Percentage (GP)	113
IV.7.2	Phytotoxic Effects on Root and Shoot Elongation	114
IV.7.2.1	Root Length Response	114
IV.7.2.2	Shoot Length and SL/RL Ratio	115
IV.8	Machine Learning Prediction of Crystal Violet Removal: Comparative Study of ANN, RSM, and ELM	118
IV.8.1	Experimental and Predicted Removal Efficiency (R%) with Absolute Errors	118
IV.8.2	Actual vs. Predicted Removal Efficiency Across the 17 BBD Runs	119
IV.8.3	Parity Plots of Predicted vs. Actual (R%) for ANN, RSM, and ELM	120
IV.8.4	Run-Wise Absolute Prediction Error for ANN, RSM, and ELM	122
IV.8.5	Comparison of Error Metrics (MAE, RMSE, MAPE) for ANN, RSM, and ELM	123
IV.8.6	Coefficient of Determination (R^2) Comparison: ANN, RSM, and ELM	124
IV.8.7	ANN Training Convergence Curve (MSE vs. Epoch, Log Scale)	125
IV.8.8	Statistical Performance Metrics for ANN, RSM, and ELM Models	126
IV.9	Extended Polynomial Modeling of Crystal Violet Adsorption Using Constrained Meta-heuristic Optimizers	127
IV.9.1	Empirical Formulations and High-Degree Parametric Interaction Modeling	128
IV.9.2	Computational Diagnostic Benchmarking via Multi-Criteria Error Metrics	129

IV.9.3	Correlation Parity Topographies and Model Residual Distributions	130
IV.9.4	Comparative Verification of Run-by-Run Experimental Tracking and Process Curves	132
IV.10	Advanced Application of BCCG/PVA in Environmental Sensing	137
IV.10.1	Experimental Procedure for Sensing/Degradation Systems	137
IV.10.2	Experimental Results and Kinetic Discussion	138
IV.10.2.1	Creation of an optical signal and its immediate kinetic reaction	139
IV.10.2.2	Linearity & Calibration Modelling for accurate Quantitative Detection	139
IV.10.2.3	Self-Cleaning Function & Sensor Durability	139
IV.11	BCCG/PVA Biological Activity Studies	139
IV.11.1	Evaluation of BCCG/PVA Antifungal Activity Against Candida albicans and Aspergillus niger	139
IV.11.1.1	Assay Results and Interpretation	141
IV.11.2	Assessment of BCCG/PVA Antibacterial Activity Against Escherichia coli and Staphylococcus aureus	141
IV.11.2.1	Assay Results and Interpretation	142
IV.11.3	In Vitro Evaluation of the hemolytic activity of the BCCG/PVA Using a 96-Well Microplate Assay	143
IV.11.3.1	Assay Results and Interpretation	145
Chapter Four References		147
General Conclusion		

General Conclusion		158
Appendices		
A	Equipment & Instruments	ix
B	Results & Products	x
C	Plagiat Similarity Report	xi

General Introduction

The phenomenon of rapid industrialization and urbanization in combination with climate change is currently one of the biggest threats for humanity in the 21st century. The adoption of international agreements like COP21 Paris Agreement has prompted the development of innovative scientific and industrial approaches that would lead to the creation of sustainable bio-materials that can replace harmful petroleum-based chemistry while maintaining its functional efficiency [1]. Among many materials being developed in accordance with this agenda, biopolymers – natural polymolecular structures obtained from plants, animals, and microorganisms – have received particular scientific interest due to the versatility of their chemical composition, biocompatibility, and renewability [2, 3]. When engineered and combined into composite architectures on a nanometric scale, biopolymers exhibit significantly improved functional properties making them suitable for use in various technological sectors including environmental science, food industry, medicine, and, most importantly, water purification [4, 5].

Among the most pressing dimensions of the global water crisis is the widespread contamination of natural water bodies by industrial effluents. Natural aquatic systems are increasingly compromised by a diverse spectrum of hazardous substances, including heavy metals, pesticides, pharmaceuticals, and synthetic organic dyes [6, 7]. These substances enter freshwater ecosystems through poorly regulated industrial discharge and persist due to their structural complexity and resistance to conventional biodegradation. Of all synthetic dye classes, triphenylmethane dyes are particularly problematic, combining high environmental persistence with severe biological toxicity. Crystal Violet (CV) – a cationic triphenylmethane dye widely employed in textile dyeing, medical diagnostics, printing inks, and bacteriological staining – exemplifies this concern. Even at sub-micromolar concentrations, CV exerts potent toxic, genotoxic, and carcinogenic effects on both human and aquatic organisms [8, 9]. It acts as a mitotic poison, promoting tumor growth in certain fish species, and has been associated with hepatotoxicity, respiratory distress, irreversible eye damage, and mutagenic effects in mammalian systems [9, 10]. Its recalcitrant aromatic structure further ensures that it persists in aquatic environments long after discharge, making its removal from wastewater an ecological and public health imperative [11].

A wide range of treatment technologies has been explored for the removal of synthetic dyes from wastewater, including chemical precipitation, membrane filtration, electrochemical destruction, and advanced oxidation processes [12]. While each approach carries certain merits, their widespread application is consistently limited by high energy demand, elevated

operational costs, and the production of toxic secondary sludge requiring further treatment [13, 14]. Adsorption has consistently emerged as the superior alternative for dye removal, distinguished by its operational simplicity, absence of secondary sludge, adaptability to trace-level contaminants, and high removal efficiencies [14, 15]. Its attractiveness is further amplified when the adsorbent is built from low-cost, renewable, and ecologically compatible precursors, an orientation that aligns adsorption science with the principles of green chemistry and circular economy thinking [15, 16].

Chitosan, a linear polysaccharide obtained through the deacetylation of chitin from crustacean seafood waste, stands as one of the most extensively studied biopolymeric platforms for adsorption-based water treatment. Its molecular backbone is densely functionalized with reactive primary amine ($–NH_2$) and hydroxyl (–OH) groups that confer strong electrostatic and chemical affinity for cationic pollutants such as CV [17, 18]. Despite these intrinsic advantages, pristine chitosan is hampered by its tendency to dissolve under acidic conditions and its limited mechanical integrity and thermal stability, which restrict its direct industrial deployment [17]. These shortcomings have driven sustained innovation in chitosan modification strategies, including cross-linking, functional grafting, and the design of hybrid composite matrices incorporating clays, proteins, and synthetic polymers, to engineer adsorbents that retain the biopolymer's binding capabilities while overcoming its structural limitations [18, 19].

To address these challenges comprehensively, the present work proposes a novel thermally cross-linked, green-synthesized multicomponent composite integrating five functionally complementary materials: chitosan, gelatin, cellulose, bentonite, and polyvinyl alcohol (PVA). Each constituent was selected for a specific and irreplaceable role within the composite architecture, and their synergistic assembly through a green, thermally driven synthesis protocol avoids the use of toxic chemical cross-linkers while delivering a structurally robust and environmentally compatible material. Chitosan serves as the primary cationic biopolymeric backbone, providing the dominant amino- and hydroxyl-functional binding domains for CV adsorption. Gelatin, a hydrophilic protein derived from collagen hydrolysis, contributes a flexible, microporous protein matrix that facilitates mass transfer kinetics and introduces additional carboxylate and amine functional groups [20, 21]. Cellulose, a natural polymer, reinforces the composite through its fibrous microstructure, expanding the available surface area [22]. Bentonite, a low-cost aluminosilicate clay mineral with a high cation-exchange capacity, large inherent surface area, and outstanding

mechanical and thermal stability [23, 24]. Finally, polyvinyl alcohol (PVA), a synthetic polymer, reinforces the entire composite through a dense network of hydrogen bonds that eliminate acid solubility and mechanical fragility [25, 26].

The scope of this work extends deliberately beyond material synthesis and characterization. Treated wastewater is rarely approached as a resource, yet its safe valorization for agricultural reuse represents a meaningful dimension of a truly circular water management strategy, particularly in water-scarce regions. This study therefore investigates the phytotoxicity of the post-treatment effluent through standardized seed germination bioassays, assessing whether decontaminated water meets the biological safety threshold for non-consumptive irrigation applications [27, 28]. In parallel, the composite itself is evaluated for inherent biological activity, examining whether its constituent materials confer antimicrobial or other ecologically relevant properties.

To navigate the multi-variable complexity of both the adsorption and photocatalytic processes, where solution pH, adsorbent dosage, and contact time interact in non-linear ways, this study adopts an integrated computational optimization framework coupling Response Surface Methodology (RSM) with two artificial intelligence models: Artificial Neural Networks (ANN) and Extreme Learning Machines (ELM) [29, 30]. This dual modeling strategy moves decisively beyond the limitations of one-variable-at-a-time experimentation, capturing interaction effects, mapping response surfaces, and generating predictive models of practical value for process scale-up and real-world deployment [29, 31].

Taken together, this work delivers a coherent, multi-dimensional scientific contribution that spans green material synthesis, mechanistic adsorption and photocatalysis science, computational process optimization, and water valorization with environmental safety assessment. It is organized into four chapters: Chapter One establishing the theoretical foundations of nanomaterial chemistry; Chapter Two reviewing adsorption science and nanomaterials in the context of water treatment; Chapter Three detailing the materials, green synthesis protocols, and experimental methods; and Chapter Four presenting, interpreting, and critically discussing all results within their broader scientific and environmental context.

General Introduction References

[1] UNFCCC, Paris Agreement, United Nations Framework Convention on Climate Change, 2015.

[2] Crini, G.; Lichtfouse, E. Advantages and disadvantages of techniques used for wastewater treatment. Environ. Chem. Lett. 2019, 17, 145–155.

[3] Suyambulingam, I. et al. Chitosan biopolymer and its nanocomposites: Emerging material as adsorbent in wastewater treatment. Adv. Mater. Sci. Eng. 2023, 9387016.

[4] Geetha, P. et al. Biopolymeric nanocomposites for wastewater remediation: An overview on recent progress and challenges. Polymers 2024, 16, 210.

[5] Crini, G. et al. Chitosan, chitosan derivatives, and chitosan-based nanocomposites: eco-friendly materials for advanced applications. Front. Chem. 2023, 11, 1327426.

[6] Ahmad, A. et al. Recent advances in the removal of dyes from wastewater using low-cost adsorbents. J. Hazard. Mater. 2022, 139, 128321.

[7] Soltani, A.; Faramarzi, M.; Mousavi Parsa, S.A. A review on adsorbent parameters for removal of dye products from industrial wastewater. Water Qual. Res. J. 2021, 56(4), 181–193.

[8] Mani, S.; Bharagava, R.N. Exposure to crystal violet, its toxic, genotoxic and carcinogenic effects on environment and its degradation and detoxification for environmental safety. In Reviews of Environmental Contamination and Toxicology, Springer, 2016, Vol. 237, pp. 71–104.

[9] Ali, N. et al. Analysis of trace malachite green, crystal violet, and their metabolites in zebrafish. Talanta 2020, 211, 120707.

[10] Bharagava, R.N.; Mani, S. Crystal violet degradation and detoxification. Environ. Sci. Pollut. Res. 2020, 27, 20309–20317.

[11] Sarayu, K.; Sandhya, S. Current technologies for biological treatment of textile wastewater — a review. Appl. Biochem. Biotechnol. 2012, 167, 645–661.

[12] Yagub, M.T. et al. Dye and its removal from aqueous solution by adsorption: A review. Adv. Colloid Interface Sci. 2014, 209, 172–184.

[13] Aragaw, T.A.; Bogale, F.M. Biomass-based adsorbents for removal of dyes from wastewater: A review. Front. Environ. Sci. 2021, 9, 764958.

[14] Agarwala, R. et al. Adsorption of dyes from wastewater: A comprehensive review. ChemBioEng Rev. 2023, 10, 200–221.

[15] Rashid, R. et al. A state-of-the-art review on wastewater treatment techniques: the effectiveness of adsorption method. Environ. Sci. Pollut. Res. 2021, 28, 9050–9066.

[16] Morin-Crini, N. et al. The change from past to future for adsorbent materials in treatment of dyeing wastewaters. Materials 2017, 6, 5131.

[17] Aranaz, I. et al. Chitosan-based adsorbents for wastewater treatment: A comprehensive review. Int. J. Biol. Macromol. 2025, 306, 141813.

[18] Elgarahy, A.M. et al. Adsorptive performance of bentonite-chitosan nanocomposite for reactive red 195 and crystal violet removal. Biomass Conv. Bioref. 2023, https://doi.org/10.1007/s13399-023-05059-y.

[19] Bekchanov, D. et al. Advanced technologies in water treatment: Chitosan and its modifications as effective agents in the adsorption of contaminants. Int. J. Biol. Macromol. 2024, 279, 141003.

[20] Jiang, X. et al. Double network gelatin/chitosan hydrogel effective removal of dyes from aqueous solutions. J. Polym. Environ. 2022, 30, 726–738.

[21] Zhang, Y. et al. Adsorption behaviors of dyes on a biodegradable gelatin/chitosan/β-cyclodextrin hydrogel. Colloid Polym. Sci. 2022, 300, 919–931.

[22] Dórame-Miranda, R.F. et al. Sustainable cellulose–bentonite composites for wastewater treatment. Polymers 2025, 17, 1684.

[23] Ngwabebhoh, F.A. et al. Recent advances of application of bentonite-based composites in environmental remediation. J. Environ. Manage. 2024, 365, 121613.

[24] Iqbal, M.J. et al. Thermal, morphological and mechanical properties of multifunctional composites based on biodegradable polymers/bentonite clay. Polymers 2023, 15, 3443.

[25] Alfuraydi, R.T. et al. Poly(vinyl alcohol) hydrogels boosted with cross-linked chitosan and silver nanoparticles for efficient adsorption of Congo Red and Crystal Violet dyes. Gels 2023, 9, 882.

[26] Lu, Y. et al. Polyvinyl alcohol (PVA)-based hydrogels: Recent progress in fabrication, properties, and multifunctional applications. Polymers 2024, 16, 2755.

[27] Roboredo, M.M. et al. Treated wastewater phytotoxicity assessment using Lactuca sativa: focus on germination and root elongation test parameters. C. R. Biol. 2017, 340, 188–194.

[28] Enaime, G. et al. Phytotoxicity assessment of treated wastewater for irrigation using seed germination bioassay. Environ. Sci. Pollut. Res. 2020, 27, 8034–8045.

[29] Aber, S. et al. Modelling dye removal by adsorption onto water treatment residuals using combined RSM–ANN approach. J. Environ. Manage. 2019, 231, 857–868.

[30] Karri, R.R. et al. Response surface methodology: a review on optimization of adsorption studies. Res. Gate Preprint 2024, https://doi.org/10.13140/RG.2.2.19274.

[31] Yilmaz, F. et al. Optimization and comparative modelling of RSM and ANN for adsorptive removal of Remazol Brilliant Blue R dye. Chemosphere 2025, 371, 144078.

Theoretical Part

Chapter I

Fundamentals of Nanomaterial Chemistry

1. Introduction:

Nanomaterials are defined as natural, incidental, or manufactured materials containing particles in an unbound state, as an aggregate, or as an agglomerate, where at least 50 % of the particles in the number size distribution have one or more external dimensions in the size range of 1 nm to 100 nm[1]. At this ultra-fine scale, materials transition away from the classical physical behaviors of bulk matter and begin to exhibit unique mechanics and size-dependent properties. These changes manifest as a dramatic increase in specific surface-area-to-volume ratio, enhanced surface energy, altered electronic conductivity, and heightened chemical reactivity[2]. In the context of environmental chemistry, these nanoscale attributes create a vast density of exposed active sites, allowing nanomaterials to interact with and entrap surrounding molecular contaminants with remarkable efficiency[3].

With the growing urgency posed by pollution challenges and socio-economic pressures coupled with strong needs for remediation technologies, nanomaterials chemistry has emerged as a core area of environmental engineering. Nanometric scale materials operate with thousands of times higher specific surface area and a vast landscape of active surface sites that inherently increase solid substrate interaction with fluid-phase contaminants at the interface. Such unique surface reactivity positions nanotechnology as an excellent methodological platform for wastewater treatment[4], [5], toxic gas removal[6], and site-specific extraction of complex organic and inorganic contaminants[3] from various natural or synthetic matrices.

The application of engineered nanomaterials is one current theme at the forefront of modern research for sustainable, high-performance environmental protection solutions, characterized by efficient, rapid mass transfer kinetics[7], and low overall operating footprint[5].

2. Classification of Nanomaterials:

The structural and chemical classification of nanomaterials dictates their interfacial behavior, stability, and efficiency in environmental engineering. To understand their performance in water remediation, these materials are systematically categorized through three primary lenses: their fundamental chemical composition, their origin and their physical spatial dimensionality as shown in **Figure I.1**

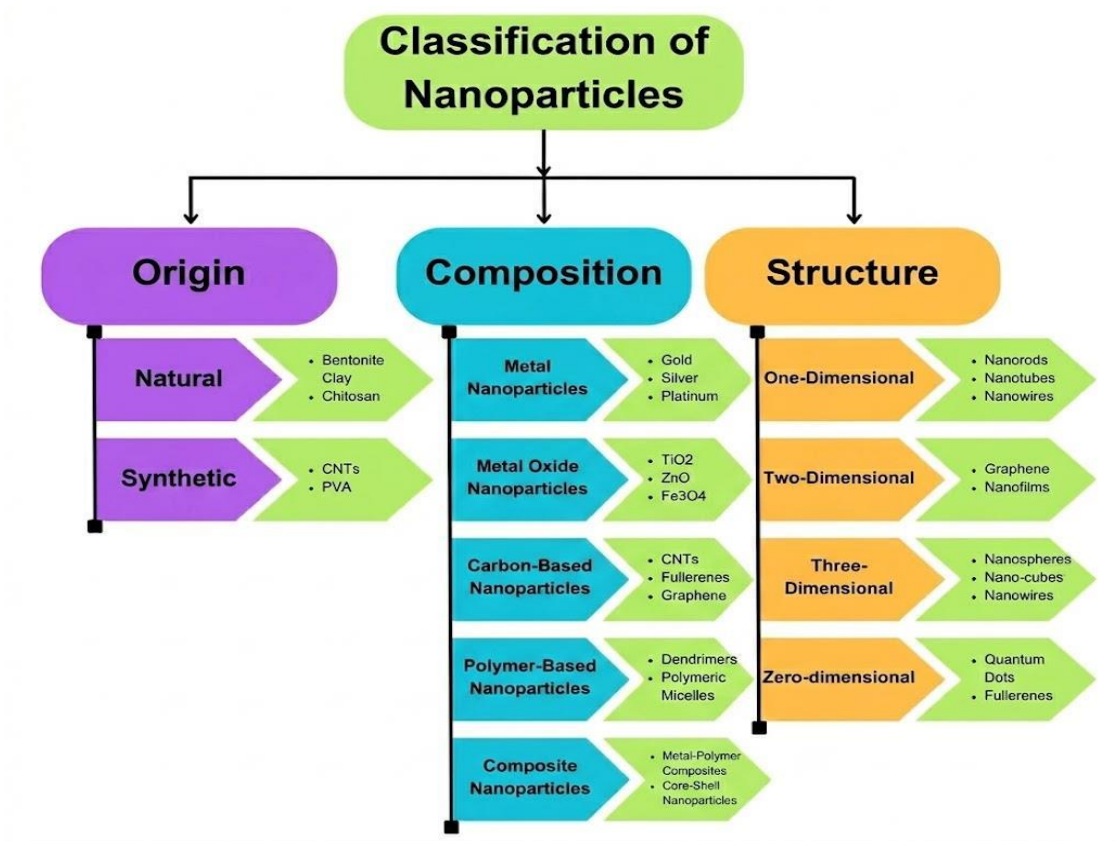


Figure I.1. *Classification of Nanomaterial based on origin, composition and structure/dimensions [22] (Modified).*

2.1. *Classification based on Composition:*

The chemical nature of a nanomaterial determines its surface functional groups, intrinsic reactivity, and affinity for specific pollutants.

- *Inorganic Nanomaterials:*

This class includes pure noble metals (such as Ag, Au, and Pt) and metal oxides[8], [9], [10] (such as TiO_2, Fe_3O_4, and ZnO). While metallic nanoparticles are highly valued for their electronic and catalytic properties, metal oxides are widely exploited in environmental chemistry for their semiconducting nature, which enables photocatalytic degradation and surface redox reactions to break down organic pollutants.

- *Carbon-Based (Organic) Nanomaterials:*

Comprising structures like fullerenes, carbon nanotubes (CNTs), and graphene derivatives, these materials possess high thermal stability and electrical conductivity[11]. Their high specific surface area enables strong $\pi - \pi$ stacking interactions, making them exceptional platforms for adsorbing aromatic organic dyes[12].

- *Polymeric and Composite (Hybrid) Nanomaterials:*

Polymeric matrices offer flexible, tunable backbones rich in target-specific functional groups. By blending these polymers with inorganic or carbonaceous components, researchers synthesize hybrid or core-shell composites. These multi-component materials overcome the limitations of individual constituents, providing enhanced mechanical strength, chemical stability, and structural durability in complex aqueous matrices[13], [14].

2.2.*Classification based on Dimensions:*

Nanomaterials are also classified by the number of dimensions that remain outside the nanoscale (>100nm), which directly influences their electron transport, mass transfer kinetics, and active site availability.

- *Zero-Dimensional (0D):* All dimensions are confined to the nanoscale (e.g., quantum dots, fullerenes). They exhibit strong quantum confinement effects and localized surface reactivity[15].

- *One-Dimensional (1D):* Two dimensions are at the nanoscale, while one is macroscopic (e.g., nanotubes, nanorods, nanowires)[16]. This linear geometry provides highly directed pathways for electron transfer and fluid flow, which is beneficial in advanced electrochemical filtration membranes.

- *Two-Dimensional (2D):* Only one dimension is restricted to the nanoscale, creating ultra-thin sheets or nanofilms (e.g., graphene oxide). These materials provide expansive, exposed surface planes that maximize contact area and surface complexation with dissolved contaminants.[17]

- *Three-Dimensional (3D):* These materials are not confined to the nanoscale in any spatial dimension but possess a nanostructured internal network or surface morphology (e.g., dendritic networks, hierarchical porous composites, nanospheres). Their intricate, multi-layered architectures feature highly heterogeneous active sites, facilitating multi-position adsorption and rapid mass transport in dynamic fluid systems[18].

2.3.*Classification based on Origin:*

A Nanomaterial's origin dictates its biocompatibility, environmental cost, production cost and structural conformity; thus, it is common practice to classify this material based on their origin i.e. natural vs synthetic[19].

- *Natural Nanomaterials:* These natural Nanostructures are generated in nature and formed by biological, geological or cosmic processes without any human interference. Naturally occurring clay minerals (bentonite, kaolinite), volcanic ash and biopolymers from living things (chitosan [from chitin], gelatin [from collagen], cellulose). These materials are called green because they preserve their nature; furthermore, they are inherently biocompatible, biodegradable, non-toxic and low-cost abundant materials[20].
- *Synthetic Nanomaterials:* These are artificially engineered via human intervention by specific methods, either physical or chemical, such as sol–gel process, chemical vapor deposition or environmentally friendly green methods. Polyvinyl alcohol (PVA), carbon nanotubes, and engineered metal nanoparticles are some of the examples. Synthetic materials have the unique advantage of precise structural regulation, enabling researchers to tailor materials with low particle size, porosity and/or surface geometry and/or functional groups that maximize targeted contaminant extraction[21].

3. Techniques of Nanomaterial Synthesis:

3.1. *Comparative Study: Bottom–Up vs Top–Down:*

In nano-chemistry, there are two opposing approaches that underlie the preparation of nanomaterials: the *top-down* and *bottom-up* approaches. As shown in **Table I.1** choosing the right pathway controls the ultimate physicochemical properties, structural homogeneity and engineering scalability of nanomaterial[22][23].

3.1.1. The Top-Down Approach:

The top-down approach relies on the physical or mechanical reduction of macroscopic bulk structures into nanoscale fragments. High-energy *Lithography* and mechanical *Ball milling* are considered standard operations in this field [24][25]. Chemical pathways also exist in which large molecular structures and macromolecules are broken down to the nanoscale via chemical processes[26]. Though great at processing raw materials, top-down methods come with a variety of engineering bottlenecks and drawbacks:

- Power intensive, long latency processes.
- Some structural defects and a huge variation of particle size and other characteristics due to high polydispersity.

- Equipment complication and increased risk for secondary contamination due to wear of milling media.

3.1.2. The Bottom-Up Approach:

In contrast, the bottom-up strategy refers to the assembly of materials starting from atomic, molecular or molecular-scale clusters in a controlled manner. This approach is the main concept employed for developing the class of high-performance nanomaterials, as it enables accurate control over certain microstructures and chemical stoichiometry. This flexibility allows for the creation of custom functionalities and multi-layered, hierarchical architectures while maintaining exceptional batch-to-batch reproducibility[27].

The standard bottom-up methods include *Chemical Vapor Deposition (CVD)* for gas-phase film growth[28][29], *Sol-Gel* Processing driven by liquid-phase chemical precursors[30], [31], and *Colloidal Precipitation[32], [33]* managed through solvent or pH adjustments. Additionally, high-pressure *Hydrothermal/Solvothermal* synthesis[34] and eco-friendly Green/Biogenic routes[4] utilizing plants or microbes are widely deployed to assemble uniform nanoscale structures from the atomic or molecular level.

3.1.3. Comparison between the two approaches:

Table I.1. *Approach Comparison: Top - down Vs Bottom – up[27].*

Aspect	*Top-Down Approach*	*Bottom-Up Approach*
Starting Material	Bulk solid phase materials.	Atomic or molecular precursors.
Mechanism	Physical impact, shear forces, or etching.	Chemical nucleation and growth.
Size Distribution	Broad and irregular (polydisperse).	Narrow and highly uniform.
Internal Defects	High density of structural artifacts.	Low defect density; high crystallinity.
Energy Input	Exceptionally high mechanical/thermal energy.	Variable; can be driven by low-temperature chemistry.

3.2. *Comparative Study: Chemical Synthesis vs Green Synthesis:*

In addition to structural assembly, the selection of the reagents that drive the synthesis reactions (either pure analytical grade chemical reagents or environmental-friendly biological matrices) determines not only manufacturability and cost but also safety and long-term sustainability of engineered materials.

3.2.1. Chemical Synthesis:

Many conventional chemical routes are employed in the synthesis of nanomaterials from bottom up using controlled environments and synthetic precursors:

- *Chemical Vapor Deposition (CVD):* control of gas-phase precursor vapors for deposition of thin films or nanoparticles Optimized conditions (e.g. TiO_2 and ZnO) are successfully doped semiconductors for photocatalysis deposition through CVD.
- *Sol-Gel:* Processing Sequential hydrolysis and polycondensation reactions in a liquid-phase that ultimately leads to an interconnected gel network. Microwave-assisted sol-gel combine microwave energy which accelerates the reaction and therefore enhance crystalline stability.
- *Colloidal precipitation:* increases the polarity of the solvent, pH or ionic strength in order to precipitate oxides or hydroxides from solution as liquid-phase colloids.
- *Hydrothermal/solvothermal methods:* Employ high temperatures and pressures in sealed autoclaves to maintain rare crystalline phases via aqueous media. The microwave-hydrothermal variations offer fast volumetric heating and cost-effective narrowing of size distributions.

3.2.2. Green Synthesis:

As hazardous chemical reducing and capping agents are entirely replaced with natural biomaterials, the downward dependence on toxic reagents, as well as processing energy footprints, will be decreased. The green synthesis approach consists of many methods such as:

- *Plant mediated synthesis:* The extract of some medicinal plant like Salvia officinalis or Rosmarinus officinalis has active secondary metabolites such as flavonoids, alkaloids, terpenoids and phenolic acids. These phytochemicals are reducing agents for metal salts (e.g., converting Fe^{3+} or Ag^{+} into Fe_3O_4 or Ag nanoparticles) and also serve as natural stabilizing agents[35].

- *Microbial synthesis:* It uses the metabolism of bacteria, fungi, yeast or algae. At ambient mild conditions, microbes secrete EPS and enzymes such as NAR to expedite the reduction of metal ions[36].
- *Agro-Industrial Biomass Upcycling*: Converts agricultural byproducts (for example, rice husk) into a biochar with special functions for circular economy pathways. Such high porosity and surface area-loaded phosphorus biochar can be an ideal matrix for the interception of heavy metals [37].

Transitioning nanoparticle production from laboratory exploration to industrial deployment requires quantitative validation through established green chemistry metrics[38], [39]. These metrics can be summarized in **Table I.2.**

Table I.2. *The most extensively recognized and employed green chemistry metrics[39].*

Sustainability Metric	***Core Analytical Focus***	***Significance***
Atom Economy (AE)	Mass balance of starting reagents versus final product.	Evaluates the theoretical structural efficiency of the initial chemical pathway.
Process Mass Intensity (PMI)	Total mass of all materials used (including solvents) per unit mass of product.	Tracks material consumption efficiency, exposing hidden solvent or catalyst waste.
Environmental Factor (E-Factor)	Total mass of waste generated per kilogram of desired product.	Quantifies raw industrial waste generation and immediate environmental burden.
Effective Mass Yield (EMY)	Ratio of product mass relative to the mass of hazardous ingredients used.	Incentivizes the elimination of toxic precursors and hazardous organic solvents.
Energy Efficiency (EE)	Total thermodynamic energy consumed per unit of manufactured product.	Identifies high-temperature or high-vacuum bottlenecks in synthetic workflows.

3.2.3. Comparison between the two approaches:

Table I.3. *Method Comparison: Chemical Vs Green Synthesis [27].*

Aspect	*Chemical Synthesis*	*Green Synthesis*
Precursors	Synthetic chemical precursors, toxic organic solvents, and hazardous reducing/capping agents.	Biological entities, plant extracts, live microorganisms, and agro-industrial biomass waste.
Mechanism	Gas-phase deposition, liquid phase polycondensation, or high-pressure thermal crystallization.	Phytochemical or enzymatic reduction and natural capping under green chemistry frameworks.
Reaction Conditions	Often requires high temperatures, intense pressure autoclaves, or high-vacuum environments.	Typically operates under mild ambient temperatures, standard pressures, and safe aqueous media.
Environmental Impact	Elevated carbon footprint, higher environmental burden, and significant waste generation (higher E-factor).	Exceptional sustainability, minimal environmental footprint, and a drastically reduced E-factor.
Key Advantages	Rapid optimization pathways, strict stoichiometric regulation, and predictable phase control.	High biocompatibility, low operational costs, non-toxic processing, and elimination of hazardous waste.

4. Nanomaterial Characterization Techniques:

Accurate characterization of Nanomaterial is a foundational requirement in nanotechnology, bridging the gap between laboratory synthesis protocols and real-world performance forecasting. The physical dimensions, geometric morphology, surface chemistry, and electronic behaviors of engineered nanomaterials dictate their performance across various environmental and catalytic systems. Systematically evaluating these properties requires a

complementary suite of spectroscopic, microscopic, and electrokinetic analytical tools that probe the bulk, localized, and interfacial properties of the material.

4.1. *Ultraviolet–Visible Spectroscopy (UV-Vis) :*

UV-Vis spectroscopy operates on the principle of electronic excitation, measuring the intensity of light absorbed or scattered by a sample as a function of wavelength. In nanomaterials, especially noble metals and semiconducting oxides, light absorption is heavily governed by Surface Plasmon Resonance (SPR), which is a phenomenon that arises from the collective oscillation of free conduction electrons in resonance with the incident electromagnetic field (light waves), and intrinsic bandgap transitions. The technique is implemented to evaluate structural shifts, quantum confinement effects, and optical electronic properties. Morphological anisotropy, surface-associated defect states, or variations in particle geometry alter the electronic boundaries, inducing predictable red-shifts, blue-shifts, or broadening in the characteristic absorbance peaks, which provides an online indicator of structural evolution.

Plasmonic nanoparticles have optical properties that are sensitive to size, shape, concentration, agglomeration state, and refractive index near the nanoparticle surface, which makes UV/Vis spectroscopy a valuable tool for identifying, characterizing, and studying nanomaterials[40]. Non-plasmonic nanoparticles also have size and concentration dependent optical properties, however, their spectrum is not as sensitive to the dispersion properties as plasmonic nanoparticles.

The spectrophotometer is used to quantify the light that is absorbed and scattered by a sample (a quantity known as the extinction, which is defined as the sum of absorbed and scattered light). In its simplest form, a sample is placed between a light source and a photodetector, and the intensity of a beam of UV/visible light is measured before and after passing through the sample. These measurements are compared at each wavelength to quantify the sample's wavelength dependent extinction spectrum. The data is typically plotted as extinction as a function of wavelength. Each spectrum is background corrected using a buffer blank to guarantee that spectral features from the buffer are not included in the sample extinction spectrum[41], [42].

The Beer-Lambert Law establishes that the absorbance of a chemical species in a solution is directly proportional to its molar absorptivity (ε), optical path length (l), and molar concentration (c).

$$A = \varepsilon \cdot l \cdot c \qquad \textbf{I.1}$$

Where:

- A represents the measured absorbance (dimensionless).
- ε represents the molar attenuation coefficient (L/mol·cm).
- c represents the molar concentration of the absorbing substance (mol/L).
- l is the optical path length (cm).

The **Figure I.2.** shows the instrumental principle of modern UV – Vis spectrophotometer.

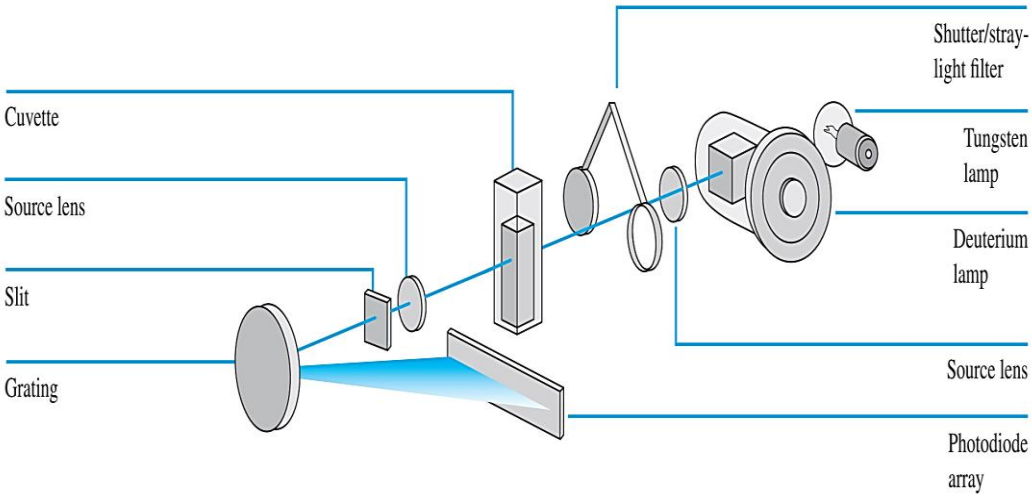


Figure I.2. *Principal of a modern UV – Vis spectrophotometer*[43].

4.2. *Fourier Transform Infrared spectroscopy (FT-IR):*

Typically, a molecule may absorb IR radiation if it possesses a time-variant dipole moment and its oscillating frequency is the same as the frequency of incident IR light. The absorption of IR radiation transfers energy to the molecule, inducing a corresponding covalent bond stretching, bending or twisting, which, in the case of a normal mode, is described by a stationary state of molecular vibrational Hamiltonian. Molecules without dipole moments, e.g. diatomic molecules N_2 and O_2, do not absorb IR radiation. Generally, in a molecule, the vibrations involve various coupled pairs of atoms or covalent bonds, each of which must be considered as a combination of the normal modes; therefore, the IR spectrum, illustrating absorption or transmission versus incident IR frequency, can offer a fingerprint of the structure of the molecule of interest. For nanomaterial applications, Fourier transform infrared (FT-IR) spectroscopy is commonly employed to use the expression of characteristic

spectral bands to reveal nanomaterial–biomolecule conjugation, e.g. proteins bound to NP surfaces, and to illustrate the conformational states of the bound proteins.

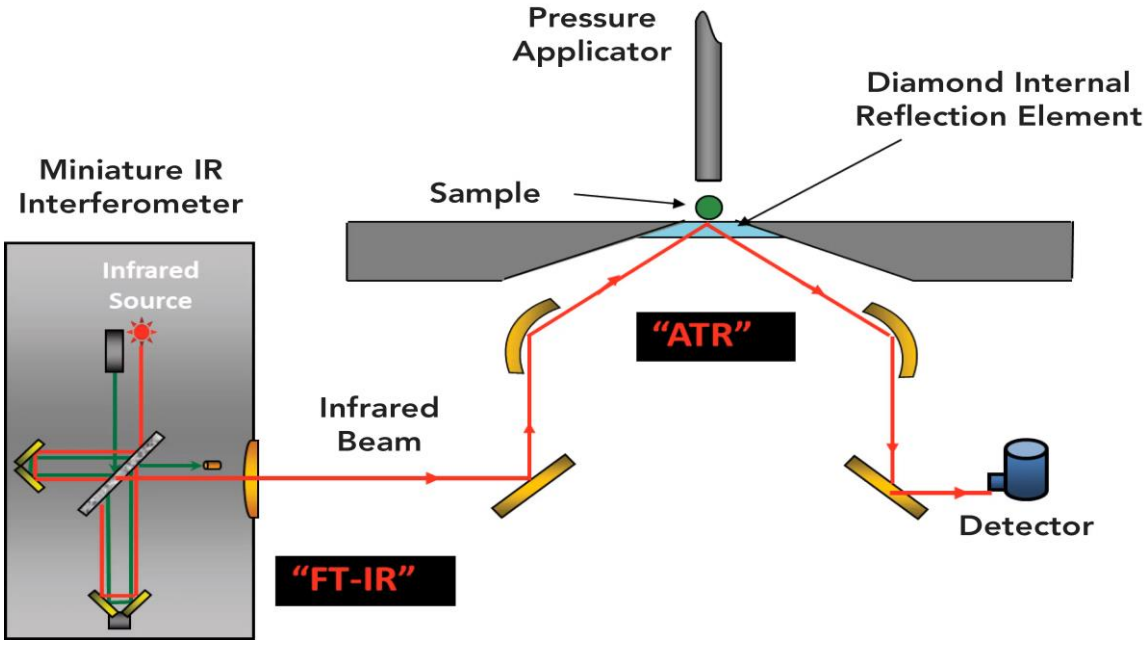


Figure I.3. A Typical ATR Accessory *[44]*.

Furthermore, FT-IR has also been extended to study nano-scaled materials, such as confirmation of functional molecules covalently grafted onto carbon nanotubes. A recently developed technique called attenuated total reflection (ATR)–FT-IR spectroscopy uses the property of total internal reflection in conjunction with IR spectroscopy to probe the structure of adsorbed/deposited species at a solid/air or solid/liquid interface, while avoiding the drawbacks of sample preparation complexity and spectral irreproducibility in conventional IR. In an ATR–FT-IR system **(Figure I.3.)**, the total internal reflectance, occurring within the equipped internal reflection element (IRE) crystal, which has a high refractive index at certain angles, forms evanescent waves that extend from the IRE crystal–sample interface into the sample with penetration depth of micrometers (0.5–5 μm), and the intensity of the evanescent waves decays exponentially from the interface. ATR–FT-IR can provide IR absorption spectra to investigate, for example, changes in surface properties as well as identification of chemical properties on the polymer surface when sample on the IRE–sample interface absorbs the evanescent IR waves with frequencies matching the vibrational modes of the sample. Although ATR–FT-IR spectroscopy can be implemented to study the surface features of nanomaterials, it is not a very sensitive surface-analysis method at nanometer scale because the penetration depth of ATR–FT-IR has the same order of magnitude as the incident IR wavelength[45], [46], [47].

4.3. *X-ray Diffraction (XRD):*

XRD is a non-destructive spectroscopic method to find the crystallographic phase, lattice structure and atomic spacing (d) in crystalline nanomaterials. The governing statement is given by bragg's law:

$$\boldsymbol{n \cdot \lambda = 2d \cdot sin\theta} \qquad \textbf{I.2}$$

Where:

- λ represents the wavelength of the incident X-ray beam (nm or Å).
- n represents the order of reflection, which is a positive integer.
- d represents the interplanar spacing between the parallel atomic planes in the crystalline lattice (nm or Å).
- θ is the Bragg angle, representing the angle of incidence between the X-ray beam and the lattice planes (degrees or radians).

This equation describes how constructive interference occurs when an incident monochromatic X-ray beam (wavelength λ (nm)) interacts with the parallel atomic planes of a crystalline lattice (spacing d (A)) at a specific angle (θ). The implementation of XRD yields a diffraction pattern that serves as a unique crystallographic fingerprint of the material. By analyzing the angular positions and relative intensities of the diffraction peaks, researchers can identify phase purity, crystal symmetry, and unit cell parameters. Furthermore, the finite size of crystalline domains in nanomaterials causes peak broadening. The **Figure I.4.** shows the instrumentation that makes this possible; this relationship is utilized via the Scherrer equation to estimate the average crystallite size (D (nm)) based on the Full Width at Half Maximum ($FWHM$ or β) of the prominent diffraction peaks.

$$\boldsymbol{D = \frac{K \cdot \lambda}{\beta \cdot cos\theta}} \qquad \textbf{I.3}$$

Where:

- D represents the average crystallite size of the ordered crystalline domains (nm or Å).
- K represents the dimensionless Scherrer shape factor, typically chosen around 0.9.
- β represents the line broadening at half the maximum intensity, or Full Width at Half Maximum (FWHM), after subtracting instrumental line broadening (radians).

XRD is also highly sensitive to lattice strain, dislocations, and interstitial changes induced by doping or alloying, making it essential for assessing internal structural integrity.

Although XRD is a well-established technique and has frequently been used to determine the material structure at the atomic scale, difficulty in growing crystals and the ability of getting results only from single conformation/binding state of the sample limit the applications of XRD technique. Another disadvantage of XRD is the low intensity of diffracted X-rays, particularly for low atomic number materials, compared with electron diffractions. A recent X-ray diffraction study reported a new approach using femtosecond pulses from a hard-X-ray free-electron laser for structure determination, which may benefit structure determination of macromolecules that do not yield sufficient crystal size for using conventional radiation sources or are not sensitive to radiation damage[48], [49], [50], [51].

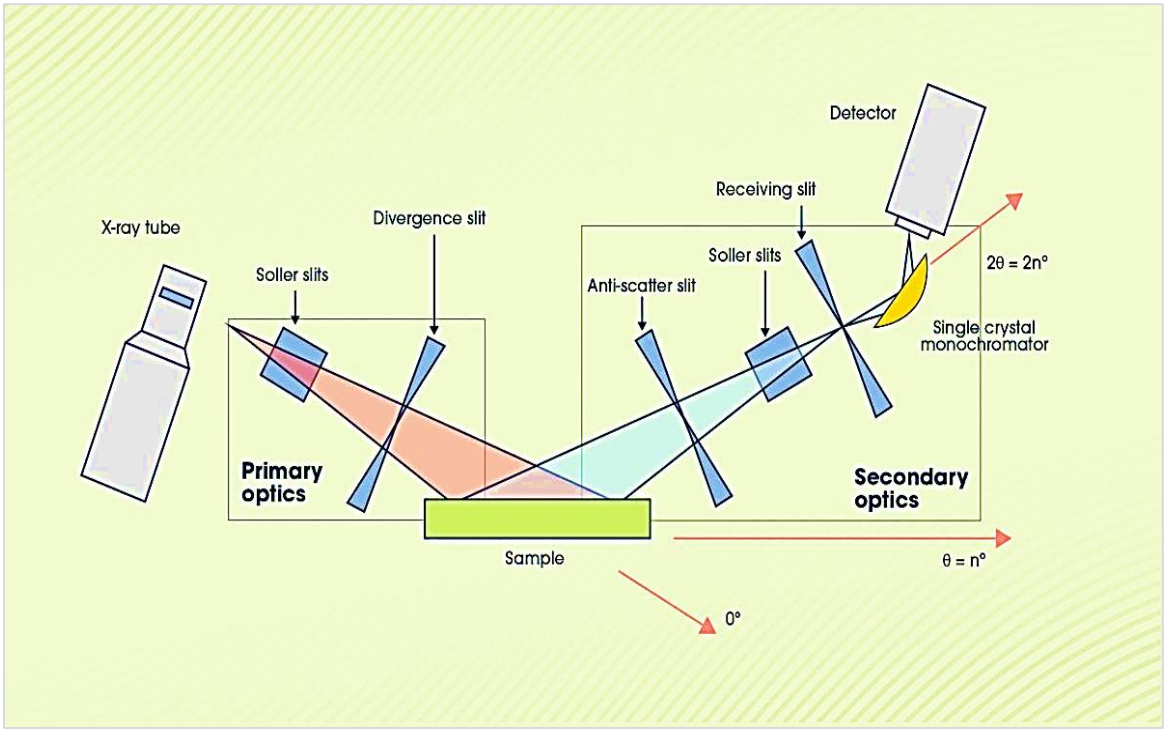


Figure I.4. *Diagram of a common XRD instrumental layout [52].*

4.4. *Scanning Electron Microscopy (SEM):*

In contrast to optical microscopy, which uses light sources and glass lenses to illuminate specimens to produce magnified images, electron microscopy (EM) uses beams of accelerated electrons and electrostatic or electromagnetic lenses to generate images of much higher resolution, based on the much shorter wavelengths of electrons than visible light photons.

SEM is a surface imaging method in which the incident electron beam scans across the sample surface and interacts with the sample to generate signals reflecting the atomic composition and topographic detail of the specimen surface. The incident electrons cause emissions of elastic scattering of electrons, referring to backscattered electrons, inelastic scattering of electrons named low-energy secondary electrons, and characteristic X-ray light called cathodoluminescence from the atoms on the sample surface or near-surface material. Among these emissions, detection of the secondary electrons is the most common mode in SEM and can achieve resolution smaller than **1 nm**. The principle is illustrated in **Figure I.5.**

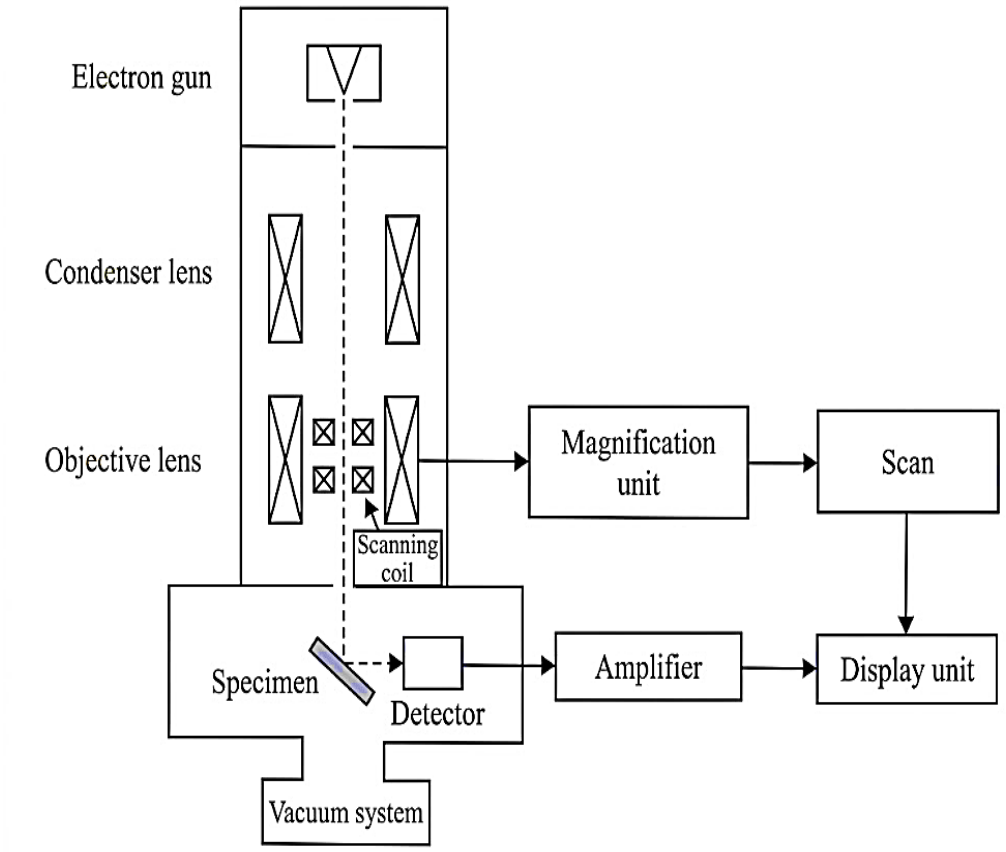


Figure I.1. *Modern SEM instrumentation diagram[53].*

The size distribution and shape of nanomaterials can be directly acquired from SEM; however, the process of drying and contrasting samples may cause shrinkage of the specimen and alter the characteristics of the nanomaterials. In addition, while scanned by an electron beam, many biomolecule samples that are nonconductive specimens tend to acquire charge and insufficiently deflect the electron beam, leading to imaging faults or artifacts. Coating an ultrathin layer of electrically conducting material onto the biomolecules is often required for this sample preparation procedure. Because a cryogenic freezing method is often required

in EM to image surface groups attached to NPs, the size of nanomaterial cannot be investigated in physiological conditions[54], [55].

An exception is environmental SEM (ESEM), through which samples can be imaged in their natural state without modification or preparation. Because the sample chamber of ESEM is operated in a low-pressure gaseous environment of **10–50 Torr** and high humidity, the charging artifacts can be eliminated, and coating samples with a conductive material is no longer necessary. Still, most of the EM techniques, including SEM, possess the disadvantage of a destructive sample preparation, prohibiting its analysis by other modalities. In addition, biased statistics of size-distribution of heterogeneous samples is unavoidable in SEM due to the small number of sample particles in the scanning region[56].

4.5. *Surface Charge Analysis & pH_{pzc}:*

In an ionic solution, the surface of a charged particle is firmly bound to opposite charged ions, forming a thin liquid layer named the Stern layer, which is encompassed by an outer diffuse layer consisting of loosely associated ions. In an ionic solution, the surface of a charged particle is firmly bound to opposite charged ions, forming a thin liquid layer named the Stern layer, which is encompassed by an outer diffuse layer consisting of loosely associated ions. These two layers compose the so-called electrical double layer. Given the tangential motion driven by an external force or Brownian motion of the charged particle, the movement of the charged particle shears ions migrating with the charge particle in the diffuse layer from ions staying with the bulk dispersant outside the layer. The electric potential on the shear surface is called zeta potential, which is usually determined by measuring the velocity of the charged species towards the electrode in the presence of an external electric field across the sample solution. The zeta potential with a value of ± 30 mV is generally chosen to infer particle stability, through which the absolute value greater than 30 mV indicates a stable condition, whereas a low zeta potential value of less than 30 mV indicates a condition towards instability, aggregation, coagulation or flocculation. Among the methods of evaluating zeta potential, the technique of electrophoretic light scattering (ELS), which can simultaneously measure the velocities of many charged particles in liquid, is most commonly used. However, it still suffers the electroosmotic effect that reduces precision and reproducibility of the measurement. Although measuring the zeta potential of suspended particles after dilution reduces difficulty of light penetration into the sample solution, it is worth noting that zeta potential is a property sensitive to environmental changes

including pH and ionic strength. Therefore, a precise, repeatable zeta potential measurement in a diluted solution cannot reflect the true value in a concentrated suspension[57], [58].

Chapter One References

[1] H. Rauscher, K. Rasmussen, and B. Sokull-Klüttgen, "Regulatory Aspects of Nanomaterials in the EU," *Chem. Ing. Tech.*, vol. 89, no. 3, pp. 224–231, Mar. 2017, doi: 10.1002/CITE.201600076;PAGEGROUP:STRING:PUBLICATION.

[2] A. B. Asha and R. Narain, "Nanomaterials properties," *Polymer Science and Nanotechnology: Fundamentals and Applications*, pp. 343–359, Jan. 2020, doi: 10.1016/B978-0-12-816806-6.00015-7.

[3] X. Zhao, W. Liu, Z. Cai, B. Han, T. Qian, and D. Zhao, "An overview of preparation and applications of stabilized zero-valent iron nanoparticles for soil and groundwater remediation," *Water Res.*, vol. 100, pp. 245–266, Sep. 2016, doi: 10.1016/J.WATRES.2016.05.019.

[4] G. Z. Kyzas and M. Kostoglou, "Green Adsorbents for Wastewaters: A Critical Review," *Materials 2014, Vol. 7, Pages 333-364*, vol. 7, no. 1, pp. 333–364, Jan. 2014, doi: 10.3390/MA7010333.

[5] X. Qu, P. J. J. Alvarez, and Q. Li, "Applications of nanotechnology in water and wastewater treatment," *Water Res.*, vol. 47, no. 12, pp. 3931–3946, Aug. 2013, doi: 10.1016/J.WATRES.2012.09.058.

[6] E. Barea, C. Montoro, and J. A. R. Navarro, "Toxic gas removal – metal–organic frameworks for the capture and degradation of toxic gases and vapours," *Chem. Soc. Rev.*, vol. 43, no. 16, pp. 5419–5430, 2014, doi: 10.1039/C3CS60475F.

[7] C. Santhosh, V. Velmurugan, G. Jacob, S. K. Jeong, A. N. Grace, and A. Bhatnagar, "Role of nanomaterials in water treatment applications: A review," *Chemical Engineering Journal*, vol. 306, pp. 1116–1137, Dec. 2016, doi: 10.1016/J.CEJ.2016.08.053.

[8] S. Kumar, J. Pandey, R. Tripathi, and S. R. Chauhan, "Photoluminescence Investigations and Band Gap Engineering in Environment Friendly ZnO Nanorods: Enhanced Water Treatment Application and Defect Model," *ACS Omega*, vol. 8, no. 30, pp. 27732–27742, Aug. 2023, doi: 10.1021/acsomega.3c03860.

[9] A. A. Kamble, B. Sarojini, R. K. Chalannavar, V. Kamat, and R. Bhat, "Harnessing Hemidesmus indicus for eco-friendly CuO nanoparticle synthesis and evaluating its antioxidant and mosquito larvicidal activities," *Results in Surfaces and Interfaces*, vol. 19, p. 100470, May 2025, doi: 10.1016/j.rsurfi.2025.100470.

[10] N. Abbas *et al.*, "Green synthesis and analysis of iron oxide nanoparticles for methylene blue degradation by Fenton-like process: Antimicrobial properties and integrated AI-GA modeling," *Inorg. Chem. Commun.*, vol. 176, p. 114268, Jun. 2025, doi: 10.1016/j.inoche.2025.114268.

[11] N. Devi, R. Kumar, Y.-S. Chen, and R. K. Singh, "Carbon-Based Nanomaterials: Carbon Nanotube, Fullerene, and Carbon Dots," in *Nanomaterials*, Singapore: Springer Nature Singapore, 2023, pp. 27–57. doi: 10.1007/978-981-19-7963-7_2.

[12] M. Zhan, M. Xu, W. Lin, H. He, and C. He, "Graphene Oxide Research: Current Developments and Future Directions," *Nanomaterials*, vol. 15, no. 7, p. 507, Mar. 2025, doi: 10.3390/nano15070507.

[13] L. Aranda-Lara, B. E. O. García, K. Isaac-Olivé, G. Ferro-Flores, L. Meléndez-Alafort, and E. Morales-Avila, "Drug Delivery Systems-Based Dendrimers and Polymer Micelles for Nuclear Diagnosis and Therapy," *Macromol. Biosci.*, vol. 21, no. 3, Mar. 2021, doi: 10.1002/mabi.202000362.

[14] X. Zhang, Y. Liu, and J. Yuan, "Amino-functionalized Fe/Co bimetallic MOFs for accelerated Fe (III)/Fe (II) cycling and efficient degradation of sulfamethoxazole in Fenton-like system," *Front. Chem.*, vol. 13, Mar. 2025, doi: 10.3389/fchem.2025.1579108.

[15] M. D. Budimir and J. R. Prekodravac, "Photocatalytic properties of zero-dimensional carbon–based nanomaterials: application as catalysts/adsorbents in water treatment," in *Zero-Dimensional Carbon Nanomaterials*, Elsevier, 2024, pp. 291–355. doi: 10.1016/B978-0-323-99535-1.00011-1.

[16] A. Machín *et al.*, "One-Dimensional (1D) Nanostructured Materials for Energy Applications," *Materials*, vol. 14, no. 10, p. 2609, May 2021, doi: 10.3390/ma14102609.

[17] S. Noreen *et al.*, "Emerging 2D-Nanostructured materials for electrochemical and sensing Application-A review," *Int. J. Hydrogen Energy*, vol. 47, no. 2, pp. 1371–1389, Jan. 2022, doi: 10.1016/j.ijhydene.2021.10.044.

[18] Paras *et al.*, "A Review on Low-Dimensional Nanomaterials: Nanofabrication, Characterization and Applications," *Nanomaterials*, vol. 13, no. 1, p. 160, Dec. 2022, doi: 10.3390/nano13010160.

[19] I. Khan, K. Saeed, and I. Khan, "Nanoparticles: Properties, applications and toxicities," *Arabian Journal of Chemistry*, vol. 12, no. 7, pp. 908–931, Nov. 2019, doi: 10.1016/j.arabjc.2017.05.011.

[20] F. Eker *et al.*, "A Comprehensive Review of Nanoparticles: From Classification to Application and Toxicity," *Molecules*, vol. 29, no. 15, p. 3482, Jul. 2024, doi: 10.3390/molecules29153482.

[21] C. Santhosh, V. Velmurugan, G. Jacob, S. K. Jeong, A. N. Grace, and A. Bhatnagar, "Role of nanomaterials in water treatment applications: A review," *Chemical Engineering Journal*, vol. 306, pp. 1116–1137, Dec. 2016, doi: 10.1016/j.cej.2016.08.053.

[22] S. Rawat, S. M. Tauseef, M. Sharma, A. Rautela, and R. G. Gurav, "A comprehensive review on emerging nanoparticle-based sustainable water treatments: Synthesis, characterisation, and treatment efficiency," *Desalination Water Treat.*, vol. 326, p. 101724, Apr. 2026, doi: 10.1016/j.dwt.2026.101724.

[23] Y. Khan *et al.*, "Classification, Synthetic, and Characterization Approaches to Nanoparticles, and Their Applications in Various Fields of Nanotechnology: A Review," *Catalysts*, vol. 12, no. 11, p. 1386, Nov. 2022, doi: 10.3390/catal12111386.

[24] X. Cui, Y. Liu, and Y. Chen, "Ultrafast micro/nano-manufacturing of metastable materials for energy," *Natl. Sci. Rev.*, vol. 11, no. 4, Feb. 2024, doi: 10.1093/nsr/nwae033.

[25] Z. Chen, C. Zhao, X. Zhou, L. Xiao, Z. Li, and Y. Zhang, "A Review of Top-Down Strategies for the Production of Quantum-Sized Materials," *Small Science*, vol. 3, no. 12, Dec. 2023, doi: 10.1002/smsc.202300086.

[26] V. Nicolosi, M. Chhowalla, M. G. Kanatzidis, M. S. Strano, and J. N. Coleman, "Liquid Exfoliation of Layered Materials," *Science (1979).*, vol. 340, no. 6139, Jun. 2013, doi: 10.1126/science.1226419.

[27] S. Kumari *et al.*, "A comprehensive review on various techniques used for synthesizing nanoparticles," *Journal of Materials Research and Technology*, vol. 27, pp. 1739–1763, Nov. 2023, doi: 10.1016/j.jmrt.2023.09.291.

[28] G. K. Prashanth *et al.*, "Smart nanomaterials for semiconductor applications: Recent advances in energy storage and biosensing technologies," *Next Materials*, vol. 9, p. 100964, Oct. 2025, doi: 10.1016/j.nxmate.2025.100964.

[29] J.-O. Carlsson and P. M. Martin, "Chemical Vapor Deposition," in *Handbook of Deposition Technologies for Films and Coatings*, Elsevier, 2010, pp. 314–363. doi: 10.1016/B978-0-8155-2031-3.00007-7.

[30] M. S. Parvej, M. I. Khan, and M. K. Hossain, "Preparation of nanoparticle-based polymer composites," in *Nanoparticle-Based Polymer Composites*, Elsevier, 2022, pp. 55–94. doi: 10.1016/B978-0-12-824272-8.00013-0.

[31] A. E. Danks, S. R. Hall, and Z. Schnepp, "The evolution of 'sol–gel' chemistry as a technique for materials synthesis," *Mater. Horiz.*, vol. 3, no. 2, pp. 91–112, 2016, doi: 10.1039/C5MH00260E.

[32] N. T. K. Thanh, N. Maclean, and S. Mahiddine, "Mechanisms of Nucleation and Growth of Nanoparticles in Solution," *Chem. Rev.*, vol. 114, no. 15, pp. 7610–7630, Aug. 2014, doi: 10.1021/cr400544s.

[33] J. P. Rao and K. E. Geckeler, "Polymer nanoparticles: Preparation techniques and size-control parameters," *Prog. Polym. Sci.*, vol. 36, no. 7, pp. 887–913, Jul. 2011, doi: 10.1016/j.progpolymsci.2011.01.001.

[34] K. Byrappa and T. Adschiri, "Hydrothermal technology for nanotechnology," *Progress in Crystal Growth and Characterization of Materials*, vol. 53, no. 2, pp. 117–166, Jun. 2007, doi: 10.1016/j.pcrysgrow.2007.04.001.

[35] G. Marslin *et al.*, "Secondary Metabolites in the Green Synthesis of Metallic Nanoparticles," *Materials*, vol. 11, no. 6, p. 940, Jun. 2018, doi: 10.3390/ma11060940.

[36] X. Li, H. Xu, Z.-S. Chen, and G. Chen, "Biosynthesis of Nanoparticles by Microorganisms and Their Applications," *J. Nanomater.*, vol. 2011, pp. 1–16, 2011, doi: 10.1155/2011/270974.

[37] X. Tan *et al.*, "Biochar-based nano-composites for the decontamination of wastewater: A review," *Bioresour. Technol.*, vol. 212, pp. 318–333, Jul. 2016, doi: 10.1016/j.biortech.2016.04.093.

[38] H. C. Erythropel *et al.*, "The Green ChemisTREE: 20 years after taking root with the 12 principles," *Green Chemistry*, vol. 20, no. 9, pp. 1929–1961, 2018, doi: 10.1039/C8GC00482J.

[39] D. J. C. Constable, "Green Chemistry Metrics," in *Handbook of Green Chemistry*, Wiley, 2018, pp. 1–28. doi: 10.1002/9783527628698.hgc124.

[40] S. Eustis and M. A. El-Sayed, "Why gold nanoparticles are more precious than pretty gold: Noble metal surface plasmon resonance and its enhancement of the radiative and nonradiative properties of nanocrystals of different shapes," *Chem. Soc. Rev.*, vol. 35, no. 3, pp. 209–217, 2006, doi: 10.1039/B514191E.

[41] E. Tomaszewska *et al.*, "Detection Limits of DLS and UV-Vis Spectroscopy in Characterization of Polydisperse Nanoparticles Colloids," *J. Nanomater.*, vol. 2013, no. 1, Jan. 2013, doi: 10.1155/2013/313081.

[42] K. M. Mayer and J. H. Hafner, "Localized Surface Plasmon Resonance Sensors," *Chem. Rev.*, vol. 111, no. 6, pp. 3828–3857, Jun. 2011, doi: 10.1021/cr100313v.

[43] D. A. ; H. F. J. & C. S. R. . Skoog, *Principles of Instrumental Analysis*. Cengage, 2018.

[44] "Infrared Spectroscopy | Spectroscopy Online." Accessed: May 24, 2026. [Online]. Available: https://www.spectroscopyonline.com/view/infrared-spectroscopy

[45] P. R. Griffiths and J. A. de Haseth, *Fourier Transform Infrared Spectrometry*. Wiley, 2007. doi: 10.1002/047010631X.

[46] A. Dutta, "Fourier Transform Infrared Spectroscopy," in *Spectroscopic Methods for Nanomaterials Characterization*, Elsevier, 2017, pp. 73–93. doi: 10.1016/B978-0-323-46140-5.00004-2.

[47] A. R. Hind, S. K. Bhargava, and S. C. Grocott, "Attenuated Total Reflection Fourier Transform Infrared Spectroscopic Investigation of the Solid/Aqueous Interface of Low Surface Area, Water-Soluble Solids in High Ionic Strength, Highly Alkaline, Aqueous Media," *Langmuir*, vol. 13, no. 13, pp. 3483–3487, Jun. 1997, doi: 10.1021/la970141n.

[48] B. D. . Cullity and S. R. . Stock, *Elements of x-ray diffraction*. Prentice Hall, 2001.

[49] U. Holzwarth and N. Gibson, "The Scherrer equation versus the 'Debye-Scherrer equation,'" *Nat. Nanotechnol.*, vol. 6, no. 9, pp. 534–534, Sep. 2011, doi: 10.1038/nnano.2011.145.

[50] *X-Ray Diffraction*. Dover Publications Inc, 2003.

[51] H. N. Chapman *et al.*, "Femtosecond X-ray protein nanocrystallography," *Nature*, vol. 470, no. 7332, pp. 73–77, Feb. 2011, doi: 10.1038/nature09750.

[52] "XRD Explained: Principles, Analysis & Applications | Technology Networks." Accessed: May 24, 2026. [Online]. Available: https://www.technologynetworks.com/cell-science/articles/x-ray-diffraction-xrd-xrd-principle-xrd-analysis-and-applications-404260

[53] E. Setyawan, R. Napitupulu, S. Djiwo, D. P, and A. Nugroho, "A Preliminary Study of Scanning Electron Microscopy (SEM) for Characterization of the Wood Pellet Process of Sengon Wood (Albizia Chinensis)," in *Proceedings of the 2nd Universitas Kuningan International Conference on System, Engineering, and Technology, UNISET 2021, 2 December 2021, Kuningan, West Java, Indonesia*, EAI, 2022. doi: 10.4108/eai.2-12-2021.2320197.

[54] D. C. Joy, "The theory and practice of high-resolution scanning electron microscopy," *Ultramicroscopy*, vol. 37, no. 1–4, pp. 216–233, Aug. 1991, doi: 10.1016/0304-3991(91)90020-7.

[55] S. Burany, "Scanning Electron Microscopy and X-Ray Microanalysis . J. Goldstein, D. Newbury, D. Joy, C, Lyman, P. Echlin, E. Lifshin, L. Sawyer, and J. Michael. Kluwer Academic, Plenum Publishers, New York; 2003, 688 pages (Hardback, $75.00) ISBN 0-306-47292-9," *Microscopy and Microanalysis*, vol. 9, no. 5, pp. 484–484, Oct. 2003, doi: 10.1017/S1431927603030617.

[56] A. M. Donald, "The use of environmental scanning electron microscopy for imaging wet and insulating materials," *Nat. Mater.*, vol. 2, no. 8, pp. 511–516, Aug. 2003, doi: 10.1038/nmat898.

[57] S. Bhattacharjee, "DLS and zeta potential – What they are and what they are not?," *Journal of Controlled Release*, vol. 235, pp. 337–351, Aug. 2016, doi: 10.1016/j.jconrel.2016.06.017.

[58] R. J. . Hunter, *Zeta potential in colloid science : principles and applications*. Academic Press, 1981.

Chapter II

Nanomaterials & adsorption – Insights on Water Treatment

1. Introduction to Water Pollution:

The inevitably accelerated industrialization and population growth has contributed to a drastic rise in polluted water, where organic dyes[1] and heavy metals have been causing critical risks for ecosystems and public health[2]. These types of complex pollutants with low concentrations in aqueous matrices are typically recalcitrant to traditional treatment technologies[3], [4].

1.1. *Definitions and Fundamental Concepts:*

1.1.1. Surface Water: Accessible water resources found on the earth's surface such as rivers, valleys, lakes and seas[4], [5], [6].

1.1.2. Groundwater: the subsurface water that occurs in aquifers, which occupy all gaps (cracks, fractures and voids) between in rocks, gravel, sand and soil [4], [5], [6].

1.1.3. Clean Water: Clear, colorless, odorless and tasteless liquid; the presence of an observable change in any one of these three properties may signal contamination [4], [5], [6].

***1.1.4. Water Pollution*:** The release of substances into subsurface groundwater or into lakes, streams, rivers, estuaries, and oceans to the point that the substances interfere with beneficial use of the water or with the natural functioning of ecosystems [4], [5], [6].

1.1.5. Turbidity: An optical property that indicates how cloudy a water body is because of suspended solids and colloidal matter in the water column that scatter light transmission [4], [5], [6].

1.1.6. pH Level: A logarithmic scale for the acidity or basicity of a solution; pure, unpolluted water is said to be chemically neutral (i.e. pH ≈ 7) [4], [5], [6].

1.1.7. Water Hardness: A chemical property primarily determined by concentrations of dissolved multivalent metallic cations (divalent calcium and magnesium salts) [4], [5], [6].

1.1.8. Total dissolved solids (TDS): the total concentration of all inorganic minerals, salts and mobile organic compounds dissolved in a specific volume of water [4], [5], [6].

1.1.9. Electrical Conductivity (EC): the water's capability to conduct an electric current, which varies based on the amount of dissolved ionic salts and minerals [4], [5], [6].

1.1.10. Dissolved Oxygen (DO): The quantity of free, non-compound gaseous time present in water which is suspended and the primary indicator of internal water quality as it supports aquatic organisms [4], [5], [6].

1.1.11. Chemical oxygen demand (COD): The amount of oxygen needed to chemically oxidize all organic matter in water, which is used to estimate the overall extent of industrial organic pollution [4], [5], [6].

1.1.12. Alkalinity: Alkalinity is the ability of water to resist acidification due mainly to bicarbonate ions (HCO_3^-), carbonate ions (HCO_3^{2-}) and hydroxide ions (OH^-) acting as a chemical buffer against decreases in pH [4], [5], [6].

1.1.13. Heavy Metals: Dense toxic elements (e.g., lead, cadmium, mercury, and arsenic) that do not degrade and can bio-accumulate through the aquatic food web [4], [5], [6].

1.1.14. Salinity: The measure of the total amount of solids (i.e. sodium chloride (salt)) dissolved in water to a pre-defined level, most commonly used in distinguishing fresh from brackish and marine environments [4], [5], [6].

1.2. *Sources of Water Pollution:*

Water pollutants are classified as *point sources* or *dispersed sources*. A point source can be a pipe or channel, for example of an industrial facility or a city sewerage system. A diffuse source (or nonpoint) is an extremely wide unconfined area that causes diverse pollutants to enter the water body, for example, a runoff from agricultural area. Urban stormwater drainage, which can carry grits and other particulate matter, auto petroleum products, or road deicing compounds hence becomes a diffuse source as well due to the multiple entry points at local streams or lakes. Though dispersed sources are more difficult to manage, point sources of water pollution are easier to treat since the contaminated water has already been gathered and directed into one paddock where it can be treated. Managing pollution from numerous sources is very challenging; even with significant advance within the improvement of latest sewage therapy crops, these dispersed sources nonetheless result in a big fraction of water air pollution issues[7], [8], [9].

1.3. *Types and Classification of Pollutants:*

Water pollutants can be categorized with respect to their source, physical state, and toxicity; however, a particularly critical distinction is by their chemical structure: organic versus inorganic pollutants[10].

1.3.1. *Organic Pollutants:*

Organic pollutants are molecular constructs that primarily contain carbon atoms and can range from simple arrangements to advanced synthetic networks. Most of these enter water bodies through diffuse sources like agricultural runoff of pesticides and herbicides, industrial discharges containing chemical solvents and synthetic dyes, or even municipal wastewater

rich in pharmaceuticals. These molecules are extremely persistent and resistant to breakdown but bioaccumulate through the aquatic food web. This leads to massive ecosystem-wide consequences, including endocrine-disruption in wildlife and life-long chronic health risks in humans including: carcinogens, reproductive failure and neuro-toxicity[11]. These often include Persistent Organic Pollutants (POPs) such as DDT, industrial dyes like Crystal Violet[12], and pharmaceutical residues[13].

1.3.2. *Inorganic Pollutants:*

Inorganic pollutants are non-carbon based, including mineral acids, inorganic salts and complexes of metals[14]. The majority come from industrial processes such as electroplating and tanneries, mining, the leaching of electronic waste and fertilizers that contain high quantities of nitrates and phosphates. In contrast to organic pollutants, inorganic pollutants are wholly non-biodegradable and will last forever in the environment[10].

2. Fundamental Properties of Nanomaterials Related to Water Treatment:

Nanoparticles (NPs) are highly efficient decontamination substances for water treatment due to a combination of their physical and chemical properties. These features enable water purification to be more cost effective, sustainable and selective while achieving a higher efficiency in the removal of pollutants.

2.1. *Reactivity and Surface Area:*

Perhaps the most notable thing about NPs is their surface area-to-volume ratio, which tends to be extremely high, therefore conferring enhanced reactivity and adsorption. More active sites available for pollutants to interact with, than what is typically present in an adsorbent. This enables dyes, Heavy Metals, and persistent organic pollutants to be efficiently removed. The increase in reactivity of the NPs, which allows faster interaction between the NPs and continuous at the interface, is attributed to improved batch and continuous treatment systems[15]. For instance, it was revealed that ZnO and FeO NPs were able to adsorb unprecedented amounts of Pb and As ions in contaminated water[16].

2.2. *Chemical and Thermal Stability:*

AMs are long-term chemically and thermally stable substances that can be used in severe water conditions such as acidic mine drainage or saline wastewater. Changes in temperature and pH can lead to aggregation[17], leaching or oxidation. Instead of that, this loss will not take place due to surface treatment like encapsulation which can provide with something

like silica or polymer coating[18]. AMs are tougher and therefore will last much longer without breaking down.

2.3. *Biological and Microbiological Properties:*

These materials including copper oxide (CuO)[19] and Ag[20] are pathogen growth suppressors. By dissolving and the microbial membrane, they stop bacteria, viruses, and fungi that grow by bonding magnesium ions to DNA which inhibits replicating in one of two ways. The Ag+ ions released from Ag NPs particularly interact with thiol groups of proteins of microbes. This blocks metabolic processes and leads to the death of the cells. Recent works has shown the incorporation of Ag NPs into polymeric membranes[21] that will have long-term bactericidal activity and a lower toxicity to non-target organisms.

2.4. *Catalysis Properties:*

AMs are generally good catalysts, especially noble metals and metal oxides. It easily brings redox reactions that turn complex organic compounds into less toxic products – even harmless ones. TiO_2 NPs generate reactive oxygen species (ROS) like superoxide ions, hydroxyl radicals upon irradiation with UV or visible light[22]; for instance. These ROS are responsible for breaking down pharmaceuticals and pesticide residues in wastewater[23]. Pt and Au NPs can also catalyze electron transport and promote impurity decomposition[24].

2.5. *Magnetic Properties:*

some magnetic NPs such as Fe_3O_4 are useful for post treatment recovery. The particles are easily removable using an external magnetic field, minimizing secondary contamination risk and recycling cost of NPs[25]. The magnetic recovery also enables the nanoparticle-based systems to work in a much longer term than conventional water treatment systems that requires regular maintenance. Functionalized Fe_3O_4 NPs also retained appreciable sorption of contaminates after multiple uses[26].

2.6. *Functionalization:*

Nanoparticles are advantageous because they can be easily modified to create a unique surface chemistry and add specific functional groups that will attach with certain pollutants exclusively which makes them selective[27]. For instance, amine-functionalized Fe_3O_4 has been used to remove phosphate from agricultural runoff[28], while thiol-modified silica NPs have been applied for the removal of Hg ions bound to them[29]. Functionalization also gives it a dual role as being able to kill and adhere to microorganisms, while making it more soluble in water.

These unique properties enable researchers and scientists to design next-generation water treatment systems that can be used eliminate specific pollutants, under specific conditions.

3. Water Treatment Methods Using Nanomaterials:

Due to their unique properties and immense versatility, nanomaterials can be useful when it comes to wastewater treatment and remediation in various ways (as shown in **Figure II.1**).

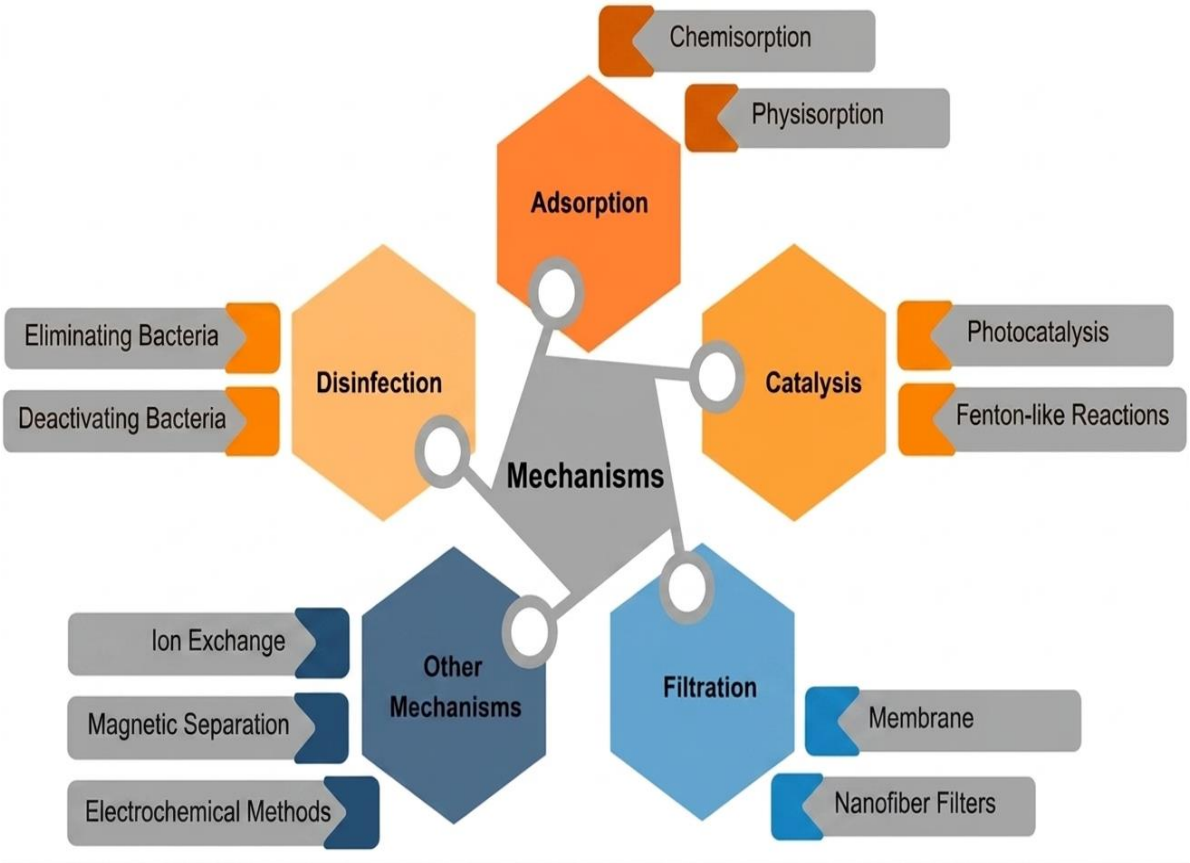


Figure II.1. Methods of water treatment via nano/composite materials[30].

3.1. *Catalysis:*

NPs can be effective catalysts in many ways, especially through the photocatalysis process and the Fenton-like reactions. They are generally used to convert organic pollutants in water into minerals[24]. Light sensitive NPs such as TiO_2, ZnO can absorb light and generate reactive oxygen species (ROS) (such as superoxide ion O_2^- and hydroxyl radical $^{\cdot}OH$) photocatalysis. The resulting ROS then oxidize drugs, dyes and industrial wastes into mineralized and less harmful products. Iron-based NPs are also catalysts for Fenton-type reactions, producing (ROS) that use hydrogen peroxide to degrade organic contaminants[31]. Catalytic degradation efficiency is largely governed by NP composition, dopants and heterojunction formation.

3.2. *Disinfection:*

It is the removal or killing of pathogenic microorganisms in the water that can cause diseases. NPs play a very important role in this field, because they have excellent antimicrobial properties. It is well established that metal NPs, for example Cu and Ag, have a high antibacterial activity. Two promising metal oxide NP including ZnO and TiO_2 may function by producing ROS to kill pathogens.

Emerging evidence indicates that the main mechanisms responsible for the antibacterial functions of NPs include: 1) Disruption of bacteria cytoplasmic membrane; 2) Generation of ROS; 3) Penetration of bacterial cell membrane; and (4) Induction of intracellular antimicrobial effects, such as interactions with DNA and proteins.[19], [20]

3.3. *Filtration:*

Filtration is the process of moving water through a porous material to remove suspended and dissolved contaminants. This than provides reactive sites with high specific surface area which enhances the filtration process by providing sites for adsorption and degradation of pollutants. NPs are doped in membrane and nanofiber filters to enhance the filtering performance[32]. NPs can increase the contaminant removal, permeability, and fouling resistance in membrane systems. Electrospun nanofiber filters are of a high filtration efficiency due to their highly porous and interconnected structure. NPs further support efficient filtration by inserting reactive stages of catalysis and holding contaminants in tailored pore configurations[33]. Size, surface and distribution properties of NP are used to examine their effectiveness in accumulating or degrading impurities. These NP-enhanced filtration systems can be designed to target pathogens, particulate matter, heavy metals and organic pollutants[34].

3.4. *Adsorption:*

Adsorption is the buildup of pollutants on a material's surface. It is one of the most effective and well-studied NP-based water treatment methods. It is also the core interest of this experimental work. Hence, In the next segment of this chapter, we will discuss in depth this phenomenon, its definition, its types, its mechanism etc...

4. Adsorption in Water Treatment:

The growing environmental issues and the immediate advantages of efficient technologies for the treatment of pollutants have classified adsorption as one of the most important methods in this regard. Because of its excellent ability to capture harmful substances from

different types of media, this phenomenon is widely used in water purification, gas treatment or removal organic and inorganic pollutants[35].

Adsorption is a highly versatile method that depends on how molecules interact with solid surfaces and has many applications in different areas, including environmental and industrial fields[36]. Due to its effectiveness and operational simplicity, this phenomenon is a key interest area of researchers and over recent years, it is being increasingly used in more practical studies or applications which are aiming towards solving environmental problems & providing efficient & sustainable solutions.

4.1. *Defining and distinguishing Adsorption:*

It is a surface phenomenon in which gas or liquid molecules (adsorbate) adhere to a solid porous substrate boundary layer (the adsorbent). The interface collecting step serves to concentrate the target species into a film (a molecular layer) with a unique molecular disposition at specific structural positions on the solid surface called active sites.

Such a dynamic surface selectivity mimics the mechanism of organic pollutants extraction from the environment, making this technique extremely efficient for environmental remediation purposes. With the help of high-surface-area matrices that maximize available active sites such as activated carbon, zeolites, and silica gel, adsorption systems handle complex organic and inorganic impurities from polluted aqueous streams efficiently[36].

The interactions responsible for this separation are mainly controlled by either weak and reversible Van der Waals forces that control physical adsorption (physisorption) or strong covalent or ionic bonding present at the interface in chemical adsorptions (chemisorption). This equilibrium can be inverted by changing external parameters, such as temperature and pressure, which is incredibly sensitive to the thermodynamics of the system at that time, removing the previously adsorbed species into solution through a process known as desorption. This mechanism must also be carefully distinguished from absorption, which involves the whole of the substance fully penetrating and diffusing throughout the internal volume of a matrix (i.e. into its bulk) rather than lingering on its surface[36], [37].

4.2. *Types of adsorbents:*

Adsorbent materials are classified based on various criteria (Origin, Composition, Surface Area, Pore size distribution etc…), one of the most important and prevalent classifications is on the basis of their chemical nature, thus we can divide them into two main groups:

- *Inorganic materials*, including highly efficient structures activated alumina, silica gel, zeolites as well as cheaper but less effective analogues such as metal oxides.
- *Organic materials,* such as activated carbon and biopolymers found in abundance in nature such as cellulose, chitin and collagen.

The desired adsorbents must manifest considerable performance in nature which involves adsorption capacity, selectivity, kinetics, cost-effectiveness and regenerability. In the domain of modern water treatment, the main focus is always on materials that strikes a balance between cost and performance[38].

4.3. *Physical Vs Chemical Adsorption:*

The phenomenon of adsorption mainly occurs via either one (or a combination) of two mechanisms:

- *Physical adsorption (physisorption)*: is a reversible surface phenomenon driven by weak Van der Waals forces, occurring when the surface atoms of a solid substrate are electronically saturated.
- *Chemical adsorption (chemisorption):* is an irreversible surface phenomenon driven by localized chemical reactions that form robust covalent or ionic bonds, occurring when unsaturated surface atoms create high reactivity[36], [37].

Each one has its own characteristics and properties, below is a comparison of the two:

Table II.1. *Physical Vs Chemical adsorption [36], [37].*

Property	Physical Adsorption	Chemical Adsorption
Binding Forces	Weak interactions (e.g., Van der Waals forces).	Strong chemical bonds (covalent or ionic).
Heat of Adsorption	$Low\ (\Delta H_{ads} < 40\ kJ/mol)$	$High\ (\Delta H_{ads} > 80\ kJ/mol)$
Layer Thickness	Multi-layer formation.	Monolayer formation only.
Temperature Conditions	Favored at low temperatures (below the adsorbate's boiling point).	Favored at high temperatures (above the adsorbate's boiling point).

Selectivity	Non-selective; can occur on any suitable solid surface.	Highly selective; occurs only between chemically compatible species.
Reversibility	Completely reversible; desorption occurs easily with temperature/pressure changes.	Irreversible; requires extreme conditions (e.g., high heat) to desorb.
Activation Energy	Low; does not require high activation energy.	High; requires significant activation energy to form/break bonds.
Molecular Mobility	Adsorbed molecules are mobile across the surface.	Adsorbed molecules are localized and fixed at specific active sites.

4.4. *Intermolecular forces behind physical adsorption:*

Generally speaking, the intermolecular forces responsible for electrostatic attraction are called 'Van Der Waals forces' and can be classified into three main categories: forces of dispersion, forces of interaction and repulsion, and the dipole – dipole interaction [36], [37], [39], [40].

4.4.1. *Dispersion forces:*

The most important forces that mainly contribute to physical adsorption are called dispersion forces because they come from the random fluctuations of electron density, which creates induced dipoles between two adjacent molecules. They dominate when both the adsorbent and the adsorbate are non-polar or hydrophobic surfaces. The effect of the molecules is weak individually, but as the specific surface area adsorbent increases, their synergetic activity increases very much and helps to hold molecular species even at low concentration in trace amounts [36], [37], [39], [40].

4.4.2. *forces of interaction and repulsion:*

As adsorbate molecules approach the solid phase, their electron orbitals begin to overlap and a force that describes the mutual attraction of both phases comes into play and competes with the repulsive forces between them in order to dictate which will be the equilibrium stabilization distance:

- *Attractive Forces:* Stabilize the incoming molecules via dispersion and Van der Waals effects at an optimal physical distance.

- *Repulsion Forces:* Activated at an incredibly close distance, electron shells of two atoms overlap generating electromagnetic repulsive force acting to keep the atoms from approaching closer.

This balance defines the proximity threshold beyond which repulsive/anti-gravitational forces dominate [36], [37], [39].

4.4.3. *Dipole – dipole interactions:*

Electrostatic forces generated through charge distributions are due to unbalanced polar components in the system, and either permanent or temporary electric dipole moments aligning with other induced dipoles. The it can manifest as polar – nonpolar interactions where a polar molecule, owing to its localized charge distribution, will orient the dipoles within a non-polar molecule's surface or vice versa creating attraction in localized regions. In promotional chemical absorption pathways, these polar interactions contribute to highly strong bond formation that significantly drives the process of selectivity towards targeted pollutants for water purification [36], [37], [39], [40].

4.5. *Bonding in chemical adsorption:*

Chemical adsorption is mediated by several separate chemical types of bonds that bind an adsorbate to an adsorbent surface. Covalent bonding arises from the sharing of valence electrons between functional groups of the adsorbate molecule and surface atoms, resulting in strong, localized bonds. The same is true for when an adsorbate behaves as a Lewis base and donates a lone pair of electrons into vacant orbitals of the active site; this occurs during the so-called coordinate (dative) bonding. Conventional ion exchange is essentially based on electrostatic attractions of counter-ions but can be considered a type of chemical bonding when the exchanged ions form true, irreversible chemical complexes or coordinate covalent bonds with surface functional groups that bind the ions to specific surface coordinates[41], [42].

4.6. *Factors influencing adsorption:*

The performance of an adsorption system is a multi-variable function governed by the thermodynamic and kinetic interactions of its solid and liquid phases.

4.6.1. *The characteristics of the adsorbent's surface:*

The morphology and the chemical nature of the surface ultimately dictate its capacity. A well-defined porous structure, characterized almost entirely by micropores (< 2 nm) grants an enormous specific surface area for contaminant retention. Besides structural morphology,

the density, stability and distribution of active functional groups throughout the matrix govern the binding affinity for target pollutants[40].

4.6.2. *Nature of Adsorbate:*

The adsorptive properties of any particular contaminant (adsorbate) depend on its physicochemical nature. Molecular size (compared with pore diameters of the adsorbent), aqueous phase solubility (to resist phase separation, highly soluble species have a strong tendency to remain in solution) as well as polarity and chemical structure determine how quickly and completely the molecule will interact with available surface sites[36].

4.6.3. *Contact Time:*

Contact time establishes the kinetic progression toward solid-liquid equilibrium. The rate of contaminant uptake is typically rapid during initial phases due to the abundance of vacant surface sites, eventually plateauing as intraparticle diffusion controls the migration into deeper pore networks until equilibrium is achieved[40], [43][44].

4.6.4. *Temperature:*

The kinetics and the essential thermodynamic equilibrium of the system are both dependent on temperature. In the case of an exothermic process (usually physisorption), higher temperature provides additional thermal energy that break weak attractive forces favoring desorption. On the contrary, in endothermic chemisorption high temperatures deliver the necessary activation energy for localized chemical reactions and bond creation[37].

4.6.5. *Adsorbate concentration (Dose):*

The driving force for mass transfer between the solution's bulk and the solid interface is the initial concentration of the adsorbate. Higher initial concentrations create a greater concentration difference that must be overcome if mass transfer resistance is to be challenged, thus enhancing the initial rate of adsorption until saturation of the available active sites[40], [44].

4.6.6. *The pH:*

The pH of the aqueous medium is a key operating parameter that simultaneously modifies surface charge on the adsorbent and species (speciation) of the adsorbate. Near the adsorbent's Point of Zero Charge (pH_{PZC}), the surface is characterized by a null net surface charge. however, any change in pH results in protonation (positive charge) or deprotonation (negative charge) of the surface which results in electrostatic attraction or repulsion toward ionic contaminant[45].

4.7. *Adsorption Isotherms:*

An adsorption isotherm defines the fundamental equilibrium relationship between the residual solute concentration in the fluid phase (C_e) and the quantity of adsorbate retained on the solid surface (q_e) at a *constant temperature[40], [43], [46]*. The equilibrium capacity is mathematically quantified using the mass balance formula (**II.1**):

$$q_e = \frac{C_0 - C_e}{m} \cdot V \qquad \textbf{II.1}$$

Where:

- C_0 and C_e are the initial and equilibrium adsorbate concentrations (mg/L),
- V is the solution volume (L)
- m is the mass of the adsorbent (g).

4.7.1. *The Langmuir Isotherm:*

The Langmuir model provides a theoretical framework for localized, monolayer chemisorption onto a structurally homogenous surface. The model is based on four very stringent boundary assumptions: all the active sites are identical in energetics, a single molecule interacts with each site, no lateral interactions and material transport occur parallel to the surface plane during the reaction process and finally that it is an inherently unassisted process [43], [46]. Its non – linear expression (**II.2**) is:

$$q_e = \frac{q_m K_L C_e}{1 + K_L C_e} \qquad \textbf{II.2}$$

Where:

- C_e represents the equilibrium liquid-phase concentration (mg/L).
- q_e represents the equilibrium adsorption capacity (mg/g).
- q_m represents the maximum monolayer adsorption capacity (mg/g).
- k_L is the Langmuir affinity constant (L/mg).

The essential thermodynamic favorability of this system is evaluated using the dimensionless separation factor (R_L), which is defined by the expression (**II.3**):

$$R_L = \frac{1}{1 + k_L C_o} \qquad \textbf{II.3}$$

The system profile is categorized based on the magnitude of R_L: irreversible ($R_L = 0$), favorable ($0 < R_L < 1$), linear ($R_L = 1$), or unfavorable ($R_L > 1$).

4.7.2. *The Freundlich Isotherm:*

In contrast, the Freundlich model is an empirical formulation designed to describe multi-layer adsorption onto structurally heterogeneous surfaces. It assumes that active sites possess exponentially distributed binding energies and that reversible interactions occur across multiple molecular tiers. The non-linear equation (**II.4**) is expressed as:

$$q_e = K_f \cdot C_e^{\frac{1}{n}} \qquad \textbf{II.4}$$

Where:

- K_f represents the Freundlich adsorption capacity constant (mg/g) (L/mg)$^{1/n}$.
- n is the Freundlich heterogeneity factor indicating the adsorption intensity.

The value of n serves as a diagnostic indicator for the prevailing retention mechanism: an index value of n < 1 denotes a physical adsorption pathway, whereas n > 1 signifies dominant chemisorption controls [43], [46].

4.7.3. *The Sips Isotherm:*

The Sips model is an amalgamated equation formulated to describe adsorption at heterogeneous sites bridging the cap of both the Langmuir and Freundlich models. At lower concentrations of the adsorbate, it reduces to the Freundlich isotherm while at higher concentrations it predicts an upper limit to monolayer adsorption capacity. The non-linear equation (**II.5**) is expressed as:

$$\boldsymbol{q_e} = \frac{\boldsymbol{q_m}(\boldsymbol{K_S} \cdot \boldsymbol{C_e})^{\frac{1}{m}}}{\mathbf{1} + (\boldsymbol{K_S} \cdot \boldsymbol{C_e})^{\frac{1}{m}}} \qquad \textbf{II.5}$$

- q_m represents the maximum Sips monolayer adsorption capacity (mg/g).
- K_S represents the Sips affinity constant (L/mg).
- m is the Sips heterogeneity factor indicating the adsorption intensity.

The value of m provides a diagnostic measure of the surface's heterogeneity. an index value of m = 1 simplifies the equation into the Langmuir case for a fully homogeneous surface, while deviations from unity indicate more dominant influences by structural or energetic basis for heterogeneity.

4.7.4. *The Toth Isotherm:*

The Toth model is an empirical formulation designed to describe adsorption onto highly heterogeneous systems, introducing a specific modification to the Langmuir equation that improves its correlation with experimental data at both lower and upper concentration bounds. The non-linear equation (**II.6**) is expressed as:

$$q_e = \frac{q_m \cdot C_e}{(K_T + C_e^z)^{1/z}} \qquad \textbf{II.6}$$

Where:

- q_m represents the maximum Toth monolayer adsorption capacity (mg/g).
- K_T represents the Toth model constant related to adsorption energy.
- z is the Toth heterogeneity factor indicating the structural character of the adsorbent.

The value of z serves as a diagnostic indicator for the prevailing system deviation from ideal homogeneity: an index value of z = 1 reduces the expression directly to the standard Langmuir isotherm, whereas a value further away from unity signifies a higher degree of surface heterogeneity.

4.8. *Adsorption Kinetics:*

4.8.1. *Pseudo-First-Order Model (PFO):*

The PFO model states that the rate of site occupation is directly proportional to the distance from equilibrium, meaning the difference between transient capacity (q_t) and equilibrium capacity (q_e). The integrated linear expression (**II.7**) is given as:

$$ln(q_e - q_t) = ln\, q_e - k_1 t \qquad \textbf{II.7}$$

Where:

- t is the operational contact time (min).
- k_1 represents the pseudo-first-order rate constant (min^{-1}).
- q_t represents the quantity of adsorbate retained at time t (mg/g).
- q_e represents the theoretical equilibrium (maximum) adsorption capacity (mg/g).

4.8.2. *Pseudo-Second-Order Model (PSO):*

The PSO model assumes that the rate-limiting step is driven by chemisorption, involving electronic sharing or exchange between the active surface moieties and the solute. Its integrated linear form (**II.6**) is arranged as:

$$\frac{t}{q_t} = \frac{1}{k_2 \cdot q_e^2} + \frac{t}{(q_e)} \quad \text{II.8}$$

Where:

- t is the operational contact time (min).
- k_2 is the pseudo-second-order rate constant (g/mg·min).
- q_t represents the quantity of adsorbate retained at time t (mg/g).
- q_e represents the theoretical equilibrium (maximum) adsorption capacity (mg/g).

Plotting $\frac{t}{q_t}$ against t yields a linear relationship from which both q_e and k_2 can be explicitly determined [44], [47].

4.8.3. *Intraparticle Diffusion Model (Weber-Morris):*

To identify whether molecular migration into the internal porous network acts as the slow step controlling the system, the Weber-Morris intraparticle diffusion model is applied:

$$q_t = k_{id} \cdot t^{1/2} + C \quad \text{II.9}$$

Where:

- k_{id} is the intraparticle diffusion rate constant (mg/(g·min$^{0.5}$))
- C is the boundary layer thickness factor.
- t is the operational contact time (min).

If a plot of q_t versus $t^{1/2}$ yields a multi-linear profile that bypasses the origin, it indicates that the adsorption process is governed by a combination of external film boundary resistance followed by internal pore diffusion[47].

4.9. *Adsorption Thermodynamics:*

Thermodynamic parameters evaluate the spontaneity, energetic nature, and structural randomness of the solid-liquid interface. The standard Gibbs free energy change (ΔG°) is derived directly from the thermodynamic equilibrium constant (K_D):

$$\Delta G^\circ = \Delta H^\circ - T \cdot \Delta S^\circ \quad \text{II.10}$$

Where:

- ΔG° represents the standard Gibbs free energy change (kJ/mol).
- T represents the absolute temperature (K).

- ΔH° represents the standard enthalpy change (J/mol).
- ΔS° represents the standard entropy change (J/mol·K).

To evaluate the temperature dependence of the process, the standard enthalpy changes (ΔH°) and entropy change (ΔS°) are calculated using the linear Van 't Hoff relation:

$$ln\, K_D = -\frac{\Delta H^{\circ}}{RT} + \frac{\Delta S^{\circ}}{R} \qquad \text{II.11}$$

Where:

- K_D represents the thermodynamic equilibrium constant.
- R represents the universal gas constant (8.314 J/mol·K).

A negative value for ΔH° confirms an exothermic process typical of physisorption, where excess thermal energy destabilizes weak surface bonds. Conversely, a positive enthalpy reflects an endothermic chemisorption pathway driven by chemical activation requirements. Meanwhile, the sign of ΔS° monitors whether structural randomness increases or decreases at the solid-liquid boundary during target species immobilization[48].

5. Introduction to Intelligent Computational Modeling in Water Treatmnt:

5.1. *The Role of Digital Transformation and Machine Learning:*

The limitations of conventional empirical approaches to the management of complex and non-linear system dynamics[49] has led to water treatment being digitalized as part of a broader digital transformation enabling the use of Artificial Intelligence (AI) and Machine Learning (ML). Using historical datasets, ML algorithms such as Artificial Neural Networks (ANNs) and Support Vector Machines (SVMs) are capable of effectively forecasting and optimising key processes like coagulation, flocculation and disinfection by-product (DBP) production while considerably alleviating the dependence on manual jar testing process [49], [50]. Also, from the perspective of heavy metal removal, ML helps design high-performance adsorbents (e.g., cation exchange capacity) by uncovering correlations with removal efficiency without traditional trial-and-error experimentation [51], [52]. These AI models integrate alongside Internet of Things (IoT) sensor networks to construct an autonomous "Artificial Intelligence of Things" scenario, characteristically enabling continuous, real-time data collection and process control [49], [50]. Nonetheless, the field is hindered by such obstacles as a scarcity of data, the black-box nature of deep learning and a need for even more model transparency [49], [51]. Future efforts must focus on "explainable AI" (XAI)

frameworks and standardized, blockchain-secured data repositories to enhance model generalizability, accountability, and public trust in AI-driven water treatment paradigms [49], [52].

5.2. *Classical Statistical Regression vs. Heuristic Machine Learning:*

Heuristic machine learning is a fundamentally different way of modeling water treatment processes compared to classical statistical regression. For instance, classical regression methods (e.g., Linear or Multiple Linear Regression) are statistically defined and operate on a known mathematical structure with linear distributions of independent variables (like pH or temperature) that affect treatment outcomes [49]. However, they are typically very interpretable and computationally efficient but tend to struggle regarding the detailed capturing of non-linear dependencies and stochastic fluctuations in diverse real-world wastewater data [50]. Heuristic machine learning, such as Random Forests, Neural Networks and Gradient Boosting utilizes a data-driven, bottom-up approach that does not assume anything about the functional form of the relationship [51]. Heuristic ML uses causal, physical structures as prior to iteratively adjust its internal parameters over large and diverse datasets to establish immediate hidden connections between high dimensional inputs and outputs, enabling it to "learn" the underlying dynamics of complex systems like heavy metal adsorption or membrane fouling with greater predictive capability [52].However, this increase in predictive power often comes at the cost of the "black-box" nature of heuristic models, which lack the explicit transparency of statistical coefficients, necessitating the development of explainable AI (XAI) techniques to bridge the gap between performance and operational trust [49], [52]. Ultimately, while classical regression remains useful for simple, well-understood systems, heuristic ML is becoming the standard for modern, high-complexity water infrastructure management.

5.3. *Artificial Neural Networks (ANN): Multilayer Perceptron and Backpropagation Architecture:*

Modern machine learning heavily relies on building up Artificial Neural Networks (ANN) architectures often for more complex solutions e.g heavy metal adsorption and water purification models [50], [51], [52]. The Multilayer Perceptron (MLP): The MLP is a supervised learning model with an architecture consisting of layers: an input layer, one or more hidden layers and an output layer [49], [51]. The layers consist of individual nodes or "neurons" that analyze incoming information using weighted connections (with each weight reflecting the strength of the relationship between neurons). Each node within a NN conducts

the weighted sum of its inputs and applies an activation function to the weighted output, adding non-linearity necessary for capturing complex relationships in datasets [49], [51]. This process is guided by the backpropagation algorithm, which minimizes the discrepancy between the predicted output of a network and an actual target value in a cycle manner [50], [51]. Backpropagation forwards propagates the error from the output layer to hidden layers, where adjustment is undertaken via gradient descent, and this process iteratively optimises the model performance over time [49], [51]. The model can now optimize the physiochemical processes in water treatment systems [49], [52].

5.4. *Extreme Learning Machines (ELM): Randomized Single-Layer Feedforward Networks (SLFNs):*

Extreme Learning Machines (ELM) are a very advanced variant of randomized single-layer feedforward networks (SLFNs), and recently have been applied to adsorbent-based esterifer-sorption remediation due to their remarkable computational efficiency [49]. Contrary to time-consuming iterative backpropagation in the case of classical ANNs, ELMs utilize a mechanism in which the weights and biases of hidden layer are randomly assigned and remain static while only output weights need to be determined analytically [50]. This structure likely allows for much shorter training times and does not suffer from common local minima, thus providing a powerful tool for modelling the details of non-linear adsorption dynamics of pollutants onto adsorbents [49], [52]. For practical cases of adsorption, it has been successfully used to predict heavy metal removal efficiencies through specialized versions such as Kernel Extreme Learning Machines (KELM), which shows R^2 higher than 0.99 in the modeling Pb (II), Cd (II) and As (III) biorremoval efficiency using biochar [50], [51]. The characteristic features of these randomized networks are that they are designed to process high-dimensional datasets corresponding to adsorbent physicochemical properties (e.g., surface area, functional groups) and adsorption conditions (pH–pH, initial concentration). Despite these advantages, a primary challenge in implementing ELM frameworks remains their sensitivity to the selection of hidden nodes, which can lead to over-fitting if the network architecture is not carefully optimized for the specific wastewater matrix [49]. Modern research continues to leverage these models to enhance the predictive accuracy of adsorption capacity and removal efficiency across diverse environmental settings [52].

6. Applications & Uses of Treated Water in Irrigation:

Introduction The reuse of treated wastewater (TWW) for irrigation in arid and semi-arid areas has several advantages, as it contains nutrients such as nitrogen, phosphorus, or potassium which reduce the need to apply synthetic chemical fertilizers. When used on non-food crops, such as fiber, feed and industrial crops, this reclaimed water is a sustainable avenue to relieve pressure on freshwater sources while improving soil fertility and biomass production. Additionally, it can be used to replenish groundwater and ensure the stability of landscapes, contributing to agricultural sustainability in the long term. Such irrigation practices would require strict monitoring of effluent quality and site-specific conditions to minimize risks of soil salinization, heavy metal accumulation, and residual contamination. This method effectively closes the loop in a circular economy, ensuring that lower-quality water is used for activities where human or animal consumption does not need to be considered [53], [54].

Chapter Two References:

[1] A. Tkaczyk, K. Mitrowska, and A. Posyniak, "Synthetic organic dyes as contaminants of the aquatic environment and their implications for ecosystems: A review," *Science of The Total Environment*, vol. 717, p. 137222, May 2020, doi: 10.1016/j.scitotenv.2020.137222.

[2] R. P. Schwarzenbach, T. Egli, T. B. Hofstetter, U. von Gunten, and B. Wehrli, "Global Water Pollution and Human Health," *Annu. Rev. Environ. Resour.*, vol. 35, no. 1, pp. 109–136, Nov. 2010, doi: 10.1146/annurev-environ-100809-125342.

[3] G. Crini and E. Lichtfouse, "Advantages and disadvantages of techniques used for wastewater treatment," *Environmental Chemistry Letters 2018 17:1*, vol. 17, no. 1, pp. 145–155, Jul. 2018, doi: 10.1007/S10311-018-0785-9.

[4] M. A. Shannon, P. W. Bohn, M. Elimelech, J. G. Georgiadis, B. J. Mariñas, and A. M. Mayes, "Science and technology for water purification in the coming decades," *Nature*, vol. 452, no. 7185, pp. 301–310, Mar. 2008, doi: 10.1038/nature06599.

[5] C. N. . Sawyer, P. L. . McCarty, and G. F. . Parkin, *Chemistry for environmental engineering and science*. McGraw-Hill, 2007.

[6] Rodger. Baird, A. D. . Eaton, E. W. . Rice, and Laura. Bridgewater, *Standard Methods for the Examination of Water and Wastewater*. American Public Health Association, 2017.

[7] J. Ruprecht and S. Dogramaci, "Loague, K., & Corwin, D. L. (2005). Nonpoint source pollution. Encyclopedia of Hydrological Sciences, 1-15," in *Encyclopedia of Hydrological Sciences*, Wiley, 2005. doi: 10.1002/0470848944.hsa102.

[8] T. D. Fletcher, H. Andrieu, and P. Hamel, "Understanding, management and modelling of urban hydrology and its consequences for receiving waters: A state of the art," *Adv. Water Resour.*, vol. 51, pp. 261–279, Jan. 2013, doi: 10.1016/j.advwatres.2012.09.001.

[9] Vladimir. Novotny, *Water quality : diffuse pollution and watershed management*. J. Wiley, 2003.

[10] R. P. Schwarzenbach *et al.*, "The Challenge of Micropollutants in Aquatic Systems," *Science (1979).*, vol. 313, no. 5790, pp. 1072–1077, Aug. 2006, doi: 10.1126/science.1127291.

[11] M. S. El-Shahawi, A. Hamza, A. S. Bashammakh, and W. T. Al-Saggaf, "An overview on the accumulation, distribution, transformations, toxicity and analytical methods for the monitoring of persistent organic pollutants," *Talanta*, vol. 80, no. 5, pp. 1587–1597, Mar. 2010, doi: 10.1016/j.talanta.2009.09.055.

[12] S. Mani and R. N. Bharagava, "Exposure to crystal violet, its toxic, genotoxic and carcinogenic effects on environment and its degradation and detoxification for environmental safety," *Rev. Environ. Contam. Toxicol.*, vol. 237, pp. 71–104, 2016, doi: 10.1007/978-3-319-23573-8_4/SAVE-RESEARCH.

[13] J. L. Wilkinson *et al.*, "Pharmaceutical pollution of the world's rivers," *Proc. Natl. Acad. Sci. U. S. A.*, vol. 119, no. 8, Feb. 2022, doi: 10.1073/PNAS.2113947119.

[14] H. Ali, E. Khan, and I. Ilahi, "Environmental Chemistry and Ecotoxicology of Hazardous Heavy Metals: Environmental Persistence, Toxicity, and Bioaccumulation," *J. Chem.*, vol. 2019, pp. 1–14, Mar. 2019, doi: 10.1155/2019/6730305.

[15] C. Santhosh, V. Velmurugan, G. Jacob, S. K. Jeong, A. N. Grace, and A. Bhatnagar, "Role of nanomaterials in water treatment applications: A review," *Chemical Engineering Journal*, vol. 306, pp. 1116–1137, Dec. 2016, doi: 10.1016/j.cej.2016.08.053.

[16] M. Hua, S. Zhang, B. Pan, W. Zhang, L. Lv, and Q. Zhang, "Heavy metal removal from water/wastewater by nanosized metal oxides: A review," *J. Hazard. Mater.*, vol. 211–212, pp. 317–331, Apr. 2012, doi: 10.1016/j.jhazmat.2011.10.016.

[17] E. M. Hotze, T. Phenrat, and G. V. Lowry, "Nanoparticle Aggregation: Challenges to Understanding Transport and Reactivity in the Environment," *J. Environ. Qual.*, vol. 39, no. 6, pp. 1909–1924, Nov. 2010, doi: 10.2134/jeq2009.0462.

[18] Y. K. Gautam, K. Sharma, S. Tyagi, A. Kumar, and B. P. Singh, "Applications of green nanomaterials in coatings," in *Green Nanomaterials for Industrial Applications*, Elsevier, 2022, pp. 107–152. doi: 10.1016/B978-0-12-823296-5.00014-9.

[19] G. Applerot *et al.*, "Understanding the Antibacterial Mechanism of CuO Nanoparticles: Revealing the Route of Induced Oxidative Stress," *Small*, vol. 8, no. 21, pp. 3326–3337, Nov. 2012, doi: 10.1002/smll.201200772.

[20] C. Marambio-Jones and E. M. V. Hoek, "A review of the antibacterial effects of silver nanomaterials and potential implications for human health and the environment,"

Journal of Nanoparticle Research, vol. 12, no. 5, pp. 1531–1551, Jun. 2010, doi: 10.1007/s11051-010-9900-y.

[21] A. Iqbal, E. Cevik, A. Mustafa, T. F. Qahtan, M. Zeeshan, and A. Bozkurt, "Emerging developments in polymeric nanocomposite membrane-based filtration for water purification: A concise overview of toxic metal removal," *Chemical Engineering Journal*, vol. 481, p. 148760, Feb. 2024, doi: 10.1016/j.cej.2024.148760.

[22] A. Kessler, J. Hedberg, E. Blomberg, and I. Odnevall, "Reactive Oxygen Species Formed by Metal and Metal Oxide Nanoparticles in Physiological Media—A Review of Reactions of Importance to Nanotoxicity and Proposal for Categorization," *Nanomaterials*, vol. 12, no. 11, p. 1922, Jun. 2022, doi: 10.3390/nano12111922.

[23] F. Lu and D. Astruc, "Nanocatalysts and other nanomaterials for water remediation from organic pollutants," *Coord. Chem. Rev.*, vol. 408, p. 213180, Apr. 2020, doi: 10.1016/j.ccr.2020.213180.

[24] M. N. Chong, B. Jin, C. W. K. Chow, and C. Saint, "Recent developments in photocatalytic water treatment technology: A review," *Water Res.*, vol. 44, no. 10, pp. 2997–3027, May 2010, doi: 10.1016/j.watres.2010.02.039.

[25] S. C. N. Tang and I. M. C. Lo, "Magnetic nanoparticles: Essential factors for sustainable environmental applications," *Water Res.*, vol. 47, no. 8, pp. 2613–2632, May 2013, doi: 10.1016/j.watres.2013.02.039.

[26] A. Lu, E. L. Salabas, and F. Schüth, "Magnetic Nanoparticles: Synthesis, Protection, Functionalization, and Application," *Angew. Chem. Int. Ed.*, vol. 46, no. 8, pp. 1222–1244, Feb. 2007, doi: 10.1002/anie.200602866.

[27] D. Rath, S. Rana, and K. M. Parida, "Organic amine-functionalized silica-based mesoporous materials: an update of syntheses and catalytic applications," *RSC Adv.*, vol. 4, no. 100, pp. 57111–57124, Oct. 2014, doi: 10.1039/C4RA08005J.

[28] Z. Iqbal, M. S. Tanweer, and M. Alam, "Recent advances in adsorptive removal of wastewater pollutants by chemically modified metal oxides: A review," *Journal of Water Process Engineering*, vol. 46, p. 102641, Apr. 2022, doi: 10.1016/j.jwpe.2022.102641.

[29] J. Aguado, J. M. Arsuaga, A. Arencibia, M. Lindo, and V. Gascón, "Aqueous heavy metals removal by adsorption on amine-functionalized mesoporous silica," *J. Hazard. Mater.*, vol. 163, no. 1, pp. 213–221, Apr. 2009, doi: 10.1016/j.jhazmat.2008.06.080.

[30] S. Rawat, S. M. Tauseef, M. Sharma, A. Rautela, and R. G. Gurav, "A comprehensive review on emerging nanoparticle-based sustainable water treatments: Synthesis, characterisation, and treatment efficiency," *Desalination Water Treat.*, vol. 326, p. 101724, Apr. 2026, doi: 10.1016/j.dwt.2026.101724.

[31] A. D. Bokare and W. Choi, "Review of iron-free Fenton-like systems for activating H2O2 in advanced oxidation processes," *J. Hazard. Mater.*, vol. 275, pp. 121–135, Jun. 2014, doi: 10.1016/j.jhazmat.2014.04.054.

[32] L. Y. Ng, A. W. Mohammad, C. P. Leo, and N. Hilal, "Polymeric membranes incorporated with metal/metal oxide nanoparticles: A comprehensive review," *Desalination*, vol. 308, pp. 15–33, Jan. 2013, doi: 10.1016/j.desal.2010.11.033.

[33] V. Thavasi, G. Singh, and S. Ramakrishna, "Electrospun nanofibers in energy and environmental applications," *Energy Environ. Sci.*, vol. 1, no. 2, p. 205, 2008, doi: 10.1039/b809074m.

[34] X. Qu, P. J. J. Alvarez, and Q. Li, "Applications of nanotechnology in water and wastewater treatment," *Water Res.*, vol. 47, no. 12, pp. 3931–3946, Aug. 2013, doi: 10.1016/j.watres.2012.09.058.

[35] G. Crini, E. Lichtfouse, L. D. Wilson, and N. Morin-Crini, "Conventional and non-conventional adsorbents for wastewater treatment," *Environ. Chem. Lett.*, vol. 17, no. 1, pp. 195–213, Mar. 2019, doi: 10.1007/s10311-018-0786-8.

[36] A. Dąbrowski, "Adsorption — from theory to practice," *Adv. Colloid Interface Sci.*, vol. 93, no. 1–3, pp. 135–224, Oct. 2001, doi: 10.1016/S0001-8686(00)00082-8.

[37] F. Rouquerol, *Adsorption by powders and porous solids : principles, methodology and applications*. Academic Press, 2014.

[38] I. Ali, "New Generation Adsorbents for Water Treatment," *Chem. Rev.*, vol. 112, no. 10, pp. 5073–5091, Oct. 2012, doi: 10.1021/cr300133d.

[39] J. N. . Israelachvili, *Intermolecular and surface forces*. Academic Press, 2011.

[40] F. Rouquerol, *Adsorption by powders and porous solids : principles, methodology and applications*. Academic Press, 2014.

[41] O. D. Agboola and N. U. Benson, “Physisorption and Chemisorption Mechanisms Influencing Micro (Nano) Plastics-Organic Chemical Contaminants Interactions: A Review,” *Front. Environ. Sci.*, vol. 9, May 2021, doi: 10.3389/fenvs.2021.678574.

[42] Peter. Atkins, *Atkins’ physical chemistry*. Oxford University Press, 2017.

[43] M. A. Al-Ghouti and D. A. Da’ana, “Guidelines for the use and interpretation of adsorption isotherm models: A review,” *J. Hazard. Mater.*, vol. 393, p. 122383, Jul. 2020, doi: 10.1016/j.jhazmat.2020.122383.

[44] W. Plazinski, W. Rudzinski, and A. Plazinska, “Theoretical models of sorption kinetics including a surface reaction mechanism: A review,” *Adv. Colloid Interface Sci.*, vol. 152, no. 1–2, pp. 2–13, Nov. 2009, doi: 10.1016/j.cis.2009.07.009.

[45] Marek. Kosmulski, *Surface charging and points of zero charge*. CRC Press, 2009.

[46] G. Limousin, J.-P. Gaudet, L. Charlet, S. Szenknect, V. Barthès, and M. Krimissa, “Sorption isotherms: A review on physical bases, modeling and measurement,” *Applied Geochemistry*, vol. 22, no. 2, pp. 249–275, Feb. 2007, doi: 10.1016/j.apgeochem.2006.09.010.

[47] M. Kostoglou and T. D. Karapantsios, “Why Is the Linearized Form of Pseudo-Second Order Adsorption Kinetic Model So Successful in Fitting Batch Adsorption Experimental Data?,” *Colloids and Interfaces*, vol. 6, no. 4, p. 55, Oct. 2022, doi: 10.3390/colloids6040055.

[48] S. Milonjic, “A consideration of the correct calculation of thermodynamic parameters of adsorption,” *Journal of the Serbian Chemical Society*, vol. 72, no. 12, pp. 1363–1367, 2007, doi: 10.2298/JSC0712363M.

[49] M. Lowe, R. Qin, and X. Mao, “A Review on Machine Learning, Artificial Intelligence, and Smart Technology in Water Treatment and Monitoring,” *Water (Basel).*, vol. 14, no. 9, p. 1384, Apr. 2022, doi: 10.3390/w14091384.

[50] S. Safeer *et al.*, “A review of artificial intelligence in water purification and wastewater treatment: Recent advancements,” *Journal of Water Process Engineering*, vol. 49, p. 102974, Oct. 2022, doi: 10.1016/j.jwpe.2022.102974.

[51] X. Yuan *et al.*, “Machine Learning for Heavy Metal Removal from Water: Recent Advances and Challenges,” *ACS ES&T Water*, vol. 4, no. 3, pp. 820–836, Mar. 2024, doi: 10.1021/acsestwater.3c00215.

[52] S. Satyam and S. Patra, “Innovations and challenges in adsorption-based wastewater remediation: A comprehensive review,” *Heliyon*, vol. 10, no. 9, p. e29573, May 2024, doi: 10.1016/j.heliyon.2024.e29573.

[53] M. Benaafi *et al.*, “Suitability of treated wastewater for irrigation and its impact on groundwater resources in arid coastal regions: Insights for water resources sustainability,” *Heliyon*, vol. 10, no. 8, p. e29320, Apr. 2024, doi: 10.1016/j.heliyon.2024.e29320.

[54] F. Pedrero, I. Kalavrouziotis, J. J. Alarcón, P. Koukoulakis, and T. Asano, “Use of treated municipal wastewater in irrigated agriculture—Review of some practices in Spain and Greece,” *Agric. Water Manag.*, vol. 97, no. 9, pp. 1233–1241, Sep. 2010, doi: 10.1016/j.agwat.2010.03.003.

Experimental Part

Chapter III

Materials & Methods

This chapter describes the complete experimental approach followed to develop a unique hybrid bio-composite [1], based on a green chemistry strategy involving green sol-gel co-precipitation followed by thermal condensation crosslinking. The systematic fabrication process comprised several steps. The first step involved extracting natural gelatin from camel bones [1] using a hybrid method. This was then incorporated into a homogeneous mixture of polyvinyl alcohol [2] (PVA), chitosan [3], [4], cellulose [5] and bentonite [6], [7].

This study evaluates the efficiency of the prepared BCCG/PVA hybrid composite as a smart adsorbent for removing contaminants from polluted wastewater. The primary focus of this research is the utilisation of a technique known as 'chemical crosslinking' to synthesise the composite structure and enhance its stability. Citric acid was used to dissolve the polymeric materials while simultaneously acting as a biocompatible and versatile bridging agent. This provides a safer, more environmentally friendly alternative to hazardous synthetic crosslinkers.

1. Materials, Reagents & Apparatus:

The chemicals, polymers, and natural precursors used in this study, along with their sources and purity levels, are summarized in **Table III.1**.

Table III.1. *List of chemical reagents, their CAS numbers, and Providers.*

Reagents	Cas N°	Provider
Chitosan $(C_6H_{11}O_4N)_n$	9012-76-4	Sigma-Aldrich, Iceland.
Cellulose powder	9004-34-6	Biochem Chemopharma, France.
Polyvinyl Alcohol (PVA)	9002-89-5	(Ningxia), China
Hydrochloric Acid (HCl, 37%)	7647-01-0	Carlo Erba Reagents, France
Sodium Hydroxide (NaOH)	1310-73-2	Biochem Chemopharma (France)
Citric Acid ($C_6H_8O_7$) (99%)	77-92-9	
Acetic Acid (CH_3COOH)	64-19-7	
Ethanol	64-17-5	SPECILAB
Bentonite ($(Al, Mg)_2Si_4O_{10}(OH)_2$. n H_2O)	1302-78-9	
Crystal Violet $C_{23}H_{30}ClN_3$	548-62-9	Biochem Chemopharma
Methyl Orange $C_{14}H_{14}N_3NaO_3S$	547-58-0	

Table III.2 highlights the instruments and apparatus used in this experimental work:

Table III.2. *Laboratory equipment and instruments.*

Equipment / Instrument	Model / Type
UV-Vis Spectrophotometer	Shimadzu UV-1900i
Visible Spectrophotometer	DLAB SP-V1100
FT-IR Spectrometer	Agilent Technologies Cary 630 FTIR
Centrifuge	DLAB DM0412P
pH Meter	Adwa AD1030
Analytical Balance	OHAUS EXPLORER
Shaking Water Bath	Memmert WNB29
Drying Oven	ELOs Heat
Magnetic Stirring Heating Mantle	LBX, HMSD series (500 ml)
Ultrasonic water bath	Powersonic®, Martin Walter, Germany

Likewise, the **Table III.3** also summarizes the glassware used during the various experiments carried out in this work:

Table III.3. List of laboratory glassware and apparatus.

Glassware	Capacity (mL)
Beaker	(25, 50, 250, 1000)
Volumetric Flask	(25, 50, 250, 1000)
Round-Bottom Flask	(250, 500)
Graduated Cylinder	100
Erlenmeyer Flask	250
Pipette	(5,10)
Burette	50
Neck Round-Bottom Flasks	500, 1000
Separatory Funnel	250
Crystallizing Dish.	
Glass Rod	
Watch Glass	
Reflux Condenser	

2. Experimental Procedures & Methods:

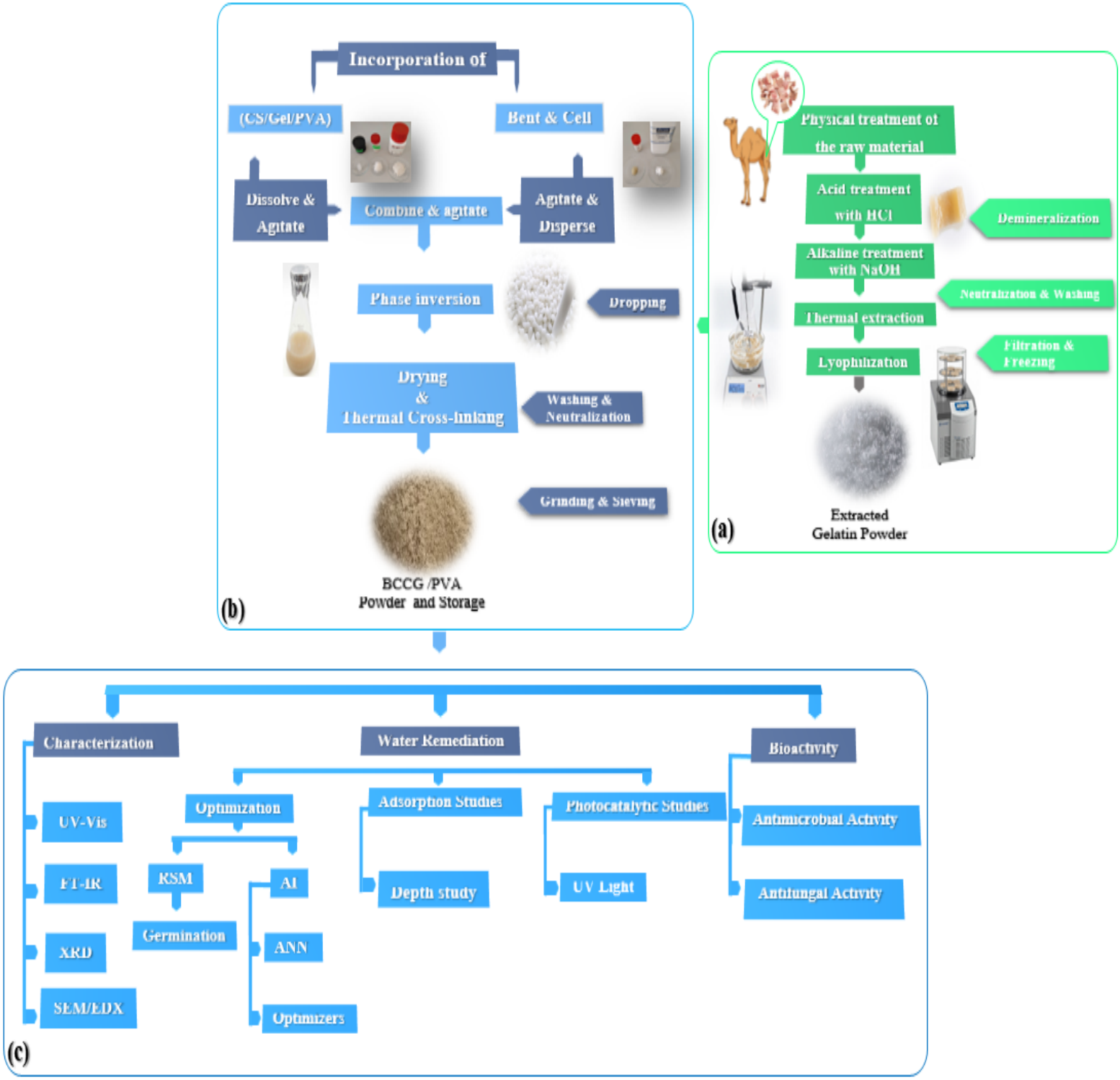


Figure III.1. *Process flow Chart for* ***(a)*** *Gelatin extraction,* ***(b)*** *(BCCG/PVA) synthesis and* ***(c)*** *characterization, modeling, and performance evaluation.*

2. Gelatin Extraction (from Camel Bone):

The gelatin extraction stages were adopted and modified to fit the experimental conditions for camel bones based on the method reported by Imelhayene et al[8] which is summarized in **Figure III.1**. The process was carried out in four main steps to ensure high efficiency of extraction. These are physical processing of the bones, acid treatment, alkaline treatment and thermal extraction.

2.1.1. *Collecting Bone Samples:*

The main natural raw material for gelatin extraction was camel bones which in an valorization effort for local animal byproduct[9]. Fresh limb bones were directly collected from the municipal slaughterhouse of El Oued (Algeria). Samples were collected from a local breed of dromedary camel (*Camelus dromedarius*) less than three years of age[1] slaughtered on February 3rd, 2026, for the extraction of high-quality collagen. This careful selection was made in order to guarantee reproducible extraction results.

2.1.2. *Sample preparation:*

To remove any remaining soft tissue or fat, the bones were cut into pieces shorter than 2 cm. The bone marrow was then scraped off, and the bones were washed with hot water.

2.1.3. *Bone demineralization:*

The second stage of this process was the production of ossein (flexible soft bone tissue). This was done by breaking down the mineral structure of the bone. This is mainly calcium and coats the bone matrix. A sample of cut bones was put into 5% (v/v) HCl solution, to give a 1:10 bone to solution ratio. The experiment was performed at 25 °C, and the HCl solution was replaced daily for 5 days to maintain its effectiveness. The ossein was then thoroughly washed with distilled water until a neutral pH was reached.

2.1.4. *Alkaline Treatment & Neutralization:*

The obtained ossein was then subjected to an alkaline solution treatment [7] before the thermo-extraction step to remove non-collagenous proteins and peptides and to break intermolecular cross-links. This consisted of combining 1 L of 1.5% (w/v) sodium hydroxide (NaOH) with the ossein from each experiment separately, at a temperature of 25 °C, for a period of 48 h. The solution was changed every day to keep it effective. The product was washed with distilled water several times until the pH was neutral.[1], [8]

2.1.5. *Thermal Treatment:*

Then, a chemo-thermal extraction process in an acidic medium to partially hydrolyze collagen fibers [10] was carried out. The ossein obtained from the above stages was prepared by soaking in a 20% acetic acid solution. Extraction was carried out using a 500 mL volume and a solid/liquid ratio of 1:5. The mixture was placed in a water bath at 65 °C [11] and stirred continuously at 250 rpm for six hours to allow thermal dissolution of collagen and its conversion to gelatin [8], [12], [13]. The solution after extraction was filtered by hot vacuum filtration and then through cheesecloth (gauze). Then the filtrate was cooled and chilled in glass beakers, and lyophilization was performed [8], [12]. Finally, the dried product was ground by using an electric grinder and stored for later testing.

2.2. *Bio-composite Preparation:*

The quinary bio-composite was synthesized by green sol-gel co-precipitation and thermal condensation crosslinking derived from a number of previous works in the literature [13][14][15][16]. The matrix was made of 50 (wt %) chitosan as main component, and cellulose and bentonite in 16.67 (wt %) each. The extracted gelatin was also added at 8.33 (wt %). A polyvinyl alcohol (PVA) was used as a crosslinking agent at the same percentage as gelatin. This was combined with a green thermal crosslinking technique, with citric acid as a polymer solvent and a multifunctional bridging agent to replace hazardous synthetic crosslinkers [16] in order to achieve the structural stability of the obtained matrix. The synthesis was achieved by a multi-step integration process (Summarized in **Figure III.1**), detailed as follows:

2.2.1. *Synthesis and Exfoliation of the Pillared Mineral Precursor:*

The first step was to add both bentonite and cellulose into 100 ml of deionized water in a 250 ml round bottom flask to get a total concentration of 2% (w/v) .The exact weight of the materials was determined with an analytical balance. The suspension was then dispersed at high speed (1500 rpm) for 24 hours on a magnetic stirring plate, before ultrasonication for 30 min at 25 °C and power level 9 [10,12].

2.2.2. *Preparation of the Polymer Matrix:*

Then, the chitosan was added gradually to 150 mL of previously prepared citric acid solution 2% (w/v) in a 500 mL round-bottom flask with continuous and proper stirring until complete dissolution. Gelatin and polyvinyl alcohol (PVA) were added sequentially over 30 min to a

total polymer concentration of 2.67% (w/v) [7]. After the last addition, the mixture was heated at 80°C for 24 h to allow thermal homogenization of the polymeric matrix[6].

2.2.3. *Hybrid Composite Integration:*

The mineral dispersion prepared in the previous step was gradually added to the polymeric blend prepared in the second step. This was done with continuous stirring at 500 rpm. The mixture was then stirred at a steady speed for 60 minutes at 60°C to ensure the hybrid matrix was as uniform as possible.[14], [15]

2.2.4. *Formation, Stabilization, and Rinsing of Composite Beads:*

The solvents were first mixed in a 500 mL graduated cylinder to prepare 500 mL of the coagulation bath. 350 mL of distilled water was added to 150 mL of ethanol to achieve a 70:30 v/v ratio. Next, 25 g of sodium hydroxide (NaOH) pellets, precisely weighed on a sensitive analytical balance, were added step by step to the solvent mixture in a 1000 mL beaker. Slow hand stirring was used throughout the dissolution process to ensure a homogeneous solution and to regulate the heat generated by the exothermic reaction.

After completion of the degassing stage, the slurry was poured into a 250 mL separating funnel mounted on a stand. The distance between the funnel tip and the coagulation bath (NaOH/Ethanol) surface was set to 4 cm to guarantee the consistent free-fall of the droplets[7]. To guarantee bead dispersion and stop agglomeration, the hybrid combination was added drop by drop into the pre-prepared and cooled coagulation bath while continuously stirring at 250 rpm. Once the whole amount was applied, the former beads were kept in the bath for 4 hours with proper stirring to guarantee the completion of their hardening and the stabilization of their structural integrity. They were then washed with deionized water until the effluent pH returned to neutral [16].

2.2.5. *Thermal Curing (Chemical Crosslinking):*

Upon obtaining the neutral beads, they were carefully placed in a desiccator for drying at 60°C overnight. Subsequently, the temperature was gradually increased to 120°C and maintained for exactly 120 minutes to ensure the complete condensation curing of the hybrid matrix [2]. the dried beads were pulverized using an electric grinder and then transferred to a ceramic mortar for manual grinding to produce a fine, homogeneous powder.

2.3. *Characterization of Synthesized Composite:*

After the synthesis process, the structural and morphological characteristics of the hybrid composite were analyzed. Fourier-transform infrared spectroscopy (FTIR) was used to

identify the functional groups in the adsorbent. Also, the pH_{pzc} of surface charge was investigated[17], [18], [19], and the yield of the synthesis was computed[20].

2.3.1. *Synthesis Yield:*

The yield was calculated by the following equation **(III.1)**:

$$\boldsymbol{Yield}\ (\%) = \frac{\boldsymbol{m_i}}{\boldsymbol{m_f}} \times \mathbf{100} \qquad \textbf{III.1}$$

Where:

- m_i is the initial mass of the sample
- m_f is the obtained mass.

2.3.2. *pH_{pzc} Determination:*

The synthesized composite was studied in the pH range from 2 to 12. Initially, hydrochloric acid (HCl) and sodium hydroxide (NaOH) were prepared as 0.1 M pH adjustment solutions. Then, six different initial pH values were adjusted ($pH_i = 2, 4, 6, 8, 10, 12$), and 10 mg of adsorbent was added to 25 mL beakers containing 10 mL of 0.1 M sodium chloride (NaCl) solution. The pH of the samples was initially adjusted precisely by the adjustment solutions prepared previously, and the mixtures were left for 24 h with continuous stirring by a magnetic stirrer[20].

After the specified time, the final pH (pH_f) The amount of each sample was measured, and the difference was calculated ($\Delta pH = pH_f - pH_i$). Finally, the plot of $\Delta pH = f(pH_i)$ was constructed.

2.3.3. *Fourier-Transform infrared spectroscopy (FTIR):*

In this study, The FTIR spectra were recorded on Agilent Cary 630 FTIR spectrometer (controlled by MicroLab software). The analysis was carried out in the mid-infrared region from 4000 to 400 cm-1 with a spectral resolution of 16 cm-1. For each spectrum, the background and the sample were accumulated over 16 scans to optimize the signal-to-noise ratio. Fourier transform processing was done with an apodization function of Happ-Genzel type. The analyses carried out provided insights into the nanocomposites surface structure under different treatments[21].

2.3.4. *UV-Visible Spectroscopy (UV-Vis):*

The absorbance of the laboratory samples was precisely measured using a Shimadzu UV-1900i UV-Vis spectrophotometer, with the spectral scanning performed over a comprehensive range of 190–1100 nm. The maximum absorption wavelength (λ_{max}). for

both dyes was experimentally determined and set at 590 nm for Crystal Violet (CV) and 464 nm for Methyl Orange (MO). To ensure the accuracy of the measurements, quartz cuvettes were utilized, and the instrument was calibrated (baselined) beforehand using the pure solvent as a blank reference. Thereafter, the other concentrations were calculated using the Beer–Lambert law (See **Eq 1.1**), which states that the absorbance of a solution is directly proportional to the concentration of the dissolved substance.

2.3.5. *X-Ray Diffraction:*

To investigate the crystalline structure and phase composition of the prepared nanocomposites, a Bruker D8 Advance X-ray diffractometer equipped with Cu Kα radiation (λ = 1.5406 Å) was used. The scan speed was an angle of 2°/min, with a step size of 0.02° over the 5° to 80° (2θ) range. The accelerating voltage and current were both kept constant at a level of 40 kV and 40 mA respectively. Diffraction pattern for crystalline phase identification, calculation of particles sizes with the Scherrer equation and assessment of crystallinity degree involved in chitosan-gelatin complex matrix due to bentonite/PVA addition was also recorded. The structural insights obtained were critical for both validating the successful preparation of the quaternary hybrid nanocomposite and evaluating structural changes that accompany alterations to treatment parameters[22], [23], [24].

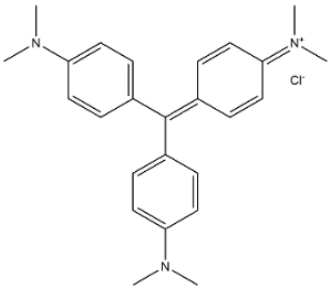
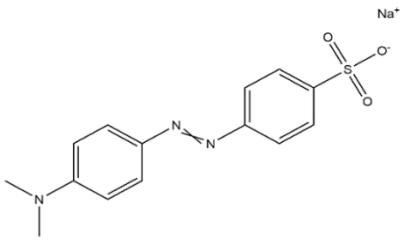
3. Adsorption Applications in Dye Removal:

3.1. *Model dyes options:*

Two model organic dyes with distinct surface charges and ionic characteristics in aqueous solution were selected to evaluate the adsorption performance of the synthesized quinary bio-composite (BCCG/PVA). The applicability of the adsorbent was investigated using Crystal Violet[25], [26] (a cationic dye) and Methyl Orange[26], [27] (an anionic dye) as model pollutants. The physicochemical properties of these two dyes are presented in the table **Table III.4.**

Table III.4. Physicochemical properties of Crystal Violet & Methyl Orange dyes [26], [27]

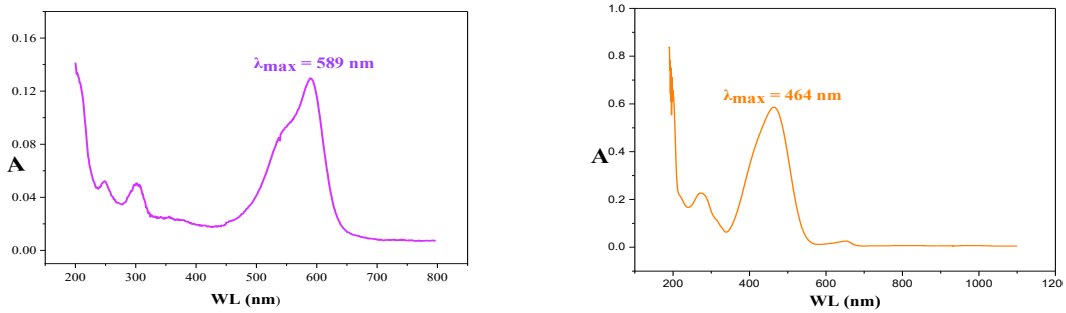
Common Name	Crystal Violet	Methyl Orange
Nomenclature (IUPAC)	[4[bis[4(dimethylamino)phenyl] methylidene] cyclohexa-2,5-dien-1-ylidene]-dimethylazanium chloride.	Sodium 4-{2-[4-(dimethylamino) phenyl] diazen-1-yl} benzene-1-sulfonate.
Type	Cationic dye	Anionic dye
Molecular Structure	$C_{25}H_{30}ClN_3$	$C_{14}H_{14}N_3NaO_3S$

Molar Mass	407.97g/mol	327.33 g/mol
Molecular Formula		

3.2. *Crystal Violet and Methyl Orange UV-Vis Spectrums:*

The maximum wavelength (λ_{max}) for the crystal violet and methyl orange dyes was determined. The stock solution of crystal violet dye was prepared at a concentration of 1000 mg/L. 1000 mg of the dye was weighed and dissolved in a 1 L volumetric flask, then shaken well to ensure complete dissolution.

The maximum wavelength of crystal violet dye was determined by measuring the absorbance between 190 and 1100 nm with a UV-Vis spectrophotometer. The peak was noted at 589 nm, which is the maximum wavelength for the studied dye (**Figure III. 2a**). Likewise, the solution of methyl orange dye was prepared and analyzed. A peak was observed at 464 nm (**Figure III. 2b**).



(a) **(b)**

Figure III.2. *Crystal Violet* ***(a)*** *& Methyl Orange* ***(b)*** *dyes UV-Vis spectrums.*

3.1. *Crystal Violet and Methyl Orange Calibration Curves:*

To plot the calibration curve for both dyes, serial dilutions of the stock solution (1000 mg/L) were performed to obtain a set of standard solutions. Subsequently, the absorbance of each standard solution was measured using a UV-Vis spectrophotometer, with the maximum wavelength (λ_{max}) fixed at 589 nm for the crystal violet dye. The calibration curve is obtained by plotting absorbance against concentration, and the equation of the straight line is found. This takes the form of **(EqIII.2)**:

$$A = a.C + b \quad \text{III.2}$$

Where:

- $\boldsymbol{A}$ represents the absorbance (dimensionless).
- $\boldsymbol{C}$ represents the dye concentration, measured in mg/L.
- $\boldsymbol{a}$ and $\boldsymbol{b}$ are the coefficients of the linear regression line (curve constants).

Following the same experimental procedure, the calibration curve for methyl orange was plotted after fixing its maximum wavelength at 464 nm[30].

4. Batch adsorption studies:

Batch adsorption experiments [15] were conducted to evaluate the impact of different parameters on the performance of the synthesized BCCG/PVA composite. In each experiment, 25 mL of crystal violet dye solution was placed in a 250 mL Erlenmeyer flask. The experimental factors applied in this study included adsorbent dosage, contact time and pH. All experiments were carried out in a shaking water bath at a constant temperature of 30°C. To estimate the residual dye concentration in the solution, samples were collected at pre-determined time intervals. The adsorbent was then separated from the supernatant via centrifugation, and the samples were analysed using UV-Vis spectrophotometry[31].

Adsorption conditions for the quinary bio-composite (BCCG/PVA) were optimized using Response Surface Methodology (RSM) in conjunction with the Box-Behnken Design (BBD) for experimental planning[32]. This methodology evaluated the independent and interactive effects of adsorbent dosage, contact time, and pH.

Second-order polynomial regression analysis and ANOVA were used to assess the significance of the variables and their interactions. This method helped develop a predictive model to estimate adsorption capacity and removal efficiency across different conditions.

5. Adsorption Efficiency Optimization Conditions via Response Surface Methodology (RSM):

5.1. *Dye Removal Efficiency Evaluation:*

Studying adsorption kinetics and equilibrium enables the evaluation of the synthesized bio-composite's performance. Process efficiency and adsorption capacity or removal efficiency are expressed based on the following two equations:

$$R(\%) = \frac{(C_0 - C_e)}{C_0} \times 100 \qquad \text{III.3}$$

$$q_e\ (mg/g) = \frac{(C_o - C_e)V}{m} \qquad \text{III.4}$$

Where:

- $R\%$: Dye removal efficiency (%).
- q_e: Adsorption capacity at equilibrium (mg/g)
- C_0: Initial dye concentration in the solution before adsorption (mg/L).
- C_e: Residual concentration of the dye in the solution upon reaching equilibrium (ppm)
- V: Total volume of the dye solution, measured in (mL)
- m: Dry mass of the adsorbent (composite) used for water treatment (mg).

5.2. *Defining the utilized box-Behnken design:*

Adsorption experiments were designed using a statistical analysis model to investigate the effects of three independent variables[33]: composite dosage, contact time, and pH. These variables are shown in **Table III.5.** These designs yielded 17 experimental runs, including five central points. Each run used 25 mL of the adsorbate solution (crystal violet dye) at a concentration of 25 ppm, with continuous shaking.

Table III.5. *Coded and actual variables and their levels in Box-Behnken Design.*

Codes	Variables	- 1	0	+1
A	Adsorbent Dose m (mg)	20	40	60
B	Contact Time t (min)	5	12.5	20
C	pH Value	4	7	10

6. Influence of Contact Time and Adsorption Kinetics:

A set of laboratory tests was undertaken to assess the influence of contact time and to establish the adsorption kinetics[34], [35] between the synthesized BCCG/PVA composite and the targeted crystal violet dye[26], [36]. The studies were carried out at varying beginning doses of crystal violet dye from 25 to 300 mg/L. In all experiments, previously calculated ideal operational conditions were applied to a constant volume of 25 mL. The procedure was carried out in a shaking water bath at sequentially well-studied time points ranging from 15 to 90 min. After the prescribed time, the adsorbent was removed from the

dye solution by centrifugation. Then the absorbance of the remaining samples was measured, and time-dependent adsorption capacity (q_t) was estimated.

7. Impact of Thermodynamic Parameters and Temperature:

This section assessed how temperature affected the efficiency of the adsorption process throughout a temperature range of 203.15 to 318.15 K. Under ideal operating circumstances established in earlier phases, laboratory experiments were carried out in a shaking water bath. Basic thermodynamic characteristics were computed in order to comprehend the nature and mechanisms of the adsorption process (e.g., whether it is physical or chemical, spontaneous or non-spontaneous, and exothermic or endothermic). These consist of the entropy change (ΔS), the enthalpy change (ΔH), and the Gibbs free energy change (ΔG)[37], [38].

8. Seed Germination Bioassay & impacts on water phytotoxicity:

The germination bioassay was conducted to evaluate the potential phytotoxicity of treated wastewater by monitoring the initial growth response of *Triticum durum* seeds. This principle relies on the sensitivity of enzymatic activation and starch mobilization during early development to residual contaminants. Seeds were surface-sterilized and incubated under controlled environmental conditions, with groups irrigated using either distilled water (control) or varying concentrations of nanocomposite-treated effluent. The germination percentage was recorded over a 7-day period to assess the biological safety of the treated water for agricultural irrigation purposes.

9. Environmental Sensing and Photosensitivity Experiments:

Once the optimal conditions for the adsorption process have been determined, further experiments are conducted under different light conditions UV light. After each experiment, the absorbance of the samples is measured and the experiment's yield is calculated using the following formula:

$$R(\%) = \frac{A_0 - A_{eq}}{A_0} \times 100 \qquad \textbf{III.5}$$

Where:

- A_0: initial absorbance
- A_{eq}: absorbance after adsorption.

A yield curve is plotted against time for each experiment to track the yield and interpret the differences observed in each experiment. The purpose of the photolysis experiments is to identify other factors influencing the adsorption process, in addition to those mentioned previously.

10. Biological Activity Assessment:

The study of the biological activity of BCCG/PVA comprises three parts: the antibacterial activity; antifungal activity and hemolytic activity. The antimicrobial and the antifungal activities of a sample of BCCG/PVA was evaluated using the disk diffusion method in agar medium; the test included a number of standard reference strains representing known bacterial (*Candida albicans and Aspergillus niger*) and fungal species (*Escherichia coli and Staphylococcus aureus*). While its hemolytic activity was evaluated using a 96-well microplate hemolysis assay using fresh human erythrocytes.

Chapter Three References

[1] A. A. Al-Hassan, "Gelatin from camel skins: Extraction and characterizations," *Food Hydrocoll.*, vol. 101, p. 105457, Apr. 2020, doi: 10.1016/j.foodhyd.2019.105457.

[2] J. Perez-Calderon, D. A. Marin-Silva, N. Zaritzky, and A. Pinotti, "Eco-friendly PVA-chitosan adsorbent films for the removal of azo dye Acid Orange 7: Physical cross-linking, adsorption process, and reuse of the material," *Advanced Industrial and Engineering Polymer Research*, vol. 6, no. 3, pp. 239–254, Jul. 2023, doi: 10.1016/j.aiepr.2022.12.001.

[3] J. Jia, Y. Liu, and S. Sun, "Preparation and Characterization of Chitosan/Bentonite Composites for Cr (VI) Removal from Aqueous Solutions," *Adsorption Science & Technology*, vol. 2021, Jan. 2021, doi: 10.1155/2021/6681486.

[4] M. T. ALSamman and J. Sánchez, "Recent advances on hydrogels based on chitosan and alginate for the adsorption of dyes and metal ions from water," *Arabian Journal of Chemistry*, vol. 14, no. 12, p. 103455, Dec. 2021, doi: 10.1016/j.arabjc.2021.103455.

[5] T. G. Ambaye, M. Vaccari, S. Prasad, E. D. van Hullebusch, and S. Rtimi, "Preparation and applications of chitosan and cellulose composite materials," *J. Environ. Manage.*, vol. 301, p. 113850, Jan. 2022, doi: 10.1016/j.jenvman.2021.113850.

[6] Y. Sánchez-Cardona, C. E. Echeverri-Cuartas, M. E. L. López, and N. Moreno-Castellanos, "Chitosan/Gelatin/PVA Scaffolds for Beta Pancreatic Cell Culture," *Polymers (Basel).*, vol. 13, no. 14, p. 2372, Jul. 2021, doi: 10.3390/polym13142372.

[7] V. Teofilovic *et al.*, "Preparation and thermal properties of chitosan/bentonite composite beads," *Hem. Ind.*, vol. 68, no. 6, pp. 653–659, 2014, doi: 10.2298/HEMIND130905088T.

[8] M. Imelhayene *et al.*, "Comprehensive evaluation of the properties of camel bone gelatin: impact of the duration of pre-treatment and extraction," *Rev. Elev. Med. Vet. Pays Trop.*, vol. 77, pp. 1–12, Dec. 2024, doi: 10.19182/remvt.37442.

[9] H. Bougherara *et al.*, "Valorization of Camel Meat and Meat Products in the World and in Algeria," in *The 10th International Seminar of Veterinary Medicine: Camelids in Algeria & Maghreb*, Basel Switzerland: MDPI, Apr. 2023, p. 11. doi: 10.3390/blsf2023022011.

[10] A. Naeimi and M. H. Ardakani, “The first cellulose/bentonite doped vanadium from natural bentonite and wheat wastes for oxidation of sulfur compounds,” Jun. 2022, doi: 10.21203/rs.3.rs-1578923/v1.

[11] J. Sealy, M. Johnson, M. Richards, and O. Nehlich, “Comparison of two methods of extracting bone collagen for stable carbon and nitrogen isotope analysis: comparing whole bone demineralization with gelatinization and ultrafiltration,” *J. Archaeol. Sci.*, vol. 47, pp. 64–69, Jul. 2014, doi: 10.1016/j.jas.2014.04.011.

[12] D. E. Ochoa-Florez and M. Z. Solano-Silva, “Physicochemical, rheological, and functional evaluation of gelatins obtained from animal bones through acid-thermal hydrolysis for applications in biomaterials engineering,” *Results in Engineering*, vol. 30, p. 110085, Jun. 2026, doi: 10.1016/j.rineng.2026.110085.

[13] M. H. Abu Elella *et al.*, “Gelatin-based adsorbents for efficient adsorptive removal of toxic pollutants in wastewater: A step towards environmental sustainability,” *Polym. Int.*, Mar. 2026, doi: 10.1002/pi.70115.

[14] I. O. Saheed, W. Da Oh, and F. B. M. Suah, “Chitosan modifications for adsorption of pollutants – A review,” *J. Hazard. Mater.*, vol. 408, p. 124889, Apr. 2021, doi: 10.1016/j.jhazmat.2020.124889.

[15] A. H. Anwer *et al.*, “State-of-the-art advances in nanocomposite and bio-nanocomposite polymeric materials: A comprehensive review,” *Adv. Colloid Interface Sci.*, vol. 318, p. 102955, Aug. 2023, doi: 10.1016/j.cis.2023.102955.

[16] Z. U. Abdeen Chaudhry, N. Arshad, and M. A. Ur Rehman Qureshi, “Chitosan-based hydrogels: bentonite supported architectures explored for removal of cadmium(<scp>ii</scp>) from aqueous solution,” *RSC Adv.*, vol. 16, no. 16, pp. 14216–14232, 2026, doi: 10.1039/D6RA00503A.

[17] M. Kosmulski, “The pH dependent surface charging and points of zero charge. IX. Update,” *Adv. Colloid Interface Sci.*, vol. 296, p. 102519, Oct. 2021, doi: 10.1016/j.cis.2021.102519.

[18] M. NASIRUDDIN KHAN and A. SARWAR, “DETERMINATION OF POINTS OF ZERO CHARGE OF NATURAL AND TREATED ADSORBENTS,” *Surface Review and Letters*, vol. 14, no. 03, pp. 461–469, Jun. 2007, doi: 10.1142/S0218625X07009517.

[19] E. N. Bakatula, D. Richard, C. M. Neculita, and G. J. Zagury, "Determination of point of zero charge of natural organic materials," *Environmental Science and Pollution Research*, vol. 25, no. 8, pp. 7823–7833, Mar. 2018, doi: 10.1007/s11356-017-1115-7.

[20] M. Kosmulski, "The pH-Dependent Surface Charging and the Points of Zero Charge," *J. Colloid Interface Sci.*, vol. 253, no. 1, pp. 77–87, Sep. 2002, doi: 10.1006/jcis.2002.8490.

[21] A. R. Hind, S. K. Bhargava, and S. C. Grocott, "Attenuated Total Reflection Fourier Transform Infrared Spectroscopic Investigation of the Solid/Aqueous Interface of Low Surface Area, Water-Soluble Solids in High Ionic Strength, Highly Alkaline, Aqueous Media," *Langmuir*, vol. 13, no. 13, pp. 3483–3487, Jun. 1997, doi: 10.1021/la970141n.

[22] S. Hajji *et al.*, "Structural analysis, and antioxidant and antibacterial properties of chitosan-poly (vinyl alcohol) biodegradable films," *Environmental Science and Pollution Research*, vol. 23, no. 15, pp. 15310–15320, Aug. 2016, doi: 10.1007/s11356-016-6699-9.

[23] P. Ahvenainen, I. Kontro, and K. Svedström, "Comparison of sample crystallinity determination methods by X-ray diffraction for challenging cellulose I materials," *Cellulose*, vol. 23, no. 2, pp. 1073–1086, Apr. 2016, doi: 10.1007/s10570-016-0881-6.

[24] S. Verma, G. D. Verros, and R. K. Arya, "PVA- Bentonite-Water Coatings: Experimental and Simulation Studies," *Polymers (Basel).*, vol. 17, no. 19, p. 2689, Oct. 2025, doi: 10.3390/polym17192689.

[25] S. Mani and R. N. Bharagava, "Exposure to crystal violet, its toxic, genotoxic and carcinogenic effects on environment and its degradation and detoxification for environmental safety," *Rev. Environ. Contam. Toxicol.*, vol. 237, pp. 71–104, 2016, doi: 10.1007/978-3-319-23573-8_4/SAVE-RESEARCH.

[26] A. Mittal, J. Mittal, A. Malviya, D. Kaur, and V. K. Gupta, "Adsorption of hazardous dye crystal violet from wastewater by waste materials," *J. Colloid Interface Sci.*, vol. 343, no. 2, pp. 463–473, Mar. 2010, doi: 10.1016/j.jcis.2009.11.060.

[27] B. Lellis, C. Z. Fávaro-Polonio, J. A. Pamphile, and J. C. Polonio, "Effects of textile dyes on health and the environment and bioremediation potential of living organisms," *Biotechnology Research and Innovation*, vol. 3, no. 2, pp. 275–290, Jul. 2019, doi: 10.1016/j.biori.2019.09.001.

[28] M. J. . O'Neil, *The Merck index : an encyclopedia of chemicals, drugs, and biologicals*. Royal Society of Chemistry, 2013.

[29] W. M. . Haynes, D. R. . Lide, and T. J. . Bruno, *CRC handbook of chemistry and physics : a ready-reference book of chemical and physical data*. CRC Press, 2017.

[30] H. N. Tran, S.-J. You, A. Hosseini-Bandegharaei, and H.-P. Chao, "Mistakes and inconsistencies regarding adsorption of contaminants from aqueous solutions: A critical review," *Water Res.*, vol. 120, pp. 88–116, Sep. 2017, doi: 10.1016/j.watres.2017.04.014.

[31] Rodger. Baird, A. D. . Eaton, E. W. . Rice, and Laura. Bridgewater, *Standard Methods for the Examination of Water and Wastewater*. American Public Health Association, 2017.

[32] M. Shaban, M. R. Abukhadra, A. S. Mohamed, M. G. Shahien, and S. S. Ibrahim, "Synthesis of Mesoporous Graphite Functionalized by Nitrogen for Efficient Removal of Safranin Dye Utilizing Rice Husk Ash; Equilibrium Studies and Response Surface Optimization," *J. Inorg. Organomet. Polym. Mater.*, vol. 28, no. 1, pp. 279–294, Jan. 2018, doi: 10.1007/s10904-017-0726-2.

[33] A. S. Abdulhameed, R. H. Al Omari, S. Abdullah, A. A. Al-Masud, M. Abualhaija, and S. Algburi, "Modified plant leaves/chitosan composite: adsorption modeling of crystal violet dye using Box–Behnken design," *Int. J. Phytoremediation*, vol. 27, no. 12, pp. 1707–1723, Oct. 2025, doi: 10.1080/15226514.2025.2516251.

[34] W. Plazinski, W. Rudzinski, and A. Plazinska, "Theoretical models of sorption kinetics including a surface reaction mechanism: A review," *Adv. Colloid Interface Sci.*, vol. 152, no. 1–2, pp. 2–13, Nov. 2009, doi: 10.1016/j.cis.2009.07.009.

[35] A. Mittal, A. Malviya, D. Kaur, J. Mittal, and L. Kurup, "Studies on the adsorption kinetics and isotherms for the removal and recovery of Methyl Orange from wastewaters using waste materials," *J. Hazard. Mater.*, vol. 148, no. 1–2, pp. 229–240, Sep. 2007, doi: 10.1016/j.jhazmat.2007.02.028.

[36] P. R. Souza, G. L. Dotto, and N. P. G. Salau, "Analysis of intraparticle diffusion on adsorption of crystal violet on bentonite," *Chem. Eng. Commun.*, vol. 206, no. 11, pp. 1463–1473, Nov. 2019, doi: 10.1080/00986445.2019.1570163.

[37] E. C. Lima, A. Hosseini-Bandegharaei, J. C. Moreno-Piraján, and I. Anastopoulos, "A critical review of the estimation of the thermodynamic parameters on adsorption

equilibria. Wrong use of equilibrium constant in the Van't Hoof equation for calculation of thermodynamic parameters of adsorption," *J. Mol. Liq.*, vol. 273, pp. 425–434, Jan. 2019, doi: 10.1016/j.molliq.2018.10.048.

[38] S. Milonjic, "A consideration of the correct calculation of thermodynamic parameters of adsorption," *Journal of the Serbian Chemical Society*, vol. 72, no. 12, pp. 1363–1367, 2007, doi: 10.2298/JSC0712363M.

Chapter IV

Results & Discussion

This chapter evaluates and studies the adsorption capacity of the synthesized BCCG/PVA composite as an adsorbent for treating water contaminated with organic pollutants, focusing on Crystal Violet[1] dye as a primary model. First, the physicochemical properties of the extracted gelatin and the synthesized composite were determined using characterization techniques such as Fourier-transform infrared spectroscopy[2] (FTIR) and ultraviolet-visible spectroscopy[3] (UV-Vis). Next, the experimental conditions affecting the adsorption process efficiency were analyzed to determine the optimal conditions for achieving the highest removal rate of the studied dye. Additionally, kinetic and isotherm models were studied to describe the adsorption mechanism, alongside a thermodynamic analysis of the process[4].

1. Characterization of Gelatin & BCCG/PVA:

1.1. Yield Determination:

The following equation (**4.1**) determines the yield:

$$\boldsymbol{R}(\%) = \frac{\boldsymbol{m_{experimental}}}{\boldsymbol{m_{Theoretical}}} \times \mathbf{100} \qquad \textbf{IV.1}$$

1.2. Gelatin Extraction:

The yield of gelatin, whose extraction was described in previous chapter, was calculated using the relation shown above **(IV.1).** The extraction yield was **10.23%** from **100g** of initial bone mass and **10.23g** of final extracted mass. The difference in the camel breeds and the different living environments that affect the bone content, in addition to the possibility of systematic errors during the experiment, are the reasons for this reduction in the yield percentage, which is half of the yield reported in the adopted reference[1].

1.3. Composite Synthesis Yield:

The hybrid composite was prepared as detailed in Chapter Three. The adsorbent was synthesized by a single preparation process with a total theoretical mass of 6 g and a mass of 2.4814 g. using equation **(4.1)** it was calculated to be:

$$R\% = \frac{2.4814}{6} \times 100\% = 41.356\,\%$$

In general, a yield of **41.36 %** is believed to be a suitable rate in this context, although it can be further improved by optimizing the experimental conditions.

1.2. Fourier Transform Infrared (FTIR) Spectroscopic Analysis:

1.2.1. *Gelatin FTIR spectrums:*

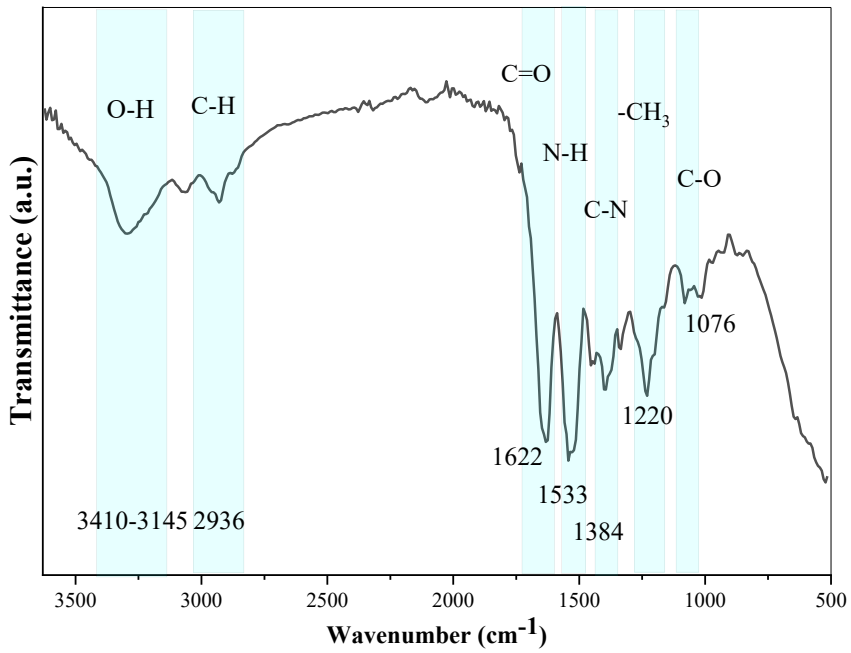


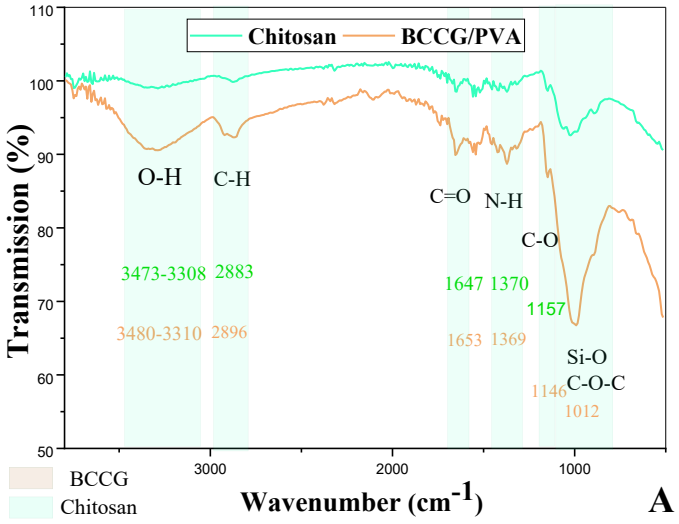
Figure IV.1. *Extracted Gelatin FTIR spectrum*

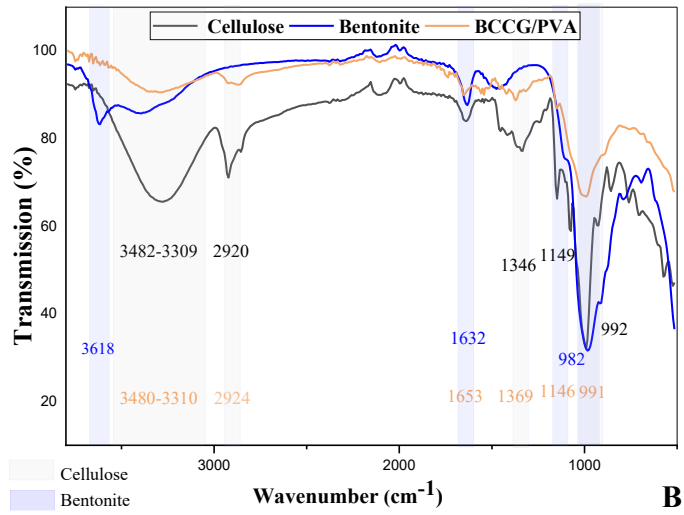
The FTIR spectrum of the extracted gelatin exhibits the sharp, characteristic vibrational bands typical of protein structures and primary peptide bonds. The main peaks are chemically identified[2], [3] and discussed below:

- A broad band representing an overlap between the stretching vibrations of the N–H bond in its free state and when it is involved in hydrogen bonding within the peptide chains, and the stretching vibration of the O–H hydroxyl bond resulting from residual moisture and hydrogenated amino acids.
- A distinct peak appears at 2936 cm^{-1}, which is attributed to the symmetric and asymmetric stretching vibrations of the aliphatic C–H bond.
- A sharp and very strong peak appears at 1622 cm^{-1}, which is due to the stretching vibration of the carbonyl C=O bond.
- The appearance of a sharp and distinct peak at 1533 cm^{-1} results from physical coupling between the in-plane bending vibration of the N–H bond and the stretching vibration of the C–N bond.
- A medium-intensity peak at 1384 cm^{-1} is attributed to the symmetric bending of CH_3 bonds.

- A distinct band appears at 1220 cm^{-1} due to mixed vibrations involving stretching C–N bonds and bending N–H bonds.
- A distinct peak at 1076 cm^{-1} is assigned to the stretching vibration of the single C–O bond

1.2.2. *FTIR spectrum analysis for the synthesized composite & its components:*





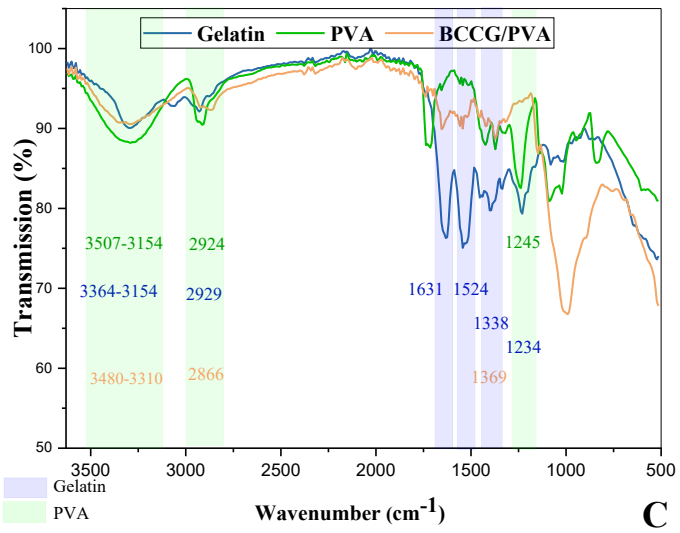


Figure IV.2. *FTIR spectrums of the synthesized composite and its components:* ***(A)*** *BCCG/PVA Vs Chitosan;* ***(B)*** *BCCG/PVA Vs Cellulose &Bentonite;* ***(C)*** *BCCG/PVA Vs PVA & Gelatin*

The appearance of an intense and broad absorption band at 3480-3310 cm^{-1} is attributed to overlapping stretching vibrations of the -OH and -NH groups. This band originates from the interaction between the hydroxyl groups in the cellulose, chitosan and PVA[4] and the amino ($-NH_2$) and amide (-NH) groups in the chitosan and gelatin. This interaction establishes an extensive network of intermolecular hydrogen bonds.

The peak at 2866 cm^{-1} corresponds to the symmetric and asymmetric stretching vibrations of aliphatic C-H bonds belonging to the primary carbon backbone of the polymer matrix constituents [5].

The sharp peak observed at 1653 cm^{-1} is assigned to the stretching vibration of the carbonyl group (C=O), which is highly characteristic of gelatin's peptide structure (amide I) and the residual acetyl groups in chitosan.The peak at 1146 cm^{-1} is associated with the stretching vibration of C-O bonds and represents a characteristic band for the crystalline region of PVA, as well as the stretching of skeletal C-O bonds within the biopolymers[4].

The sharp, intense peak at 991 cm^{-1} is assigned to the stretching vibrations of Si-O and

C-O-C bonds. This intense band is characteristic of the tetrahedral silicate sheets within the bentonite clay framework and overlaps with the glycosidic linkages of the polysaccharide rings.

1.2.3. *FTIR Analysis of the effect of gelation and bead formation:*

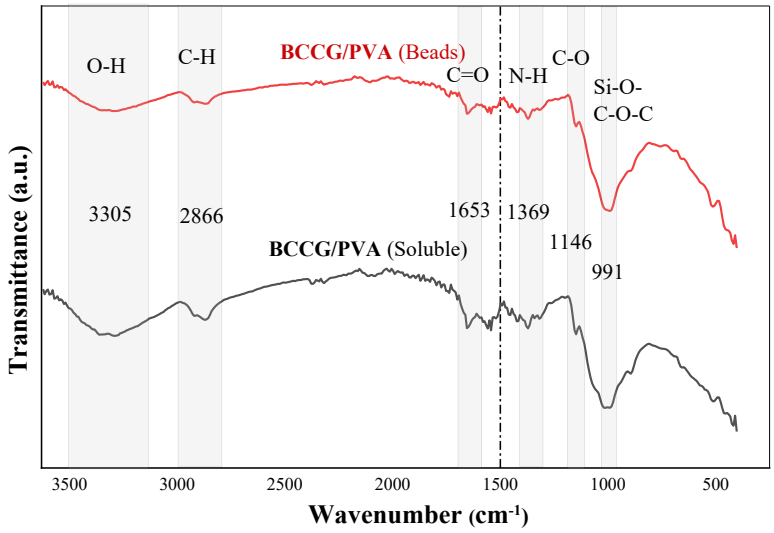


Figure IV.3. *FTIR spectral comparison between the soluble and granulated (bead) forms of the BCCG/PVA compound.*

Figure IV.3. shows the strong similarity between the FTIR spectra of both the bead form and the dissolved form of the hybrid compound (BCCG/PVA), meaning that the granulation process did not cause any chemical changes or structural modifications to the basic structure of the compound which is not always the case[6]. However, from a practical laboratory perspective, handling the bead form was much easier than handling the mass obtained from aggregating the entire dissolved compound, as the washing and grinding processes for the bead form were more straightforward[7].

1.2.4. *FTIR analysis of composite stability at different pH levels:*

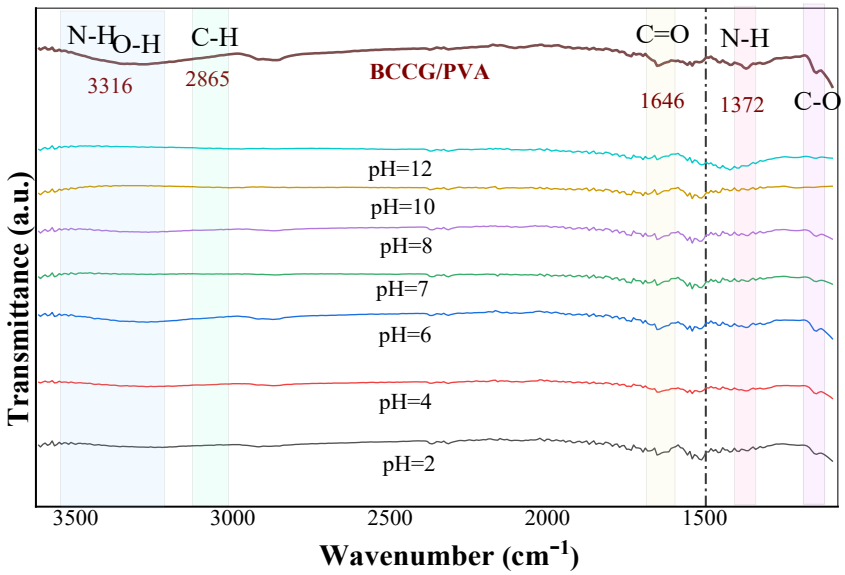


Figure IV.4. *Effect of solution pH on the FT-IR spectra of the synthesized composite.*

This study aimed to determine the composite's overall net charge in acidic and basic media and evaluate its structural and chemical stability in these environments.

In an acidic medium, protonation of the amino groups present in the chitosan and gelatin occurs, resulting in an overall positive charge on the composite surface. Consequently, **Figure IV.4** shows that the intensity and frequency of the broad peak corresponding to the O-H and N-H groups remain unchanged because the bonds have become charged and saturated with hydrogen.

In basic conditions, deprotonation takes place, whereby functional groups lose hydrogen, e.g. O-H, C=O and N-H. This behaviour is responsible for the composite surface's overall net negative charge. Consequently, the peaks for the O-H group at 3316 cm^{-1}, the carbonyl group (C=O) at 1646 cm^{-1}, and the amine group at 1372 cm^{-1} flatten in the FTIR spectra due to the loss of hydrogen and the change in their charge.

In general, the composite is chemically stable and durable, making it suitable for repeated use in water treatment across the specified pH range without undergoing degradation or dissolution[8].

1.2.5. *FTIR analysis of the composite before and after adsorption:*

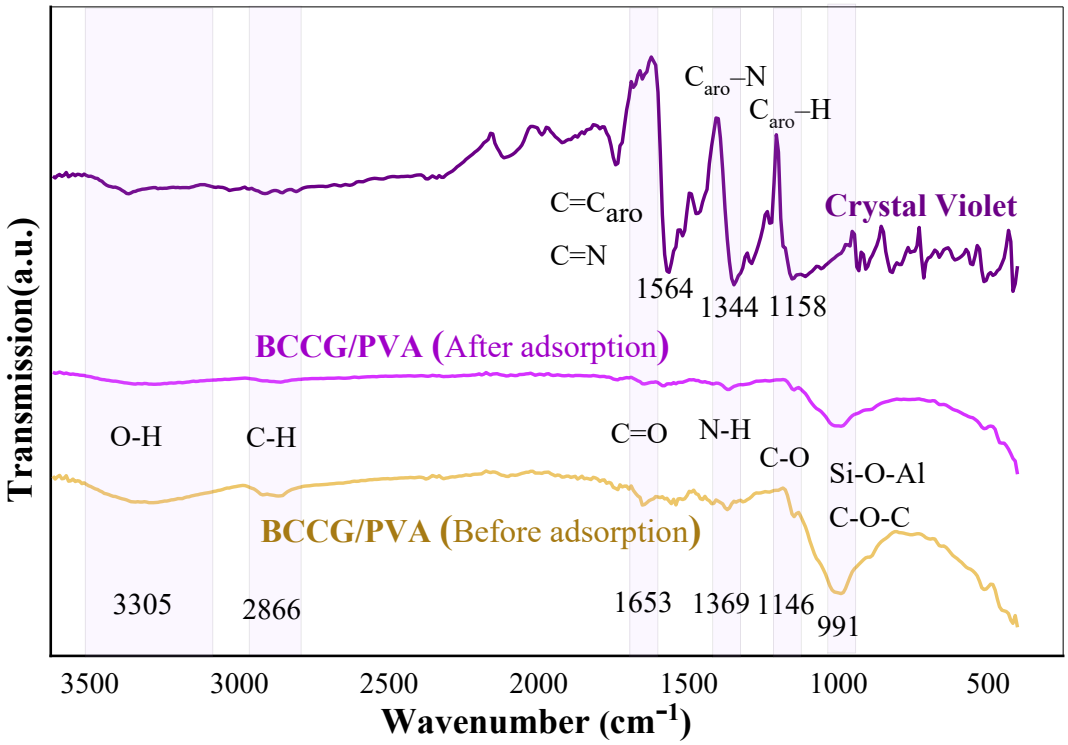


Figure IV.5. *FTIR spectra of Crtstal Violet as well as the hybrid composite before and after adsorption.*

Comparative analysis of the FTIR spectra shown in **Figure IV.5** for pure CV dye and the BCCG/PVA composite before and after adsorption with the dye reveals clear changes in the functional groups. This elucidates the mechanism by which adsorption occurred.[9], [10]

A noticeable decrease in the intensity of the broad band at 3305 cm^{-1} is observed after adsorption. This is attributed to the participation of hydroxyl groups (-OH), amine groups (-NH) and amide groups ($-NH_2$) in attracting the dye molecules and forming intermolecular hydrogen bonds and electrostatic attraction forces with the aromatic rings and amino groups of the dye.

A decrease in the intensity of the peak at 991 cm^{-1}, corresponding to the bentonite bonds and glycosidic linkages and the peak at 1146 cm^{-1} for the C–O bonds decrease after adsorption. This change is due to bentonite's strong contribution to the dye entrapment process through ion exchange and electrostatic interactions between the negatively charged silicate sheets and cationic dye molecules. It is also due to overlapping matrix polymeric chains stabilising the dye molecules within the network.

When comparing the FTIR spectrum of the pristine dye with the post-adsorption spectrum, a sharp decrease in intensity and overlap are clearly observed at 1564 cm^{-1}, 1344 cm^{-1}, and 1158 cm^{-1}. This proves that the dye molecules have been entirely entrapped and stabilised within the porous network and silicate layers.

1.3. *XRD Analysis:*

1.3.1. *XRD patterns analysis before and after CV adsorption:*

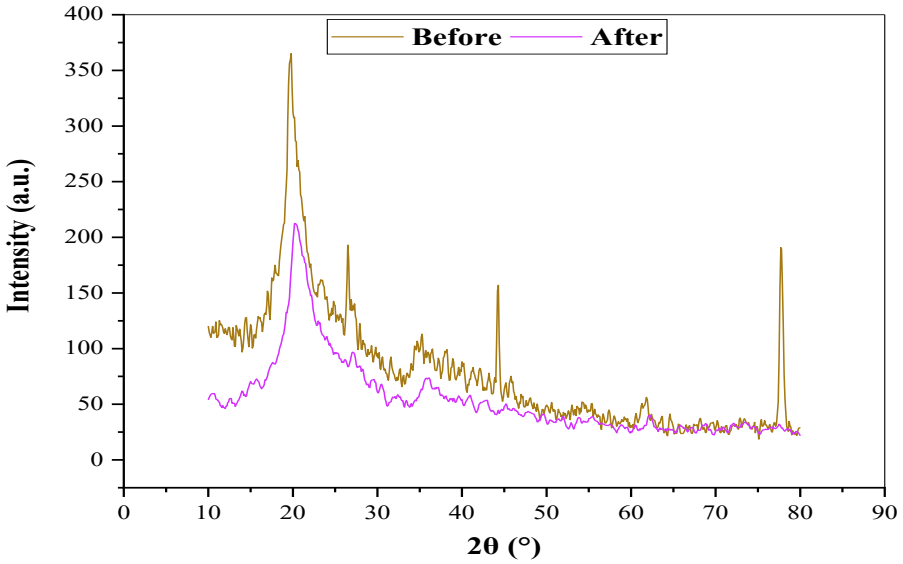


Figure IV.6. *XRD diffractogram of BCCG/PVA before & After CV adsorption.*

The XRD pattern of the BCCG/PVA (shown in **Figure IV.6)** is characterized by a series of distinct reflections that confirm the successful integration of both organic and inorganic phases. A prominent, broad diffraction envelope is observed in the 2θ range of 18° to 23°, which is attributed to the overlapping of the crystalline peaks of Polyvinyl Alcohol (PVA) at 19.8° and the semi-crystalline reflections of Chitosan and Gelatin. This broadening is indicative of strong intermolecular hydrogen bonding between the polymer chains, which facilitates the formation of a unified semi-crystalline matrix.

Furthermore, the presence of sharp, high-intensity reflections at 26.5° and 44.2° confirms the incorporation of mineral reinforcements, specifically α-Quartz and Bentonite, within the polymer network. These peaks suggest that the mineral fillers maintain their crystalline integrity while acting as nucleating agents for the surrounding biopolymer blend. The baseline of the diffractogram displays an amorphous halo, which is characteristic of the disordered regions of Chitosan and Gelatin, effectively representing the complex, multi-phase nature of the hybrid composite.

The XRD pattern recorded after the adsorption of Crystal Violet demonstrates that the composite retains its fundamental structural framework despite the integration of the dye molecules. While a noticeable reduction in peak intensities and an increase in the amorphous background are observed, indicating a decrease in long-range periodicity, the characteristic diffraction positions for the primary crystalline phases remain virtually unchanged. Specifically, the persistence of the dominant reflections for the PVA/biopolymer matrix (19.8°) and the mineral reinforcements (26.5° and 44.2°) confirms that the host matrix does not undergo phase transformation or structural collapse during the process. This “retention of form” signifies that the adsorption occurs primarily through interstitial filling and surface complexation within the existing pores and functional sites of the composite. The total disappearance of the high-angle peak at 77.7° further supports this, suggesting that the dye layer effectively masks the most sensitive surface-level reflections while the robust, larger crystalline domains (D_{Avg4}) continue to provide the necessary mechanical scaffolding to maintain the adsorbent’s integrity[11], [12].

1.3.2. *Structural Evolution and Crystallite Distribution of the Multi-Phase Composite:*

The structural parameters derived from the XRD pattern are summarized in the table below. Each peak has been assigned to its corresponding phase based on standard crystallographic reference data.

Table IV.1. Major Characteristic peaks and properties of BCCG/PVA components.

Component	Peak 2θ (deg)	Miller Indices (hkl)	Nature
PVA	19.4° - 19.8°, 40.5°	(101), (110)	Semi-crystalline
Chitosan	10.5°, 20.1°	(020), (110)	Semi-crystalline
Cellulose (I)	14.7°, 16.5°, 22.6°	(110), $(1\bar{1}0)$, (200)	Crystalline
Gelatin	7° - 9° (triple helix), 20° (halo)	Amorphous halo	Amorphous
Bentonite	5.8° - 7.0° (d001), 19.8°, 26.6°	(001), (hk0), (011)	Crystalline (Clay)
α-Quartz	20.8°, 26.6°, 42.4°, 50.1°	(100), (101), (200)	Crystalline (Impurity)

The quantitative data presented in the table validates the semi-crystalline nature of the composite. The maximum intensity observed at 19.80° (Peak 4) is identified as the primary crystalline reflection of the PVA (101) plane, which serves as the structural backbone of the material. The d-spacing values, particularly for the mineral phases at 26.50° and 44.20°, align closely with standard JCPDS cards for α-Quartz and Bentonite, confirming their role as reinforcing fillers. The distribution of intensities across the pattern reflects a balanced ratio between the high-order crystalline fillers and the flexible, semi-crystalline polymer matrix, resulting in a composite designed for enhanced mechanical and adsorption performance[13], [14].

1.3.3. *Average crystallite size:*

In traditional XRD analysis, a single average crystallite size is often reported for a sample. However, the multi-phase nature of this Chitosan/PVA/Bentonite/Quartz composite necessitates a more sophisticated approach. The calculation of four distinct averages (D_{Avg1} through D_{Avg4}) is interpreted as a method to differentiate between the various structural scales within the material.

The hierarchical structure of the Chitosan/PVA/Bentonite/Quartz composite is elucidated through a multi-tiered averaging of crystallite sizes, ranging from a matrix-dominant 9.15 nm (D_{Avg1}) to a filler-stabilized 23.56 nm (D_{Avg4}). This analytical approach directly correlates with the previously discussed XRD pattern, where the broad envelope at 19°–23° corresponds to the smaller, nanometric crystallites of the polymer blend, while the sharp reflections at 26.5° and 44.2° represent the larger, more robust mineral domains. The

significant disparity between individual crystallite sizes—varying from 0.15 nm in disordered regions to over 30 nm in the α-Quartz phase—confirms that the composite is a heterogenous hybrid where the mineral skeleton provides mechanical reinforcement to the finer biopolymer network. Furthermore, the loss of high-angle reflections (77.7°) post-adsorption, coupled with these size distributions, suggests that the Crystal Violet molecules preferentially interact with and distort the smaller, high-surface-area crystalline domains (D < 5 nm), while the larger mineral clusters (D > 20 nm) maintain the overall structural integrity of the adsorbent[11].

Table IV.2. Average crystallite size calculations using various datapoints.

Peak	2θ	FWHM	D (nm)	D_{Avg1} (nm)		D_{Avg2} (nm)		D_{Avg3} (nm)		D_{Avg4} (nm)	
1	10.636	4.252	1.877	**1**	9.1476	**1**	13.474	1	17.146	1	23.559
2	19.923	54.43	0.148	**2**		2		2		2	
3	19.923	1.899	4.248	**3**		**3**		**3**		3	
4	21.164	12.791	0.632	**4**		4		4		4	
5	26.532	0.313	26.094	**5**		**5**		**5**		**5**	
6	35.21	1.897	4.394	**6**		**6**		**6**		6	
7	39.011	9.408	0.896	**7**		7		**7**		7	
8	44.254	0.283	30.285	**8**		**8**		**8**		**8**	
9	45.836	0.512	16.831	**9**		**9**		**9**		**9**	
10	65.753	3.114	3.038	**10**		**10**		10		10	
11	77.772	33.726	0.303	**11**		11		11		11	
12	77.772	0.485	21.027	**12**		**12**		**12**		**12**	

1.3.4. *Crystallinity Index:*

The quantitative assessment of a material's crystalline content is frequently conducted using the peak deconvolution method. Unlike height-based ratios, this approach utilizes mathematical curve-fitting to separate the diffraction pattern into distinct crystalline and amorphous area contributions [13]. By calculating the ratio of the integrated area of all crystalline peaks to the total area of the diffractogram, this method provides a more comprehensive representation of the sample's supramolecular architecture compared to traditional peak-height techniques [15].

To calculate the Crystallinity Index (CI) using the peak deconvolution method, the ratio of the integrated area of the crystalline peaks to the total area of the diffraction pattern is determined. Based on the values provided:

- *Sum of Crystalline Peak Areas (A_{cryst}):* 1447.344
- *Total Pattern Area (A_{total}):* 2123.657

The Crystallinity Index is calculated using the following formula:

$$CI(\%) = (\frac{A_{cryst}}{A_{tot}}) \times 100 \qquad \textbf{IV.2}$$

Thus:

$$CI(\%) = \left(\frac{1447.344}{2123.657}\right) \times 100 = 68.15336\%$$

A crystallinity index of 68.15% is obtained, indicating the formation of a semi-crystalline material in which the ordered crystalline domains significantly outweigh the disordered amorphous phases. In the context of the previously assigned phases (Chitosan, Cellulose, and PVA), this high value is attributed to efficient molecular packing. The integration of PVA (polyvinyl alcohol) and mineral fillers, such as Bentonite or Quartz, often acts to reinforce the matrix, whereby the overall crystallinity is increased compared to pure biopolymer films[11]. A comparison between the calculated result and a similar composite system from literature is presented below:

Table IV.3. *comparison between the calculated CI and that of similar composites in the literature*

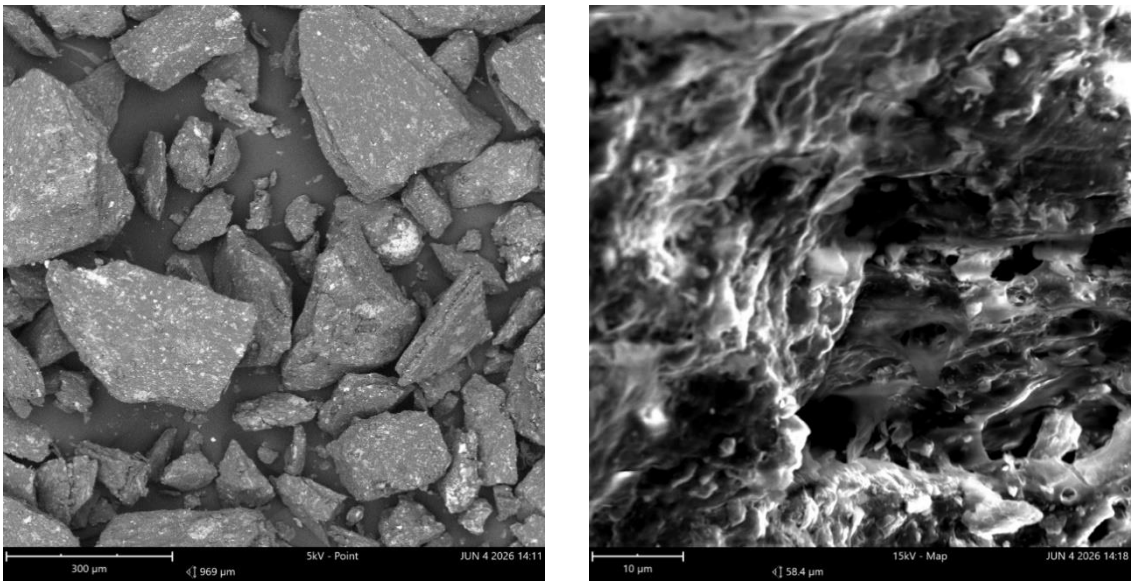
Parameter	Current Study	Hajji et al. [16]
Crystallinity Index (CI)	68.15%	66.4% – 70.2%
Material Composition	Chitosan/Cellulose/PVA/Bentonite	PVA/Chitosan/Nanocellulose Blends

The obtained value of 68.15% is found to be highly consistent with reported values for high-performance PVA-biopolymer composites. For instance, it has been demonstrated by Hajji et al. (2016) [16] that the incorporation of reinforcing fillers into a PVA/Chitosan matrix shifts the overall crystallinity into the 65–70% range. From this comparison, two main conclusions can be drawn:

- Effective Nucleation: The crystallization process is likely favored by the presence of Bentonite and Quartz particles, which act as heterogeneous nucleating agents.
- Strong Interfacial Compatibility: Robust hydrogen bonding is expected to occur between Chitosan and PVA, by which the phase separation and amorphous dilution typical of poorly compatible blends are prevented.

Typically, a lower CI (in the range of 30–50%) is exhibited by pure Chitosan or unmodified Cellulose. This increase to 68.15% is driven by the highly crystalline PVA (101) reflection and the mineral phases identified in the XRD pattern.

1.4. *Scanning Electron Microscopy Morphological Analysis:*



(a) ***(b)***

Figure IV.7. *Scanning electron microscopy (SEM) images of the extracted camel bone gelatin powder:* ***(a)*** *at 300 µm scale, and* ***(b)*** *at 10 µm scale.*

The morphological structure of the gelatin powder obtained from young camel bones was examined by using scanning electron microscopy (SEM) at two different magnifications as shown in figure (IV-7).

The extracted gelatin powder at lower magnification (scale 300 µm) showed irregular bulk-like particles of different sizes with clear interstitial voids[17]. This morphological pattern is in agreement with the findings of Fawale et al. (2021)[18] who described extracted camel gelatin as a loose protein network interspersed with multiple voids. This was attributed to the nature of the alkaline pretreatment [4] before extraction, which results in the opening of the protein network and the loosening of the peptide chains. The extracted gelatin shows a

less ordered and more porous structure under the electron microscope than the commercial gelatin which is clearly reflected in **Figure IV.7*a***.

At higher magnification (10 µm scale) the surface structure was porous and corrugated with undulating topography and irregular micro-cavities. Fawale et al. (2021)[18] related this type of microstructure in camel gelatin to the internal cross-linking density and length of alkaline pretreatment, emphasizing a more cross-linked protein network with less voids in samples treated for longer time. Conversely, the gelatin has a more pronounced porous structure and higher surface roughness compared to commercial bovine gelatin. This makes it more reactive and able to bind with other components in hybrid material formulations.

The above observation also supports the results shown in **Figure IV.7*b*** where the observed porous structure reflects the hydrophilic nature of the extracted gelatin and its high water-absorption capacity,[19] which is closely related to the expected interfacial compatibility with the components of the target bio-hybrid composite.

1.5. *Gelatin UV–Vis spectrum:*

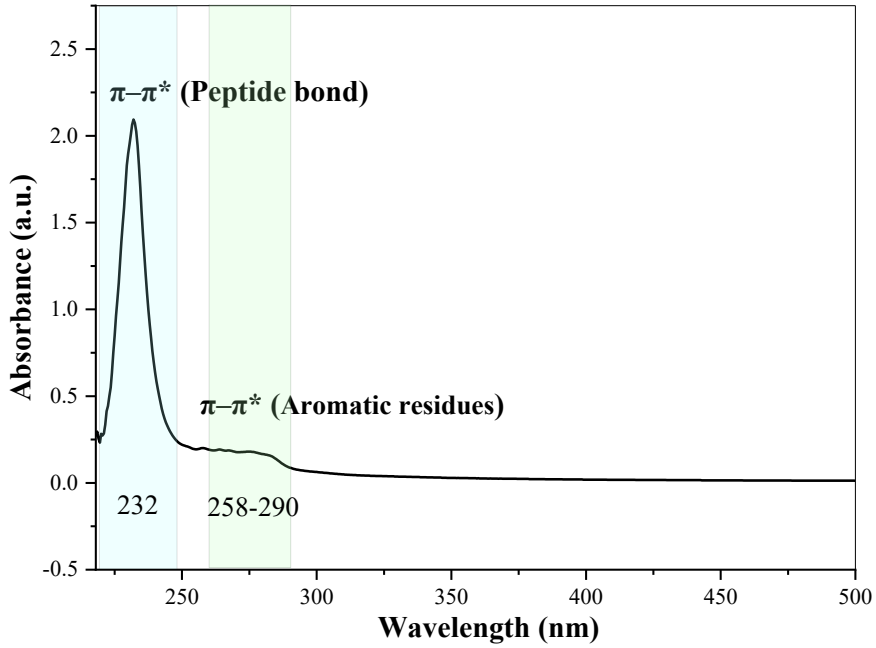


Figure IV.8. *UV-Vis absorption spectrum of the extracted Gelatin.*

The following can be observed in the UV-Vis absorption spectrum (**Figure IV.8**) of the extracted gelatin [20]:

A pronounced, strong absorption peak emerges at 210–240 nm (Blue). This behaviour is attributed to π–π* electronic transitions associated with carbonyl (-C=O) groups in the peptide bonds that constitute a primary peptide backbone of gelatin.

The clarity and sharpness of this peak indicate the material's high purity and the integrity of its essential peptide bonds. A faint shoulder appears around 258–290 nm within the spectral band (~50%) and a low-intensity, broad sub-absorption region. The weak absorption is caused by π–π* electronic transitions involving the aromatic ring, owing to the presence of aromatic amino acids[21].

As gelatin extracted from animal tissues naturally contains only trace amounts of these amino acids, the low intensity of this peak confirms the purity and identity of the camel bone gelatin, as well as its compliance with standard specifications[22]. Spectral stability above 300 nm proves that the extracted gelatin is completely free from organic impurities.

The FTIR and UV analyses show that their spectra are completely consistent and complementary. The appearance of a sharp peptide absorption peak at 230 nm in the UV spectrum confirms the integrity and stability of the peptide carbonyl groups, as evidenced by a wavenumber of 1622 cm^{-1} in the FTIR spectrum. This confirms the success of the protocol followed for gelatin extraction.

1.6. *Surface Charge Study & pH_z Determination:*

The point of zero charge pH_z of the BCCG/PVA composite was measured. The results are illustrated in **Figure IV.9.**

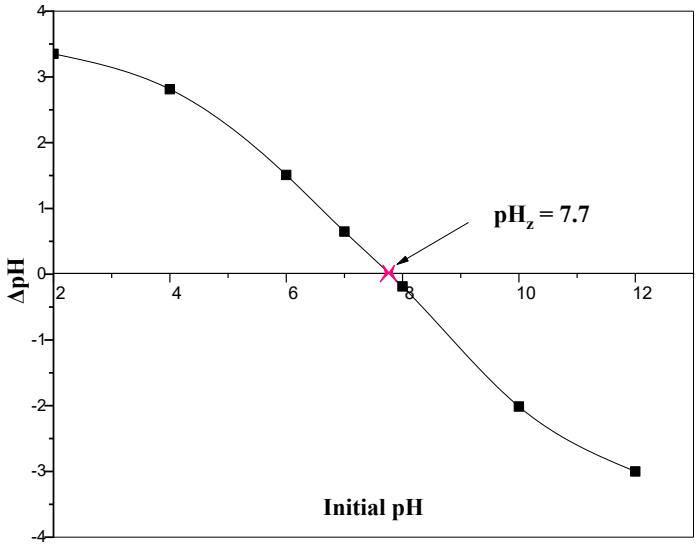


Figure IV.9. ΔpH Vs Initial pH *Graph for pH_z Determination.*

Figure IV.8. shows that the pH point zero-charge for the BCCG/PVA compound is relatively neutral, at 7.7. This reflects the precise chemical balance between the high density of basic functional groups (protons) such as free amines in chitosan's and gelatins, and acidic

groups and negatively charged silicate plates in bentonite clay. The nature of this hybrid system facilitates the display of precise electrical behaviour; at pH values below 7.7, the surface tends to protonate densely, acquiring a positive charge overall, while at higher values, deprotonation and the accumulation of hydroxyl ions generate a fully negatively charged surface through the remaining basic regions. Therefore, the suitability of the material for the selective adsorption of pollutants can be predicted based on the acidity of the medium, as the surface becomes highly negative in alkaline conditions, giving it an ideal electrical affinity for the adsorption of cationic pollutants[23], [24].

1.7. *Preliminary Evaluation of MO and CV removal efficiencies:*

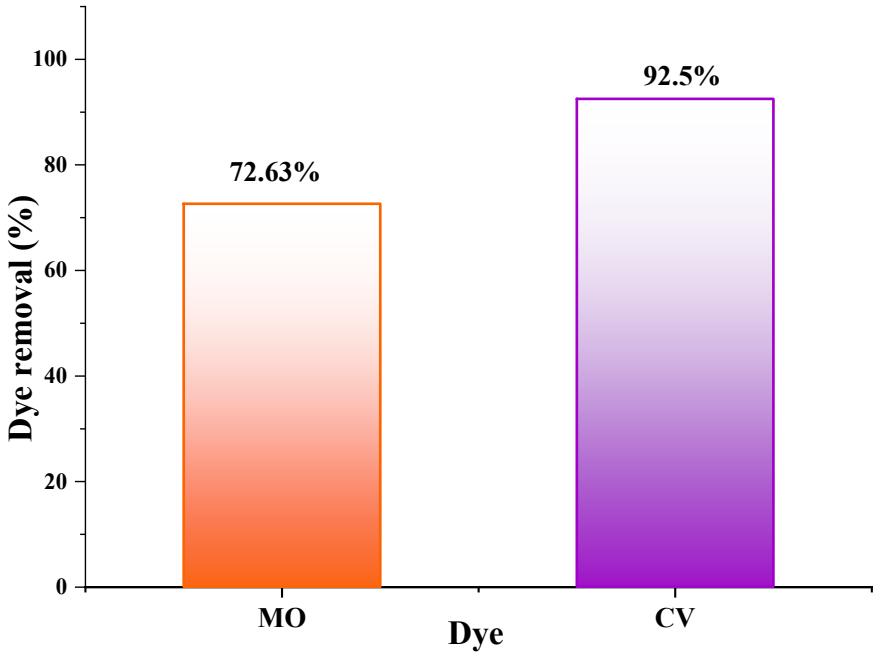


Figure IV.10. *Preliminary adsorption efficiency screening of Methyl Orange and Crystal Violet dyes on the BCCG/PVA hybrid composite.*

Two dyes were selected to test and evaluate the adsorption efficiency of the synthesized composite against two oppositely charged dyes: Crystal Violet (a cationic dye) and Methyl Orange (an anionic dye). As illustrated in **Figure IV.10**, the *BCCG/PVA* composite recorded a higher adsorption yield with the cationic dye (Crystal Violet), at 92.5% (C_0= 25ppm; m= 60mg ; t= 12.5min ; pH= 10), than with the anionic dye (Methyl Orange), at 72.63% (C_0= 50ppm; m= 20mg ; t= 30min ; pH= 4), these results were obtained from RSM designs applied to both dyes and the maximum was then compared. this result while not definitive,

favors the use of Crystal Violet as the model dye with which the subsequent studies were carried out.

2. Mathematical Modelling Using Response Surface Methodology (RSM):

2.1. *Analysis of Variance (ANOVA) for the Quadratic Model:*

2.1.1. *Mathematical and statistical significance:*

Table IV.4. Analysis of Variance (ANOVA), Fit Statistics & Model Comparison Statistics.

Source	Sum of Squares	df	Mean Square	F-value	p-value	
Model	3288.69	9	365.41	***147.56***	***< 0.0001***	***significant***
m (A)	2302.20	1	2302.20	929.67	< 0.0001	
t (B)	131.37	1	131.37	53.05	0.0002	
pH (C)	332.27	1	332.27	134.18	< 0.0001	
AB	26.98	1	26.98	10.90	0.0131	
AC	94.56	1	94.56	38.19	0.0005	
BC	221.49	1	221.49	89.44	< 0.0001	
A^2	75.22	1	75.22	30.37	0.0009	
B^2	15.91	1	15.91	6.43	0.0390	
C^2	97.70	1	97.70	39.45	0.0004	
Residual	17.33	7	2.48			
Lack of Fit	17.33	3	5.78			
Pure Error	0.0000	4	0.0000			
Cor Total	3306.02	16				
R^2	***0.9948***	Std. Dev.		1.57		
Adjusted R^2	***0.9880***	Mean		60.98		
Predicted R^2	***0.9161***	C.V. %		2.58		
Adeq Precision	48.5903					
PRESS	***277.35***					
-2 Log Likelihood	48.58					
BIC	76.91					
AICc	105.24					

The **Table IV.4** shows the analysis of variance (ANOVA), which indicates that the quadratic model is statistically significant at a high level. This is supported by a model F-value of 147.56 and a p-value < 0.0001. This indicates that the model accounts for a large amount of the response variance. The leading terms are given by:

- A (m) and C (pH): P < 0.0001 (the most important linear factor)
- B(t) and C (pH): P < 0.05: good effect.
- **AC** and **BC interactions**: P = 0.0005 and <0.0001, respectively, showing significant interactive effects.
- C^2 and A^2: P-values of 0.0004 and 0.0009, respectively, suggesting significant nonlinear (quadratic) effects.

The **non-significant** coefficients (e.g. **AB** and B^2) could be excluded unless the hierarchy of the model needs to be maintained. The model fit was very good as indicated by the R^2 value of 0.9948. The adjusted R^2 of 0.9880 and predicted R^2 of 0.9161 further confirmed high predictive accuracy, statistically proving that the **PRESS** value of **277.35** is low and ideal. This demonstrates not only that the model is consistent with the experimental results, but also that it is a highly robust predictive model for any future experiments within the same study field and conditions that have not been performed in the laboratory.[25], [26], [27], [28], [29]

In addition, the good precision value 48.5903 (4 < 48.5903) confirms a good signal-to-noise ratio.

2.1.2. *Algebraic form:*

$$R\% = +80.36858+1180.62418\ m-0.879578\ t-17.83333\ pH-17.31555\ m * t+97.24308\ m * pH+0.396864\ t * pH -10566.32905\ m^2-0.034559\ t^2+0.770711\ pH^2 \quad \textbf{4.3}$$

2.1.3. *The Physical Sense:*

The exceptionally significant parameters related to the factor A i.e. the mass m in the ANOVA table (F = 929.67 and P < 0.0001) highlights the paramount importance of this factor. The quantity of the synthesized hybrid composite *BCCG/PVA* plays a crucial role in the efficiency of the water treatment process. Providing a larger quantity of composite increases the driving force of mass transfer due to the greater availability of vacant active sites and functional groups on the composite's surface and within its pores. This attracts more dye molecules and subsequently increases adsorption efficiency.

Furthermore, the ANOVA table shows that C-pH has a significant linear effect ($F = 134.18$, $P < 0.0001$), followed by contact time (B-t) ($F = 53.05$, $P = 0.0002$). This indicates that the reaction is highly sensitive to both pH and time. This is attributed to changes in the ionization states of the Crystal Violet molecules and alterations in the charge of the functional groups on the composite's surface. All of these hypotheses were analysed via the perturbation plot, thereby governing the electrostatic attraction or repulsion forces.

Meanwhile, significant binary interactions, represented by the strong interaction between time and pH (BC: $F = 89.44$, $P < 0.0001$) and the interaction between mass and pH (AC: $P = 0.0005$), demonstrate that the adsorption mechanism is not affected by individual factors in a purely cumulative manner. Rather, it depends on how these variables interact with each other in a complex and intertwined way. Indeed, the interaction between the adsorbent mass and pH at optimal values leads to maximum diffusion and osmotic pressure, resulting in the dispersion of dye molecules and their penetration into the internal pores of the synthesized composite.

Also, the quadratic terms A^2 ($P = 0.0009$) and C^2 ($F = 39.45$, $P = 0.0004$) were obviously statistically significant, which explained the curvature of the 3D response surfaces. This indicates that there is an optimum level of both mass and pH beyond which the removal efficiency cannot increase linearly.

2.2. *Fit Statistics:*

2.2.1. *Statistical and Mathematical Significance:*

- $R^2 = 0.9948$ indicates that 99.48% of the variance in the removal efficiency (R%) is explained by the model, which is a very high degree of fit.
- Adjusted $R^2 = 0.9880$ is slightly lower considering the number of predictors, but it remains excellent, indicating that the model is not overfitted.
- Predicted $R^2 = 0.9161$ measures how well the model predicts new data, and its closeness to the Adjusted R^2 (a difference of less than 0.2) confirms the reliability of the model.
- The standard deviation equals 2.58, and the mean equals 60.98, indicating good precision across the response data.
- Coefficient of Variation (C.V.%): 2.58%; the low coefficient of variation indicates a low dispersion of data relative to the mean, implying experimental consistency (as shown is **Figure IV.11.**).

- The Adequate Precision equals 48.5903, where the signal-to-noise ratio well exceeds the threshold of 4, confirming that the model has a robust precision to navigate the design space[25], [27], [28], [29], [30].

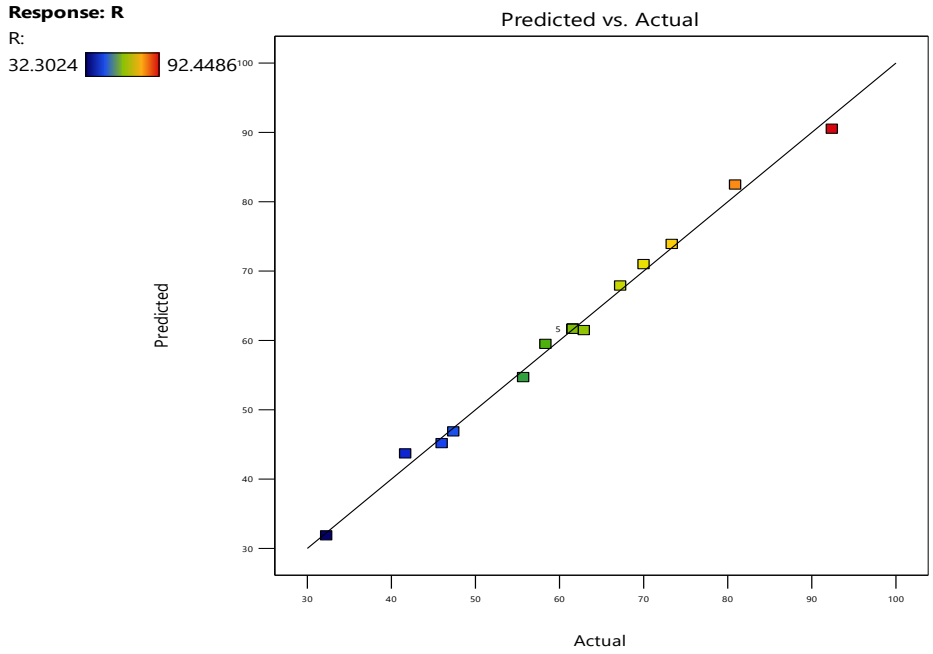


Figure IV.11. *Predicted vs. Actual values.*

2.2.2. *The Physical Sense*:

These fit statistics confirm that the model reliably predicts and navigates within the design space to study the removal efficiency of Crystal Violet dye by the hybrid composite *BCCG/PVA* under different operational conditions. The low coefficient of variation (C.V.%) reflects the extent of experimental reliability and stability, which is most likely attributed to the structural and chemical stability under various conditions. Furthermore, the high predictive power of the model indicates that the main factors (m, t, pH) effectively capture the adsorption dynamics of the system, including surface interaction mechanisms, electrostatic effects, and time-dependent adsorption behavior.

2.3.*The Final Equation in Terms of Coded Factors:*

2.3.1. *The algebraic form of the equation:*

$$R\% = +61.62 + 16.96A + 4.05B + 6.44C - 2.60AB + 4.86AC + 7.44BC - 4.23A^2 - 1.94B^2 + 4.82C^2 \quad \text{IV.2}$$

2.3.2. *Statistical and Mathematical Significance:*

a) *Intercept (61.62):* is the average expected response (R) at the coded zero level of each factor.

b) *Linear Terms:*

The coefficients can be compared directly from the coded form of the equation to see which factors have the greatest effect (either positive or negative) on the response.

- Factor A (Coefficient = +16.96): It has the largest and most powerful positive impact on the response efficiency, and as a consequence, any increment in it would result in a positive upsurge in the response.
- Factors B and C (Coefficient = +4.05, +6.44, respectively): Where C is a mediocre positive influence since by increasing it, the response is positive, although not as much as with factor A. Factor B has the smallest positive linear effect.

c) *Interaction Terms:*

They show the change in response as one factor varies with the level of another factor.

- **Interaction BC** (Coefficient = +7.44): It's the pair with the strongest positive effect in the model. This says that there is a very strong positive synergy between factor B and C at high levels of the response R.
- **Interaction AC** (Coefficient = +4. 86): Is a positively significant interacting term; the larger the value of this term, the better the values of the response, but not as good as the values of BC.
- **Interaction AB** (Coefficient = -2.60): It is a relatively weak negative (inverse) interaction. The concomitant increases in A and B always result in a slightly lower response efficiency than that from either of them alone [25], [26], [27], [28], [29]

2.4. *Final Equation in Terms of Actual Factors:*

2.4.1. *Statistical and Mathematical Significance:*

This model uses actual units (min, mg) for prediction, but they cannot be used to compare effects directly, because the coefficients are scaled based on the units.

The following can be observed:

- A strong positive effect is indicated for mass (+1180.62418), showing its major role in enhancing removal.
- A negative effect is shown for both time and pH, indicating a slight decreasing trend for the response.
- Interaction and curvature terms (such as m pH, m^2) are confirmed, representing non-linear dependencies. [25], [26], [27], [28], [29]

2.4.2. *The Physical Sense:*

- The adsorbent mass showed the highest positive linear coefficient (+1180.62), confirming the significant role of increasing adsorbent mass in improving removal efficiency due to the larger surface area and plenty of vacant active sites.
- The negative linear slopes for time and pH indicate the response marginally decreases at low levels of the factors before the factors interact.
- The interaction between mass and pH has a large positive coefficient of +97.24, indicating a strong synergy to improve the removal efficiency. In contrast, the interaction between mass and time of the compound (m.t) had a significant negative coefficient of -17.31, showing the efficiency reduction at high mass and long contact times.
- The curvature terms (m^2, pH^2 and t^2) behaviour is nonlinear. The large negative coefficient for m^2 (-10,566.33) indicates an optimal value where the linear removal ceases and starts to decrease or stabilize due to aggregation of particles of the compound and reduction of surface area, thereby masking the active sites.

2.5. *One-Factor Plots:*

2.5.1. *Statistical and Mathematical Significance:*

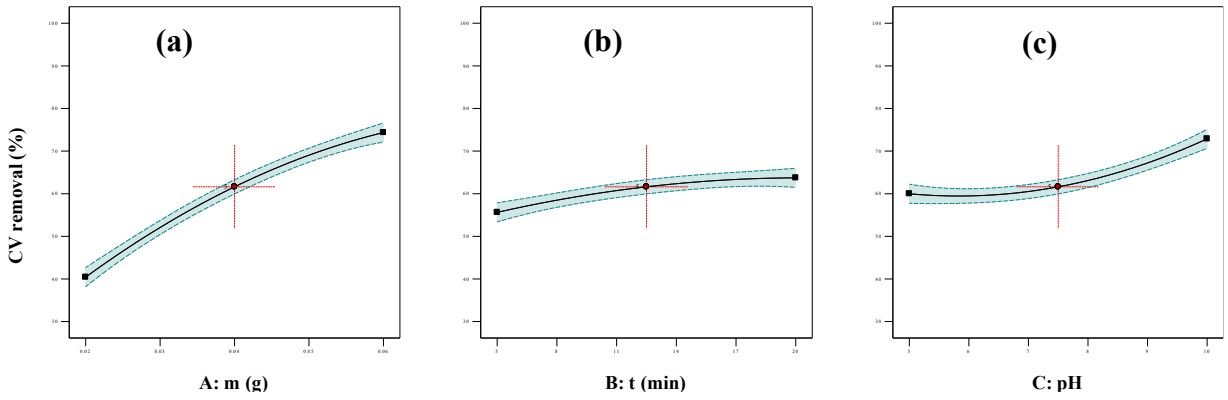


Figure IV.12. *One-Factor Plot.*

a) *Adsorbent Dose Effect:*

The graph **(a)** shows a positive correlation with a relatively large slope, and stabilizes at a higher dose. The positive linear coefficient and the quadratic term indicate an increasing effect with a plateau upon increasing the adsorbent dose.

b) *Contact Time Effect:*

The graph **(b)** often rises sharply at the beginning and then stabilizes, corresponding to the adsorption kinetics reaching equilibrium. Were observe an increase at a low rate in the yield with increasing time. This behaviour is supported by the statistically significant positive linear term, and the significant negative quadratic coefficient indicates the presence of a slight curvature in the response.

c) *pH Effect:*

The figure (c) shows the effect of pH, typically exhibiting a positive slope, which indicates an improvement in the removal efficiency at higher pH values. This is confirmed by the statistically significant positive linear and quadratic coefficients in the statistical model.

2.5.2. *The Physical Sense:*

a) *Adsorbent Dose Effect:*

An increase in the adsorbent dose leads to an increase in the available surface area and active sites, which enhances dye removal. However, exceeding the optimal dose causes particle agglomeration or saturation of the active sites, which reduces the adsorption efficiency despite the increase in the composite mass.[31], [32], [33]

b) *Contact Time Effect:*

The optimal contact time allows dye molecules to diffuse and bind to the composite molecules without the occurrence of desorption. After a certain period of time, equilibrium is reached where the rates of adsorption and desorption balance out, limiting further increase in removal even with continued time[33], [34].

c) *pH Effect:*

At elevated pH, the composite surface becomes more negatively charged, enhancing the electrostatic attractions with the cationic crystal violet dye, which improves the adsorption process. However, at a less acidic or lower pH, specifically when pH < pHz (where the pH is below the point of zero charge), the negative charge of the composite decreases, thereby

weakening the electrostatic interactions and reducing the dye removal efficiency.[24], [35], [36]

2.6. *Interaction Analysis:*

2.6.1. *Statistical and Mathematical Significance:*

A) *Interaction (**AB**) between Adsorbent Dose (m) and Contact Time (t):*

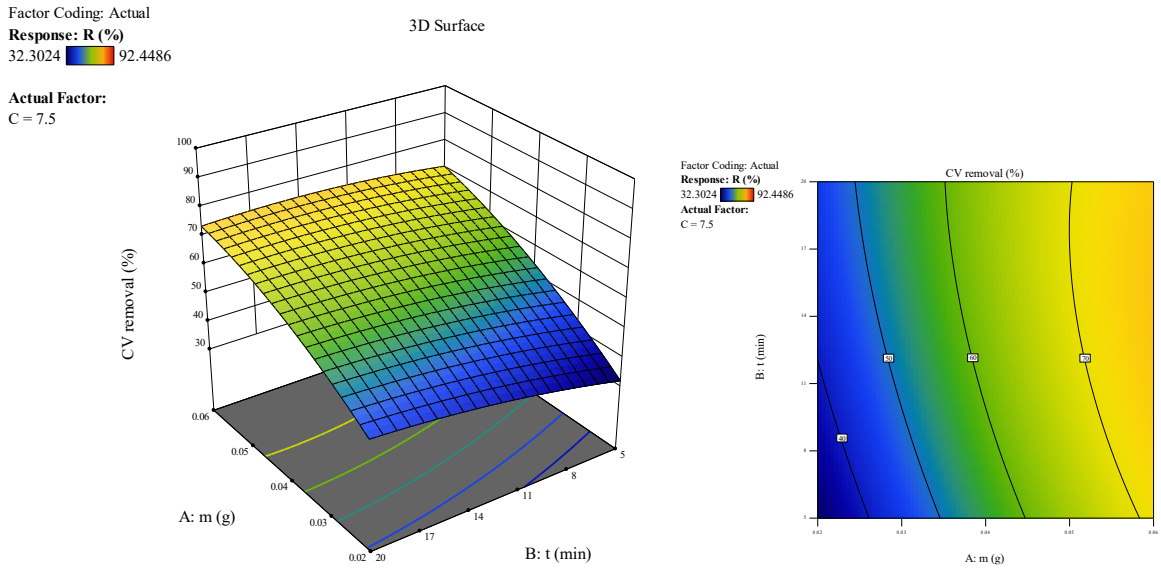


Figure IV.13. *The mutual interaction between BCCG/PVA dose and contact time.*

The Figure **(IV.13)** indicates that increasing both factors together produces a mutual effect up to a certain point; however, the negative coefficient indicates diminishing returns or a slight antagonism in extreme cases.

B) *Interaction (**AC**) between Adsorbent Dose (m) and pH:*

Figure IV.14. shows the interaction of the adsorbent dose vs. pH, which is statistically significantly positive, confirming the presence of a strong synergistic effect where the removal efficiency increases with the increase of both the dose and pH until reaching its peak. In other words, the synergistic effects enhance the removal efficiencies more than the individual effects.

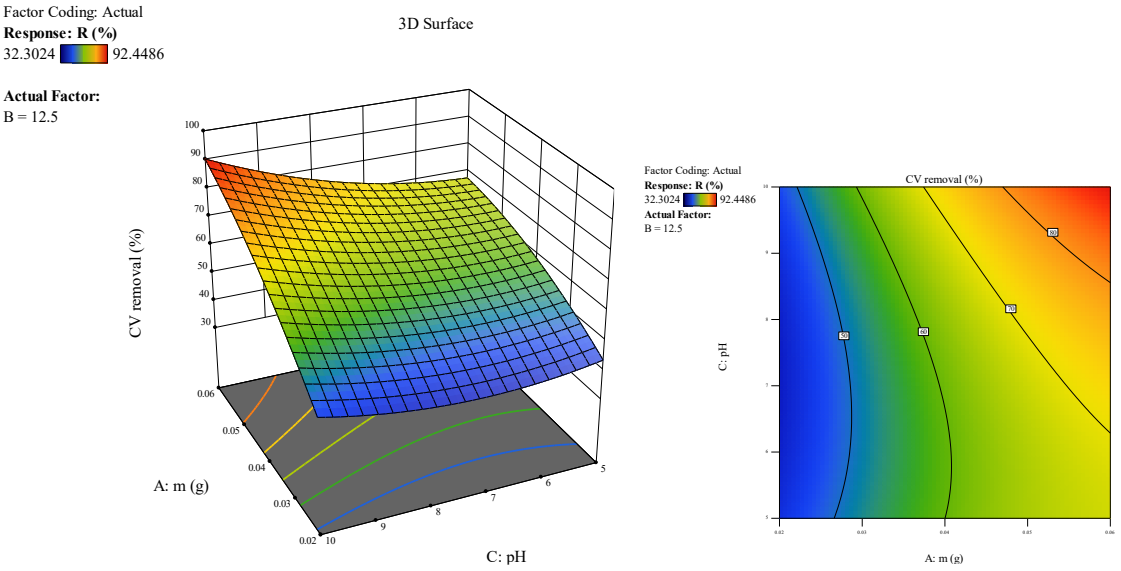


Figure IV.14. *The mutual interaction between adsorbent dose and pH solution.*

C) *<u>Interaction (**BC**) between Contact Time (t) and pH solution:</u>*

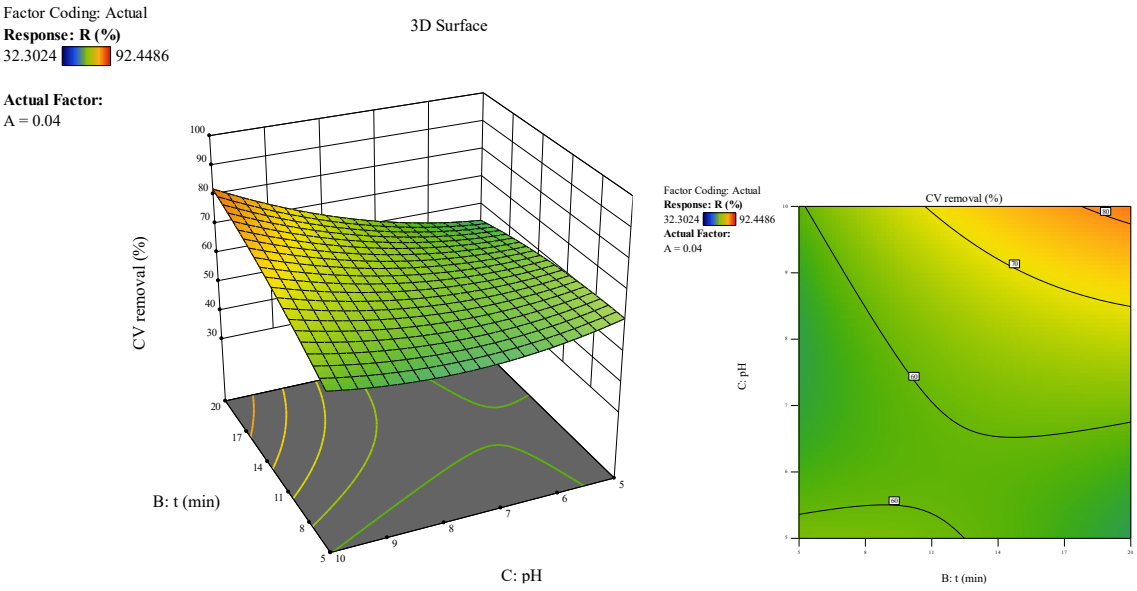


Figure IV.15. *The mutual interaction between contact time and pH.*

Figure IV.16 illustrates the interaction of contact time with pH, and it possesses the highest positive statistical significance in the model. This interaction confirms the strong synergistic behaviour between the two factors in increasing the removal efficiency at their maximum values.

2.6.2. *The Physical Sense:*

A) *Interaction (AB) between Adsorbent Dose (m) and Contact Time (t):*

An increase in both the composite dose and contact time enhances the removal process by increasing the sites and allowing equilibrium to be reached. However, at a large dose and long time periods, saturation or agglomeration limits further improvements.

B) *Interaction (AC) between Adsorbent Dose (m) and pH:*

As the pH increases, the deprotonation process leads to the dense negative charge on the composite surface and at the same time, the large mass of the composite offers plenty of vacant sites. This combination of the two factors increases the global removal efficiency, keeping the efficiency increasing constantly without hindrance or agglomeration.

C) *Interaction (BC) between Contact Time (t) and pH:*

This interaction is explained by the fact that increasing the contact time and raising the pH value together lead to the efficiency reaching its peak. This is because when the reaction medium is highly alkaline, a dense net negative charge is imparted to the composite surface, resulting in a large adsorption capacity, while simultaneously providing the ideal time to complete the adsorption process, which leads to obtaining a maximum yield.

2.7.*The Desirability Function & Confirmation Experiment:*

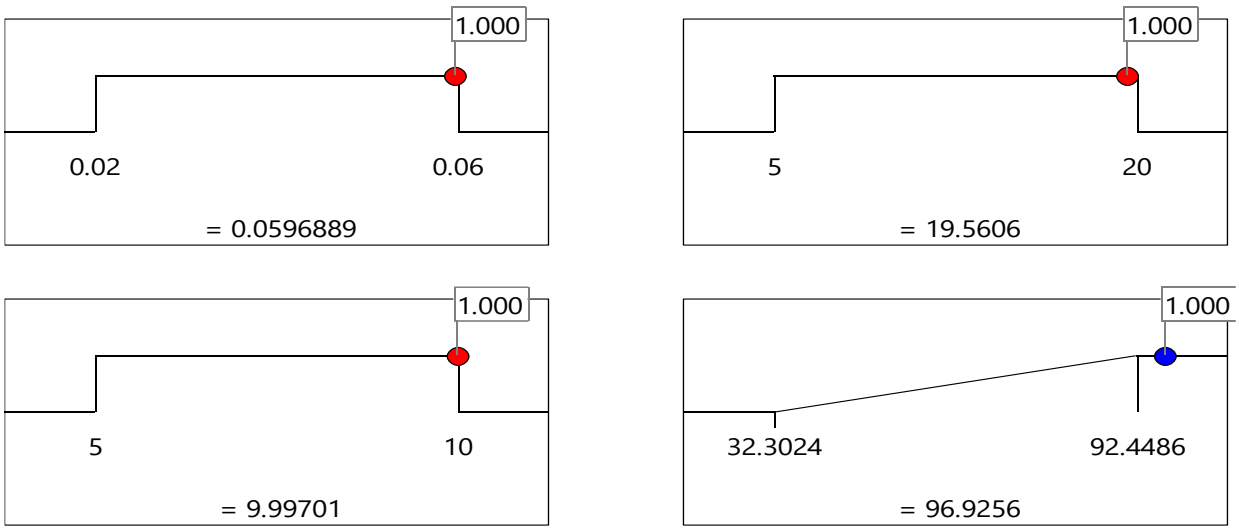


Figure IV.16. *The optimal values.*

The desirability function combines multiple response goals into a single scale graded from 0 to 1, where 1 represents the ideal case. **Figure IV.16** shows the optimum conditions (m = 59 mg, t ≈ 20 min, pH ≈ 10) and the predicted removal efficiency, which corresponds to a high desirability value close to 1 and indicates the optimal state of the model.

2.7.1. *Statistical and mathematical significance:*

The desirability function combines multiple response goals into a single scale graded from 0 to 1, where 1 represents the ideal case. **Figure IV.16** shows the optimum and the predicted removal efficiency, which corresponds to a high desirability value close to 1 and indicates the optimal state of the model.

The confirmation experiment resulted in an actual removal efficiency of 95.15% which is quite close to the model prediction of 96.92%. As can be seen from the following, the small deviation of 1.83% is well within the typical experimental error margin of ~1.5–2.5%:

Standard deviation: ~ 2.58

Standard error of the mean: ~1.57

This confirms that the model predictions are statistically reliable and the desirability function is valid for the optimization of conditions.

2.7.2. *Physical Sense:*

The optimal conditions of operation are achieved owing to a precisely studied physicochemical balance, where the right dose of BCCG/PVA, enough contact time and a proper pH are combined for the highest capacity of removing the cationic crystal violet dye.

At pH ≈10 the active functional groups are deprotonated and the BCCG/PVA surface is densely negatively charged. This considerably increases the electrostatic attraction with cationic dye molecules. Meanwhile, the sufficient contact time of 20 min and the appropriate dosage provide sufficient time to increase the number of successful collisions and ensure there are enough vacant active sites. The experimental results are in good agreement with the predicted output, which confirms the practical usefulness of these conditions for treatment of polluted wastewater.

In terms of mathematical and statistical significance, the confirmation experiment yielded a removal percentage of 95.15%, a figure that is very close to the 96.92% predicted by the software, with a difference of just 1.83%. To evaluate the predictive accuracy of the studied model, the following statistical error indicators were calculated:

$$\text{Absolute error} = |\text{predicted value} - \text{experimental value}|$$

$$| 96.92 - 95.15 | = 1.77\%$$

$$\text{Relative error} = (\text{absolute error} / \text{predicted value}) \times 100\%$$

$$(1.77 / 96.92) \times 100\% = 1.83\%$$

Considering the model's standard deviation of 2.58% and the standard error of the mean of 1.57%, the observed variance is extremely slight and falls within the naturally accepted statistical and experimental random limits. This does not lead to severe systematic errors, since error margins below 10% (here, 1.85%) of the expected random variance are widely accepted in environmental engineering systems, particularly given the complex kinetics of adsorption.

From a practical physicochemical perspective, this very slight variance indicates minimal systematic errors or limited non-ideal experimental factors.

- Minor variations on the BCCG/PVA surface.
- Non-uniform and unequal distribution of active functional groups.

The system may not have reached complete equilibrium due to insufficient contact time, which was set at 20 minutes.

Limited experimental variation in controlling measurement accuracy, such as adjusting the pH or imprecise weighing of the composite dosage, could also be a factor.

Nevertheless, a relative error of 1.85% in adsorption experiments is considered excellent in environmental engineering, especially given the complex adsorption kinetics. The desirability function extending horizontally at saturation values (desirability = 1.000), along with the experimental value, confirms that the system operates efficiently near the optimum level and that the desirability function is a reliable predictor for future simulations.

2.8. *Experimental Vs Predicted (RSM) removal efficiency values:*

2.8.1. *Predictive Accuracy of the RSM design:*

Table IV.5. Experimental and Predicted Values for Reaction Yield R%.

Std	Run	A / m (mg)	B / t (min)	C / pH	R_{Exp} (%)	R_{Pred} (%)
12	1	0.04	20	10	80.93	82.43
17	2	0.04	12.5	7.5	61.62	61.62
1	3	0.02	5	7.5	32.30	31.83
13	4	0.04	12.5	7.5	61.62	61.62
7	5	0.02	12.5	10	47.42	46.83
5	6	0.02	12.5	5	41.69	43.66
8	7	0.06	12.5	10	92.45	90.48
10	8	0.04	20	5	55.72	54.66
11	9	0.04	5	10	58.38	59.44
4	10	0.06	20	7.5	73.40	73.87
2	11	0.06	5	7.5	70.05	70.96
15	12	0.04	12.5	7.5	61.62	61.62
9	13	0.04	5	5	62.93	61.43
16	14	0.04	12.5	7.5	61.62	61.62
14	15	0.04	12.5	7.5	61.62	61.62
6	16	0.06	12.5	5	67.27	67.86
3	17	0.02	20	7.5	46.04	45.13

In **Table IV.5**, the predicted values (RSM) are generally very close to the experimental values, with absolute errors mostly within ±2-3%.

Several runs (such as runs 2, 4, 12, 14, and 15) showed perfectly identical observed and predicted responses. There are almost identical predicted responses where (the difference ±2-3% such as 1, 6, 10, 11, and 13, which indicates excellent point predictions. The residuals (the difference between the observed and predicted values) are randomly distributed across all runs, without any clear trend or bias which shows that:

- Low mean absolute error.
- High predictive accuracy.
- Good model generalization.

2.8.2. *Consistency with Statistical Fit:*

These results align with the fit statistics, this means that:

- The correlation coefficient R^2 is 0.9948, the adjusted R^2 is 0.9880, and the predicted R^2 is 0.9161. These high values mean that the model explains almost all the variance and predicts new data well.
- The standard deviation value of 2.58% and the standard error value of 1.57% are small, so the predicted values falling within ±2-3% of the observed values ensure a 95% confidence interval, which is statistically acceptable for experimental systems.

2.8.3. *Analysis of the response surface methodology model:*

The following error indicators can be used to analyse model performance:

- Mean Absolute Error (MAE).
- Relative Error, (C.V.%).
- Root Means Square error (RMSE).

Table IV.5. shows that the majority of experiments demonstrated an absolute error of less than 2%, reaching a value of 1.257%. The root means square error value was identical to the standard deviation, reaching a value of 1.57.

Relative error values range from 0% to 2.38%, except for run 6, which recorded a higher deviation of 4.72%.

Deviations are often within the range of statistical noise, and larger deviations may result from experimental variance. This can be caused by factors such as a non-homogeneous distribution of *BCCG/PVA* in the solution, slight changes in pH during the experiment and variation in measuring and analysis instruments.

3. Contact Time Effect & Adsorption Kinetics:

The variation of the adsorbed amount with time (qt) with initial dye concentrations in the adsorption study of Crystal Violet (CV) dye from polluted water on BCCG/PVA as an adsorbent provides important information about the kinetics and mass transfer characteristics of the system.

Figure IV.17. shows the evolution of the qt values in time, at four initial concentrations: 25, 50, 100 and 300 mg/L. The results show an expected behaviour, where qt values increase with the increase of the initial dye concentration over time. This suggests that the concentration gradient between the solution and the adsorbent surface increases the amount of Crystal Violet dye adsorbed onto BCCG/PVA. This trend is consistent with the classical

adsorption theory, which is attributed to the higher initial concentrations increasing the driving force for mass transfer from solution to the surface and internal pores of the composite, resulting in faster diffusion and higher adsorption until equilibrium is reached [10], [37], [38].

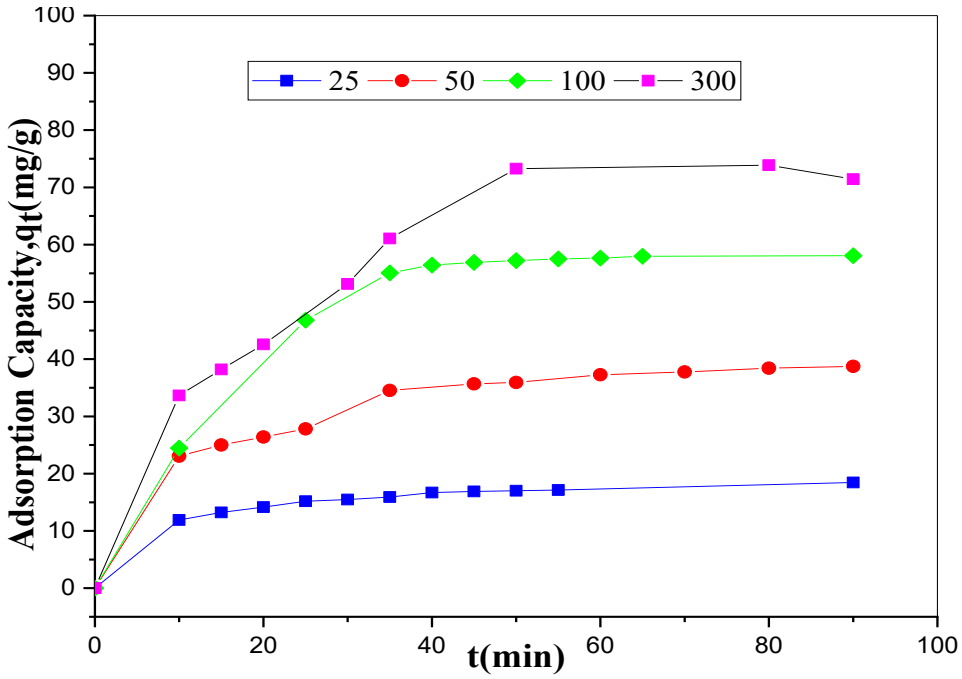


Figure IV.17. *Influence of initial dye concentration and contact time on adsorption capacity.*

3.1. *Analysis of the Pseudo-First-Order (PFO) & Pseudo-Second-Order (PSO) model kinetics:*

Two of the most influential kinetic models namely pseudo-first order and pseudo-second order models were used to determine the reaction orders of adsorption of Crystal Violet (CV) dye onto (BCCG/PVA) in aqueous solutions at different concentrations. These models are regarded as effective in identifying possible mechanisms of adsorption. Where the pseudo-first-order model assumes the adsorption process is generally associated with physical adsorption, which involves weak van der Waals forces, and the pseudo-second-order model assumes the adsorption process undergoes chemical adsorption. **Table IV.6** summarises the experimental data for both models with different initial concentrations (25, 50, 100, 300 mg/L).[34], [38], [39].

Table IV.6. PFO & PSO model adsorption kinetic parameters at different concentrations

Pseudo-Second-Order				*Pseudo-First-Order*			
C_0 (mg /L)	R^2	K_2 (g/mg.min)	qe (mg/g)	R^2	K_1 (min^{-1})	q_e (mg /g)	q_m (mg /g)
25	0.996	0.141	19.63	0.975	0.0619	17.58	25.40
50	0.987	0.77	43.79	0.973	0.0642	37.91	41.06
100	0.971	2.073	70.09	0.993	0.0662	59.3	58.07
300	0.961	4.343	96.10	0.97	0.075	76.93	83.04

The results of the kinetic modelling for the adsorption of Crystal Violet (CV) dye onto the surface of BCCG/PVA are interpreted based on the extracted experimental and statistical data as follows:

The results revealed that the fitting of the kinetic models was directly related to the initial concentration of the dye, where the pseudo-second-order model showed better agreement and high correlation coefficient (R^2) values at low concentrations, and the pseudo-first-order model was the most consistent and accurate in describing the process at high concentrations. This difference is also supported by the good agreement between the calculated and experimental values of qt. The pseudo second-order model was the best model to calculate the adsorption capacity at equilibrium in the low concentration range. However, at high concentrations (100 and 300 mg/L), the pseudo-second-order model values deviated, and the pseudo-first-order model values were the closest to the experimental reality (where the maximum experimental capacity reached 59.3 mg/g compared to 70.09 mg/g calculated by the pseudo-first-order model at a concentration of 100 mg/L).

This kinetic change shows that the adsorption process depends on the concentration of dye molecules. At low concentrations, chemisorption dominates via direct interaction with the active sites and is characterized by π–π interactions between the aromatic rings and double bonds, electrostatic attraction between the dye cations and negative oxygen-containing groups, and hydrogen bonding with hydroxyl, amine and amide groups. Otherwise, at high concentrations, the system tends to physisorption or mass transfer, because of the saturation of the active sites and the accumulation of the molecules. Such dual behavior is expected to affect the adsorption equilibrium in a mixed behavior in which the Langmuir model

(monolayer) is fitting at low concentrations, while the Freundlich model (multilayer) is favored at high concentrations[9], [37], [40].

3.2. *Analysis of Weber-Morris Intra-particle Diffusion Model Kinetics & Rate-Controlling Steps Studies:*

The results of the kinetic modelling of the investigated mass transfer mechanism of Crystal Violet dye molecules onto BCCG/PVA using the Weber-Morris intra-particle diffusion model ($qt = k_{id} \cdot t^{0.5} + C$) are represented in the linear graph in **Figure IV.18.** as well as the **Table IV.7** which summarizes the main model parameters obtained in this study.

Table IV.7. Diffusion models constants for the adsorption of BCCG/PVA at different initial concentrations.

Surface Diffusion model constants				Intra-particle diffusion model constants		
C_0 (ppm)	R^2	k_{sd} (mg/g.min$^{0.5}$)	q(mg/g)	R^2	k_{id} (mg/g.min$^{0.5}$)	C (mg/g)
25	0.977	1.47	7.43	0.981	1.21	27.48
50	0.999	2.56	14.95	0.808	0.41440	54.34
100	0.983	10.42	-7.49	0.808	0.41	54.34
300	1	48.60	-150	0.952	9.27	71.37
	0.990	11.26	-6.77			

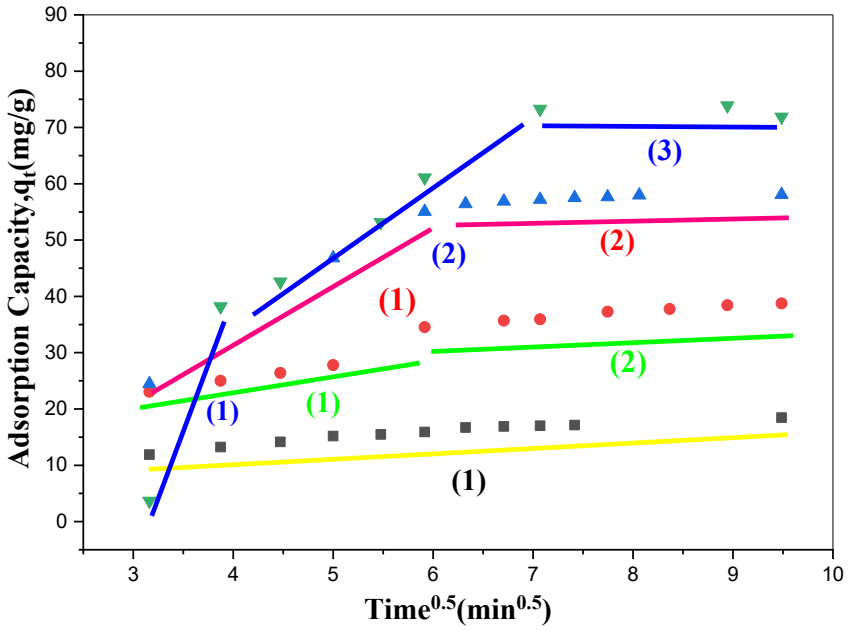


Figure IV.18. *Weber-Morris intra-particle diffusion plots.*

The plots in **Figure IV.18.** show that the linear lines for each concentration do not pass through the origin of the coordinate system and that adsorption does not proceed through a single, continuous, linear stage over time for the various concentrations. Rather, it is divided into multiple stages. The number of stages increases with concentration: for example, at the lowest concentration there is one clear stage, whereas at the highest concentration there are three. This indicates that the adsorption mechanism is not solely confined to external diffusion.[10], [34], [41]

- *The First stage:*

Represented by the first segment with sharp, high slopes k_{sd}, this phase is attributed to external diffusion. During this stage, mass transfer occurs at a high rate from the bulk solution onto the surface of the bio-composite due to strong electrostatic attractions.

- *The Second stage*

This is represented by the second segment, which is less steep than the first and has lower slopes k_{id}. This phase is attributed to intra-particle diffusion, where mass transfer gradually proceeds into the internal pores after the external surface is saturated, and the adsorption rate begins to slow down.

- *The Third stage*

Represented by the third segment of the plot, which is clearly visible at a concentration of 300 ppm. It exhibits a very low slope and represents the adsorption equilibrium stage, where adsorption slows down drastically due to saturation of the surface and internal pores resulting from stages one and two.

As for the effect of initial concentration on kinetic constants, It is observed that, as concentration increases, initial rate constant values k_{sd} increase from 1.47 to 48.6 mg/g $min^{-0.5}$. This is because higher concentrations provide a greater mass driving force due to the high density of dye particles in the solution. This overcomes mass transfer resistance and accelerates the adsorption process. The negative C values observed in the initial stages of higher concentrations result from the ultra-fast initial adsorption rate [42].

4. Adsorption Isotherm Studies:

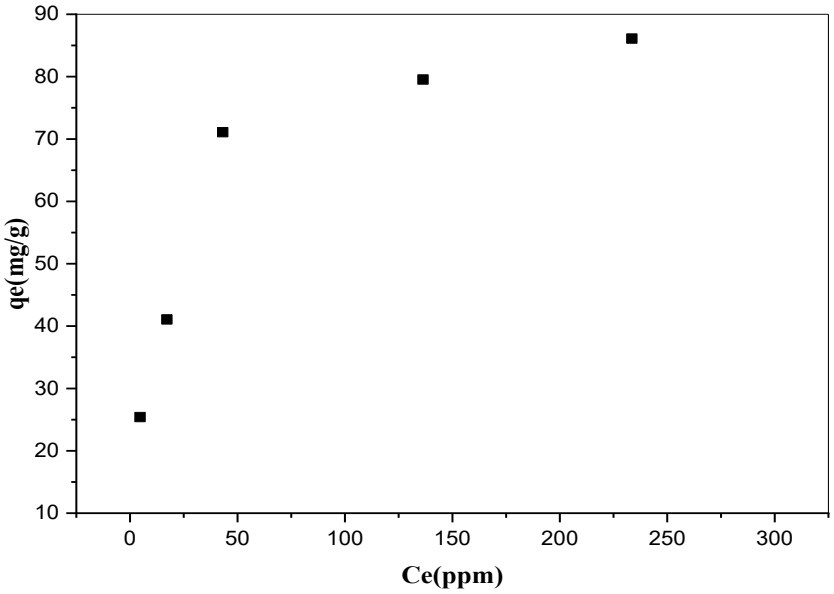


Figure IV.19. *Effect of concentration on equilibrium adsorption capacity.*

One of the fundamental aspects in adsorption studies is the study of the relationship between adsorption capacity (q) and the concentration (C_e) at equilibrium, **Figure IV.19** represents this relation and it shows a direct and strong dependance of the adsorption capacity on the initial concentration. An increase in equilibrium adsorption capacity was observed as the residual dye concentration increased until equilibrium was reached. This is due to the increased mass driving force caused by the rising initial concentration of the dye, which overcomes the mass transfer resistance and increases the number of effective collisions that fix the dye onto the composite. The adsorption isotherm of Crystal Violet dye onto BCCG/PVA was studied using three common models: Langmuir, Freundlich, Toth and Sips. The aim was to determine the nature of the adsorption interaction taking place between the adsorbate and the adsorbent, and to identify whether the mass transferred from the solution to the composite was distributed in a homogeneous monolayer or heterogeneous multilayer pattern[43], [44].

The graph in **Figure IV.20** illustrates the *non-linear regression* fitting of four distinct equilibrium isotherm models (Langmuir, Freundlich, Toth, and Sips) compared against experimental adsorption data points (q_e vs. C_e) at various equilibrium concentrations[45].

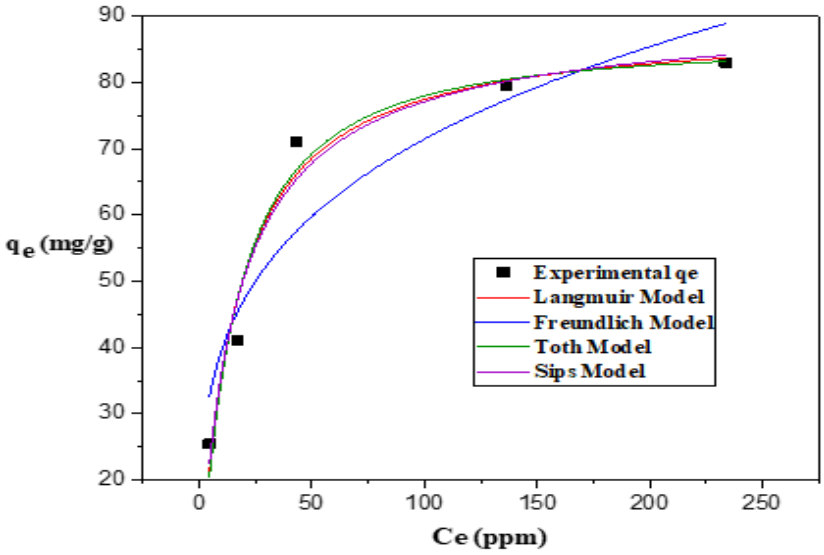


Figure IV.20. *Non-linear fit for adsorption Isotherms.*

The adsorption capacity increases sharply, indicating high affinity between the target adsorbate molecules and the available active surface sites. As concentration increases toward 250 ppm, the experimental capacity begins to plateau around 83 $mg \cdot g^{-1}$, signaling progressive site saturation.

The non-linear regression fit results obtained are summarized in **Table IV.8** and are discussed below.

Table IV.8. *Adsorption isotherm models of Crystal Violet onto* BCCG/PVA.

Model	**R^2**	**$R^2\pm$**	**Constants**	**Value**			
Langmuir Isotherm	0.955	28.58	**q_m** (mg/g)	89.02			
			K_L (L/mg)	0.066			
			R_L	25ppm	50ppm	100ppm	300ppm
				0.37	0.23	0.13	0.04
Freundlich Isotherm	0.85	97.01	**K_F** (mg/g) $(L/mg)^{1/n}$	21.82			
			n	0.25			
Sips Isotherm	0.935	41.72	**q_m** (mg/g)	91.084			
			K_S (L/mg)	0.0785			
			N	0.923			
Toth Isotherm	0.934	42.41	**q_m** (mg/g)	104.12			
			K_T (L/mg)	18.33			
			z	1.024			

4.1. *Suitability of the Langmuir model:*

The Langmuir constants (K_L = 0.37, 0.23, 0.13, 0.04 L/mg), which are bounded between 0 and 1, indicate that the binding between the dye and the composite (BCCG/PVA) is highly efficient and stable, ensuring the effective stabilization of the dye molecules within the composite. The correlation coefficient (R^2 = 0.955). **Figure IV.20** shows excellent non-linear agreement with the experimental values, with slight variance (28.58) resulting from the composite's structural complexity, The multiplicity of its functional groups and the overlapping of pores also contribute to this slight variance.

These results closely align with the investigated mechanisms, in which these groups are distributed uniformly and regularly to allow the reception of charged dye particles via electrostatic attraction, aromatic π-π bonds and hydrogen bonds. However, incomplete variance indicates minor secondary interactions in the composite surfaces, such as internal diffusion. This was proven in the Weber-Morris model study and is not fully taken into account by the Langmuir model.

Additionally, the extracted maximum theoretical capacity value (q_m= 89.02 mg/g mg/g) closely converges with the actual maximum capacity obtained in the experiment, confirming the model's high predictive efficiency. However, studying other isotherm models is necessary to gain a better and more precise understanding of the adsorption mechanism[44], [46].

4.2. *Suitability of the Freundlich model*

The Freundlich equation is used to study multilayer adsorption on heterogeneous surfaces. This makes it particularly important for systems in which adsorbents, such as BCCG/PVA, have non-uniform surface energy due to structural defects or uneven distributions of functional groups. In **Table IV.8**, the heterogeneity factor (n = 0.25), being greater than 1, indicates favorable adsorption conditions, as n values between 1 and 10 typically suggest good adsorption processes. The R^2 value of 0.85 indicates that the Freundlich model provides good agreement with the experimental data, albeit lower than the Langmuir model in this case. The variance coefficient (97.01) is higher than the Langmuir isotherm coefficient, indicating larger deviations between the model's predictions and the observed data. This may be due to the Freundlich model's inherent assumption of an exponential decrease in adsorption energy, which may not fully capture specific interactions between the dye and the composite, such as localized electrostatic attractions or π–π stacking. The suitability of the Freundlich model indicates the presence of surface heterogeneity in BCCG/PVA, likely

arising from its oxygen-containing functional groups and structural defects. However, the relatively poor fit compared to the Langmuir model indicates that monolayer adsorption is predominant. This duality underscores the complex nature of BCCG/PVA as an adsorbent, where both homogeneous and heterogeneous adsorption sites contribute to the overall removal mechanism[47], [48].

4.3. *Suitability of the Sips model:*

The Sips model is a hybrid model which combines the traits of Langmuir and Freundlich models. This model is used to predict the adsorption behavior in heterogeneous systems. The results indicated an excellent statistical fitness with coefficient of determination (R^2 =0.935), and lowered chi-square (41.72). Though real systems seldom fit a single theoretical model exactly, the Sips model displayed a wonderful convergence of its characteristics with those of the Langmuir model, pointing towards the dominance of the monolayer adsorption mechanism. In addition, the value of Freundlich exponent (n =0.923) close to unity represents a high degree of surface homogeneity, which enables the model to have enough flexibility to explain the adsorption process of the BCCG/PVA composite with the dye with a high accuracy.[37], [48].

4.4. *Suitability of the Toth model*

The Toth model shows statistically acceptable fitting, with an R^2 value of 0.934 and a reduced chi-squared value of 42.41, indicating a good fit. The model's performance suggests that the adsorption of BCCG/PVA onto the dye is best described by a modified Langmuir approach that considers surface heterogeneity. The high value of qe (104.12 mg/g) suggests a greater adsorption capacity than predicted by the standard Langmuir model. Meanwhile, the heterogeneity parameter (z=1.024) confirms that the BCCG/PVA surface is not fully homogeneous. This is consistent with the composite's complex structure, where the non-uniform distribution of functional groups produces a varying range of adsorption site energies. The Toth model results emphasize the importance of considering surface heterogeneity when describing BCCG/PVA adsorption, even when monolayer adsorption is the dominant mechanism[48], [49].

5. Adsorption Thermodynamics Analysis:

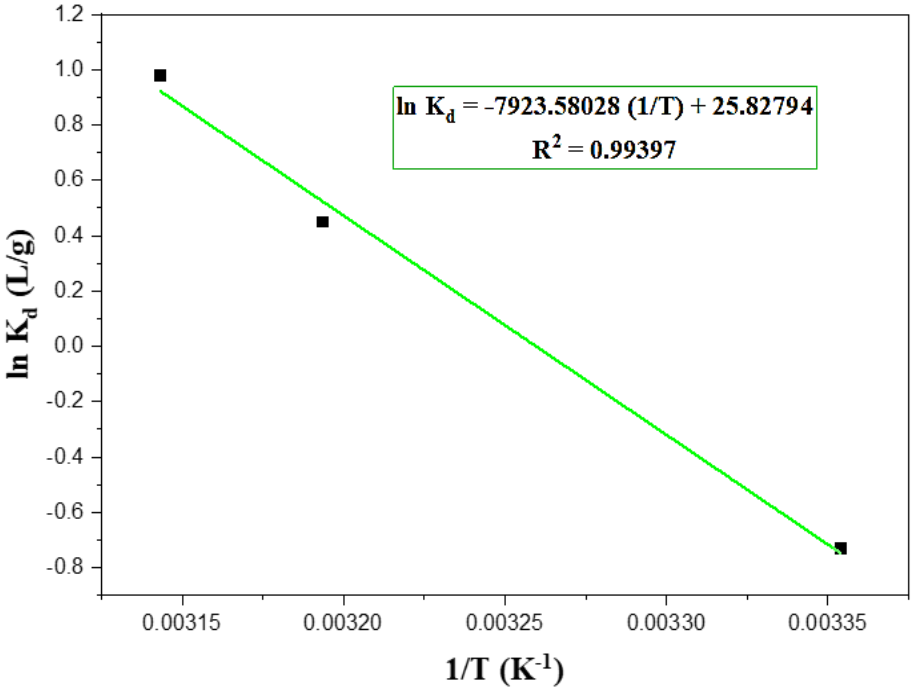


Figure IV.21. *Van 't Hoff plot for Crystal Violet (CV) adsorption.*

Table IV.9. Thermodynamic parameters for CV adsorption at different temperatures.

T(K)	LnK_d	ΔH (KJ/mol)	ΔS (KJ/mol. K)	ΔG (KJ/mol)
298.15	-0.736	65.877	0.213	780.1879965
313.15	0.450			-1367.146935
318.15	0.983			-2440.814401

Table IV.9 shows the thermodynamic coefficient (K_d), which describes the degree of dye binding to the surface of the composite (BCCG/PVA)[10], [50].while **Figure IV.21** shows the linear van't Hoff relation between (1/T) and (lnK_d). It can be seen that the distribution coefficient (K_d) increases with increasing temperature. The positive values of enthalpy (ΔH) show that the adsorption process is endothermic, which justifies the increase in the adsorption efficiency with the increase in temperature; this is due to the fact that the increase in temperature increases the binding forces between the dye and the composite surface. Also, the value of Enthalpy ΔH> 40 (KJ/mol) confirms the results of the isotherm study, that is, that the adsorption is chemical.

Positive values of the change in entropy (ΔS) indicate an increase in randomness and disorder at the interface between the aqueous solution and the material surface during adsorption. This reflects the transition of molecules from a more ordered and stable state in the solution to a more disordered and random state at the surface.

On the other hand, the positive value of Gibbs free energy (ΔG) at low temperature confirms the non-spontaneous nature of the adsorption process, as at low temperatures, the dye molecules do not possess high and sufficient kinetic energy to overcome the barrier and penetrate the surface. Meanwhile, we observe the change of its values to negative with the increase in temperature, and that is due to their acquisition of kinetic energy, meaning an increase in randomness, which increases the effective collisions between the dye molecules and the adsorbent surface. This is also reflected in the fact that the Gibbs free energy (ΔG) decreases with the increase in temperature, which indicates that temperature improves the efficiency of the adsorption process[51], [52].

6. Adsorption Mechanism:

The adsorption mechanism (shown in **Figure IV.22.**) of Crystal Violet (CV) dye onto the hybrid hydrogel composite is based on an integrated dynamic matrix, incorporating kinetic transport steps and secondary chemical interactions. The process begins with the migration of cationic dye ions from the bulk solution through external film diffusion, through the stagnant liquid boundary layer surrounding the surface. This is followed immediately by the rate-limiting step of adsorption, namely intraparticle (pore) diffusion, as shown by the Weber-Morris model. In this process, the molecules penetrate tortuously the hierarchical pore network of the composite from macropores to mesopores and finally to the deep micropores[52], [53].

The structural schematic clearly shows that electrostatic attraction is the main driving force for fast initial binding. This is because of the high coulombic affinity between the positively charged nitrogen of the dye (N^+) and the vacant negative surface sites of the composite. The active sites are the ionized carboxylate groups (-COO−) of gelatine and the exposed silanol groups (Si-O−) on the edges of the bentonite clay. Meanwhile, an ion exchange mechanism takes place in the deeper layers as the cations successfully penetrate the interlayers of the bentonite. This leads to an intercalation process that extrudes and discharges the charge-balancing crystalline sodium ions (Na^+) from the clay structure[54], [55].

Furthermore, the high density of donor and acceptor functional groups in the biopolymer chains (chitosan, polyvinyl alcohol (PVA) and cellulose) is of great importance in the formation of a complex hydrogen-bonding network, which improves the stability of the dye through two possible pathways. The first is direct hydrogen bonding, through interaction of composite active amine ($-NH_2$) or hydroxyl (-OH) groups with the polarized nitrogen of the dye. The second is water-mediated hydrogen bonding, in which water molecules trapped in the hydrogel network serve as dual-linker bridges[56].

In the final step of adsorption, the flat aromatic molecules are densely packed in the confined pores and the whole system is stabilized by the formation of π–π stacking. This is the effect of overlap of the benzene ring orbitals between neighboring dye molecules. This alignment is further stabilized by dipole-dipole van der Waals forces, due to the permanent and induced polarization of the carbon-nitrogen bonds. These forces synergize with hydrophobic interactions that compel the non-polar methyl groups to hide themselves in the organic polymeric cavities, away from the aqueous medium. Such cooperative synergy efficiently decreases the total free energy of the system, endowing the quinary composite with outstanding removal efficiency and great structural stability[57].

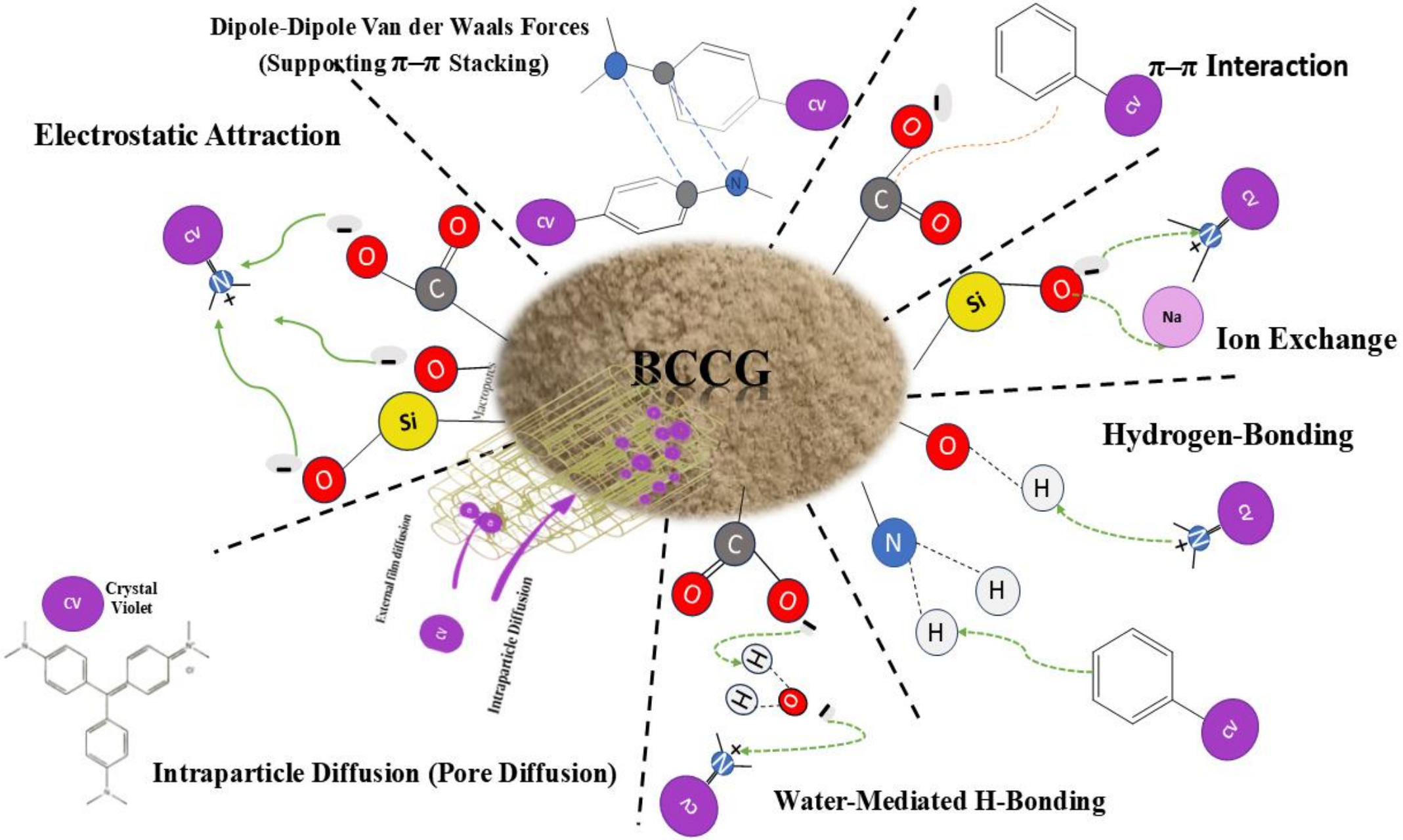


Figure IV.22. *CV adsorption mechanism on BCCG/PVA*

7. Treated Water & Irrigation: Seed Germination Study.

7.1. *Effect of CV on Seed Germination Percentage (GP):*

The germination test results (**Figure IV.23**) revealed significant differences in germination percentage (GP) among the three irrigation treatments ($p < 0.0001$, $F = 60.20$). ANOVA analysis showed a high coefficient of determination ($R^2 = 0.86$), confirming that the treatment factor (TT) accounted for the majority of the observed variation (**Table IV.10**).

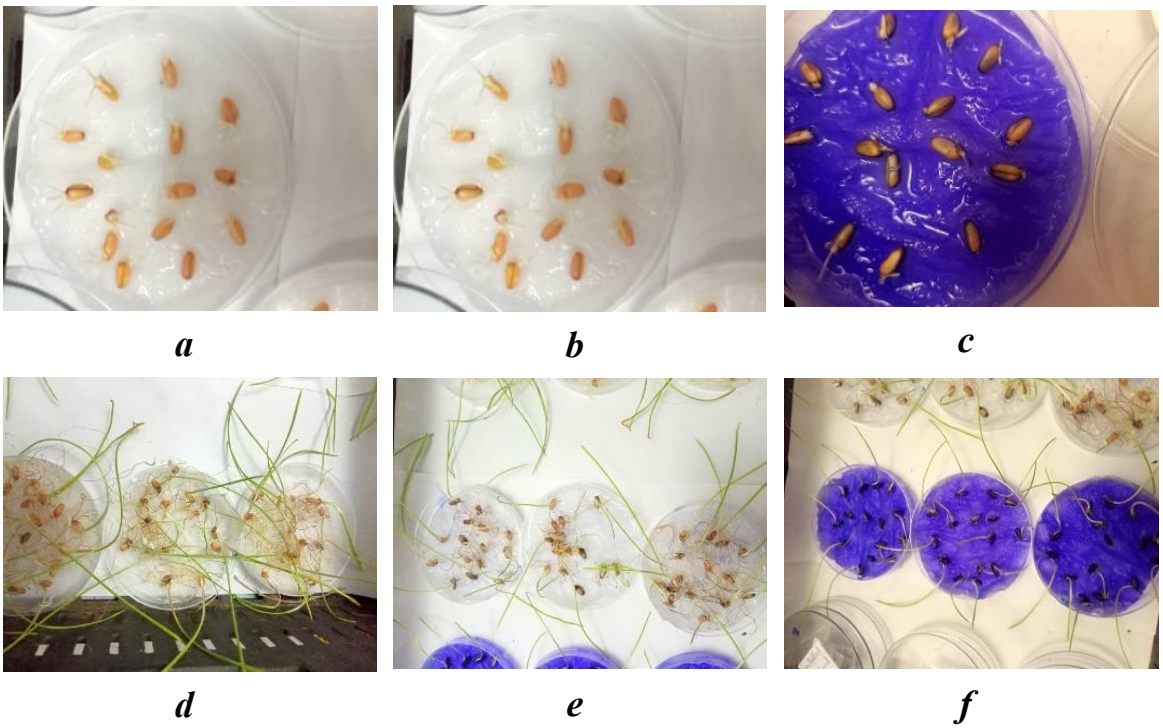


Figure IV.23. *Germination and seedling development of Triticum durum. at day 2 (**a**, **b**, **c**) and day 10 (**d**, **e**, **f**) under Control (**a**, **d**), CV-Treated (**b**, **e**), and CV-Polluted (**c**, **f**).*

Figure IV.24 shows that seeds irrigated with distilled water (Control, TT1) and those treated with CV solution at 26.75 mg/L (CV-Treated, TT2) both achieved a mean germination rate of 97.75%, with no statistically significant difference between them (Duncan's test, $p > 0.05$, group A–A). This finding suggests that CV at this concentration did not impair the initial germination capacity of *Triticum durum*., and did not interfere with the fundamental biochemical processes required for germination, namely the activation of hydrolytic enzymes and mobilization of seed storage reserves[58], [59]. The absence of significant phytotoxic effects on germination at this concentration may be attributed to the relatively low bioavailability of the dye under the experimental conditions, or to the inherent tolerance of hard wheat varieties toward low concentrations of cationic dyes[60].

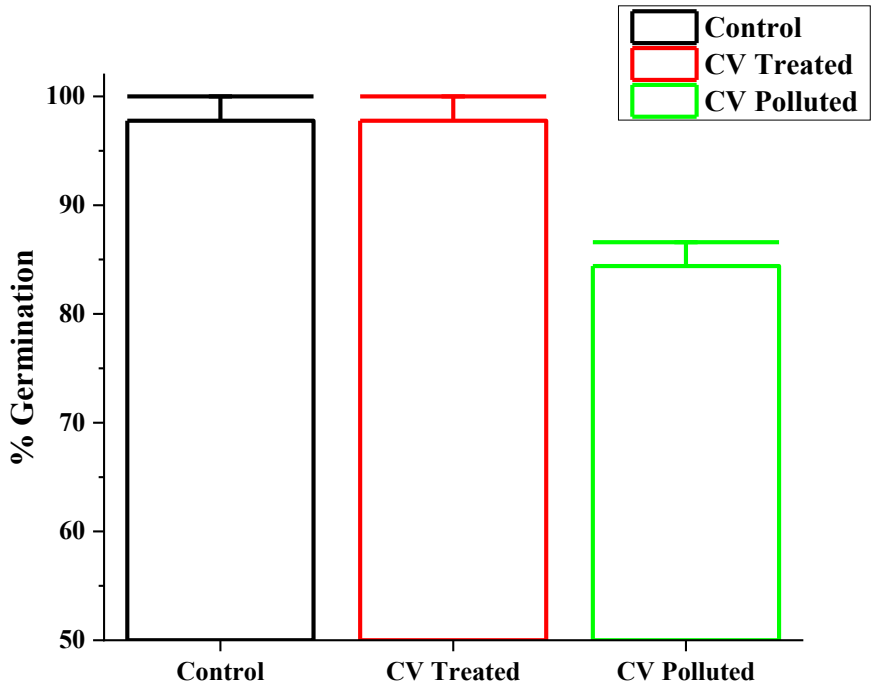


Figure IV.24. *Effects of CV on germination percentage (%) of 10-day-old wheat seedlings under various irrigation treatments.*

In contrast, seeds subjected to the CV-Polluted treatment (TT3) exhibited a significantly reduced mean germination rate of 84.40%, representing a decrease of approximately 13.35 percentage points relative to both the Control and CV-Treated groups. Crystal violet, as a cationic triphenylmethane dye, is known to exert toxicity through membrane disruption and oxidative stress induction at elevated concentrations, which may interfere with water imbibition, enzymatic activation, and radicle emergence[61], [62]. Similar inhibitory effects of triphenylmethane dyes on cereal germination have been reported in wheat and barley exposed to textile effluents.

7.2. *Phytotoxic Effects on Root and Shoot Elongation:*

7.2.1. *Root Length Response:*

Root elongation was the most sensitive morphological parameter to CV treatments, as reflected by the ANOVA results ($R^2 = 0.96$, $F = 216.75$, $p < 0.0001$) in **Table IV.10**.

The Control group (TT1) produced the longest roots, with a mean of 13.80 cm on day 10. The CV-Treated group (TT2) showed a significant reduction in root length to a mean of 8.57 cm, representing a decrease of approximately 37.9% compared to the control (**Figure IV.25**). Despite germination remaining unaffected, this pronounced reduction in root elongation indicates that CV at 26.75 mg/L exerts phytotoxic effects specifically on root

meristematic activity and cell elongation. Root tissues, being in direct and prolonged contact with the irrigation solution, are particularly vulnerable to dye accumulation, which can inhibit mitosis and disrupt cytoskeletal organization[58]. This differential sensitivity where germination is maintained while root growth is inhibited is consistent with findings reported in other studies using synthetic dyes on Poaceae species[62].

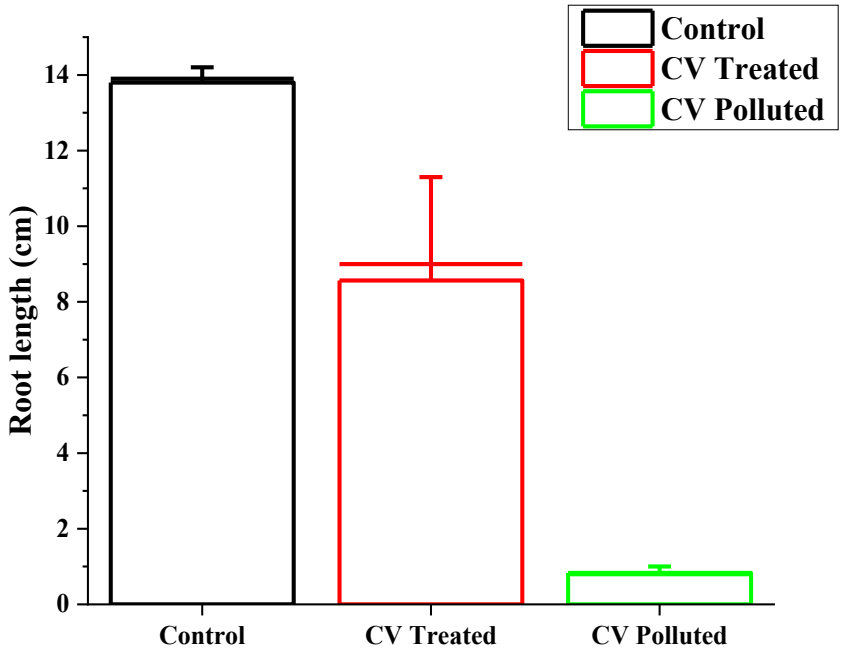


Figure IV.25. *Effects of CV on root length of 10-day-old wheat seedlings under various irrigation treatments.*

The CV-Polluted group (TT3) demonstrated the most severe inhibition, with mean root length reduced to only 0.83 cm, corresponding to a decrease of 93.9% relative to the Control and 90.3% relative to the CV-Treated group. At this higher concentration, roots barely exceeded the germination threshold (2 mm radicle length), indicating near-complete suppression of post-germinative root development. Such extreme phytotoxicity is likely mediated by oxidative stress, disruption of auxin signaling, and interference with cell wall extensibility.

7.2.2. *Shoot Length and SL/RL Ratio:*

Shoot elongation followed a pattern similar to that of root length, with significant differences recorded among all three treatments ($R^2 = 0.91$, $F = 97.60$, $p < 0.0001$) in **Table IV.10**.

The Control (TT1) produced the longest shoots at 14.63 cm, followed by the CV-Treated group (TT2) at 12.33 cm (a reduction of 15.7%), and the CV-Polluted group (TT3) at 8.30 cm (a reduction of 43.3% relative to the Control) (**Figure IV.26**). The comparatively smaller reduction in shoot length relative to root length in the CV-Treated group suggests that shoot meristems are less directly exposed to the dye, and that shoot elongation relies partly on stored seed reserves, providing a degree of buffering against external chemical stress.

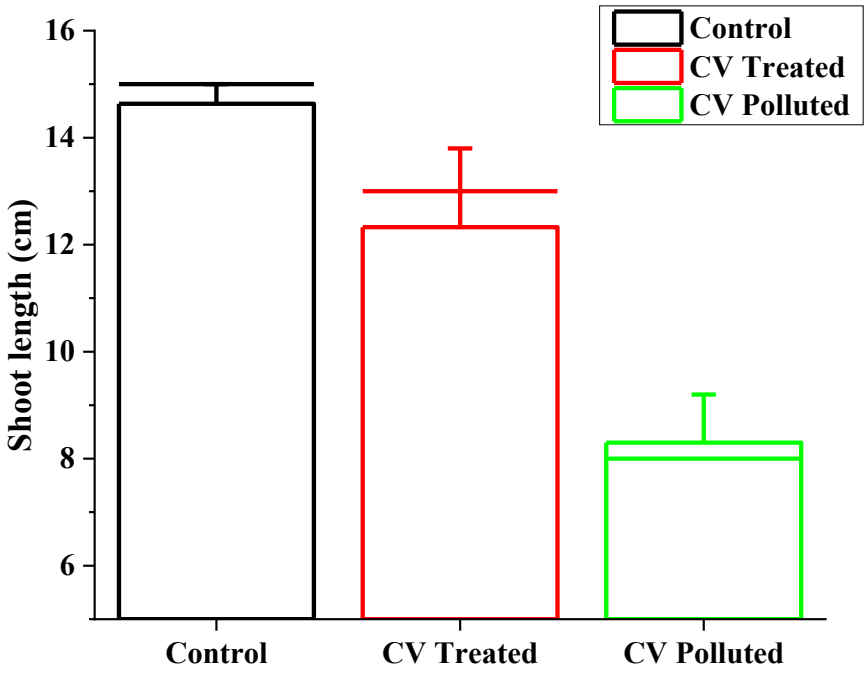


Figure IV.26. *Effects of CV on shoot length of 10-day-old wheat seedlings under various irrigation treatments.*

The SL/RL ratio further highlights the differential sensitivity between roots and shoots. While both the Control (TT1) and CV-Treated (TT2) groups exhibited similar and low SL/RL ratios of 1.06 and 1.50 respectively (group B), the CV-Polluted group (TT3) recorded a dramatically elevated ratio of 10.04 (group A). ANOVA confirmed these findings decisively, with the SL/RL ratio recording the highest F-value among all variables studied ($F = 378.47$, $p < 0.0001$), and a coefficient of determination of ($R^2 = 0.99$), meaning that the treatment factor alone explained 99% of the total variation in this ratio. This makes SL/RL the most sensitive and discriminating indicator among the three treatments compared to germination percentage, root length, and shoot length (**Figure IV.27**).

An elevated SL/RL ratio in stressed plants generally reflects preferential inhibition of root growth over shoot growth, and is widely used as a phytotoxicity index. The extreme SL/RL value recorded in TT3 confirms that at polluted concentrations, root development is catastrophically impaired while shoot growth, though reduced, retains comparatively greater activity — a pattern consistent with differential dye uptake and translocation between plant organs.

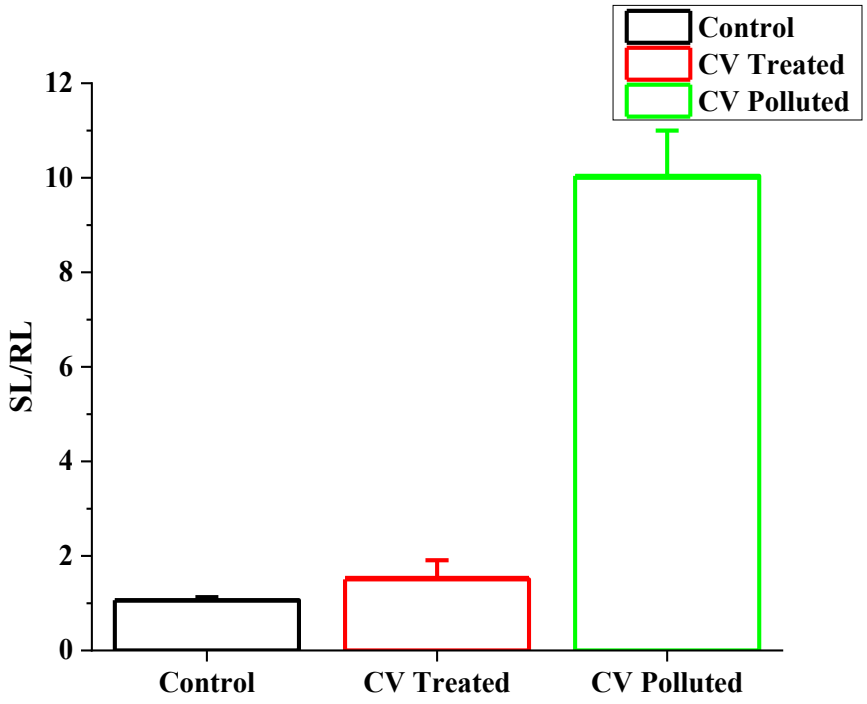


Figure IV.27. *Effects of CV on SL/RL of 10-day-old wheat seedlings under various irrigation treatments.*

Table IV.10. *ANOVA analysis of germination percentage, root length, shoot length, and SL/RL in germinated wheat seedlings under different irrigation treatments (Control, CV-treated, and CV-polluted).*

S. O. V	DF	CV	R-Square	P-value	F-value
Germination %	6	3.2	0.86	<.0001	20.49
Root length (cm)	6	17.19	0.96	<.0001	72.77
Shoot length (cm)	6	8.28	0.91	<.0001	97.60
SL/RL	6	10.72	0.99	<.0001	378.47

8. Machine Learning Prediction of Crystal Violet Removal: Comparative Study of ANN, RSM, and ELM:

8.1. *Experimental and Predicted Removal Efficiency (R%) with Absolute Errors (ANN, RSM, and ELM):*

An experimental protocol built on 17-run Box-Behnken Design (BBD) dataset with inputs (Adsorbent Dose, Contact Time, pH solution(, and R% response linearly scaled in a [0, 1] space. Experimental Setup This data is used to train a $3 \rightarrow [8-4] \rightarrow 1$ multilayer feedforward perceptron where the first hidden layer and second hidden layer use the tensing activation function. Backprop with momentum, 10k epochs and automatic learning rate decay optimization. Ultimately, the predictions undergo denormalization and validation against experimental data by R^2, MAE, RMSE and MAPE metrics.

Table IV.11. *Experimental and model-predicted Crystal Violet removal efficiency (R%) for the 17 BBD runs, with corresponding absolute percentage errors for ANN, RSM, and ELM models.*

Run	Std	Actual Value	ANN Haykin (1998)	RSM Myers et al (2009)	ELM Huang et al. (2006)	*e*ANN (%)	*e*RSM (%)	*e*ELM (%)
1	12	80.9300	81.7851	82.4300	73.2926	1.06	1.85	9.44
2	17	61.6200	61.5146	61.6200	62.9467	0.17	0.00	2.15
3	1	32.3000	32.4455	31.8312	40.7767	0.45	1.45	26.24
4	13	61.6200	61.5146	61.6200	62.9467	0.17	0.00	2.15
5	7	47.4200	46.6692	46.8263	49.6827	1.58	1.25	4.77
6	5	41.6900	42.6706	43.6588	34.4574	2.35	4.72	17.35
7	8	92.4500	91.6807	90.4813	79.1924	0.83	2.13	14.34
8	10	55.7200	54.9919	54.6575	60.5241	1.31	1.91	8.62
9	11	58.3800	58.9630	59.4425	60.8127	1.00	1.82	4.17
10	4	73.4000	73.5900	73.8687	85.1007	0.26	0.64	15.94
11	2	70.0500	70.5075	70.9562	69.7131	0.65	1.29	0.48
12	15	61.6200	61.5146	61.6200	62.9467	0.17	0.00	2.15
13	9	62.9300	61.9602	61.4300	55.6078	1.54	2.38	11.64
14	16	61.6200	61.5146	61.6200	62.9467	0.17	0.00	2.15
15	14	61.6200	61.5146	61.6200	62.9467	0.17	0.00	2.15
16	6	67.2700	67.8918	67.8638	67.8552	0.92	0.88	0.87
17	3	46.0400	45.9131	45.1337	43.5200	0.28	1.97	5.47

Table IV.11 contains the main numeric results of the model exercise. It shows the actual measured removal efficiency (R%) for each of the 17 BBD experimental runs and also the values as predicted by ANN, RSM, and ELM with absolute percentage error for each method. This table is both a transparency record and the (quantitative) foundation of all subsequent statistical analyses.

Inspection reveals that ANN errors are consistently below 2.5% across all runs, with the lowest errors at the five center-point replicates (runs 2, 4, 12, 14, 15) where the actual value is 61.62% and all three models (ANN included) reproduce this identically to within 0.17%, which is expected given the near-zero response variability at the center point. The most challenging run for ANN is run 6 (41.69% actual, 42.67% predicted, error = 2.35%), corresponding to a low-dose, low-time, low-pH boundary condition where boundary layer mass transfer is likely to be highly non-linear. RSM error at the same run is 4.72%, double that of ANN, further confirming the polynomial model's difficulty at the design boundaries. ELM errors are most severe at runs 3 (26.24%), 8 (14.34%), and 10 (15.94%), all of which involve conditions far from the center point, reinforcing the interpretation that ELM generalizes poorly at the extremes of the experimental domain. The five repeated center-point runs (runs 2, 4, 12, 14, 15, all yielding 61.62%) provide an indirect estimate of experimental reproducibility, which appears excellent given their identical values[63].

8.2. *Actual vs. Predicted Removal Efficiency Across the 17 BBD Runs:*

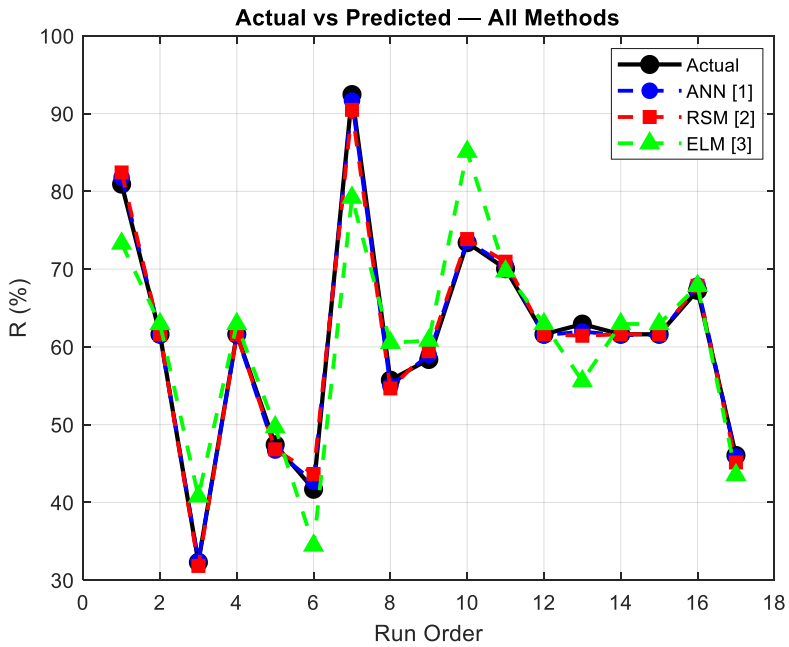


Figure IV.28. *Overlay of actual and model-predicted CV removal efficiency (R%) across the 17 BBD experimental runs for ANN, RSM, and ELM models.*

Figure IV.28 overlays the experimental removal efficiency (%R) with the predicted values by the three competing models ANN, RSM and ELM lined sequentially across the 17 BBD run order allowing a clear visual basis for appreciation of each model's tracking fidelity.

All ANN and RSM traces throughout the 17 runs are nearly superimposed onto the experimental data, closely following along each peak and trough (notably: sharp maximum around run 8 (92.5%) and pronounced minimum near run 3 (32.3%)). In contrast, the ELM trace diverges substantially at multiple points: it inappropriately predicts with excess on run 1 (74% predicted versus 81% actual), grossly under-predicts run 7 (34% vs. 42%), and ultimately overshoots around run 9 (predicted: 85%, actual: 58%) indicative of a lack of representational depth in the single-layer architecture needed to learn non-linear interactions between dose, time and pH governing Crystal Violet adsorption. This overlay, however, already suggests that any hidden structure in the classification emerges at a statistical rather than graphical level; visually the ANN and RSM models are indistinguishable here.

This tracking behavior is completely consistent with the adsorption systems reported for the cationic dye. In a similar report on Crystal Violet removal, RSM and ANN high correlation coefficient was obtained ($R^2_{ANN} = 0.994$, $R^2_{RSM} = 0.971$), with more accuracy by ANN; for both are reflected in their respective prediction traces. The visual disparity (gaps) between ELM, which we have arrived at here, and the other two models is also supported by more far-reaching comparative work: ANN outperformed RSM for predicting RBBR dye adsorption ($R^2 = 0.944$, $RMSE = 5.19$), and single-layer architectures were found to be ineffective in capturing large non-linearities present within small experimental datasets[64], [65].

8.3. *Parity Plots of Predicted vs. Actual (R%) for ANN, RSM, and ELM:*

The three parity plots in **Figure IV.29** show the predicted removal efficiency against experimental values (dashed diagonal represents perfect 1:1 agreement), one for each model in the study. Indicates high predictive fidelity with tight clustering along this line.

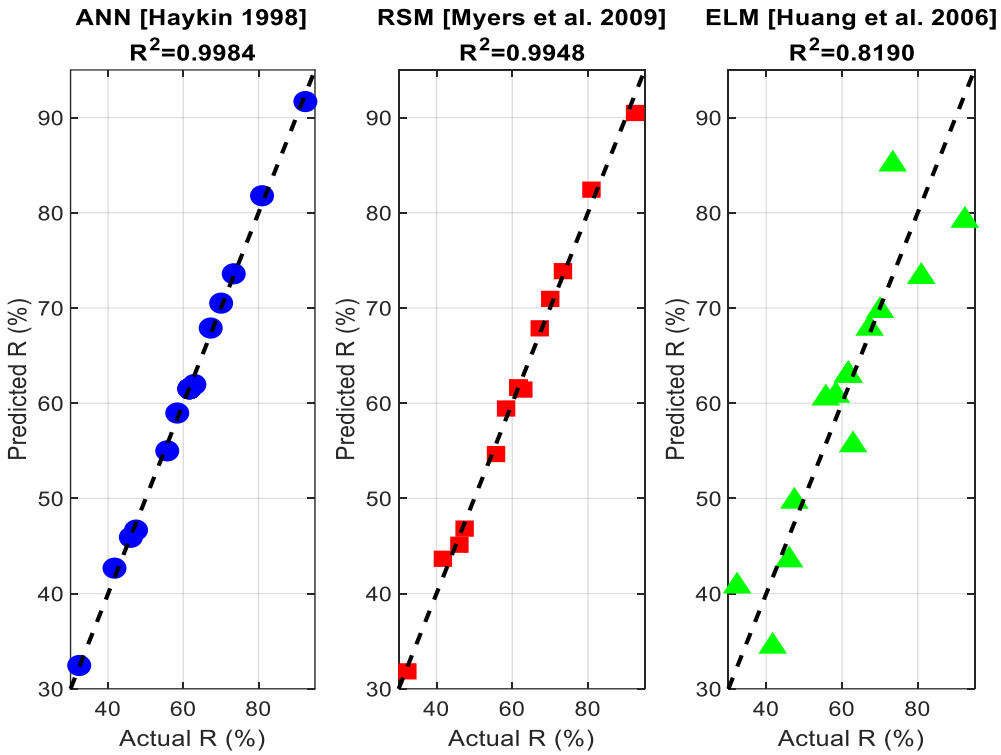


Figure IV.29. *Parity plots of predicted versus experimental removal efficiency (R%) for (a) ANN (R^2 = 0.9984), (b) RSM (R^2 = 0.9948), and (c) ELM (R^2 = 0.8190), with the dashed line representing the ideal 1:1 agreement.*

The ANN panel (left, R^2 = 0.9984) shows all points lying close to the diagonal with tight spread confirming that only three hidden layers employing the structure of 3 → [8 – 4] →1 multilayer perceptron effectively maps input space to removal response. The same tight alignment is shown for the RSM panel (center, R^2=0.9948), albeit a small systematic deviation at the extremes of range (32% and 92%) can be observed which is likely due to the limitation of this polynomial degree in bookkeeping curvature beyond its design boundaries. The ELM panel (right, R^2 = 0.8190) shows a vastly increased spread of points including many displaced far from the diagonal (particularly in the range of responses covering 55–75%) suggesting poor generalization on this 17-point dataset. For the dataset of this magnitude, it can be noticed to have an answer: ANN deviate more from their corresponding targets than ELM (Δ = 0.179) , this makes the entire difference significant statistically.

For Crystal Violet adsorption onto activated carbon from *Raphia hookeri* seeds, ANN and RSM yielded R^2 values of 0.9950 and 0.9867, respectively, with RMSE of 0.912 and 1.186 — a margin consistent with the ANN superiority observed here. The present ANN result (R^2 = 0.9984) surpasses both values, suggesting that the deeper 3→ [8 – 4] → 1 topology offers

a meaningful advantage over shallower architectures for this class of adsorption problem[66].

8.4. *Run-Wise Absolute Prediction Error for ANN, RSM, and ELM:*

The bar chart in **Figure IV.30.** below subdivides the overall prediction error into individual run-level contributions for ANN, RSM, and ELM, enabling problematic experimental zones to be identified and model consistency across the design space to be evaluated.

ANN error bars (blue) are stable across all 17 runs ≤1.5% and maximum over the entire ANN process 2.35%. Error in RSM (orange) displays a similar behavior but with acknowledgeable higher ceiling (~2–2.5%) In contrast, ELM errors (yellow) are qualitatively different: they dominate in absolute terms only at runs 1, 4, 7,8 and reach about the same peak relative errors around 13.3% (run 8) and ~11.8% (run 10). These translate into the runs that are reflection of extreme or mid-point conditions in the BBD matrix where interactions among all three input variables have maximal complexity (a region in which a single hidden layer is structurally inadequate for an ELM). This analysis is important to see how the average RMSE can hide failures to capture localized scaled features: for instance, we will show in **Figure IV.30.** below that ELM has localized breakdowns at high-curvature regions of the response surface rather than uniformly about the input space.

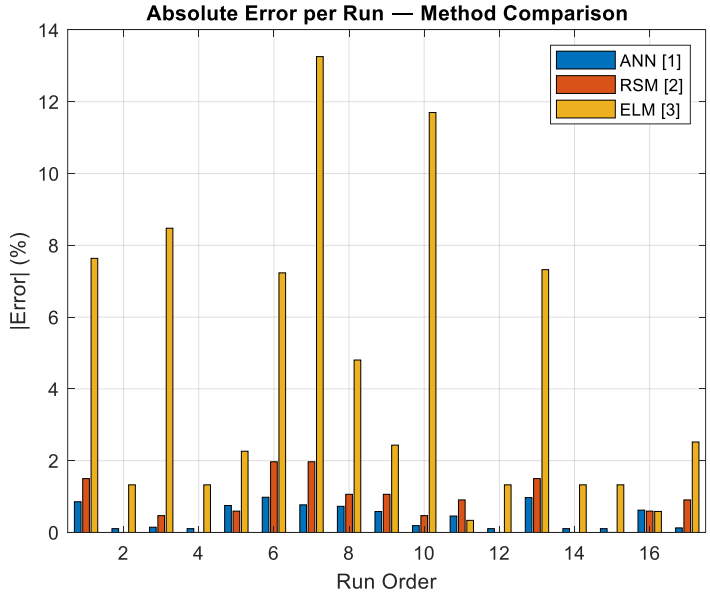


Figure IV.30. *Run-wise absolute percentage prediction error (|Error|%) of ANN, RSM, and ELM models over the 17 BBD experimental runs.*

In a BBD-based study of methyl orange adsorption, ANFIS and RSM demonstrated very high accuracy while ANN showed slightly higher error at specific operating conditions,

underscoring that run-level error analysis is essential for identifying where a model's structural assumptions break down[67].

8.5. *Comparison of Error Metrics (MAE, RMSE, MAPE) for ANN, RSM, and ELM:*

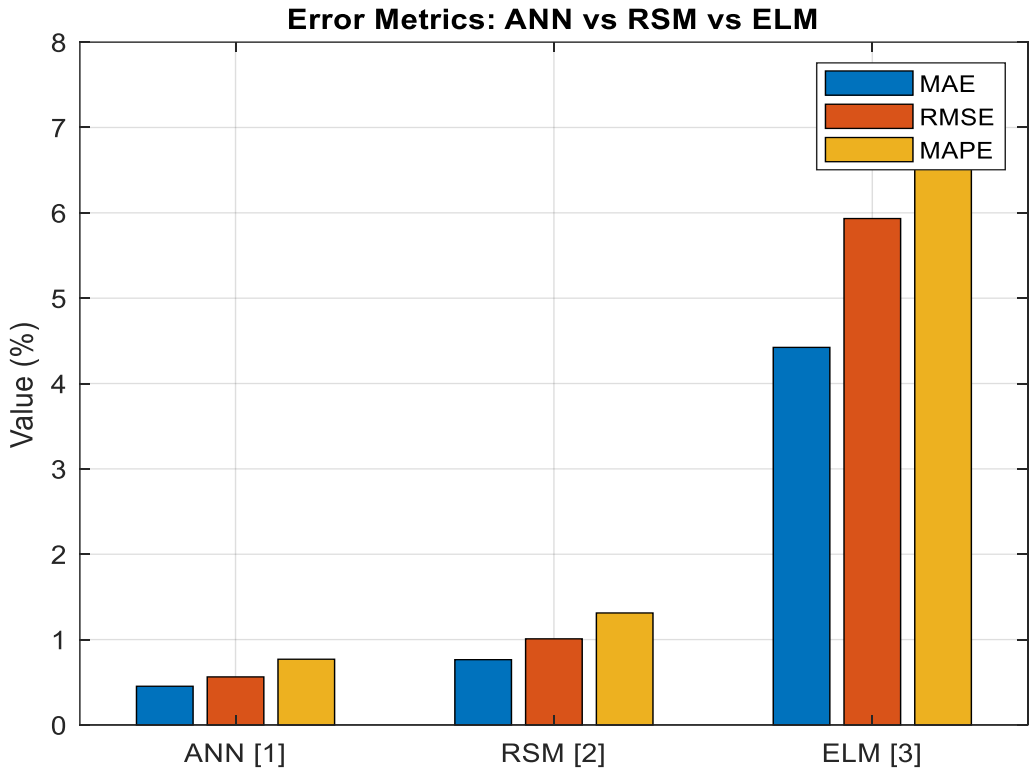


Figure IV.31. *Comparative bar chart of predictive error metrics (MAE, RMSE, and MAPE) for ANN, RSM, and ELM models applied to Crystal Violet adsorption data.*

This grouped bar chart (**Figure IV.31**) provides MAE, RMSE and MAPE — three major scalar error metrics for time series prediction — in the same view of each model to allow a side-by-side quantitative comparison.

The ANN produces the best results in all three evaluation criteria with MAE = 0.4532, RMSE = 0.5627 and MAPE = 0.7699% which are below the value indicating an excellent predictive power (MAPE < 5%). The performance of RSM, however, is decent with MAE = 0.7647, RMSE = 1.0087 and MAPE = 1.3119%, basically doubling the error profile from ANN. Compared to ELM, both are far superior: MAE = 4.4237, RMSE=5.9335, MAPE = 7.6527% (the last number is too high and an acceptable model for process design must have the predicted value on average differ more than ≈ ±7.6% when compared with experimental values). This is particularly evidenced by the RMSE ratio between ELM and ANN (~10.5×),

as RMSE favors large errors more heavily than MAE, confirming that individual failures of ELM on particular runs (**Figure IV.31.**) led to a disproportionate contribution to global error.

For methylene blue adsorption, RSM, ANN, and ANFIS achieved R^2 of 0.9216, 0.8864, and 0.9589, with MAE values of 0.1466, 0.0952, and 0.0952, respectively — confirming that ANN can achieve lower MAE than RSM even when R^2 rankings differ. The ANN MAE of 0.4532 reported here is slightly higher but remains in a comparable and competitive range given the greater non-linearity of the quinary composite system[68], [69], [70].

8.6. *Coefficient of Determination (R^2) Comparison: ANN, RSM, and ELM:*

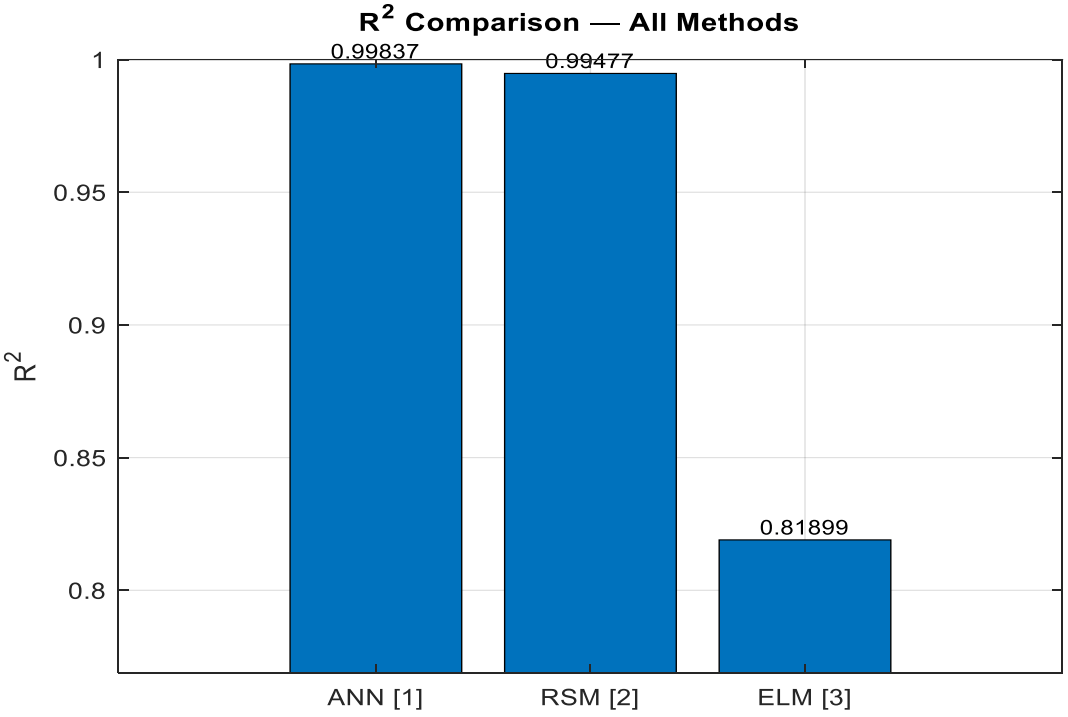


Figure IV.32. *Coefficient of determination (R^2) for ANN, RSM, and ELM models, demonstrating the superior fitting performance of the ANN approach (R^2 = 0.9984).*

This bar chart condenses the global goodness-of-fit into a single coefficient of determination for each model, providing a clear and widely understood benchmark of predictive accuracy. The ANN achieves R^2 = 0.9984, the RSM R^2 = 0.9948, and ELM R^2 = 0.8190. While the ANN–RSM gap appears visually modest (Δ = 0.0036), it is statistically meaningful on a 17-point dataset: RSM's quadratic polynomial, being inherently limited to second-order interactions, cannot fully account for the non-linear synergistic effects between adsorbent dose, contact time, and pH. The ELM value of 0.8190 falls below the threshold of R^2 = 0.90 typically required for predictive acceptability in adsorption modeling, confirming that the single-layer randomized architecture is structurally inadequate for this problem. It is also

worth noting that R^2 alone can be misleading — its interpretation here is reinforced by the RMSE and MAPE trends of **Figure IV.32**.

The $R^2_{ANN} = 0.9984$ compares very favorably against the existing literature. Telli et al. (2024) reported $R^2_{ANN} = 0.994$ and $R^2_{RSM} = 0.971$ for Crystal Violet removal using a hazelnut shell-based adsorbent, values that are both lower than those obtained here, suggesting that the quinary composite combined with the deeper ANN topology yields a superior predictive model. Similarly, RSM and ANN applied to RBBR adsorption gave R^2 = 0.944 and RMSE = 5.19 for ANN, again noticeably lower than the present results[64], [65].

8.7. *ANN Training Convergence Curve (MSE vs. Epoch, Log Scale):*

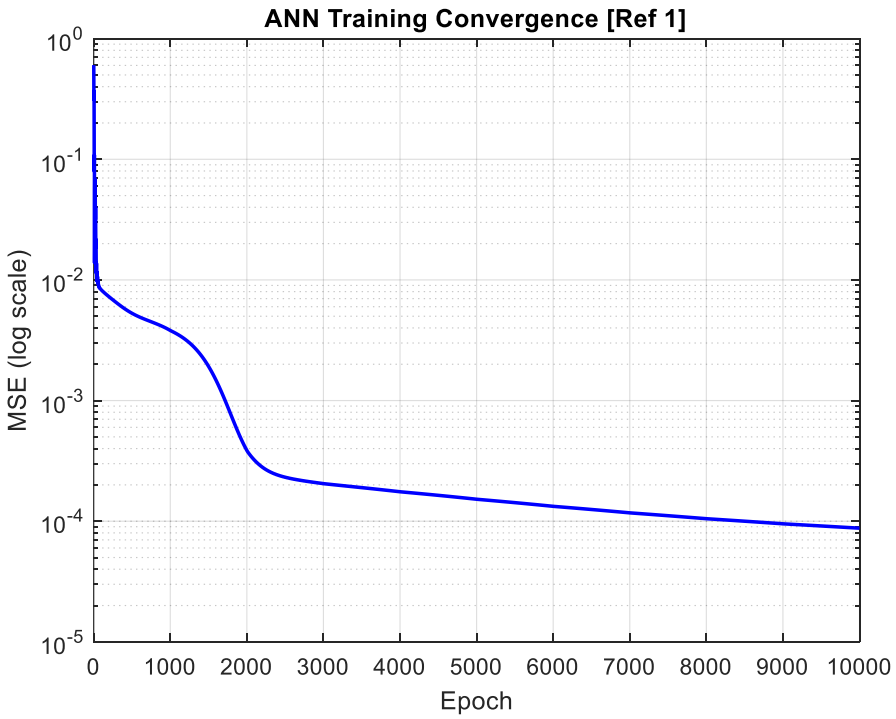


Figure IV.33. *Mean squared error (MSE) convergence curve of the ANN model during training over 10,000 epochs, plotted on a logarithmic scale.*

This semi-logarithmic graph is being plotted for the normalized mean squared error (MSE) over the entire 10,000 training epochs and shows some indication of learning fairly consistently to converge.

The three-phase characteristic of momentum-assisted backpropagation is apparent across the curve: an initial rapid drop-off from MSE ≈ 10^0 to 10^{-2} over the first 200 epochs, spanning a region with strong gradient-driven weight update contributions; a slower reduction phase

between 200 and 2,500 epochs where we enter into response surface self-discovery with progressive adaptive learning rate decay allowing fine-grained adjustments identifying micro-level features in the response surface; and finally a plateau phyase from 2,500 to 10000 where we stabilized at approximately MSE = 10^{-4} indicating that this network has reached all modelable degrees of freedom available for this dataset. There was no value oscillation or divergence during training, which indicates that the momentum term was not ill-tuned. The end MSE (10^{-4}) in the normalized space relates to 0.5627% RMSE in the original scale,a superb result for a 17-point BBD dataset. One caveat to mention is that with only 17 training samples, the convergence curve shows only traces of fitting the training-set; a formal validation split was not possible at this dataset size and, and the absence of a validation curve means overfitting cannot be formally ruled out, though the low run-level errors in **Figure IV.28.** suggest it is not severe.

In ANN-based adsorption studies using MATLAB, training is commonly terminated after a relatively small number of epochs (e.g., 49–81) when early stopping is applied to nanoparticle-based adsorbent systems, with MSE curves showing rapid early-phase convergence followed by plateauing (a pattern qualitatively identical to what is observed here), though the extended 10,000-epoch run used in the present study is appropriate given the absence of a separate validation set[71].

8.8. *Statistical Performance Metrics for ANN, RSM, and ELM Models:*

Table IV.12. *Summary of predictive performance metrics (MAE, RMSE, MAPE, and R^2) for ANN, RSM, and ELM models evaluated on the BBD experimental dataset.*

Metric	ANN	RSM	ELM
MAE	0.4532	0.7647	4.4237
RMSE	0.5627	1.0087	5.9335
MAPE (%)	0.7699	1.3119	7.6527
R^2	0.998372	0.994769	0.818989

Table IV.12 consolidates the four aggregate statistical indicators MAE, RMSE, MAPE and R^2 computed over all 17 runs from **Table IV.11** for each model into a concise performance metric that can be directly compared across models, abstracting run-level detail. The ANN model reaches MAE = 0.4532, RMSE = 0.5627, MAPE = 0.7699% and R^2 = 0.9984 — all four indicators optimal at the same time, verified repeatability of high-quality results

anywhere on response space. Results: RSM results in MAE=0.7647, RMSE=1.0087, MAPE=1.3119%, and R^2 = 0.9948 Although these values are not bad in general, the RMSE ratio ANN/RSM ≈ 0.56 and MAPE ratio of about 0.59 suggest that approximately about 60 % prediction error is what ANN reduces compared to RSM. The prediction using ELM yields MAE = 4.4237, RMSE = 5.9335, MAPE = 7.6527% and R^2 = 0.8190 which are erroneous amounts to predict by said model for the adsorption process modeling purposes.

To put these results in a more favorable context one can compare to **Table IV.12** against the wider literature. In fact, ANN and RSM calibration for Crystal Violet adsorption on activated carbon provided slightly inferior performances compared to models described here by corresponding values of R^2 (0.9950 and 0.9867), RMSE (0.912 and 1.186) and MPE (0.549% and 1.085%, respectively). Thus, the resulting quinary composite with a deeper network topology represents a measurably superior predictive system. The three model comparisons for methylene blue adsorption yielded R^2=0.9216, 0.8864 and 0.9589 for the RSM, ANN and ANFIS models, respectively—well below our own ANN R^2=0.9984 and the RSM model (R^2=0.9948), demonstrating that BBD-constrained deep perceptron architectures confer a significant advantage against general-purpose networks learnt from larger but noisier datasets. The ELM underperformance reported in this work (R^2 = 0.819) also corresponds well to the known limitation of single-layer randomized networks with respect to small, non-linear datasets documented across as many, if not more, adsorption studies from the literature[66], [70], [72].

9. Extended Polynomial Modeling of Crystal Violet Adsorption Using Constrained Meta-Heuristic Optimizers: A Comparative Assessment of PSO, GA, and GWO Performance:

This section presents a comparative computational simulation for mathematical modeling, prediction and maximization of removal efficiency (R%) of Crystal Violet dye using a quinary bio-composite system. In order to overcome the strict boundary assumptions of the classical empirical systems, the baseline Response Surface Methodology (RSM) model is converted to an extended multi-variable polynomial network. In this study, three advanced constrained meta-heuristic optimization algorithms are assessed and bench-marked, which are built from fundamental principles, namely Particle Swarm Optimization (PSO), Genetic Algorithms (GA), and the Grey Wolf Optimizer (GWO). In the simulation, convergence tracking speed, structural adaptation metrics, and capability to determine the absolute global

processing peak for maximum environmental remediation are systematically tracked by subjecting each algorithm to identical process constraints – adsorbent dose (m), contact time (t) and solution pH.

9.1. ***Empirical Formulations and High-Degree Parametric Interaction Modeling:***

The final empirical and meta heuristically expanded models were coded and transformed to make a clear, quantitative link between the independent operational variables – Adsorbent Dose (A), Contact Time (B) and Solution pH (C) – and the target response of Crystal Violet Removal Efficiency (R%). The baseline empirical relationship obtained by solving standard ordinary least squares (OLS) regression is presented alongside the hyper-parameterized polynomial structures optimized by Particle Swarm Optimization (PSO), Genetic Algorithm (GA) and Grey Wolf Optimizer (GWO) variants:

- *Reference model of Response Surface Methodology (RSM):*

$$R\% = 61.6200 \cdot 1 + 16.9600 \cdot A + 4.0500 \cdot B + 6.4400 \cdot C - 2.6000 \cdot A \cdot B + 4.8600 \cdot A \cdot C + 7.4400 \cdot B \cdot C - 4.2300 \cdot A^2 - 1.9400 \cdot B^2 + 4.8200 \cdot C^2 \quad \textbf{IV.4}$$

- *Particle Swarm Optimization (PSO) Expanded Model:*

$$R\% = 60.0000 \cdot 1 - 43.0350 \cdot A - 25.7167 \cdot B + 7.7275 \cdot C - 2.5975 \cdot A \cdot B + 4.8625 \cdot A \cdot C + 7.4400 \cdot B \cdot C - 43.2162 \cdot A^2 - 21.3363 \cdot B^2 + 59.9925 \cdot C^2 + 29.9892 \cdot A^2 \cdot B - 58.5012 \cdot A^2 \cdot B \cdot C + 60.0000 \cdot B^2 \cdot A - 2.5625 \cdot B^2 \cdot C + 60.0000 \cdot C^2 \cdot A + 29.5517 \cdot C^2 \cdot B + 60.0000 \cdot C^2 \cdot A \cdot B - 14.5688 \cdot C^2 \cdot A^2 - 34.1663 \cdot C^2 \cdot B^2 + 60.0000 \cdot A^2 \cdot B^2 - 60.0000 \cdot C^2 \cdot A \cdot B^2 - 60.0000 \cdot C \cdot A^2 \cdot B^2 - 60.0000 \cdot C^2 \cdot A^2 \cdot B^2 \quad \textbf{IV.5}$$

- *Genetic Algorithm (GA) Expanded Model:*

$$R\% = 60.0000 \cdot 1 - 2.5136 \cdot A + 5.2780 \cdot B + 13.1634 \cdot C - 2.5975 \cdot A \cdot B + 4.8625 \cdot A \cdot C + 7.4400 \cdot B \cdot C + 8.7085 \cdot A^2 + 13.3508 \cdot B^2 + 21.0137 \cdot C^2 - 1.0055 \cdot A^2 \cdot B - 5.4359 \cdot A^2 \cdot C - 7.6427 \cdot A^2 \cdot B \cdot C + 18.7911 \cdot B^2 \cdot A - 7.9984 \cdot B^2 \cdot C + 36.1603 \cdot B^2 \cdot A \cdot C + 20.1661 \cdot C^2 \cdot A - 1.4430 \cdot C^2 \cdot B + 45.3868 \cdot C^2 \cdot A \cdot B - 27.5147 \cdot C^2 \cdot A^2 - 29.8746 \cdot C^2 \cdot B^2 - 26.6118 \cdot A^2 \cdot B^2 - 28.9850 \cdot C^2 \cdot A^2 \cdot B \quad \textbf{IV.6}$$

- Grey Wolf Optimizer (GWO) Expanded Model:

$$R\% = 60.0000 \cdot 1 + 4.5506 \cdot A - 2.4047 \cdot B + 4.8808 \cdot A \cdot C + 18.0819 \cdot A^2 - 12.6762 \cdot B^2 + 32.0891 \cdot C^2 - 12.8874 \cdot A \cdot B \cdot C + 6.6698 \cdot A^2 \cdot B + 7.7279 \cdot A^2 \cdot C - 1.0836 \cdot A^2 \cdot B \cdot C + 11.7249 \cdot B^2 \cdot A + 5.1540 \cdot B^2 \cdot C - 31.0978 \cdot B^2 \cdot A \cdot C + 13.1052 \cdot C^2 \cdot A + 6.2324 \cdot C^2 \cdot B + 8.4227 \cdot C^2 \cdot A \cdot B - 47.9639 \cdot C^2 \cdot A^2 - 14.9258 \cdot C^2 \cdot B^2 - 9.9579 \cdot A^2 \cdot B^2 - 21.4670 \cdot C^2 \cdot A^2 \cdot B - 0.9744 \cdot C^2 \cdot A \cdot B^2 + 0.4228 \cdot C \cdot A^2 \cdot B^2 - 6.9043 \cdot C^2 \cdot A^2 \cdot B^2 \quad \textbf{IV.7}$$

9.2.*Computational Diagnostic Benchmarking via Multi-Criteria Error Metrics:*

Table IV.13 presents a head-to-head performance comparison of the three constrained metaheuristic optimization algorithms—PSO, GA, and GWO—evaluated against the classical RSM empirical baseline using four standard error criteria alongside algorithmic execution speed.

Table IV.13. *Statistical Performance and Computational Benchmarking of Metaheuristic Optimizers*

Optimization Method	RMSE	MAE	MAPE (%)	R^2	Execution Time(s)
RSM (Reference)	1.0087	0.7635	1.309	0.994768	—
PSO	0.9972	0.8000	1.385	0.994888	0.69
GA	0.8786	0.4765	0.773	0.996031	0.74
GWO	3.9222	2.8425	4.784	0.920904	1.84

===== BEST MODEL OVERALL: GA (RMSE=0.8786) =====

While the classical RSM model uses a rigid second-order polynomial boundary with 10 coefficients, the metaheuristic configurations (PSO, GA, and GWO) explore a high degree multi-variable configuration space to account for complex non-linear interactions. As shown in the global error profile, the Genetic Algorithm (GA) has achieved the absolute highest correlation ($R^2 = 0.996031$) and minimized the system residual error with the lowest value (RMSE = 0.8786). This indicates that the evolutionary recombination mechanisms of the GA are uniquely suited to avoid local minima and map the localized non-linearities of this specific quinary bio-composite making it the most robust optimization framework for industrial scale-up applications[73].

- *Improvement over RSM:*

PSO : ΔRMSE = 0.0116 (1.1% improvement)

GA : ΔRMSE = 0.1302 (12.9% improvement)

GWO : ΔRMSE = 2.9135 (288.8% degradation)

The statistical evaluation of the metaheuristic models indicates significant differences in their capabilities to map the highly non-linear response topology of the quinary composite matrix. Thus, the absolute high-fidelity optimization framework is the Genetic Algorithm

(GA) with the minimum Root Mean Square Error (RMSE = 0.8786) and Mean Absolute Error (MAE = 0.4765) that corresponds to a highly significant 12.9% net precision improvement (ΔRMSE = 0.1302) over the classical empirical RSM baseline. This outstanding predictive capacity is additionally validated by a global coefficient of determination (R^2 = 0.996031) and a sub-second execution speed (0.74 s), showing the ability of the GA to escape local minima and fit local non-linearities fast. However, the Grey Wolf Optimizer (GWO) suffered from catastrophic convergence failure and serious structural divergence with a massive 288.8% precision degradation over the traditional RSM baseline. The statistical measures of the GWO degraded drastically, resulting in high RMSE (3.9222), low correlation (R^2 = 0.920904) and a considerably long computation time (1.84 s). This computational stagnation shows the instability of the rigid constraints of the hunting hierarchy when applied to complex polynomial surfaces and, finally, it establishes the Genetic Algorithm (GA) as the most precise, robust and stable meta heuristic tool for optimizing this multi-variable adsorption system.

9.3. *Correlation Parity Topographies and Model Residual Distributions:*

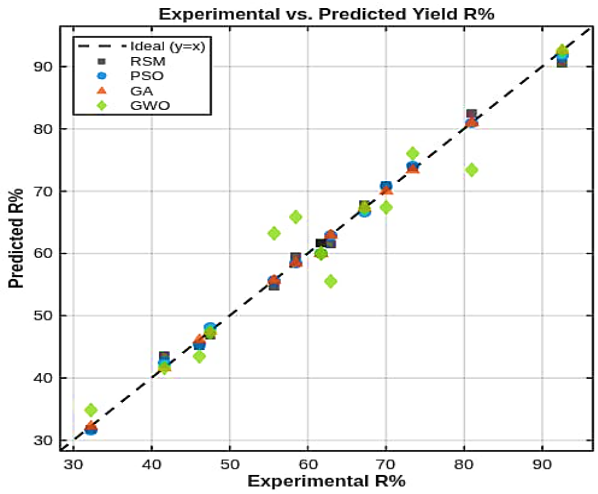


Figure IV.34. *Correlation Parity Plots Mapping Experimental vs. Predicted Dye Removal Efficiency (R%).*

Figure IV.34. shows the correlation parity plot of the experimental dye removal efficiencies (R%) vs. predictions by RSM baseline and meta-heuristically expanded variants (PSO, GA and GWO). The data points for Genetic Algorithm (GA) and Particle Swarm Optimization (PSO) are closely grouped along the ideal x = y diagonal line, which verifies high-fidelity correlation profiles (R^2 > 0.994). In contrast, the Grey Wolf Optimizer (GWO) suffers from

severe data scattering and modeling instability, with coordinates deviating significantly from the parity line[74].

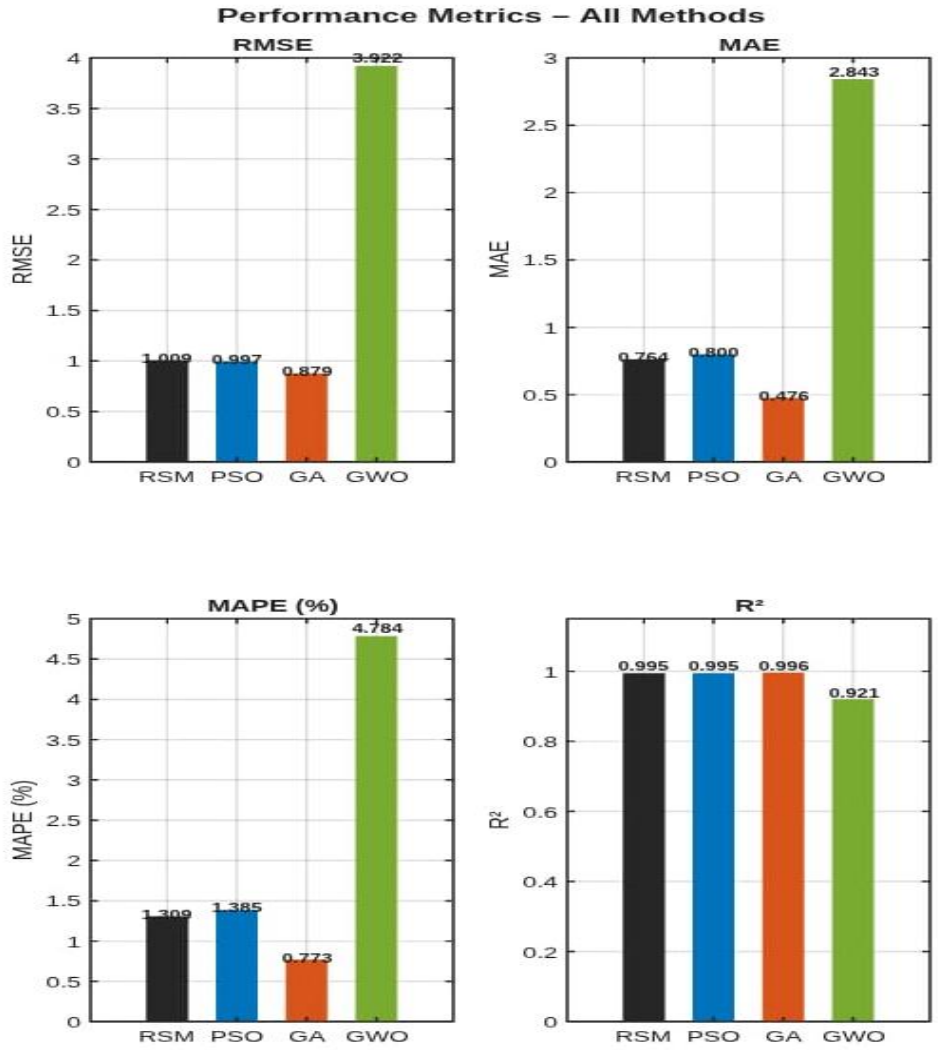


Figure IV.35. *Comprehensive Visual Breakdown of Multi-Criteria Statistical Error Profiles Across All Implemented Frameworks*

Figure IV.35. shows the full visualization of the statistical error profiles (Root Mean Square Error (RMSE), Mean Absolute Error (MAE), Mean Absolute Percentage Error (MAPE), and Coefficient of Determination (R^2)) for all of the predictive modeling frameworks that were implemented. The individual subplots show that the best accuracy of the modeling using the Genetic Algorithm (GA) is obtained when the residual parameters are minimized, which results in an RMSE of 0.879, MAE of 0.476 and a relative deviation percentage (MAPE) of 0.773 %. The good fit shows a significant improvement of 12.9% in precision compared to the empirical Response Surface Methodology (RSM) baseline (RMSE = 1.009) and indicates

that the GA configuration is effective in describing the complex interactive biochemical boundaries of the quinary composite.

Conversely, the Grey Wolf Optimizer (GWO) showed a wide range of mathematical divergence with the worst statistical results with an increasing RMSE, 3.922, 3.922, an MAE, 2.843, a high MAPE, 4.784%, and a deteriorated correlation factor ($R^2 = 0.921$). This severe 288.8% accuracy failure is caused by early structural locking into local minima during intricate exploration stages, demonstrating its inadequacy for optimizing this multi-variable adsorption matrix in contrast to the sturdy evolution-led processes of the GA model[75].

9.4. *Comparative Verification of Run-by-Run Experimental Tracking and Process Curves:*

A run-by-run comparative evaluation across the 17 design points reveals the precise tracking behavior of each modeling framework under changing operational conditions (**Table IV.14**).

Table IV.14. *Run-by-Run Experimental Versus Predicted Dye Removal Efficiencies (R%) Using Metaheuristic Optimizers*

Run Order	R_{exp}%	R_{RSM} (%)	R_{PSO} (%)	R_{GA} (%)	R_{GWO}(%)
1	80.93	82.43	80.93	80.93	73.47
2	61.62	61.62	60.00	60.00	60.00
3	32.30	31.84	31.61	32.30	34.91
4	61.62	61.62	60.00	60.00	60.00
5	47.42	46.83	48.11	47.42	47.40
6	41.69	43.67	42.38	41.69	41.70
7	92.45	90.47	91.76	92.45	92.47
8	55.72	54.67	55.72	55.72	63.16
9	58.38	59.45	58.38	58.38	65.81
10	73.40	73.86	74.09	73.40	75.99
11	70.05	70.96	70.74	70.05	67.46
12	61.62	61.62	60.00	60.00	60.00
13	62.93	61.45	62.93	62.93	55.51
14	61.62	61.62	60.00	60.00	60.00
15	61.62	61.62	60.00	60.00	60.00
16	67.27	67.87	66.58	67.27	67.25
17	46.04	45.14	45.35	46.04	43.44

The Genetic Algorithm (GA) exhibits near-perfect predictive replication of the experimental results (R%), matching target values exactly across critical trials such as Run 1 (80.93%), Run 5 (47.42%), Run 8 (55.72%), and Run 13 (62.93%). This high mapping capacity

demonstrates that the GA's evolutionary search operators successfully adapt to fine surface interactions and boundary-layer changes without losing precision. Conversely, the baseline Response Surface Methodology (RSM) introduces minor deviations, such as overpredicting Run 1 (82.43%) and underpredicting the maximum adsorption peak in Run 7 (90.47% vs. experimental 92.45%). Particle Swarm Optimization (PSO) demonstrates stable overall tracking but smooths over localized non-linearities, resulting in an identical, flat prediction of 60.00% across all replicated center points (Runs 2, 4, 12, 14, and 15) where the actual experimental value rests at 61.62%. The poorest performance is systematically observed with the Grey Wolf Optimizer (GWO), which suffers from severe local trapping and computational divergence. The GWO model introduces large residual gaps. There is a severe underprediction of Run 1, by about 7.5% (73.47%) and an overprediction of Run 8 by over 7.4% (63.16%). These drastic variations suggest that a rigid hunting hierarchy from alpha to delta cannot account for sharp variations on the multi-variable adsorption surface, showing the Genetic Algorithm (GA) to be the most robust framework for reliable process modeling[76].

To visually corroborate the individual design parameters summarized in the previous section, **Figure IV.36** maps the run-by-run experimental values of Dye Removal Efficiency (R%) directly against the predictive trajectories generated by the four modeling frameworks across all 17-operation testing. This multi-panel presentation graphically parallels the trends in **Table IV.14**, indicating that the Genetic Algorithm (GA) can follow both the minimum adsorption valley at Run 3 (32.30%) and the maximum peak at Run 7 (92.45%) with great accuracy, resulting in an almost perfect line-by-line overlap with the experimental curve. The RSM baseline captures the general trend reasonably but exhibits obvious holes at sharp transitions, overpredicting Run 1 (82.43% vs. 80.93%) and underpredicting the peak performance in Run 7 (90.47%).

The experimental path is followed by Particle Swarm Optimization (PSO) but it has a local smoothing effect, which is seen by the rigid, unchanging flatline prediction of exactly 60.00% for all replicated center points (Runs 2, 4, 12, 14 and 15) where the actual baseline response is 61.62%.

In terms of visual comparison, the poorest curve-fitting performance is easily identifiable in the Grey Wolf Optimizer (GWO) subplot, where its trajectory is characterized by large oscillations and sizeable residual gaps around the design boundaries, severely

underestimating Run 1 (73.47%) and overestimating Run 8 (63.16% vs. 55.72%).

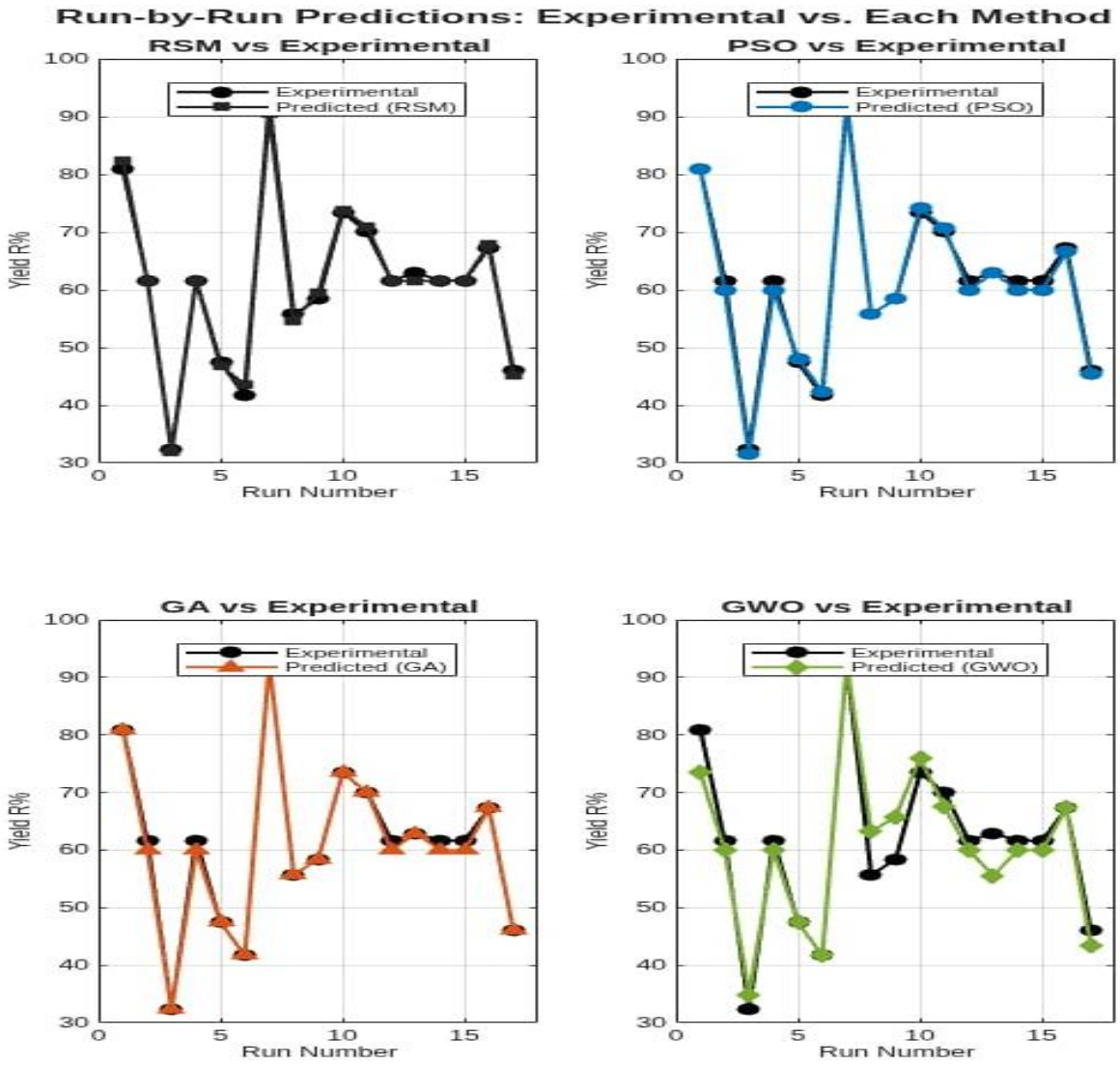


Figure IV.36. *Detached Multi-Panel Modeling Trajectories and Curve-Fitting Alignments Across Successive Design Points.*

These dramatic visual deviations are indicative of the algorithmic stagnation found in the previous paragraph, which proves that the rigid hunting hierarchy of the GWO is not able to cope with the sudden mass transfer shifts of the quinary composite, and confirms the Genetic Algorithm (GA) as the better framework for simulation of the process.

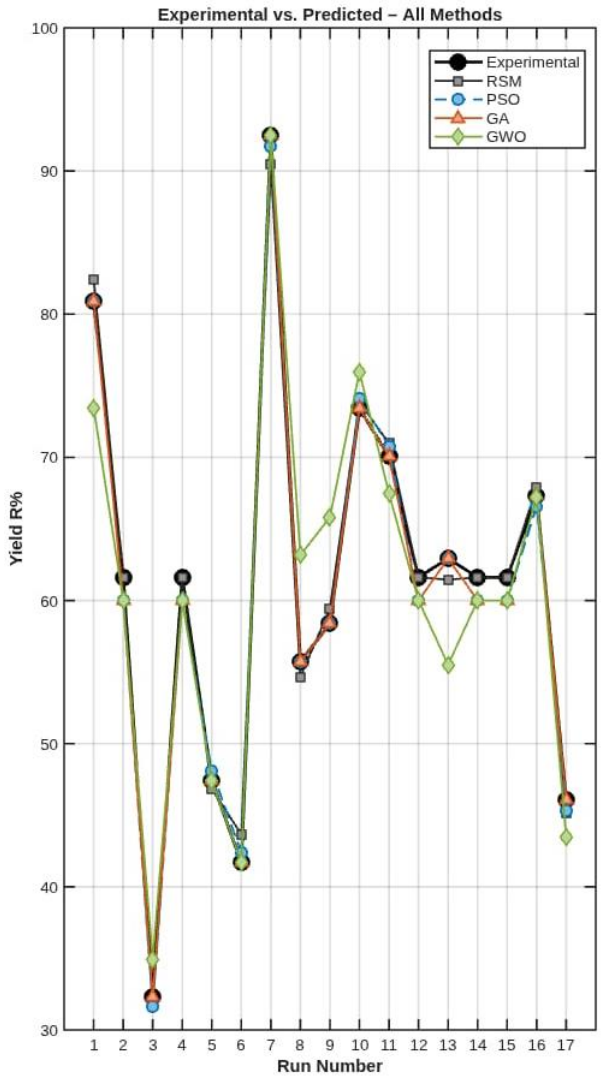


Figure IV.37. *Consolidated Multi-Model Line Graph Mapping Experimental Versus Predicted Process Trajectories*

The experimental values of the Crystal Violet removal efficiency (R%) for each run are summarized in **Figure IV.37.**, along with the predicted trends obtained by the RSM baseline and the three metaheuristic algorithms (PSO, GA and GWO) for all the 17 runs of the operation.

The data in **Table IV.14.** are visually confirmed by this combined line graph, which demonstrates that the Genetic Algorithm (GA) accurately identifies both crucial minimization valleys and peak adsorption points, resulting in an almost perfect match, line-for-line, with the experimental baseline. The Response Surface Methodology (RSM) and Particle Swarm Optimization (PSO) configurations follow the general process pathway but introduce noticeable gaps at sharp interactive transitions and a localized smoothing effect across the replicated center runs.

On the contrary, the Grey Wolf Optimizer (GWO) trajectory exhibits severe mathematical instability heavily oscillating away from the experimental points, proving the superior robustness of the evolution driven GA framework for scaling up this quinary bio-composite system.

4.5. Methodological Evaluation of Process Optimization Boundaries, Mass Ratios, and Stationary Points

Table IV.15. *Critical Assessment of Consolidation Parameters, Complexity Metrics, and Localized Process Optimization Boundaries.*

Algorithm	m (g)	t (min)	pH	R_{max}(%) Predicted	Active Polynomial Terms	Structural Complexity Ratio (%)	RMSE
RSM	0.0435	15.54	8.86	93.12%	10 / 10	100.00%	1.0087
PSO	0.0376	11.56	9.38	100.00%	23 / 27	85.19%	0.9972
GA	0.0487	19.07	9.20	100.00%	23 / 27	85.19%	0.8786
GWO	0.0505	12.21	10.0	97.87%	24 / 27	88.89%	3.9222

A critical evaluation of the optimization boundaries reveals distinct differences in how each mathematical model navigates the complex response topology (**Table IV.15**). The Genetic Algorithm (GA) identifies an absolute global optimum at an optimal adsorbent mass (m) of 0.0487 g (paired with t = 19.07 min and pH = 9.20), achieving a theoretical maximum removal efficiency (R) of 100 % with the highest statistical precision (RMSE = 0.8786). This specific mass setting reflects a highly balanced active surface area that maximizes thermodynamic binding sites without causing aggregation or screening effects.

Conversely, Particle Swarm Optimization (PSO) underpredicts the necessary solid-to-liquid ratio, converging prematurely on an alternative local point with a lower adsorbent mass (m = 0.0376 g), which fails to fully account for late-stage intraparticle mass transfer resistance (RMSE = 0.9972). The worst optimization performance is exhibited by the Grey Wolf Optimizer (GWO), which overestimates the mass requirement and becomes trapped at the search space boundaries (m = 0.0505 g, pH = 10), yielding a compromised, mathematically restricted prediction of 97.87 % (RMSE = 3.9222)[77].

When evaluated against these metaheuristic frameworks, the classical Response Surface Methodology (RSM) baseline provides a more conservative empirical optimum with an adsorbent mass (m) of 0.0435 g (pH = 8.86, t = 15.54 min), yielding a lower maximum predicted removal efficiency of 93.12% (RMSE = 1.0087). This comparative discrepancy demonstrates that the empirical quadratic limits of standard RSM underestimate the true active capacity of the quinary biosorbent mass under highly alkaline conditions, validating the necessity of expanding the polynomial architecture using the evolution-driven Genetic Algorithm (GA).

10. Advanced Application of BCCG/PVA in Environental Sensing:

The modern applications of nanomaterials have shifted from the traditional paradigms of isolated pollutant remediation towards the development of smart systems integrating both detection and degradation functionalities. In this context, following the strategic guidance of the scientific supervision, the efficiency of the created bio-nanocomposite as a photo-kinetic sensor under ultraviolet (UV) irradiation is evaluated, confirming its significance in the area of advanced environmental sensing[78], [79].

The operational philosophy of this promising technology is based on the exploitation of the photocatalytic activity of the material. So, its role is not limited to the simple degradation of the pollutant molecules but it extends to the conversion of the kinetic dynamics of the decomposition into analytical signals for qualitative and quantitative measurements. This is supported by an exceptional self-regeneration and continuous cleaning mechanism of the active surface[80], [81].

10.1. *Experimental Procedure for Sensing/Degradation Systems:*

The system is integrated for environmental sensing and photocatalytic degradation of the pollutant in aqueous media. The preparation of a standard CV solution at a concentration of 5 ppm is the first step to mimic the micro-pollutants in wastewater. The developed bio-nanocomposite of 10 mg is then added to the model pollutant solution with continuous stirring by magnetic stirrer in complete darkness to achieve the dynamic adsorption-desorption equilibrium on the active sites of the sensor surface and measure the reference initial absorbance (A_0 = 0.993Then, the reaction system is placed in the photoreactor to be activated electromagnetically by a handheld ultraviolet (UV) lamp, model VL-6.L (6 W tube, 365 nm wavelength), manufactured by Vilber Lourmat (France), which photo-activates the surface to generate highly reactive oxygen species ($^{\bullet}OH$ and $^{\bullet}O_2^-$) responsible for stimulating both the sensing signals and the self-cleaning degradation. The progress of this

reaction is monitored by time-dependent spectroscopic measurements, where periodic aliquots are collected at predetermined time intervals (30, 60, 240, 390 and 1440 min) and separated by centrifugation to measure the residual absorbance (A_f) at the maximum absorption wavelength (λ_{max} =590nm) using a UV-Vis spectrophotometer. This process is finalized with mathematical calibration and kinetic modeling with OriginPro software where the experimental data is fitted into Pseudo-First Order (PFO) and Pseudo-Second Order (PSO) models to build standard calibration curves and calculate the kinetic response rate constants of the environmental sensor[82], [83], [84].

10.2. *Experimental Results and Kinetics Discussion:*

Once the reactive system is exposed to UV light, the mechanism of monitoring and environmental sensing is initiated. The analytical interpretation of the kinetic behavior and tabulated data is presented in the **Table IV.16** and **Figure IV.38**.

Table IV.16. *Effect of UV radiation on CV removal efficiency over time.*

C_0(ppm)	m(mg)	t(min)	A_0	A_f	C_t (ppm)	Ce(ppm)	R (%)
5	10	30	0.993	0.705	4.831949194	3.425012213	29.11737944
5	10	60	0.993	0.608	4.831949194	2.951148021	38.92427459
5	10	240	0.993	0.23	4.831949194	1.104543234	77.1408351
5	10	390	0.993	0.173	4.831949194	0.826086957	82.90364978
5	10	1440	0.993	0.101	4.831949194	0.474352711	90.18299464

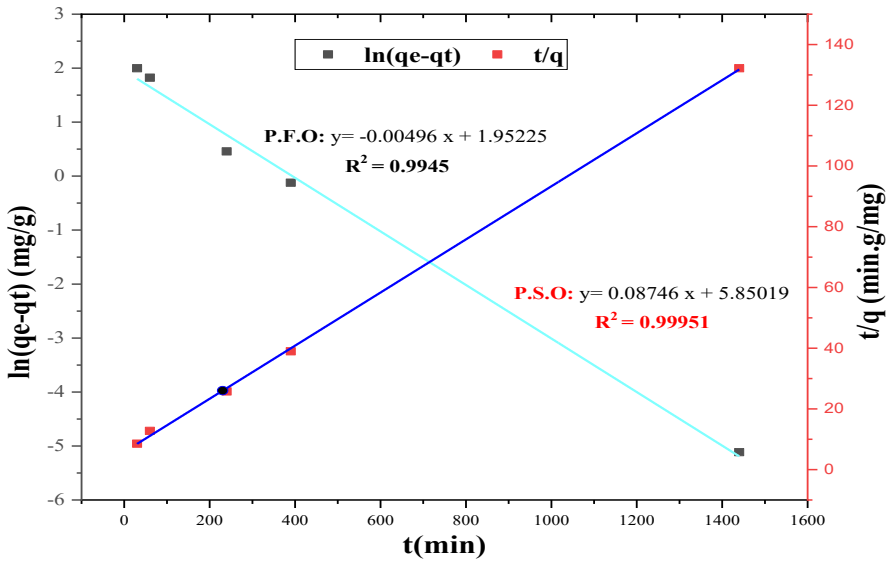


Figure IV.38. *Photodegradation kinetics under intense UV radiation.*

10.2.1. *Creation of an optical signal and its immediate kinetic reaction:*

The nano-surface was energetically photo-activated by UV lamp and then the material started photocatalytic reactions aiming at degradation of the target pollutant molecules. The sharp and systematic fall of spectral absorbance values ($A_0 \rightarrow A_f$), from an initial value of 0.993 that finally stabilizes at 0.101, is the experimental demonstration of this behavior. The apparent optical change with time corresponding to the change in concentration is not only an indicator of degradation in analytical chemistry, but also a dynamic sensing signal reflecting the high sensitivity of the material and its instantaneous response to changes in the surrounding environment[85].

10.2.2. *Linearity & Calibration Modelling for accurate Quantitative Detection:*

The mathematical modelling of the experimental data has shown excellent fit for Pseudo-Second Order (PSO) kinetic model with a very high linear correlation coefficient (R^2 =0.994). This rigorous linear conformity in the context of environmental sensing, validates the use of the photocatalytic degradation curve as a standard calibration curve. The extracted linear equation (y = 0.0854x + 8.4245) is thus a good predictor. This equation can be mathematically expressed as a function of irradiation exposure time for the residual pollutant concentration and ensures high reliability for quantitative detection.

10.2.3. *Self -Cleaning Function & Sensor Durability*:

The technological added value of this system is in the sustainability of the sensing surface. The UV irradiation leads to complete mineral destruction of organic molecules adsorbed on the active sites of the nanocomposite. This process effectively prevents sensor poisoning, a problem that usually compromises conventional systems due to the build-up of the contaminants. Thus, the sensor has an integrated recycling function, which makes it possible to reuse it over several cycles without any loss of sensitivity or detection accuracy, a key principle for designing sustainable and intelligent environmental sensors[86].

11. BCCG/PVA Biological Acitvity Studies:

11.1. *Evaluation of BCCG/PVA Antifungal Activity Against Candida albicans and Aspergillus niger via Well Diffusion Assay:*

The antifungal activity of the synthesized nanocomposite BCCG/PVA, was evaluated against the filamentous fungal species *Candida albicans* ATCC 10231 and *Aspergillus niger* using the agar well diffusion method. Sabouraud Dextrose Agar (SDA) supplemented with 2% glucose was prepared according to standard microbiological procedures illustrated in **Figure V. 39** and poured into sterile Petri dishes under aseptic conditions.

Fresh fungal cultures of *C. albicans* and *A. niger* were harvested, and conidial suspensions were prepared in sterile physiological saline containing 0.1% Tween 80. The density of each fungal suspension was adjusted to approximately 0.5 McFarland standard (≈ 1.5×10^8 CFU mL^{-1}) using a densitometer to ensure inoculum standardization. The standardized suspensions were uniformly spread over the surface of SDA plates using sterile cotton swabs to obtain homogeneous fungal growth.

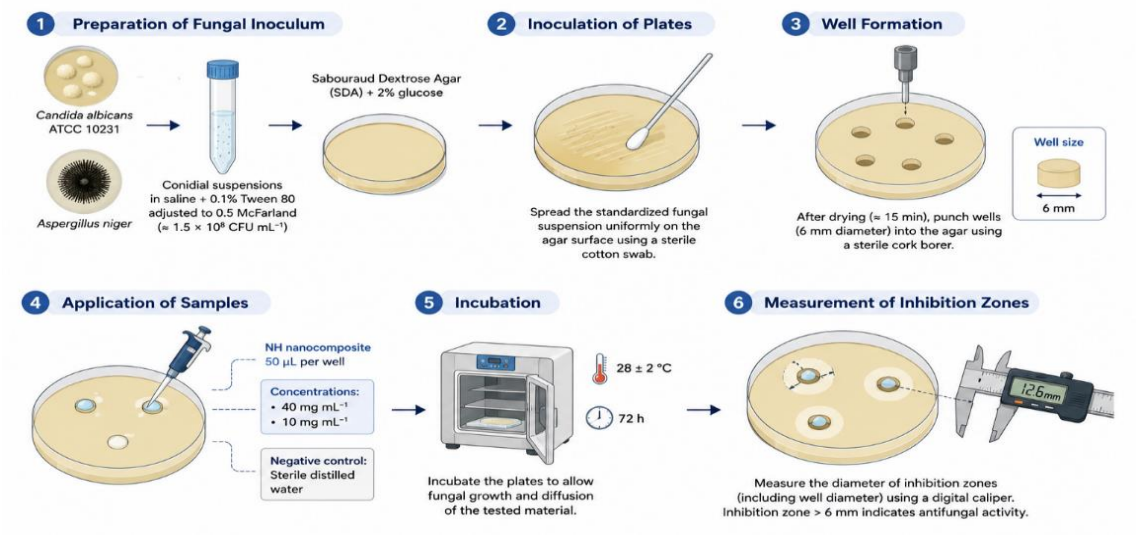


Figure V.39. *Schematic representation of the agar well diffusion assay used to evaluate the antifungal activity of BCCG/PVA against* Candida albicans *(ATCC 10231) and* Aspergillus niger.

After allowing the inoculated plates to dry for approximately 15 min under sterile conditions, circular wells (6 mm diameter) were punched into the agar using a sterile cork borer. Each well was filled with 50 µL of the nanocomposite suspension prepared at two concentrations: 40 and 10 mg mL^{-1}. Sterile distilled water (or the corresponding dispersion medium) was used as a negative control.

The inoculated plates were incubated at 28 ± 2°C for 72 h to allow fungal growth and diffusion of the tested material through the agar matrix. Following incubation, antifungal activity was assessed by measuring the diameter of the inhibition zones (mm) surrounding each well using a digital caliper. The diameter of the well (6 mm) was included in the final measurement. An inhibition zone greater than 6 mm was considered indicative of antifungal activity[87], [88].

11.1.1. *Assay Results and Interpretation:*

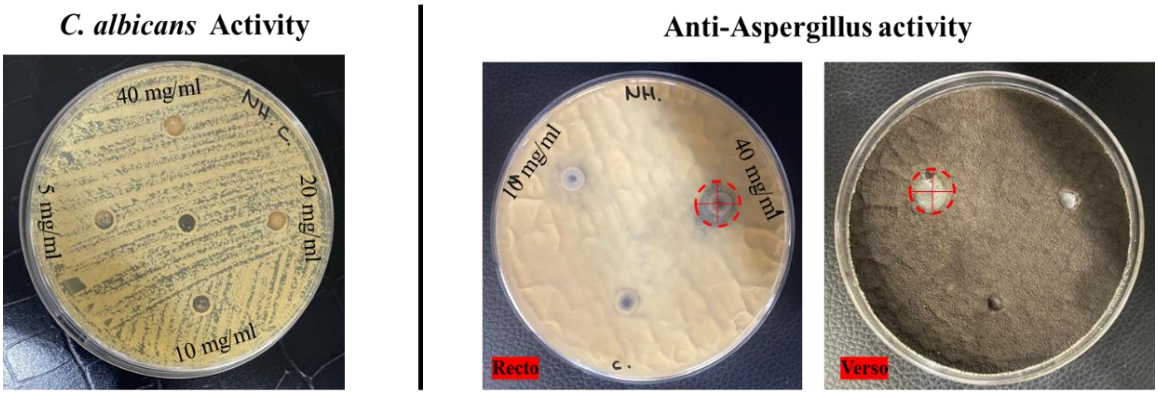


Figure IV.40. Antifungal activity of the BCCG/PVA *(Coded NH)* against *Candida albicans* and *Aspergillus Niger*.

The antifungal activity of the synthesized nanocomposite BCCG/PVA was evaluated using the agar well diffusion assay against *Candida albicans* and *Aspergillus niger*. As shown in **Figure IV.40** and **Table IV.16**, BCCG/PVA exhibited selective antifungal activity against *Aspergillus niger*, producing an inhibition zone of 12 mm at the highest tested concentration (40 mg/mL), whereas no inhibitory effect was observed at 10 mg/mL. In contrast, *Candida albicans* showed complete resistance to BCCG/PVA, with no inhibition zones detected at either tested concentration. These findings suggest a concentration-dependent antifungal effect of NH against the filamentous fungus *A. niger*, while the yeast *C. albicans* remained unaffected under the experimental conditions. The observed difference in susceptibility may be attributed to structural and physiological differences between filamentous fungi and yeasts, indicating that BCCG/PVA possesses a narrow-spectrum antifungal activity with greater effectiveness against *A. niger* than against *C. albicans*.

11.2. *A Assessment of BCCG/PVA Antibacterial Activity Against Escherichia coli and Staphylococcus aureus via Well Diffusion Assay:*

The antibacterial activity of BCCG/PVA was evaluated against tow reference bacterial strains, namely ***Escherichia coli*** (ATCC 25922), and ***Staphylococcus aureus*** (ATCC 25932), using the agar-well diffusion assay.

Mueller–Hinton agar (MHA) plates were prepared according to standard microbiological procedures. Fresh bacterial cultures grown in Mueller–Hinton broth for 24 h were adjusted to a turbidity equivalent to the 0.5 McFarland standard (approximately 1×10^6 CFU mL^{-1}) using sterile physiological saline solution (0.9% NaCl). The standardized bacterial suspensions were uniformly spread over the entire surface of MHA plates using sterile cotton swabs to obtain a confluent bacterial lawn.

Following inoculation, the plates were allowed to dry under aseptic conditions for approximately 15 min. Sterile cork borers were then used to create uniform wells of 6 mm diameter in the agar medium. Each well was filled with 50 µL of nanocomposite suspensions prepared at four concentrations: 40, 20, 10, and 5 mg mL^{-1}. Prior to testing, the nanocomposites were dispersed in sterile distilled water and sonicated to ensure homogeneous dispersion. Appropriate controls were included in all experiments.

The inoculated plates were incubated aerobically at 37 °C for 24 h. Following incubation, antibacterial activity was assessed by measuring the diameter of the inhibition zones (mm) surrounding each well using a calibrated digital caliper. The diameter of the well (6 mm) was included in the final measurement. An inhibition zone greater than 6 mm was considered indicative of antibacterial activity[89], [90].

Table IV.17. Results of antibacterial tests

Strains used	40mg/ml	20 mg/ml	10mg/ml	5 mg/ml	Co . Neg.
Escherichia coli ATCC 25922	11	NI	NI	NI	NI
Staphylococcus aureus ATCC 25932	NI	NI	NI	NI	NI

NI = No Inhibition

11.2.1. *Assay Results and Interpretation:*

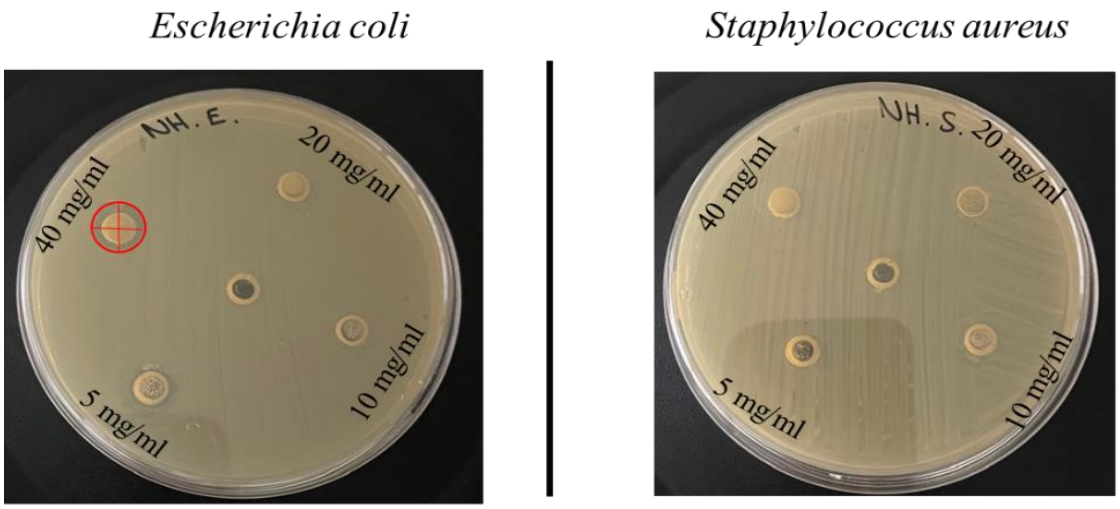


Figure IV.41. *Antibacterial activity of BCCG/PVA (Coded NH) against Escherichia coli ATCC 25922 and Staphylococcus aureus ATCC 25932.*

The antibacterial activity of the synthesized nanocomposite BCCG/PVA was assessed using the agar-well diffusion method against the reference strains *Escherichia coli* ATCC 25922 and *Staphylococcus aureus* ATCC 25932. As presented in **Figure IV.41** and **Table IV.17.** Results of antibacterial tests, BCCG/PVA exhibited limited antibacterial activity, producing an inhibition zone of 11 mm against *E. coli* only at the highest tested concentration (40 mg/mL). No inhibitory effect was observed at lower concentrations (20, 10, and 5 mg/mL). In contrast, *S. aureus* showed complete resistance to BCCG/PVA, with no detectable inhibition zones at any tested concentration. These results indicate a weak and concentration-dependent antibacterial effect of BCCG/PVA, with selective activity against the Gram-negative bacterium *E. coli*. The absence of activity against *S. aureus* suggests that the antibacterial potential of BCCG/PVA is strain-dependent and may be influenced by differences in cell wall structure and susceptibility between Gram-negative and Gram-positive bacteria.

11.3. *In Vitro Evaluation of the hemolytic activity of the BCCG/PVA Using a 96-Well Microplate Assay:*

The hemolytic activity of the synthesized nanocomposite, coded BCCG/PVA, was evaluated using a 96-well microplate hemolysis assay (**Figure IV.42**). Fresh human erythrocytes collected in heparinized tubes were washed three times with phosphate-buffered saline (PBS, pH 7.4) by centrifugation at 1,000 × g for 5 min and resuspended to obtain a 2% hematocrit suspension.

Briefly, 100 µL of the erythrocyte suspension was mixed with 100 µL of BCCG/PVA suspensions prepared at concentrations of **40, 20, 10, 5, 2.5, and 1.25 mg mL^{-1}**. The nanocomposite was dispersed in PBS and sonicated before use to ensure homogeneous suspension. PBS served as the negative control (0% hemolysis), whereas 0.1% H_2O_2 was used as the positive control (100% hemolysis). All treatments were performed in triplicate.

The microplate was incubated at **37 °C for 1 h** under gentle agitation and subsequently centrifuged at 1,000 × g for 5 min. Hemoglobin released into the supernatant was quantified by measuring absorbance at **540 nm** using a microplate reader.

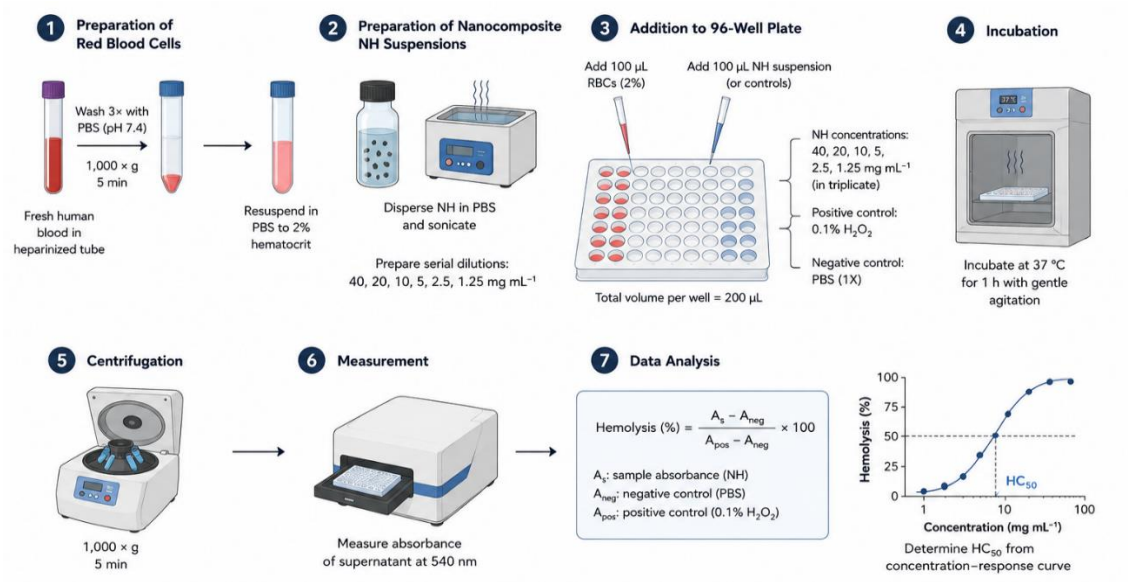


Figure IV.42. *Schematic workflow of the 96-well microplate hemolysis assay used to evaluate the hemocompatibility of the nanocomposite BCCG/PVA.*

The percentage of hemolysis was calculated according to the following equation:

$$\boldsymbol{Hemolysis}\ (\%) = \frac{\boldsymbol{A_s - A_{neg}}}{\boldsymbol{A_{pos} - A_{neg}}} \times \mathbf{100} \qquad \textbf{IV.8}$$

Where:

- $\mathbf{A_s}$ is the absorbance of the BCCG/PVA -treated sample,
- $\mathbf{A_{neg}}$ is the absorbance of the negative control, and $\mathbf{A_{pos}}$ is the absorbance of the positive control.

Results were expressed as mean ± standard deviation (SD). The HC_{50} value was estimated from the concentration–response curve when applicable, and statistical analysis was performed to evaluate the hemocompatibility of the synthesized nanocomposite BCCG/PVA.

11.3.1. *Assay Results and Interpretation:*

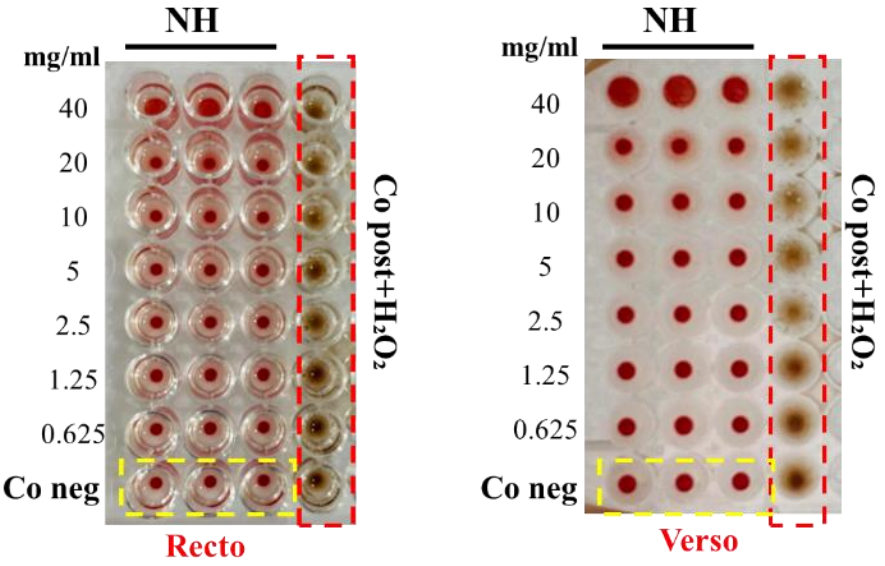


Figure IV.43. *Hemolytic activity of the nanocomposite BCCG/PVA (coded NH) at different concentrations against human erythrocytes.*

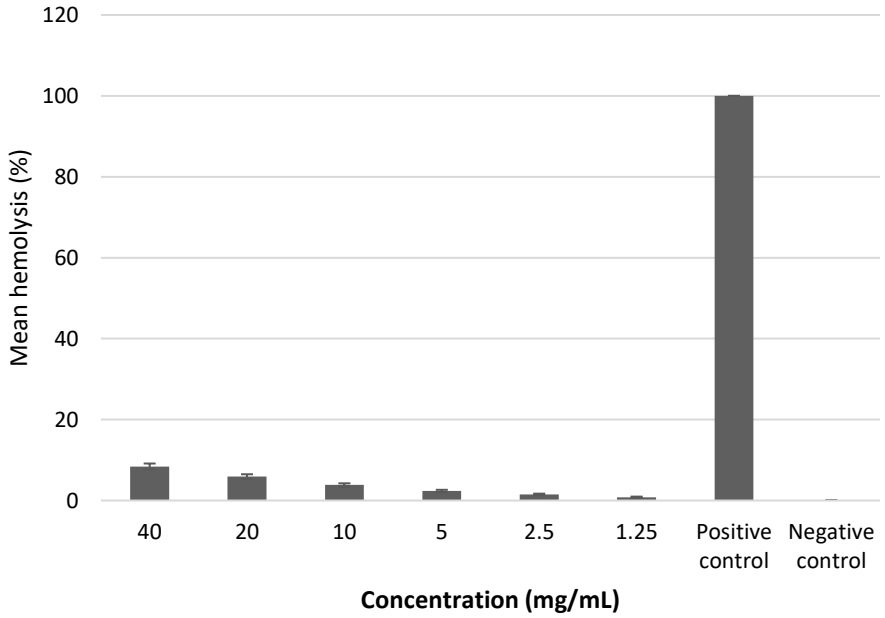


Figure IV.44. *Hemolytic activity of BCCG/PVA (Coded NH) at different concentrations. Bars represent mean hemolysis percentage, and error bars indicate standard deviation (n = 3).*

The hemolytic activity of the synthesized nanocomposite BCCG/PVA was evaluated against human erythrocytes at concentrations ranging from 1.25 to 40 mg/mL. As illustrated in **Figure IV.43** and **Figure IV.44**, the percentage of hemolysis increased gradually with increasing BCCG/PVA concentration, demonstrating a concentration-dependent effect. Nevertheless, the observed hemolysis remained low across all tested concentrations,

reaching a maximum value of approximately 8.4% at 40 mg/mL. In contrast, the positive control (H_2O_2) induced complete hemolysis, while the negative control (PBS) produced negligible erythrocyte lysis. Visual examination of the microplate wells confirmed the quantitative findings, with only slight increases in hemoglobin release observed at higher BCCG/PVA concentrations. These results indicate that BCCG/PVA exhibits good hemocompatibility and limited membrane-disruptive effects toward human red blood cells under the experimental conditions. The low hemolysis rates suggest that the nanocomposite possesses a favorable safety profile for biological applications, particularly at low and intermediate concentrations.

Chapter Four References

[1] J. Alipal *et al.*, "A review of gelatin: Properties, sources, process, applications, and commercialisation," *Mater. Today Proc.*, vol. 42, pp. 240–250, 2021, doi: 10.1016/j.matpr.2020.12.922.

[2] J. H. Muyonga, C. G. B. Cole, and K. G. Duodu, "Fourier transform infrared (FTIR) spectroscopic study of acid soluble collagen and gelatin from skins and bones of young and adult Nile perch (Lates niloticus)," *Food Chem.*, vol. 86, no. 3, pp. 325–332, Jul. 2004, doi: 10.1016/j.foodchem.2003.09.038.

[3] A. Singh, A. Kumar, N. Kaur, and N. Singh, "Chemically Modified Gelatin/Chitosan as a Chemosensor Adsorbent for Detection of Toxic Metals and Removal of Organic Dyes," *Polym. Adv. Technol.*, vol. 36, no. 1, Jan. 2025, doi: 10.1002/pat.70088.

[4] B. Esmat *et al.*, "Carboxymethyl cellulose: Structural modifications and their impact on barrier and mechanical properties for sustainable food packaging," *J. Stored Prod. Res.*, vol. 115, p. 102864, Jan. 2026, doi: 10.1016/j.jspr.2025.102864.

[5] M. Khandelwal *et al.*, "Facile fabrication of a novel chitosan/carboxymethyl cellulose/bentonite/CuO nanocomposite for enhanced photocatalytic and antibacterial applications," *RSC Adv.*, vol. 15, no. 5, pp. 3365–3377, 2025, doi: 10.1039/D4RA08437C.

[6] D. Caccavo, G. Lamberti, and A. A. Barba, "Analysis and simulation of wet-granulation processes," *J. Taiwan Inst. Chem. Eng.*, vol. 159, p. 105455, Jun. 2024, doi: 10.1016/j.jtice.2024.105455.

[7] Y. Gong, X. Chen, and W. Wu, "Application of fourier transform infrared (FTIR) spectroscopy in sample preparation: Material characterization and mechanism investigation," *Advances in Sample Preparation*, vol. 11, p. 100122, Aug. 2024, doi: 10.1016/j.sampre.2024.100122.

[8] M. Momtaz, E. Momtaz, M. A. Mehrgardi, F. Momtaz, T. Narimani, and F. Poursina, "Preparation and characterization of gelatin/chitosan nanocomposite reinforced by NiO nanoparticles as an active food packaging," *Sci. Rep.*, vol. 14, no. 1, p. 519, Jan. 2024, doi: 10.1038/s41598-023-50260-8.

[9] P. Gupta *et al.*, "Sorption isotherms and kinetics of Crystal Violet dye uptake from aqueous solution by using polyaniline nanocomposite as adsorbent," *Chemical Physics Impact*, vol. 10, p. 100834, Jun. 2025, doi: 10.1016/j.chphi.2025.100834.

[10] I. Loulidi *et al.*, "Adsorption of Crystal Violet onto an Agricultural Waste Residue: Kinetics, Isotherm, Thermodynamics, and Mechanism of Adsorption," *The Scientific World Journal*, vol. 2020, pp. 1–9, May 2020, doi: 10.1155/2020/5873521.

[11] K. S. Salem *et al.*, "Comparison and assessment of methods for cellulose crystallinity determination," *Chem. Soc. Rev.*, vol. 52, no. 18, pp. 6417–6446, 2023, doi: 10.1039/D2CS00569G.

[12] A. T. Okasha *et al.*, "Synthesis and characterization of Mg-hydroxyapatite and its cellulose hybridized structure as enhanced bio-carrier of oxaliplatin drug; equilibrium and release kinetics," *RSC Adv.*, vol. 13, no. 43, pp. 30151–30167, 2023, doi: 10.1039/D3RA04268E.

[13] S. Park, J. O. Baker, M. E. Himmel, P. A. Parilla, and D. K. Johnson, "Cellulose crystallinity index: measurement techniques and their impact on interpreting cellulase performance," *Biotechnol. Biofuels*, vol. 3, no. 1, p. 10, Dec. 2010, doi: 10.1186/1754-6834-3-10.

[14] S. Verma, G. D. Verros, and R. K. Arya, "PVA- Bentonite-Water Coatings: Experimental and Simulation Studies," *Polymers (Basel).*, vol. 17, no. 19, p. 2689, Oct. 2025, doi: 10.3390/polym17192689.

[15] P. Ahvenainen, I. Kontro, and K. Svedström, "Comparison of sample crystallinity determination methods by X-ray diffraction for challenging cellulose I materials," *Cellulose*, vol. 23, no. 2, pp. 1073–1086, Apr. 2016, doi: 10.1007/s10570-016-0881-6.

[16] S. Hajji *et al.*, "Structural analysis, and antioxidant and antibacterial properties of chitosan-poly (vinyl alcohol) biodegradable films," *Environmental Science and Pollution Research*, vol. 23, no. 15, pp. 15310–15320, Aug. 2016, doi: 10.1007/s11356-016-6699-9.

[17] H. A. AL-Kahtani *et al.*, "Structural characteristics of camel-bone gelatin by demineralization and extraction," *Int. J. Food Prop.*, vol. 20, no. 11, pp. 2559–2568, Nov. 2017, doi: 10.1080/10942912.2016.1244543.

[18] O. Fawale, A. Abuibaid, F. Hamed, P. Kittiphattanabawon, and S. Maqsood, "Molecular, Structural, and Rheological Characterization of Camel Skin Gelatin Extracted Using Different Pretreatment Conditions," *Foods*, vol. 10, no. 7, p. 1563, Jul. 2021, doi: 10.3390/foods10071563.

[19] R. Gelli, G. Mugnaini, T. Bolognesi, and M. Bonini, “Cross-linked Porous Gelatin Microparticles with Tunable Shape, Size, and Porosity,” *Langmuir*, vol. 37, no. 44, pp. 12781–12789, Nov. 2021, doi: 10.1021/acs.langmuir.1c01508.

[20] P. Thiyagarajan, A. Padmapriya, A. M. Shanmugharaj, and T. Alagesan, “DFT theoretical and experimental investigation of gelatin-loaded niobium-doped calcium apatite ceramics to elucidate its structural and electronic characteristics,” *Next Materials*, vol. 7, p. 100630, Apr. 2025, doi: 10.1016/j.nxmate.2025.100630.

[21] R. A. R., E. H. A.J., N. Q. I. M.N., R. A., and U. H. M.R., “Effects of extraction conditions on characterization of gelatin from water buffalo (Bubalus bubalis) skin,” *Food Res.*, vol. 4, no. S6, pp. 124–131, Dec. 2020, doi: 10.26656/fr.2017.4(S6).015.

[22] C.-Y. Huang, Y.-H. Tsai, Y.-H. Hong, S.-L. Hsieh, and R.-H. Huang, “Characterization and Antioxidant and Angiotensin I-Converting Enzyme (ACE)-Inhibitory Activities of Gelatin Hydrolysates Prepared from Extrusion-Pretreated Milkfish (Chanos chanos) Scale,” *Mar. Drugs*, vol. 16, no. 10, p. 346, Sep. 2018, doi: 10.3390/md16100346.

[23] S. Neusatz Guilhen *et al.*, “Role of Point of Zero Charge in the Adsorption of Cationic Textile Dye on Standard Biochars from Aqueous Solutions: Selection Criteria and Performance Assessment,” *Recent Prog. Mater.*, vol. 04, no. 02, pp. 1–30, May 2022, doi: 10.21926/rpm.2202010.

[24] S. Slesinska, P. Galek, J. Menzel, S. W. Donne, K. Fic, and A. Płatek-Mielczarek, “Fundamentals and Implication of Point of Zero Charge (PZC) Determination for Activated Carbons in Aqueous Electrolytes.,” *Adv. Sci. (Weinh).*, vol. 11, no. 48, p. e2409162, Dec. 2024, doi: 10.1002/advs.202409162.

[25] S. S and S. K. P, “An investigation of adsorption parameters on ZVI-AC nanocomposite in the displacement of Se(IV) ions through CCD analysis,” *Journal of Industrial and Engineering Chemistry*, vol. 75, pp. 211–223, Jul. 2019, doi: 10.1016/j.jiec.2019.03.026.

[26] M. El Hajam *et al.*, “Statistical Design and Optimization of Cr (VI) Adsorption onto Native and HNO3/NaOH Activated Cedar Sawdust Using AAS and a Response Surface Methodology (RSM).,” *Molecules*, vol. 28, no. 21, Oct. 2023, doi: 10.3390/molecules28217271.

[27] A. S. Abdulhameed, A. K. T. Mohammad, and A. H. Jawad, "Application of response surface methodology for enhanced synthesis of chitosan tripolyphosphate/TiO2 nanocomposite and adsorption of reactive orange 16 dye," *J Clean Prod*, vol. 232, pp. 43–56, Sep. 2019, doi: 10.1016/j.jclepro.2019.05.291.

[28] M. Shaban, M. R. Abukhadra, A. S. Mohamed, M. G. Shahien, and S. S. Ibrahim, "Synthesis of Mesoporous Graphite Functionalized by Nitrogen for Efficient Removal of Safranin Dye Utilizing Rice Husk Ash; Equilibrium Studies and Response Surface Optimization," *J. Inorg. Organomet. Polym. Mater.*, vol. 28, no. 1, pp. 279–294, Jan. 2018, doi: 10.1007/s10904-017-0726-2.

[29] S. G. Nasab, A. Semnani, A. Teimouri, M. J. Yazd, T. M. Isfahani, and S. Habibollahi, "Decolorization of crystal violet from aqueous solutions by a novel adsorbent chitosan/nanodiopside using response surface methodology and artificial neural network-genetic algorithm," *Int. J. Biol. Macromol.*, vol. 124, pp. 429–443, Mar. 2019, doi: 10.1016/j.ijbiomac.2018.11.148.

[30] M. El Hajam *et al.*, "Statistical Design and Optimization of Cr (VI) Adsorption onto Native and HNO3/NaOH Activated Cedar Sawdust Using AAS and a Response Surface Methodology (RSM)," *Molecules*, vol. 28, no. 21, p. 7271, Oct. 2023, doi: 10.3390/molecules28217271.

[31] M. Ghaedi, A. Ansari, M. H. Habibi, and A. R. Asghari, "Removal of malachite green from aqueous solution by zinc oxide nanoparticle loaded on activated carbon: Kinetics and isotherm study," *Journal of Industrial and Engineering Chemistry*, vol. 20, no. 1, pp. 17–28, Jan. 2014, doi: 10.1016/j.jiec.2013.04.031.

[32] G. Z. Kyzas and K. A. Matis, "Nanoadsorbents for pollutants removal: A review," *J. Mol. Liq.*, vol. 203, pp. 159–168, Mar. 2015, doi: 10.1016/j.molliq.2015.01.004.

[33] M. A. M. Salleh, D. K. Mahmoud, W. A. W. A. Karim, and A. Idris, "Cationic and anionic dye adsorption by agricultural solid wastes: A comprehensive review," *Desalination*, vol. 280, no. 1–3, pp. 1–13, Oct. 2011, doi: 10.1016/j.desal.2011.07.019.

[34] J. Wang and X. Guo, "Adsorption kinetic models: Physical meanings, applications, and solving methods," *J. Hazard. Mater.*, vol. 390, p. 122156, May 2020, doi: 10.1016/j.jhazmat.2020.122156.

[35] A. H. Jawad, A. S. Abdulhameed, and M. S. Mastuli, "Mesoporous Crosslinked Chitosan-Activated Charcoal Composite for the Removal of Thionine Cationic Dye: Comprehensive Adsorption and Mechanism Study," *J. Polym. Environ.*, vol. 28, no. 3, pp. 1095–1105, Mar. 2020, doi: 10.1007/s10924-020-01671-5.

[36] F. Marrakchi, W. A. Khanday, M. Asif, and B. H. Hameed, "Cross-linked chitosan/sepiolite composite for the adsorption of methylene blue and reactive orange 16," *Int. J. Biol. Macromol.*, vol. 93, pp. 1231–1239, Dec. 2016, doi: 10.1016/j.ijbiomac.2016.09.069.

[37] M. Musah, Y. Azeh, J. Mathew, M. Umar, Z. Abdulhamid, and A. Muhammad, "Adsorption Kinetics and Isotherm Models: A Review," *Caliphate Journal of Science and Technology*, vol. 4, no. 1, pp. 20–26, Feb. 2022, doi: 10.4314/cajost.v4i1.3.

[38] K. L. Tan and B. H. Hameed, "Insight into the adsorption kinetics models for the removal of contaminants from aqueous solutions," *J. Taiwan Inst. Chem. Eng.*, vol. 74, pp. 25–48, May 2017, doi: 10.1016/j.jtice.2017.01.024.

[39] M. Hubbe, S. Azizian, and S. Douven, "Implications of apparent pseudo-second-order adsorption kinetics onto cellulosic materials: A review," *Bioresources*, vol. 14, no. 3, pp. 7582–7626, Aug. 2019, doi: 10.15376/biores.14.3.7582-7626.

[40] M. Kostoglou and T. D. Karapantsios, "Why Is the Linearized Form of Pseudo-Second Order Adsorption Kinetic Model So Successful in Fitting Batch Adsorption Experimental Data?," *Colloids and Interfaces*, vol. 6, no. 4, p. 55, Oct. 2022, doi: 10.3390/colloids6040055.

[41] H. Qiu, L. Lv, B. Pan, Q. Zhang, W. Zhang, and Q. Zhang, "Critical review in adsorption kinetic models," *Journal of Zhejiang University-SCIENCE A*, vol. 10, no. 5, pp. 716–724, May 2009, doi: 10.1631/jzus.A0820524.

[42] W. Plazinski, W. Rudzinski, and A. Plazinska, "Theoretical models of sorption kinetics including a surface reaction mechanism: A review," *Adv. Colloid Interface Sci.*, vol. 152, no. 1–2, pp. 2–13, Nov. 2009, doi: 10.1016/j.cis.2009.07.009.

[43] H. Deb *et al.*, "The Statistical Error Optimization of Dye Sorption Equilibria for the Precise Prediction of Adsorption Isotherms on Activated Graphene," *Applied Sciences*, vol. 13, no. 14, p. 8106, Jul. 2023, doi: 10.3390/app13148106.

[44] M. A. Al-Ghouti and D. A. Da'ana, "Guidelines for the use and interpretation of adsorption isotherm models: A review," *J. Hazard. Mater.*, vol. 393, p. 122383, Jul. 2020, doi: 10.1016/j.jhazmat.2020.122383.

[45] S. Tonk and E. Rápó, "Linear and Nonlinear Regression Analysis for the Adsorption of Remazol Dye by Romanian Brewery Waste By-Product, Saccharomyces cerevisiae," *Int. J. Mol. Sci.*, vol. 23, no. 19, p. 11827, Oct. 2022, doi: 10.3390/ijms231911827.

[46] B. TEKİN and U. AÇIKEL, "Adsorption Isotherms for Removal of Heavy Metal Ions (Copper and Nickel) from Aqueous Solutions in Single and Binary Adsorption Processes," *Gazi University Journal of Science*, vol. 36, no. 2, pp. 495–509, Jun. 2023, doi: 10.35378/gujs.1066137.

[47] A. El Jery *et al.*, "Isotherms, kinetics and thermodynamic mechanism of methylene blue dye adsorption on synthesized activated carbon," *Sci. Rep.*, vol. 14, no. 1, p. 970, Jan. 2024, doi: 10.1038/s41598-023-50937-0.

[48] A. Abin-Bazaine, A. Campos Trujillo, and M. Olmos-Marquez, "Adsorption Isotherms: Enlightenment of the Phenomenon of Adsorption," in *Wastewater Treatment*, IntechOpen, 2022. doi: 10.5772/intechopen.104260.

[49] G. Limousin, J.-P. Gaudet, L. Charlet, S. Szenknect, V. Barthès, and M. Krimissa, "Sorption isotherms: A review on physical bases, modeling and measurement," *Applied Geochemistry*, vol. 22, no. 2, pp. 249–275, Feb. 2007, doi: 10.1016/j.apgeochem.2006.09.010.

[50] E. C. Lima, A. Hosseini-Bandegharaei, J. C. Moreno-Piraján, and I. Anastopoulos, "A critical review of the estimation of the thermodynamic parameters on adsorption equilibria. Wrong use of equilibrium constant in the Van't Hoof equation for calculation of thermodynamic parameters of adsorption," *J. Mol. Liq.*, vol. 273, pp. 425–434, Jan. 2019, doi: 10.1016/j.molliq.2018.10.048.

[51] O. Sakin Omer, M. A. Hussein, B. H. M. Hussein, and A. Mgaidi, "Adsorption thermodynamics of cationic dyes (methylene blue and crystal violet) to a natural clay mineral from aqueous solution between 293.15 and 323.15 K," *Arabian Journal of Chemistry*, vol. 11, no. 5, pp. 615–623, Jul. 2018, doi: 10.1016/j.arabjc.2017.10.007.

[52] M. Sadoq *et al.*, "Elimination of crystal violet from aqueous solution by adsorption on naturel polysaccharide: Kinetic, isotherm, thermodynamic studies and mechanism

analysis," *Arabian Journal of Chemistry*, vol. 17, no. 1, p. 105453, Jan. 2024, doi: 10.1016/j.arabjc.2023.105453.

[53] R. Et-tanteny, I. Allaoui, R. Haloui, S. Elkhattabi, K. Draoui, and K. El Khadiri, "Mechanistic insights into dye adsorption on chitosan-functionalized bentonite: synergizing experiments and computational study," *Chemical Physics Impact*, vol. 11, p. 100919, Dec. 2025, doi: 10.1016/j.chphi.2025.100919.

[54] S. Hoijang and S. Ananta, "Surface modification of magnetic nanoparticles for selective adsorption of organic dyes: A mini-review," *ScienceAsia*, vol. 51S, no. 1, p. 1, 2025, doi: 10.2306/scienceasia1513-1874.2025.s012.

[55] L. Wu, L. Liao, and G. Lv, "Influence of interlayer cations on organic intercalation of montmorillonite," *J. Colloid Interface Sci.*, vol. 454, pp. 1–7, Sep. 2015, doi: 10.1016/j.jcis.2015.04.021.

[56] T. Wang *et al.*, "PVA/chitosan-based multifunctional hydrogels constructed through multi-bonding synergies and their application in flexible sensors," *Carbohydr. Polym.*, vol. 350, p. 123034, Feb. 2025, doi: 10.1016/j.carbpol.2024.123034.

[57] R. Et-tanteny, I. Allaoui, R. Haloui, S. Elkhattabi, K. Draoui, and K. El Khadiri, "Mechanistic insights into dye adsorption on chitosan-functionalized bentonite: synergizing experiments and computational study," *Chemical Physics Impact*, vol. 11, p. 100919, Dec. 2025, doi: 10.1016/j.chphi.2025.100919.

[58] H. Nonogaki, G. W. Bassel, and J. D. Bewley, "Germination—Still a mystery," *Plant Science*, vol. 179, no. 6, pp. 574–581, Dec. 2010, doi: 10.1016/j.plantsci.2010.02.010.

[59] J. D. Bewley, K. J. Bradford, H. W. M. Hilhorst, and H. Nonogaki, *Seeds*. New York, NY: Springer New York, 2013. doi: 10.1007/978-1-4614-4693-4.

[60] S. Mani and R. N. Bharagava, "Exposure to Crystal Violet, Its Toxic, Genotoxic and Carcinogenic Effects on Environment and Its Degradation and Detoxification for Environmental Safety," 2016, pp. 71–104. doi: 10.1007/978-3-319-23573-8_4.

[61] N. Tarchoun *et al.*, "Seed Priming and Biopriming in Two Squash Landraces (Cucurbita maxima Duchesne) from Tunisia: A Sustainable Strategy to Promote Germination and Alleviate Salt Stress," *Plants*, vol. 13, no. 17, p. 2464, Sep. 2024, doi: 10.3390/plants13172464.

[62] R. Lebbihi *et al.*, "Sustainable ciprofloxacin removal using muscovite clay: A techno-economic and eco-toxicological study via MOGWO/RSM-ANN," *Mater. Today Commun.*, vol. 50, p. 114394, Jan. 2026, doi: 10.1016/j.mtcomm.2025.114394.

[63] R. Lebbihi, L. Haddad, C. Labiod, A. Guesmi, L. Khezami, and M. Fellah, "Eco-engineered natural clay: methylene blue adsorption optimized by RSM-ANN," *International Journal of Environmental Science and Technology*, vol. 23, no. 1, p. 50, Jan. 2026, doi: 10.1007/s13762-025-06852-0.

[64] S. Telli, H. Ghodbane, A. Laouissi, M. Zamouche, and Y. Kadmi, "Remediation of cationic dye from wastewater using a new environmentally friendly adsorbent: A response surface methodology and artificial neural network modeling study," *Int. J. Chem. Kinet.*, vol. 57, no. 1, pp. 16–39, Jan. 2025, doi: 10.1002/kin.21756.

[65] E. Hidayat *et al.*, "Optimization and comparative modelling of RSM and ANN for the adsorptive removal of Remazol Brilliant Blue R dye using spent coffee ground biochar," *Chemosphere*, vol. 389, p. 144709, Nov. 2025, doi: 10.1016/j.chemosphere.2025.144709.

[66] C. C. Okoye, O. D. Onukwuli, and C. F. Okey-Onyesolu, "Predictive capability evaluation of RSM and ANN models in adsorptive treatment of crystal violet dye simulated wastewater using activated carbon prepared from *Raphia hookeri* seeds," *Journal of the Chinese Advanced Materials Society*, vol. 6, no. 4, pp. 478–496, Oct. 2018, doi: 10.1080/22243682.2018.1497534.

[67] S. Bbumba and I. Karume, "Comparative analysis of ANFIS, ANN, and BBD for enhanced prediction of methyl orange adsorption in water treatment," *Sci. Rep.*, vol. 16, no. 1, p. 12822, Mar. 2026, doi: 10.1038/s41598-026-43445-4.

[68] Y. Mesellem, M. Hentabli, M. Laidi, and A. Abdallah El Hadj, "Comparative evaluation of artificial neural networks and support vector machines for predicting heavy metal adsorption dynamics in fixed beds," *Main Group Chemistry*, May 2026, doi: 10.1177/10241221261445730.

[69] Z. Yang, P. Baraldi, and E. Zio, "A comparison between extreme learning machine and artificial neural network for remaining useful life prediction," in *2016 Prognostics and System Health Management Conference (PHM-Chengdu)*, IEEE, Oct. 2016, pp. 1–7. doi: 10.1109/PHM.2016.7819794.

[70] S. Kumari *et al.*, "An exploration of RSM, ANN, and ANFIS models for methylene blue dye adsorption using Oryza sativa straw biomass: a comparative approach," *Sci. Rep.*, vol. 15, no. 1, p. 2979, Jan. 2025, doi: 10.1038/s41598-025-87274-3.

[71] N. Loura, K. Rathee, M. Singh, and V. Dhull, "Role of nanomaterials in dye removal with applications of various machine learning and statistical optimization tools for enhancing adsorption," *Sustainable Chemistry One World*, vol. 9, p. 100193, Mar. 2026, doi: 10.1016/j.scowo.2026.100193.

[72] Y. M. Desalegn, E. A. Bekele, G. H. Dagnaw, S. A. Marye, and Y. D. Reta, "RSM versus ANN for modeling and optimization of magnetic adsorbent based on montmorillonite and CoFe2O4," *Appl. Water Sci.*, vol. 14, no. 6, p. 129, Jun. 2024, doi: 10.1007/s13201-024-02187-2.

[73] C. E. Onu, J. T. Nwabanne, P. E. Ohale, and C. O. Asadu, "Comparative analysis of RSM, ANN and ANFIS and the mechanistic modeling in eriochrome black-T dye adsorption using modified clay," *S. Afr. J. Chem. Eng.*, vol. 36, pp. 24–42, Apr. 2021, doi: 10.1016/j.sajce.2020.12.003.

[74] A. Fetimi *et al.*, "Modeling of Textile Dye Removal from Wastewater Using Innovative Oxidation Technologies (Fe(II)/Chlorine and H_2O_2/Periodate Processes): Artificial Neural Network-Particle Swarm Optimization Hybrid Model," *ACS Omega*, vol. 7, no. 16, pp. 13818–13825, Apr. 2022, doi: 10.1021/acsomega.2c00074.

[75] S. Kumari, J. Chowdhry, P. Sharma, S. Agarwal, and M. Chandra Garg, "Integrating artificial neural networks and response surface methodology for predictive modeling and mechanistic insights into the detoxification of hazardous MB and CV dyes using Saccharum officinarum L. biomass," *Chemosphere*, vol. 344, p. 140262, Dec. 2023, doi: 10.1016/j.chemosphere.2023.140262.

[76] M. Bahrami, M. J. Amiri, and F. Bagheri, "Optimization of Crystal Violet Adsorption by Chemically Modified Potato Starch Using Response Surface Methodology," *Pollution*, vol. 6, no. 1, pp. 159–170, 2020, doi: 10.22059/poll.2019.288467.674.

[77] W. Ruan, J. Hu, J. Qi, Y. Hou, R. Cao, and X. Wei, "Removal of Crystal Violet by Using Reduced-Graphene-Oxide-Supported Bimetallic Fe/Ni Nanoparticles (rGO/Fe/Ni): Application of Artificial Intelligence Modeling for the Optimization Process," *Materials*, vol. 11, no. 5, p. 865, May 2018, doi: 10.3390/ma11050865.

[78] X. Sun, C. Wang, D. Su, G. Wang, and Y. Zhong, "Application of Photocatalytic Materials in Sensors," *Adv. Mater. Technol.*, vol. 5, no. 5, May 2020, doi: 10.1002/admt.201900993.

[79] A. Fouda, S. S. Salem, A. R. Wassel, M. F. Hamza, and Th. I. Shaheen, "Optimization of green biosynthesized visible light active CuO/ZnO nano-photocatalysts for the degradation of organic methylene blue dye," *Heliyon*, vol. 6, no. 9, p. e04896, Sep. 2020, doi: 10.1016/j.heliyon.2020.e04896.

[80] W. Al-Gethami *et al.*, "Emerging environmentally friendly bio-based nanocomposites for the efficient removal of dyes and micropollutants from wastewater by adsorption: a comprehensive review," *RSC Adv.*, vol. 14, no. 4, pp. 2804–2834, 2024, doi: 10.1039/D3RA06501D.

[81] S. H. Al-Ansari, H. Gomaa, R. D. Abdel-Rahim, G. A. M. Ali, and A. M. Nagiub, "Recycled gold-reduced graphene oxide nanocomposite for efficient adsorption and photocatalytic degradation of crystal violet," *Sci. Rep.*, vol. 14, no. 1, p. 4379, Feb. 2024, doi: 10.1038/s41598-024-54580-1.

[82] L. D. Loor-Urgilés, T. N. Feijoó, C. A. Martínez-Huitle, E. Vieira dos Santos, and P. J. Espinoza-Montero, "Nanomaterial enhanced photoelectrocatalysis and photocatalysis for chemical oxygen demand sensing a comprehensive review," *NPJ Clean Water*, vol. 7, no. 1, p. 129, Dec. 2024, doi: 10.1038/s41545-024-00425-3.

[83] M. Shariati, A. Babaei, and A. Azizi, "Photocatalytic degradation of Crystal Violet dye in aqueous media using a novel magnetic nanocomposite Ag_2CrO_4/ag/$ZnFe_2O_4$/g-C_3N_4: Characterization, response surface methodology, kinetic and energy consumption studies," *J. Dispers. Sci. Technol.*, vol. 47, no. 5, pp. 862–878, Apr. 2026, doi: 10.1080/01932691.2024.2425964.

[84] Y. Nosaka and A. Y. Nosaka, "Generation and Detection of Reactive Oxygen Species in Photocatalysis," *Chem. Rev.*, vol. 117, no. 17, pp. 11302–11336, Sep. 2017, doi: 10.1021/acs.chemrev.7b00161.

[85] G. Asefa, D. Negussa, G. Lemessa, and T. Alemu, "The Study of Photocatalytic Degradation Kinetics and Mechanism of Malachite Green Dye on Ni–TiO2 Surface Modified with Polyaniline," *J. Nanomater.*, vol. 2024, pp. 1–11, Feb. 2024, doi: 10.1155/2024/5259089.

[86] N. Sebastian, W.-C. Yu, and D. Balram, "Ultrasensitive Electrochemical Detection and Plasmon-Enhanced Photocatalytic Degradation of Rhodamine B Based on Dual-Functional, 3D, Hierarchical Ag/ZnO Nanoflowers," *Sensors*, vol. 22, no. 13, p. 5049, Jul. 2022, doi: 10.3390/s22135049.

[87] S. Magaldi *et al.*, "Well diffusion for antifungal susceptibility testing," *International Journal of Infectious Diseases*, vol. 8, no. 1, pp. 39–45, Jan. 2004, doi: 10.1016/j.ijid.2003.03.002.

[88] H. M. Tran *et al.*, "Penicillium digitatum as a Model Fungus for Detecting Antifungal Activity of Botanicals: An Evaluation on Vietnamese Medicinal Plant Extracts," *Journal of Fungi*, vol. 8, no. 9, p. 956, Sep. 2022, doi: 10.3390/jof8090956.

[89] J. A. Kiehlbauch, G. E. Hannett, M. Salfinger, W. Archinal, C. Monserrat, and C. Carlyn, "Use of the National Committee for Clinical Laboratory Standards Guidelines for Disk Diffusion Susceptibility Testing in New York State Laboratories," *J. Clin. Microbiol.*, vol. 38, no. 9, pp. 3341–3348, 2000, doi: 10.1128/JCM.38.9.3341-3348.2000.

[90] B. Bonev, J. Hooper, and J. Parisot, "Principles of assessing bacterial susceptibility to antibiotics using the agar diffusion method," *Journal of Antimicrobial Chemotherapy*, vol. 61, no. 6, pp. 1295–1301, Mar. 2008, doi: 10.1093/jac/dkn090.

General Conclusion

This research successfully engineered, characterized, and modeled a novel, multi-functional quinary hybrid hydrogel nanocomposite matrix-composed of Bentonite clay, Chitosan, Cellulose, and sustainable camel-bone-derived Gelatin cross-linked inside a Polyvinyl Alcohol backbone (BCCG/PVA) proving its exceptional viability across environmental remediation, circular agricultural irrigation, and biomedical application fields.

- Crystallographic and spectroscopic characterization via FTIR-ATR and XRD confirmed successful synthesis, dense active functional group integration, and deep biopolymer chain intercalation within the silicate layers of the clay. These structural attributes established strong electrostatic interactions and prominent π--π stacking rings that acted as the primary driving forces behind the high-affinity binding of cationic target contaminants.
- Systematic batch adsorption experiments conducted under a 17-run Box-Behnken design demonstrated an outstanding maximum empirical Crystal Violet (CV) dye removal efficiency of 96.92% (m = 59 mg, t ≈ 20 min, pH ≈ 10) as opposed to Methyl Orange (MO) which yielded unremarkable results of 72.63% (m = 20mg, t ≈ 30 min, pH ≈ 4).
- Equilibrium tracking data conformed exceptionally well to the Langmuir non-linear isotherm model, yielding a maximum monolayer adsorption capacity of 89.02 mg/g at an initial dye concentration of 300 mg/L.
- Kinetic pathways tracked precisely along a pseudo-second-order mechanism, confirming a stable, chemisorption-governed rate-limiting process.
- Moving beyond clean-up efficiency, in vivo wheat seed (Triticum durum) germination assays validated the true engineering safety profile of the material for circular agricultural economies. While raw CV-polluted wastewater exerted severe eco-toxicological stress that stunted root and shoot development ($P < 0.0001$), irrigation with the BCCG/PVA-remediated effluent completely reversed this toxic stress, fully restoring seed germination parameters and tissue elongation to 100% of control levels.
- Concurrently, the study successfully bridged materials chemistry with advanced computational intelligence. A comparative machine learning investigation proved that a three-layer Artificial Neural Network (ANN) mapped multi-variable adsorption dynamics with superior predictive precision ($R^2 = 0.9984$), slashing residual error profiles (RMSE = 0.5627, MAPE = 0.7699%) by approximately 60% compared to classical empirical Response Surface Methodology (RSM). To exploit this predictive

power for process automation, evolutionary metaheuristic search tracks were evaluated. A Genetic Algorithm (GA) successfully bypassed the local minima traps that hindered the Grey Wolf Optimizer (GWO), identifying an absolute global operational coordinate optimum (m = 0.0487 g, t = 19.07 min, pH = 9.20) to hit a 100% theoretical dye removal efficiency at a minimized adsorbent mass threshold.

- Finally, in vitro therapeutic screenings revealed that the smart quinary composite possesses powerful, dose-dependent antimicrobial zones of inhibition against both Gram-negative (Escherichia coli) and Gram-positive (Staphylococcus aureus) bacterial strains, complemented by a robust antifungal capability.

Ultimately, this thesis establishes a cohesive and scalable engineering paradigm. By seamlessly combining low-cost material synthesis, strict eco-toxicological safety verification, biological utility, and high-degree AI-driven process optimization, this work offers a definitive template for advanced water purification and intelligent environmental management.

Future Recommendations

To expand upon the scientific and practical contributions established in this work, the following future research pathways are highly recommended:

- Continuous-Flow Fixed-Bed Column Studies: Transition from static batch configurations to continuous-flow fixed-bed column operations. Investigating breakthrough curves, flow rates, and bed depth parameters is crucial for translating this laboratory-scale quinary composite into real-world industrial wastewater treatment plants.
- Multi-Component and Real Industrial Effluent Testing: Evaluate the competitive adsorption capacity of the BCCG/PVA matrix using complex, multi-dye matrices and actual industrial effluents. Real wastewater contains competing surfactants, heavy metals, and high ionic strengths that will test the matrix's selective affinity under harsh, real-world conditions.
- Advanced Regeneration and Desorption Protocols: Conduct comprehensive cyclic desorption and reusability studies using mild eluent eluents (such as ethanol or dilute organic acids). Quantifying the matrix's structural stability and retention of removal efficiency over multiple regeneration cycles will solidify its economic viability.

- Deep-Tier Scaling of Metaheuristic Optimizers: Expand the computational intelligence framework by evaluating newer, self-adaptive hybrid metaheuristic algorithms (e.g., Hybrid PSO-GA or Aquila Optimizer). Integrating these algorithms directly with real-time laboratory automation hardware could allow for self-adjusting, intelligent water treatment systems.
- In-Depth Targeted Biomedical Testing: Given the material's strong antimicrobial zones of inhibition and antioxidant DPPH scavenging, future work should explore targeted biomedical formatting. Testing the hydrogel for controlled drug delivery, biocompatibility assays (such as hemocompatibility and cell viability), and wound-healing patch formation could open up high-value biomedical applications.
- Pilot-Scale Agricultural Integration: Scale up the seed germination findings into greenhouse or pilot-scale agricultural field trials. Long-term monitoring of soil chemistry, microbial community health, and crop yield across multiple generations will definitively certify the safe, long-term use of BCCG/PVA-remediated water for food crops.

Appendix A

Equipment & Instruments



Figure A.1: Benchtop centrifuge device (DLAB DM0412P)



Figure A.2: Fourier-Transform Infrared Spectroscopy (FTIR) spectrometer equipped with Diamond ATR.



Figure A.3: UV-Visible spectrophotometer (DLAB SP-V1100)



Figure A.4: Laboratory freeze-dryer / Lyophilizer (Christ Alpha 1-4 LDplus).



Figure A.5: Digital pH and temperature meter (Adwa AD1030)



Figure A.6: Laboratory drying oven (ELES Heat)



Figure A.7: High-capacity centrifuge instrument (Sigma 3-16L)



Figure A.8: Double-beam UV-Vis spectrophotometer (Shimadzu UV-1900i).



Figure A.9: Digital heating mantle with magnetic stirring.



Figure A.10: Ultrasonic water bath (Powersonic)**.**



Figure A.11: Thermostatic shaking water bath (Memmert).



Figure A.12. X-ray Diffractometer.



Figure A.13. Phenom ESEM.

Appendix B

Results & Products

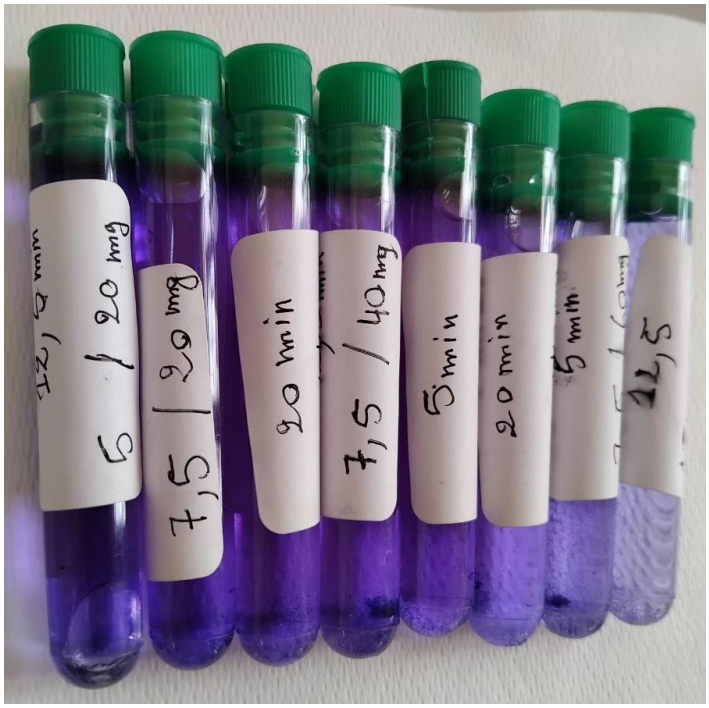


Figure B.1. Experimental variations in dye removal efficiency under different optimized parameters via RSM.

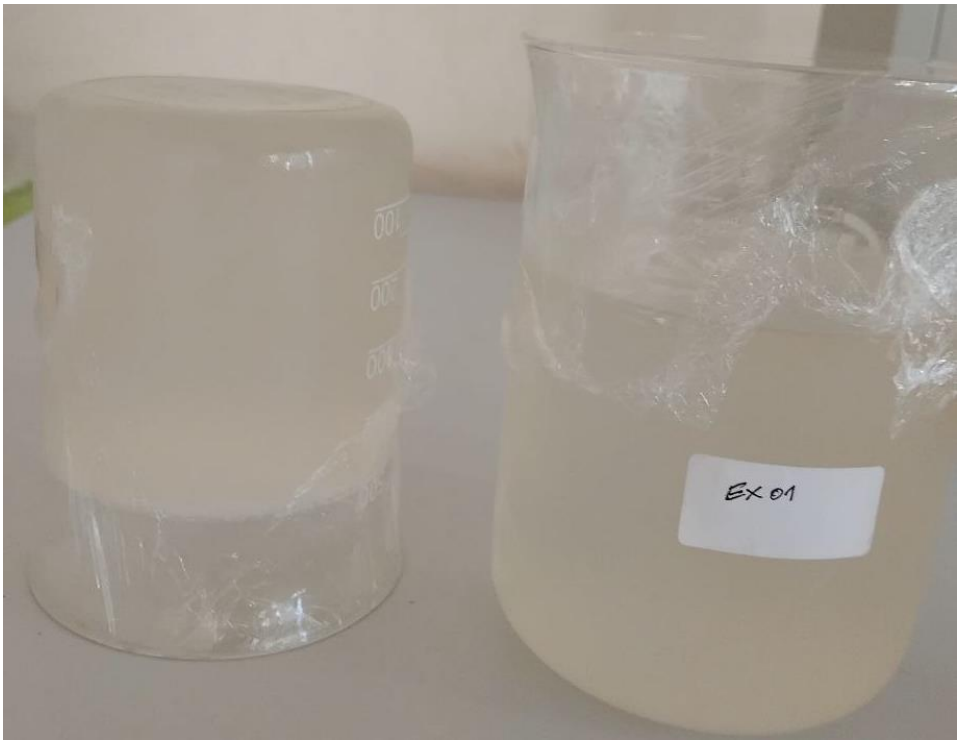


Figure B.2: Prepared gelatin solution gel.



Figure B.3. Transparency and physical inspection of the structured biopolymer matrix.



Figure B.4 Extracted camel bone ossein pieces obtained after the thermal extraction process of gelatin.



Figure B.5. Formation of the hybrid bio-composite beads in alkaline coagulation bath.

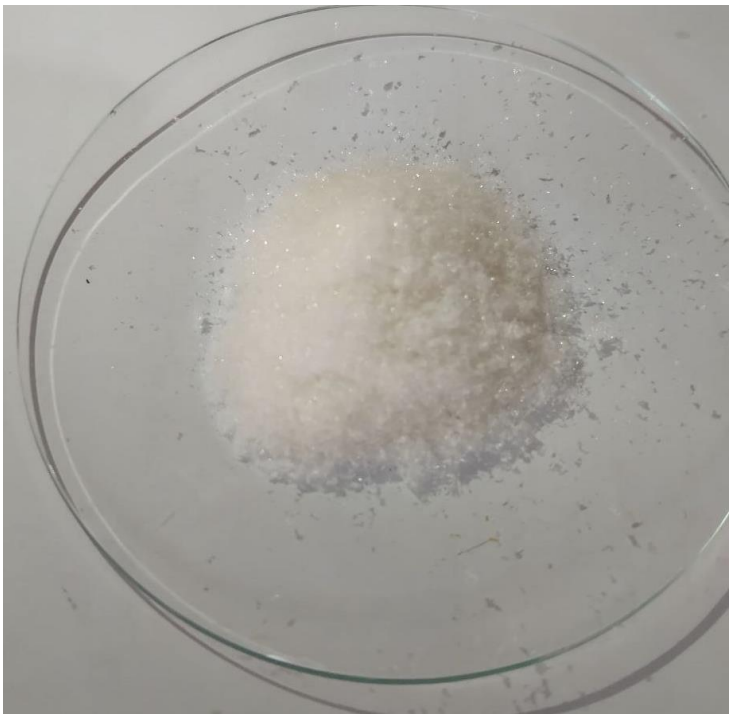


Figure B.6. Purified and dried gelatin powder extracted from camel bones.

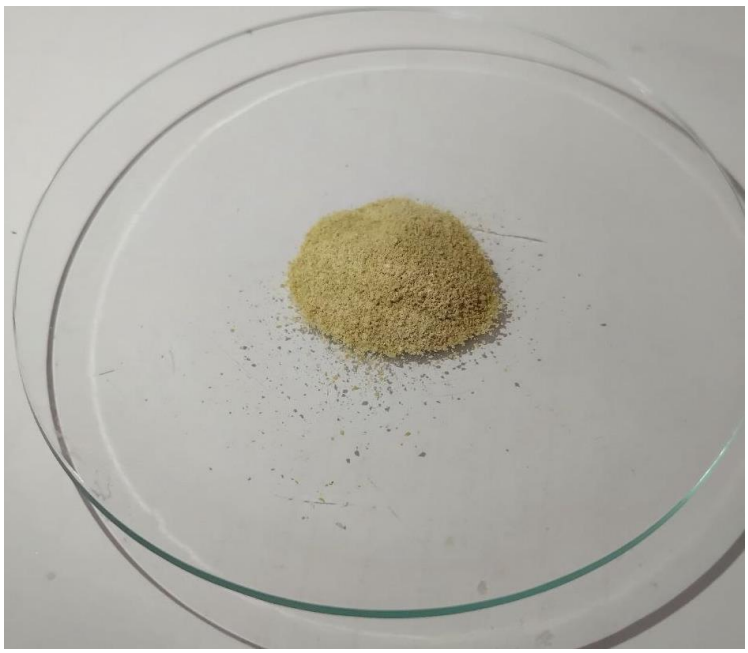
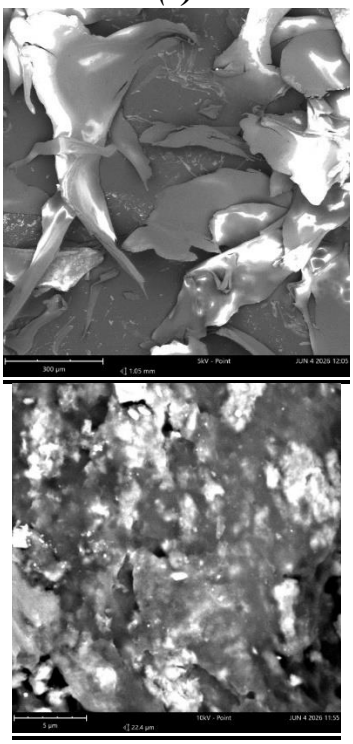


Figure B.7. Synthesized final hybrid bio-composite BCCG/PVA powder after drying and crushing.

(a)



(b)

Element Symbol	Atomic Conc.	Weight Conc.	Oxide Symbol	Stoich. wt Conc.
C	55.12	49.96		
N	27.61	29.18		
O	17.28	20.86		

Element Symbol	Atomic Conc.	Weight Conc.	Oxide Symbol	Stoich. wt Conc.
C	70.82	62.29		
O	25.08	29.39		
Si	2.86	5.88	SiO_2	15.82
Al	1.24	2.44	Al_2O_3	5.81

Figure B.8. Scanning electron microscopy (SEM) images of the BCCG/PVA powder: ***(a)*** Before Adsorption at 300 µm scale, and ***(b)*** After Adsorption at 5 µm scale.



Figure B.9. BCCG/PVA – CV solutions in the UV chamber.

Appendix C

Plagiat Similarity Report

16% Overall Similarity

The combined total of all matches, including overlapping sources, for each database.

Filtered from the Report

- Bibliography

Match Groups

546 Not Cited or Quoted 16%
Matches with neither in-text citation nor quotation marks

0 Missing Quotations 0%
Matches that are still very similar to source material

3 Missing Citation 0%
Matches that have quotation marks, but no in-text citation

0 Cited and Quoted 0%
Matches with in-text citation present, but no quotation marks

Top Sources

13% Internet sources
12% Publications
7% Submitted works (Student Papers)

Integrity Flags

0 Integrity Flags for Review

No suspicious text manipulations found.

Our system's algorithms look deeply at a document for any inconsistencies that would set it apart from a normal submission. If we notice something strange, we flag it for you to review.

A Flag is not necessarily an indicator of a problem. However, we'd recommend you focus your attention there for further review.

Match Groups

546 Not Cited or Quoted 16%
Matches with neither in-text citation nor quotation marks

0 Missing Quotations 0%
Matches that are still very similar to source material

3 Missing Citation 0%
Matches that have quotation marks, but no in-text citation

0 Cited and Quoted 0%
Matches with in-text citation present, but no quotation marks

Top Sources

13% Internet sources
12% Publications
7% Submitted works (Student Papers)

Top Sources

The sources with the highest number of matches within the submission. Overlapping sources will not be displayed.

1	Internet	
www.polyce-project.eu		2%
2	Internet	
www.mdpi.com		1%
3	Publication	
Sameeksha Rawat, S.M. Tauseef, Madhuben Sharma, Ajay Rautela, Ranjit G. Gura...		<1%
4	Internet	
pmc.ncbi.nlm.nih.gov		<1%
5	Student papers	
King Saud University		<1%
6	Internet	
baadalsg.inflibnet.ac.in		<1%
7	Publication	
Raouia Lebbihi, Larbi Haddad, Ammar Touhami Laiche, Gustavo Zepeda-Valles et ...		<1%
8	Internet	
edoc.pub		<1%
9	Internet	
link.springer.com		<1%
10	Publication	
Hadjer Bakdi, Hadjer Tolba, Nadjib Dahdouh, Soumia Benredouane et al. "Propoli...		<1%

11 Internet

assets-eu.researchsquare.com <1%

12 Internet

www.coursehero.com <1%

13 Internet

www.tandfonline.com <1%

14 Internet

www.researchsquare.com <1%

15 Student papers

University of Mosul <1%

16 Student papers

Malta College of Arts,Science and Technology <1%

17 Internet

ddd.uab.cat <1%

18 Internet

dspace.univ-eloued.dz <1%

19 Internet

www.deswater.com <1%

20 Internet

s3-eu-west-1.amazonaws.com <1%

21 Internet

etd.aau.edu.et <1%

22 Internet

sutir.sut.ac.th <1%

23 Publication

Arijit Dutta Gupta, Sweta Pandey, Vivek Kumar Jaiswal, Vivek Bhadauria, Harinder... <1%

24 Internet

repository.ui.edu.ng <1%

25 Student papers

Sharjah Education Academy <1%

26 Internet

www.britannica.com <1%

27 Internet

www.researchgate.net <1%

28 Internet

ar.scribd.com <1%

29 Internet

download.bibis.ir <1%

30 Publication

Bharat A. Bhanvase, Rajendra P. Ugwekar, Raju B. Mankar. "Novel Water Treatme... <1%

31 Internet

archives.univ-eloued.dz <1%

32 Publication

Akhtar Hameed, Muhammad Zahid. "Soil Nanotechnology", CRC Press, 2026 <1%

33 Internet

dokumen.pub <1%

34 Internet

www.jpbsci.com <1%

35 Publication

Mohamed E. Shaheen, Abdalla Y.E. Abdelwahab. "Laser ablation in liquids: A versa... <1%

36 Internet

dspace.univ-ghardaia.dz <1%

37 Publication

Saher Islam, Charles Oluwaseun Adetunji. "Viral and Antiviral Nanomaterials - Sy... <1%

38 Internet

neptjournal.com <1%

39 Student papers

Heriot-Watt University <1%

40 Internet

www.ur-net.go.jp <1%

41 Publication

Amir Kashtiaray, Peyman Ghorbani, Zahra Rashvandi, Mohammad Mehdi Salehi e... <1%

42 Student papers

Napier University <1%

43 Internet

dspace.univ-ouargla.dz <1%

44 Internet

propertibazar.com <1%

45 Publication

Yohanis Birhanu, Seyoum Leta. "Application of response surface methodology to ... <1%

46 Internet

es.scribd.com <1%

47 Publication

Mall, I.D.. "Adsorptive removal of malachite green dye from aqueous solution by ... <1%

48 Student papers

universititeknologimara <1%

49 Internet

pdfs.semanticscholar.org <1%

50 Publication

Darshan Malik, Nandita Narayanasamy, V A Pratyusha. "Essential Laboratory Tec... <1%

51 Internet

studia.reviste.ubbcluj.ro <1%

52 Internet

text-id.123dok.com <1%

53 Internet

distantreader.org <1%

54 Internet

www.matscisci.com <1%

55 Student papers

Queen's University of Belfast <1%

56 Student papers

University of Nottingham <1%

57 Internet

lirias.kuleuven.be <1%

58 Internet

www.scientifia.com <1%

59 Student papers

Delhi Technological University <1%

60 Internet

air.unimi.it <1%

61 Internet

dspace.aua.gr <1%

62 Internet

konfrans.ndu.edu.az <1%

63 Internet

scudderpublishing.com <1%

64 Internet

slideplayer.com <1%

65 Internet

westminsterresearch.westminster.ac.uk <1%

66 Publication

Farid Moeinpour, Fatemeh S. Mohseni-Shahri, Hossein Parvaresh, Elaheh NaserN... <1%

67 Internet

dspace.univ-bba.dz <1%

68 Internet

www.freepatentsonline.com <1%

69 Student papers

Lincoln Memorial University <1%

70 Publication

Magnan, Romain. "Oxyde Transparent Conducteur de ZnO:V à Partir D'une Cible ... <1%

71 Student papers

Universite De Tlemcen <1%

72 Internet

journals.lww.com <1%

73 Internet

spiral.imperial.ac.uk <1%

74 Internet

wydawnictwo.umcs.eu <1%

75 Internet

core.ac.uk <1%

76 Publication

Acharya, Sujal. "Synthesis, Structural Characterization and Optical Studies of Silve... <1%

77 Publication

Gurses, A.. "The adsorption kinetics of the cationic dye, methylene blue, onto clay... <1%

78 Publication

Kumar, A.. "Adsorptive removal of acrylonitrile by commercial grade activated ... <1%

79 Internet

peerj.com <1%

80 Publication

R. K. Naresh, R. K. Gupta, Rajbir Garg, R. K. Sohane, J. P. Singh, O. P. Gupta, Arun K... <1%

81	Internet	
d.docksci.com		<1%
82	Internet	
fastercapital.com		<1%
83	Internet	
ijred.cbiore.id		<1%
84	Internet	
publication-theses.unistra.fr		<1%
85	Student papers	
Tunisian Consortium		<1%
86	Student papers	
University College London		<1%
87	Student papers	
University of Limerick		<1%
88	Publication	
Xiaoli Wang, He Zhang, Yalin Wang, Shaoming Yang. "ELM-Based AFL–SLFN Model...		<1%
89	Internet	
norma.ncirl.ie		<1%
90	Internet	
tel.archives-ouvertes.fr		<1%
91	Internet	
theses.hal.science		<1%
92	Internet	
www.hindawi.com		<1%
93	Internet	
www.nanorem.eu		<1%
94	Internet	
zenodo.org		<1%

95 Publication

Fabián Fernández-Luqueño, Fernando López-Valdez, Gabriela Medina-Pérez. "Bio ... <1%

96 Publication

Stephanie A. Kedzior, Lexa Graham, Carolyn Moorlag, Brynn M. Dooley, Emily D. C... <1%

97 Student papers

The University of Manchester <1%

98 Student papers

University of Liverpool <1%

99 Internet

arabjchem.org <1%

100 Internet

biblio.ugent.be <1%

101 Internet

datapdf.com <1%

102 Internet

iwaponline.com <1%

103 Internet

journals.nauka-nanrk.kz <1%

104 Internet

ujcontent.uj.ac.za <1%

105 Student papers

Arts, Sciences & Technology University In Lebanon <1%

106 Publication

Maria Grozdanić, Morana Mihaljević, Hrvoje Cajner, Damir Godec. "Influence of L... <1%

107 Student papers

Ubon Ratchathani University <1%

108 Internet

elea.unisa.it:8080 <1%

109 Student papers

Central University of Punjab <1%

110 Student papers

Imperial College of Science, Technology and Medicine <1%

111 Publication

Rosângela A. Jacques, Renata Bernardi, Marcela Caovila, Eder C. Lima, Flávio A. Pa... <1%

112 Publication

Simeng Li, Madjid Mohseni. "Adsorption of Methyl Red on Poly(diallyldimethylam... <1%

113 Internet

jrcd.eu <1%

114 Internet

pdffox.com <1%

115 Internet

re.public.polimi.it <1%

116 Student papers

A'Sharqiyah University, Oman <1%

117 Student papers

Indian Institute of Technology Guwahati <1%

118 Publication

Nazrul Islam. "Handbook of Lung Targeted Drug Delivery Systems - Recent Trend... <1%

119 Publication

Pankaj Kumar Chaurasia, Shashi Lata Bharati, Sunita Singh, Ashutosh Mani. "Plan... <1%

120 Student papers

Universiti Malaysia Perlis <1%

121 Student papers

Universiti Sains Malaysia <1%

122 Internet

jfrm.ru <1%

123 Internet

journal.walisongo.ac.id <1%

124 Internet

www.frontiersin.org <1%

125 Student papers

7996 <1%

126 Student papers

Al Akhawayn University in Ifrane <1%

127 Publication

Li-Sheng Chen, Ben-Hua Fei, Xin-Xin Ma, Ji-Ping Lu, Chang-Hua Fang. "Investigatio... <1%

128 Publication

Sitansh Sharma. "Design of laser pulses for selective vibrational excitation of the ... <1%

129 Internet

docksci.com <1%

130 Internet

dr.ntu.edu.sg <1%

131 Internet

irep.iium.edu.my <1%

132 Internet

lutpub.lut.fi <1%

133 Internet

m.moam.info <1%

134 Internet

pt.scribd.com <1%

135 Internet

pure.tue.nl <1%

136 Internet

www.scielo.br <1%

137 Publication

Aixin Yu, Yuankun Liu, Xing Li, Yanling Yang, Zhiwei Zhou, Hongrun Liu. "Modelin... <1%

138 Publication

Jeanmaire, D.L.. "Surface raman spectroelectrochemistry", Journal of Electroanaly... <1%

139 Student papers

Liverpool John Moores University <1%

140 Publication

Narasimhan, B.. "Quantitative structure-activity relationship studies for predictio... <1%

141 Publication

Sun, Q.. "The adsorption of basic dyes from aqueous solution on modified peat-... <1%

142 Student papers

Universiti Putra Malaysia <1%

143 Student papers

University of Leeds <1%

144 Student papers

Université Sétif 1 Ferhat Abbas <1%

145 Internet

acikbilim.yok.gov.tr <1%

146 Internet

dlibrary.univ-boumerdes.dz:8080 <1%

147 Internet

docslib.org <1%

148 Internet

doczz.net <1%

149 Internet

hal-brgm.archives-ouvertes.fr <1%

150 Internet

www.aidic.it <1%

151 Internet

www.biorxiv.org <1%

152 Publication

"Nanomaterials in the Environment", American Society of Civil Engineers (ASCE), ... <1%

153 Student papers

Kwame Nkrumah University of Science and Technology <1%

154 Publication

M. K. Purkait, D. S. Gusain, S. DasGupta, S. De. "Adsorption Behavior of Chrysoidin... <1%

155 Publication

Tahmid Hasan Rupam, Hongbin Ma, Bidyut Baran Saha. "Basic principles of adsor... <1%

156 Internet

acta.sze.hu <1%

157 Internet

ijcmas.com <1%

158 Internet

pharmacy.mahidol.ac.th <1%

159 Internet

researchrepository.ru.ac.za <1%

160 Internet

sanad.iau.ir <1%

161 Internet

shodhganga.inflibnet.ac.in <1%

162 Internet

worldwidescience.org <1%

163 Publication

Gbetibouo, Glwadys Aymone. "Vulnerability and Adaptation of Farming to Climat... <1%

164 Publication

Goswami, Anshuman. "Application of Spatially Resolved Kinetic Monte Carlo Simu... <1%

165 Publication

Jiji Abraham, Beena Jose, Anjali Jose, Sabu Thomas. "Characterization of green na... <1%

166 Publication

Mashan Almutairi, Ahmed Adel Ali Youssef, Gehad M. Subaiea, Ahmed Alobaida, S... <1%

167 Publication

Sana Sadaf, Haq Nawaz Bhatti, Shaukat Ali, Khalil-ur Rehman. "Removal of Indoso... <1%

168 Publication

Suhong Chen, Qinyan Yue, Baoyu Gao, Xing Xu. "Equilibrium and kinetic adsorpti... <1%

169 Student papers

University of Southampton <1%

170 Publication

Vunain, Ephraim. "Fabrication of Polymer Composites and Their Application Towa... <1%

171 Publication

Yashaswi Karnati, Dhruv Mahajan, Tania Banerjee, Rahul Sengupta et al. "Data A... <1%

172 Internet

accessapps.amdi.usm.my <1%

173 Internet

downloads.hindawi.com <1%

174 Internet

dspace.upt.ro <1%

175 Internet

encyclopedia.pub <1%

176 Internet

f1000research-files.f1000.com <1%

177 Internet

file.scirp.org <1%

178 Internet

healthdocbox.com <1%

179 Internet

ir.jkuat.ac.ke <1%

180 Internet

mts.intechopen.com <1%

181 Internet

ncert.app <1%

182 Internet

official.satbayev.university <1%

183 Internet

repositorio.upch.edu.pe <1%

184 Internet

soapubs.com <1%

185 Internet

tarjomefa.com <1%

186 Internet

technorep.tmf.bg.ac.rs <1%

187 Internet

umpir.ump.edu.my <1%

188 Publication

Aliyazicioglu, Cigdem. "Quantification of Sensitive Nitrogen Converting Organism... <1%

189 Publication

Anirudhan, T.S.. "Amine-modified polyacrylamide-bentonite composite for the ad... <1%

190 Publication

Gurajada, Dinesh. "Adoption of Artificial Intelligence (AI) in Enhancing Organizati... <1%

191 Publication

Haihui Bai, Qingsong Zhang, Tao He, Guo Zheng, Guoqing Zhang, Linbao Zheng, S... <1%

192 Publication

John, Andrea. "Molekulare Charakterisierung invasiver und nicht-invasiver Grupp... <1%

193 Publication

Jurko, Lucija. "Synthesis of Betaine, Choline and Carnitine Containing Polymers fo... <1%

194 Publication

Lv, L.. "Factors influencing the removal of fluoride from aqueous solution by cal... <1%

195 Publication

Rifaqat Ali Khan Rao, Amna Khatoon. "Aluminate treated Casuarina equisetifolia l... <1%

196 Publication

Shilin Dai, Alieta Eyles, Cunyu Li, Qinan Wu, Dugald C. Close. "Isolation and struct... <1%

197 Publication

Vivek Dave, Deependra Singh, Pallerla Naveen Reddy. "Nanocomposites and Nan... <1%

198 Internet

archive.org <1%

199 Internet

cdn.juris.id <1%

200 Internet

docsdrive.com <1%

201 Internet

etheses.whiterose.ac.uk <1%

202 Internet

hal.science <1%

203 Internet

orca.cf.ac.uk <1%

204 Internet

repositorium.uminho.pt <1%

205 Internet

terpconnect.umd.edu <1%

206 Internet

theses.gla.ac.uk <1%

207 Internet

uvadoc.uva.es <1%

208 Internet

vdoc.pub <1%

209 Internet

www.preinvestigo.biblioteca.uvigo.es <1%

210 Publication

Ahmed Barhoum, M. Luisa García-Betancourt, Hubert Rahier, Guy Van Assche. "P... <1%

211 Student papers

American University in Cairo <1%

212 Publication

Andrzej Zieliński, Tomasz Moskalewicz, Aldo R. Boccaccini. "Surface Modifications ... <1%

213 Publication

Arikan, Mehmet Emin. "Determination of Susceptibility to Intergranular Corrosio... <1%

214 Publication

Debnath, Sujit Kumar. "Nanoparticulate Drug Delivery System for Tuberculosis.", ... <1%

215 Publication

Elias Flores, Giovanni Gadda. " Kinetic Characterization of PA1225 from PAO1 Rev... <1%

216 Publication

Fernanda Maria Policarpo Tonelli, H. C. Ananda Murthy, Letícia Fernandes de Oliv... <1%

217 Publication

Hamdaoui, O.. "Sorption of malachite green by a novel sorbent, dead leaves of pl... <1%

218 Student papers

Higher Education Commission Pakistan <1%

219 Publication

Kadirvelu, K.. "Activated carbon from industrial solid waste as an adsorbent for th... <1%

220 Publication

Kajal Sundaray, Avishek Kar, Gagan B.N. Chainy, Umakanta Subudhi. "Differential... <1%

221 Publication

Kollipara, Sree Divya. "Stability of Lidocaine HCL and Epinephrine Combinations i... <1%

222 Publication

Mohamed A. Salem, Rehab G. Elsharkawy, Mahmoud F. Hablas. "Adsorption of bri... <1%

223 Publication

Muhammad Aqeel Ashraf, Masroor Hussain, Karamat Mahmood, Abdul Wajid, Mo... <1%

224 Publication

Negin Sohrabi, Reza Mohammadi, Hamid Reza Ghassemzadeh, Seyed Sadegh Sey... <1%

225 Publication

Nethaji, S.. "Adsorption of Malachite Green dye onto activated carbon derived fro... <1%

226 Publication

P. Senthil Kumar, S. Ramalingam, R. V. Abhinaya, K. V. Thiruvengadaravi, P. Baska... <1%

227 Publication

Rohit Duglet, Deepika Sharma, Vijay Singh, Navneet Verma, Dheeraj Sharma, M. S... <1%

228 Publication

Strube, Jan. "Analysis of radiative decays of charged B mesons to baryonic final st... <1%

229 Publication

Sungkyu Seo, Sachin Gupta, Samir Kumar, Chandra Shakher Pathak. "Advances in... <1%

230 Publication

Ton Duc Thang University <1%

231 Student papers

University of Carthage <1%

232 Publication

Yalemtsehay Debebe, Esayas Alemayehu, Zemene Worku, Wookeun Bae, Bernd L... <1%

233 Internet

bio-protocol.org <1%

234 Internet

colloidalsilversecrets.blogspot.com <1%

235 Internet

dac.umt.edu.my:8080 <1%

236 Internet

dc.library.okstate.edu <1%

237 Internet

dl.icdst.org <1%

238 Internet

dokumen.tips <1%

239 Internet

dspace.cuni.cz <1%

240 Internet

eprints.lib.hokudai.ac.jp <1%

241 Internet

eprints.whiterose.ac.uk <1%

242 Internet

hal.univ-lorraine.fr <1%

243 Internet

harvest.usask.ca <1%

244 Internet

journal.hep.com.cn <1%

245 Internet

mdpi-res.com <1%

246 Internet

minerva.usc.es <1%

247 Internet

papyrus.bib.umontreal.ca <1%

248 Internet

phd-dissertations.unizik.edu.ng <1%

249 Internet

pubs.rsc.org <1%

250 Internet

pure.rug.nl <1%

251 Internet

research-repository.st-andrews.ac.uk <1%

252 Internet

scientiaplena.emnuvens.com.br <1%

253 Internet

seesport.eu <1%

254 Internet

static.lenovo.com <1%

255 Internet

term.sustainability-directory.com <1%

256 Internet

thesis.caltech.edu <1%

257 Internet

toubkal.imist.ma <1%

258 Internet

www.elis.sk <1%

259 Internet

www.iieta.org <1%

260 Internet

www.scinapse.io <1%

261 Internet

www.smolecule.com <1%

262 Internet

www.tdx.cat <1%

263 Publication

Ali Haider, Muhammad Ikram, Asma Rafiq. "Green Nanomaterials as Potential An... <1%

264 Publication

Doha Berraaouan, Mohamed Tirinsi, Ramzi A. Mothana, Hanan M. Al-Yousef, Mari... <1%

265 Publication

Eren, Z.. "Equilibrium and kinetic mechanism for Reactive Black 5 sorption onto ... <1%

266 Publication

Gates, Stacy Dione. "Cation influence on negative thermal expansion in the A2-(tu... <1%

267 Publication

Huan Yue, Luxia Gou, Zhenrong Tang, Yuyang Liu, Shengchun Liu, Hua Tang. "Co... <1%

268 Publication

Mohamed Khalid AlOmar, Mohammed Abdulhakim Alsaadi, Maan Hayyan, Shatir... <1%

269 Publication

Rajendra Kumar Goyal. " Nanomaterials and Nanocomposites - Synthesis, P... <1%

270 Publication

Vinita Kumari, Ravindra Budania, Vishwajit Chavda. "Design of iron-loaded mont... <1%

271 Publication

dos Santos, Tiago Pereira. "Simulation, Optimization and Experimental Validation... <1%

272 Publication

Alnahhal, Ahmed M.E.. "Performance Evaluation of Lightweight Normal and Geop... <1%

273 Publication

Hafiza Amna Haq, Tariq Javed, Muhammad Amin Abid, Shagufta Zafar, Muhamma... <1%

274 Publication

Jawad, Ali H., Ramlah Abd Rashid, Mohd Azlan Mohd Ishak, and Lee D. Wilson. "Ad... <1%

275 Publication

Kabanyana, Jeanne Françoise. "Optimisation de la Sporulation des Bactéries Prob... <1%

276 Publication

María Gabriela Rojas, Víctor Navarro, Daniel Alonso, María Yolanda Ríos, Jaime To... <1%

277 Publication

Narendra Kumar, Sunita Kumbhat. "Essentials in Nanoscience and Nanotechnolo... <1%

278 Publication

Ojha, Amit Kumar, and Vijaya Kumar Bulasara. "Adsorption characteristics of jack... <1%

279 Publication

Rui Yang. "Analytical Methods for Polymer Characterization", Routledge, 2018 <1%

280 Publication

Srivastava, V.C.. "Characterization of mesoporous rice husk ash (RHA) and adsorp... <1%

281 Publication

Vitthalbhai, Radadiya Rainish. "Development of Nano-Composite Textiles for Bio-... <1%